

Advancements in Angular Domain Optical Imaging in Biological Tissue

by

Fartash Vasefi

M.A.Sc., University of Western Ontario, 2005
B.Sc., Iran University of Science and Technology, 2001

Thesis Submitted in Partial Fulfillment
of the Requirements for the Degree of
Doctor of Philosophy

in the
Engineering Science
Faculty of Applied Sciences

© Fartash Vasefi 2010

SIMON FRASER UNIVERSITY

Fall 2010

All rights reserved.

However, in accordance with the *Copyright Act of Canada*, this work may be reproduced, without authorization, under the conditions for "Fair Dealing." Therefore, limited reproduction of this work for the purposes of private study, research, criticism, review and news reporting is likely to be in accordance with the law, particularly if cited appropriately.

APPROVAL

Name: **Fartash Vasefi**
Degree: **Ph. D of Applied Science**
Title of Thesis: **Advancements in angular domain optical imaging in biological tissues**

Examining Committee:

Chair: **Dr. Carlo Menon, PEng**
Chair
Assistant Professor, School of Engineering Science

Dr. Bozena Kaminska
Senior Supervisor
Professor, School of Engineering Science

Dr. Glenn H. Chapman, PEng
Supervisor
Professor, School of Engineering Science

Dr. Jeffrey J.L. Carson
Supervisor
Assistant Professor, University of Western Ontario

Dr. Marinko Sarunic, PEng
Internal Examiner
Assistant Professor, School of Engineering Science

Dr. Haishan Zeng
External Examiner
Associate Professor, Dermatology and Skin Science,
University of British Columbia

Date Defended/Approved: 30 March 2010



SIMON FRASER UNIVERSITY
LIBRARY

Declaration of Partial Copyright Licence

The author, whose copyright is declared on the title page of this work, has granted to Simon Fraser University the right to lend this thesis, project or extended essay to users of the Simon Fraser University Library, and to make partial or single copies only for such users or in response to a request from the library of any other university, or other educational institution, on its own behalf or for one of its users.

The author has further granted permission to Simon Fraser University to keep or make a digital copy for use in its circulating collection (currently available to the public at the "Institutional Repository" link of the SFU Library website <www.lib.sfu.ca> at: <<http://ir.lib.sfu.ca/handle/1892/112>>) and, without changing the content, to translate the thesis/project or extended essays, if technically possible, to any medium or format for the purpose of preservation of the digital work.

The author has further agreed that permission for multiple copying of this work for scholarly purposes may be granted by either the author or the Dean of Graduate Studies.

It is understood that copying or publication of this work for financial gain shall not be allowed without the author's written permission.

Permission for public performance, or limited permission for private scholarly use, of any multimedia materials forming part of this work, may have been granted by the author. This information may be found on the separately catalogued multimedia material and in the signed Partial Copyright Licence.

While licensing SFU to permit the above uses, the author retains copyright in the thesis, project or extended essays, including the right to change the work for subsequent purposes, including editing and publishing the work in whole or in part, and licensing other parties, as the author may desire.

The original Partial Copyright Licence attesting to these terms, and signed by this author, may be found in the original bound copy of this work, retained in the Simon Fraser University Archive.

Simon Fraser University Library
Burnaby, BC, Canada

ABSTRACT

Angular Domain Imaging (ADI) is a technique for performing optical imaging through highly scattering media. The basis for the technique is the micro-machined Angular Filter Array (AFA), which provides a parallel collection of micro-tunnels that accept ballistic/quasi-ballistic image-bearing photons and reject multiply scattered photons that result in image-destroying background noise. At high scattering levels, ADI image contrast declines due to the non-uniform scattered background light within the acceptance angle of the AFA. In this thesis, I developed multiple methodologies to correct for this problem and enhance ADI image contrast at higher scattering levels. These methodologies included combining ADI with time gating, polarization gating and employing image processing to estimate the background scattered light and use this information to enhance ADI image contrast and resolution. Furthermore, I conducted a comprehensive experimental investigation on a new AFA geometry designed to reduce the reflections within the micro-tunnels to reduce the unwanted background noise caused by multiply scattered photons.

Building on previous studies with ADI in a trans-illumination configuration, I demonstrated that ADI could also be used to capture information-carrying photons from diffuse light back-reflected from tissue, where illumination was from the same side as the AFA. This mode of operation will enable applications of ADI where trans-illumination of samples is not possible. I also developed a

tomographic ADI modality that rotated the sample and compiled ADI shadowgrams at each angle into a sinogram, followed by reconstruction of a transverse image with depth information. I also exploited the collimation detection capabilities of the AFA to extract photons emitted by a fluorophore embedded at depth within a turbid medium. The fluorescent imaging system using AFA offered higher resolution and contrast compared to a conventional lens and lens-pinhole fluorescent detection system in both in vitro and animal tests.

Optical imaging with an AFA does not depend on coherence of the light source or the wavelength of light. Therefore, it is a promising candidate for multispectral/hyperspectral imaging to localize absorption and/or fluorescence in tissue and may have particular importance in cancer optical imaging.

Keywords: Imaging through turbid media, Multispectral and Hyperspectral imaging, Noise in imaging systems, Light propagation in tissues, Time-resolved imaging, Tomographic imaging.

CO-AUTHORSHIP

The thesis includes material from six publications, all of which had contributions from co-authors, as follows:

Chapter 2: F. Vasefi, B. Kaminska, P. K. Y. Chan, and G. H. Chapman, "Multi-spectral angular domain optical imaging in biological tissues using diode laser sources," *Optics Express* 16, 14456-14468 (2008)

Mr. Chan wrote the scanning software for the imaging system and involved in part of the optical setup; Dr. Kaminska provided project concept, read and edited the manuscript and provided supervision; Dr. Chapman provided project concept, read and edited the manuscript and provided supervision. I designed and performed the optical setup for the imaging system, quantified imaging performance for homogenous and tissue samples, analyzed and interpreted the results and wrote the manuscript.

Chapter 3: F. Vasefi, B. Kaminska, G. H. Chapman, and J. J. L. Carson, "Image contrast enhancement in angular domain optical imaging of turbid media," *Opt. Express* 16, 21492-21504 (2008)

Dr. Kaminska provided project concept, read and edited the manuscript and provided supervision; Dr. Chapman provided project concept especially the noise estimation using wedge prism, read and edited the manuscript and provided supervision; Dr. Carson provided project concept using polarization filtering,

provided fabrication facility in University of Western Ontario, read and edited the manuscript and provided supervision; I designed and fabricated the new square shape Angular filter array employed in the experiments, developed and designed the optical system as well as software analysis for the contrast enhancement analysis, quantified imaging performance of imaging system in turbid medium, analyzed and compared the results and wrote the manuscript.

Chapter 4: F. Vasefi, M. Najiminaini, E. Ng, B. Kaminska, G. H.

Chapman, and J. J.L. Carson, “Angular domain trans-illumination imaging optimization with an ultra-fast gated camera”, submitted to Journal of Biomedical optics, SPIE (2010)

Mr. Najiminaini was involved on the theoretical analysis for micro-channel wall reflection analysis. Mr. Ng was involved on experimental work specially scanning software development using time-gated camera. Dr. Kaminska provided project concept, read and edited the manuscript and provided supervision. Dr. Chapman provided project concept of patterning channel walls for reflection suppression, read and edited the manuscript and provided supervision. Dr. Carson provided project concept, fabrication facility, and time gating experimental instruments in University of Western Ontario, read and edited the manuscript and provided supervision. I designed and fabricated the new reflection-trapped square shape Angular filter array employed in the experiments, developed and designed the optical system as well as software analysis for the contrast enhancement analysis, quantified imaging performance of imaging system in turbid medium, analyzed and compared the results and wrote the manuscript.

Chapter 5: F. Vasefi, P. K. Y. Chan, B. Kaminska, G. H. Chapman, and N. Pfeiffer, "An Optical Imaging Technique Using Deep Illumination in the Angular Domain", IEEE Journal of Selected Topics in Quantum Electronics. 13(6): 1610-1620 (2007)

Mr. Chan wrote the scanning software for the imaging system and involved in part of the optical setup using Argon laser; Dr. Kaminska provided project concept, read and edited the manuscript and provided supervision; Dr. Chapman provided project concept, read and edited the manuscript and provided supervision. Dr. Pfeiffer involved on project discussions. I designed and performed the optical setup for the imaging system, quantified imaging performance for homogenous and tissue samples, designed and performed digital image processing algorithm, analyzed and interpreted the results and wrote the manuscript.

Chapter 6: F. Vasefi, E. Ng, B. Kaminska, G. H. Chapman, K. Jordan, and J. J. L. Carson, "Transmission and fluorescence angular domain optical projection tomography of turbid media," Applied Optics 48, 6448-6457 (2009)

Mr. Ng was involved on experimental work specially scanning software development for sample rotation. Dr. Kaminska provided project concept, read and edited the manuscript and provided supervision; Dr. Chapman read and edited the manuscript and provided supervision. Dr. Carson provided project concept, fabrication facility, and required experimental instruments in University of Western Ontario, read and edited the manuscript and provided supervision. I,

developed and designed the optical system as well as software development for tomographic reconstruction and image enhancements, quantified imaging performance of imaging system in turbid medium, analyzed and compared the results and wrote the manuscript.

Chapter 7: F. Vasefi, M. Belton, B. Kaminska, G. H. Chapman, and J. J. L. Carson, “ Angular Domain Fluorescence Imaging for Small Animal Research”, Journal of Biomedical Optics, 15(01) (2010)

Ms. Belton prepared the mouse samples tagged with fluorescent dye. Dr. Kaminska provided project concept, read and edited the manuscript and provided supervision; Dr. Chapman read and edited the manuscript and provided supervision. Dr. Carson provided project concept, fabrication facility, and required experimental instruments in University of Western Ontario, read and edited the manuscript and provided supervision. I designed and fabricated the new reflection-trapped square shape Angular filter array employed in the experiments, developed and designed the optical system as well as software development for removing artefacts and image enhancements, quantified imaging performance of imaging system in turbid medium, analyzed and compared the results and wrote the manuscript.

Dedicated to

***My beloved family and friends who give me exceptional support,
determination, and enthusiasm.***

ACKNOWLEDGEMENTS

I would like to express my sincere appreciation to my senior supervisor, Dr. Bozena Kaminska who gave me a chance to work on this project. Without her guidance, patience, and support, this thesis would never have been completed. I am also grateful to have the support of my co- supervisor Dr. Glenn H. Chapman who provided valuable discussions which were essential toward completing my thesis. Special thanks to my co-supervisor, Dr. Jeferry J. L. Carson who taught me a lot while I was conducting my research in his lab at Lawson Health Research Institute, and provided me necessary tools to conduct my research. I am also very thankful of Dr. Marinko Sarunic for his precious suggestion and enthusiasm he gave me throughout my studies. I really appreciate Dr. Haishan Zeng for expressing his enthusiasm in my research studies and acting as the external examiner for my PhD defence.

I would like to acknowledge the support of my co-workers who turned out to be my best friends during my PhD studies. Special thanks for Mr. Kouhyar Tavakolian, and Mohamadreza Najiminaini for their help and support. I am very thankful of ADI project members specially Mr. Paulman Chan for his unconditional support and patience helping me to start in ADI, Dr. Nicholas Pfeiffer as our senior PhD student for his valuable discussions, and also Mr. Eldon Ng for his grateful teamwork and enthusiasm.

I would like to thank Mr. William Woods, for helping me in my clean room activities in Simon Fraser University. I am also very thankful of Dr. Todd Simpson and Dr. Rick Glew for their support and guidance in Nanofabrication lab at University of Western Ontario.

This work was supported in part by the Natural Sciences and Engineering Research Council of Canada, Simon Fraser University, the Lawson Health Research Institute, and the London Regional Cancer Program.

TABLE OF CONTENTS

Approval.....	ii
Abstract.....	iii
Co-authorship.....	v
Acknowledgements.....	x
Table of Contents.....	xii
List of Figures.....	xvi
List of Tables.....	xxii
Glossary.....	xxiii
1: Introduction.....	1
1.1 Background.....	1
1.2 Light-tissue interactions.....	5
1.2.1 The radiation transport model.....	6
1.2.2 Scattering phase function approximation.....	9
1.2.3 Diffusion approximation.....	10
1.2.4 Collimated transmission through turbid media.....	12
1.3 Overview of prior works in optical imaging.....	15
1.3.1 Time domain optical imaging.....	16
1.3.2 Optical coherence tomography.....	18
1.3.3 Diffuse optical tomography.....	20
1.3.4 Photoacoustic tomography.....	22
1.3.5 Optical imaging modalities review.....	24
1.4 Angular domain imaging.....	25
1.4.1 Overview of ADI methodology.....	27
1.5 Angular filter array fabrication.....	29
1.6 Prior work in ADI.....	31
1.7 Thesis objective and scope.....	34
1.8 Research approach.....	34
1.9 Reference list.....	38
2: Multi-spectral angular domain optical imaging in biological tissues using diode laser sources.....	43
2.1 Abstract.....	43
2.2 Introduction.....	43
2.3 Light tissue interaction.....	46
2.4 Angular domain imaging principle.....	48
2.5 Methodology.....	55
2.6 Results and discussions.....	60
2.7 Conclusion.....	67

2.8	Reference list	68
3: Image contrast enhancement in angular domain optical imaging of turbid media		
71		
3.1	Abstract.....	71
3.2	Introduction	71
3.3	Light-tissue interaction	73
3.4	Angular domain imaging.....	76
3.4.1	Principle of operation	76
3.4.2	Mechanisms of loss of image contrast in ADI	80
3.5	Methodology	84
3.5.1	Experimental setup (ADI).....	84
3.5.2	Phantoms	86
3.5.3	Estimation of background scattered light using polarization discrimination (PADI & PADI-CS)	87
3.5.4	Estimation of background scattered light using deviated light (ADI-WS).....	89
3.5.5	Combined approach (PADI-WS).....	90
3.6	Results and discussion.....	91
3.6.1	Detection limit imposed by sample thickness and Intralipid™ concentration	91
3.6.2	Image contrast enhancement by wedge-based subtraction (ADI-WS)	91
3.6.3	Image contrast enhancement by polarization-based subtraction (PADI)	93
3.6.4	Image contrast enhancement by combined use of wedge and polarization-based subtraction (PADI-WS).....	94
3.6.5	Comparison of image contrast enhancement methods	94
3.7	Conclusion	96
3.8	Reference list.....	97
4: Angular domain trans-illumination imaging optimization with an ultra-fast gated camera.....		
100		
4.1	Abstract.....	100
4.2	Introduction	101
4.2.1	Background and motivation	101
4.2.2	Angular domain imaging principle	103
4.2.3	Improvement of ADI by new AFA designs and time-gating	104
4.2.4	Objective and approach.....	106
4.3	Methods	107
4.3.1	Fabrication of tissue mimicking phantoms	107
4.3.2	Conventional angular filter arrays	110
4.3.3	Reflection-trapped angular filter arrays	111
4.3.4	Ray trace analysis of AFA geometries	112
4.3.5	Wedge subtraction method	115
4.3.6	Angular domain imaging (CW) setup	116
4.3.7	Time-angular domain imaging system setup.....	117
4.3.8	Image analysis.....	118
4.4	Results and discussion.....	119

4.4.1	Ray trace analysis of AFA geometries	119
4.4.2	Micro-channel wall reflection suppression with reflection-trapped AFAs	121
4.4.3	Background suppression by wedge subtraction for various AFA geometries.....	122
4.4.4	Background suppression by time-angular domain imaging	126
4.4.5	Implications of scattering level to scan time	131
4.5	Conclusion	132
4.6	Acknowledgment.....	134
4.7	References.....	134
5: An Optical Imaging Technique Using Deep Illumination in the Angular Domain.....		138
5.1	Abstract.....	138
5.2	Introduction	139
5.3	Light-tissue Interaction	140
5.4	Current works in optical imaging	143
5.5	Angular domain imaging (ADI)	146
5.5.1	Angular filter and test phantom fabrication process	149
5.6	Deep illumination technique in angular domain	151
5.6.1	The methodology.....	151
5.6.2	Experimental setup.....	154
5.7	Experimental results.....	157
5.8	Deep illumination ADI with biological tissue.....	160
5.9	Digital image processing for deep illumination ADI.....	162
5.9.1	Full image reconstruction.....	163
5.9.2	Periodic noise removal	164
5.9.3	Contrast enhancement	166
5.10	Conclusion	169
5.11	Reference list.....	170
6: Transmission and Fluorescence Angular Domain Optical Projection Tomography of Turbid Media		174
6.1	Abstract.....	174
6.2	Introduction	176
6.2.1	Background and motivation	176
6.2.2	Concept of angular domain imaging in transillumination	178
6.3	Objective and approach	179
6.4	Methods	180
6.4.1	Angular filter array	180
6.4.2	Tissue mimicking phantom	181
6.4.3	Sample rotation	181
6.4.4	t-ADOPT.....	181
6.4.5	f-ADOPT.....	183
6.4.6	Depth of field analysis.....	185
6.4.7	Image reconstruction	185
6.4.8	Wedge subtraction and digital image processing	185

6.5	Results and discussion.....	187
6.6	Conclusion	196
6.7	Reference list	197
7:	Angular Domain Fluorescence Imaging for Small Animal Research	201
7.1	Abstract.....	201
7.2	Introduction	201
7.3	ADFI principle	202
7.4	ADFI methods	203
7.5	ADFI results	206
7.6	Acknowledgement.....	211
7.7	Reference list	211
8:	Summary and Futurework.....	213
8.1	Overview.....	213
8.2	Technology advancement	213
8.2.1	Angular filter array development	214
8.2.2	Image enhancement methods	217
8.3	Application development	225
8.3.1	Multispectral/ Hyperspectral imaging	225
8.3.2	Deep illumination ADI	231
8.3.3	Angular domain optical projection tomography	232
8.3.4	Angular domain fluorescence imaging	233
8.4	Conclusions	236
8.5	Reference list	238
Appendices.....	239	
Appendix A:	Fabrication process of reflection trapped angular filter array	239
	Overview of process flow	239
	Photomask design and wafer preparation	240
	Photolithography	240
	Wet Etching SiO ₂ process	242
	DRIE for silicon substrate	244
	Carbon sputtering (optional).....	244
	Dicing the wafer	245
	References.....	247
Appendix B:	Angular domain florescent lifetime imaging in turbid media	248
	Abstract.....	248
	Introduction	248
	Angular domain imaging principle	250
	Angular filter array.....	252
	Objective and approach	254
	Experiment setup	255
	Results and discussions.....	259
	Conclusion	264
	Acknowledgment.....	265
	References.....	265

LIST OF FIGURES

Figure 1-1: Photon transmission through a scattering medium.	6
Figure 1-2: The light energy passing through a surface element (dA) inside a cone of $d\Omega$ directed to the vector s	7
Figure 1-3: The collimated transmission method.	13
Figure 1-4: Time domain imaging setup using a streak camera to capture ballistic and quasiballistic photons [1-19].	17
Figure 1-5: OCT system measures the echo time delay of reflected light beam by low-coherence interferometry. Longitudinal scan can be done by moving the reference mirror and transverse scan be done by moving the sample [1-21].	19
Figure 1-6: Diffuse Optical Tomography system diagram including multiple detectors, and light source.	21
Figure 1-7: Stages of photoacoustic process.....	23
Figure 1-8: Typical setup for Angular Domain Imaging using high aspect ratio collimators.....	27
Figure 1-9: Silicon Micro-machined Collimating Array (SMCA) [1-47].....	28
Figure 1-10: Scanning details for ADI experiments.....	28
Figure 1-11: Microscope images of patterned photoresist and oxide layers on a silicon wafer, (a) Photoresist layer – (5x magnification) (b) Oxide layer – (5x magnification).....	29
Figure 1-12: Microscope images of etched silicon tunnels with and without the oxide mask. (a) Oxide mask with etched tunnels– (80x magnification) (b) Silicon tunnels – (5x magnification).....	30
Figure 1-13– Completed silicon wafer with AFA devices.	31
Figure 1-14– SEM picture of AFA channel [1-40].	31
Figure 2-1. Basic ADI experiment setup in transillumination mode.	52
Figure 2-2. Angular filter array.....	52
Figure 2-3. Resolution target to measure the spatial resolution of ADI.	52
Figure 2-4. Image of small resolution targets placed in a 2 cm optical cell filled with homogenous scattering milk/water solution using an 808 nm laser diode at (a) $SR \approx 10^3:1$ [$\mu'_s = 1 \text{ cm}^{-1}$, $\mu'_a = 0.01 \text{ cm}^{-1}$] and (b) $SR \approx 10^7:1$ [$\mu'_s = 2.5 \text{ cm}^{-1}$, $\mu'_a = 0.01 \text{ cm}^{-1}$]. (Total scan area is 6.6 mm by 6.5 mm).....	54
Figure 2-5. ADI setup with diode laser and a collimation system.	56

Figure 2-6. Collimated transmission measurement results; Scattering ratio versus concentration of 2% fat partly skimmed milk (in percentage) diluted by water in 1 cm container.	58
Figure 2-7. Chicken breast scattering ratio measurement results with vertical log scale.	60
Figure 2-8. Resolution targets placed in diluted milk sample with SR $\sim 10^6:1$ scattering media [$\mu'_s = 0.8 \text{ cm}^{-1}$, $\mu'_a = 0.01 \text{ cm}^{-1}$]: at 2.5 cm depth in a 5 cm optical path cuvette with the (a) 670 nm, (b) 808 nm, or (c) 975 nm diode laser system; and at 5 cm depth with the (d) 670 nm, (e) 808 nm, or (f) 975 nm diode laser system. (All images are histogram equalized and gamma curve corrected)	62
Figure 2-9. Large resolution target slide in front of 2.2 ± 0.2 mm chicken breast with the (a) 670 nm, (b) 808 nm, or (c) 975 nm diode laser system. (Total scan area is approximately $7.8 \text{ mm} \times 8.8 \text{ mm}$; white scale bar is $500 \mu\text{m}$).....	63
Figure 2-10. Large resolution targets in front of a chicken breast sample of 4 mm thickness with the (a) 670 nm, (b) 808 nm, or (c) 975 nm diode laser system, and for 5 mm thick chicken breast with the (d) 670 nm, (e) 808 nm, or (f) 975 nm diode laser system. (Total scan area is approximately $7.8 \text{ mm} \times 8.8 \text{ mm}$; white scale bar is $500 \mu\text{m}$)	64
Figure 2-11. Large resolution targets in front of 3 mm chicken breast (a) without digital image processing, and (b) after digital image processing. (Total scan area is approximately $7.8 \text{ mm} \times 8.8 \text{ mm}$).....	66
Figure 3-1. Angular domain imaging in transillumination mode.....	77
Figure 3-2. Silicon micromachined angular filter array (etched bottom section).	79
Figure 3-3. Illustration of limited field of view in one dimensional AFA.	79
Figure 3-4. ADI scan of sample including resolution target (L-shaped targets with lines and spaces of $150 \mu\text{m}$, $200 \mu\text{m}$, $300 \mu\text{m}$, and $400 \mu\text{m}$) placed in the middle position of 1 cm thick optical cell filled (a) Water, (b) 0.6% Intralipid™ ($\mu'_s = 4.8 \text{ cm}^{-1}$, $\mu_a = 0.01 \text{ cm}^{-1}$), and (c) 0.75% Intralipid™ ($\mu'_s = 6 \text{ cm}^{-1}$, $\mu_a = 0.01 \text{ cm}^{-1}$) using an 808 nm laser diode.	81
Figure 3-5. ADI setup with 808 nm laser diode and aspheric and cylindrical lens collimation system. (a) Top view (b) Side view.	88
Figure 3-6. Contrast enhancement of ADI scan of L-shape target (line and space width of $400 \mu\text{m}$) at 808nm for a scattering medium composed of 0.3% Intralipid™ in a 2 cm thick optical cell. (a) Original ADI scan, (b) Wedge inserted ADI scan (c) Wedge subtraction image (d) Parallel polarized ADI scan (PADI) (e) cross polarized ADI scan (f) subtraction result of parallel and cross orientation (PADI-CS).	92
Figure 3-7. Comparison of image contrast enhancement using polarization contrast enhancement and wedge subtraction methods in different scattering ratio levels.	95
Figure 4-1. (a) Photon trajectories through a turbid medium. (b) ADI scanning procedure of an L-shape resolution target in a turbid used to collect a	

2D projection image. (c) Possible photon reflections due to channel walls. (θ_a : acceptance angle, θ_b : blocking angle, θ_i : incident angle)	105
Figure 4-2. Experimental setup for the proposed techniques, (a) Different AFA geometries (b) Diagram of the Time Angular Domain Imaging (TADI) system. (c) Diagram describing wedge subtraction method where images were collected with and without a wedge prism so that the contributions from image forming quasi-ballistic photons and background scattered photons could be estimated.....	109
Figure 4-3. Reflected light intensity using AFA-60-1 placed at two different distances from a point source with uniform angular distribution.....	114
Figure 4-4. ADI scan results in turbid media (Intralipid™) with $\mu'_s \approx 7$ using four different AFA geometries (a) – (d). Contrast-enhanced images using the wedge technique for background scattered light estimation and subtraction (e)- (h).....	123
Figure 4-5. Temporal profiles of transmitted light obtained in time-resolved measurements using Picostar camera (250 ps temporal gate width): (a) through scattering medium with 2 cm optical cuvette filled with 0.2% Intralipid™ at $\lambda = 780$ nm, (b) 0.25% Intralipid™, and (c) 0.3% Intralipid™	127
Figure 4-6. ADI and TADI scanning results (using AFA-60-1) of a 350 μm L-shape resolution target at the middle of a turbid medium with and without wedge subtraction procedure at different scattering levels: (a) through scattering medium with 2 cm optical cuvette filled with 0.25% Intralipid™ at $\lambda = 780$ nm, (b) 0.3% Intralipid™, and (c) 0.35% Intralipid™	128
Figure 4-7. TADI image contrast as a function of gate delay and scattering level of (a) through scattering medium with 2 cm optical cuvette filled with 0.25% Intralipid™ at $\lambda = 780$ nm, (b) 0.3% Intralipid™, using femtosecond pulsed laser.	131
Figure 5-1. Light interaction in the turbid medium [5-10].....	141
Figure 5-2. High aspect ratio micro-channel proving angular filters.	146
Figure 5-3. Experimental setup for Angular domain imaging in transillumination mode.....	148
Figure 5-4. Silicon micro-machined angular filter array.....	148
Figure 5-5. Two-dimensional phantom test structures ranging from 204 μm line width and spacing down to 51 μm	148
Figure 5-6. Deep illumination and angular filtering system overview.....	153
Figure 5-7. Deep illumination ADI experimental setup.	154
Figure 5-8. Scan of sample medium across angular filter array.	155
Figure 5-9. Images captured by Deep Illumination ADI at $\mu'_{eff} = 4.7$ and 5.8 cm^{-1} and depths of 1 - 3 mm.	158

Figure 5-10. Scan results for the deep illumination method, with (a) 52 μm , (b) 26 μm , and (c) 13 μm vertical step size. (phantom size = 153 μm , depth = 1 mm, $\mu'_{\text{eff}} = 4.7 \text{ cm}^{-1}$)	159
Figure 5-11. Deep illumination ADI of biological tissue diagram using 670nm laser diode.	160
Figure 5-12. (a) Deep illumination ADI scan of the chicken breast sample, (b) the 1 mm thick paper clip, 2.5 mm deep inside the tissue, and (c) the histogram equalized version of (b).	161
Figure 5-13. Full image reconstruction using two different scans that differ by a 50 μm horizontal shift. (a) Original image result with dark vertical lines. (b) Full image after reconstruction. (Deep Illumination, phantom size = 153 μm , depth = 1 mm, $\mu'_{\text{eff}} = 4.7 \text{ cm}^{-1}$)	164
Figure 5-14. Stages in the periodic noise removal procedure. (a) Fourier transform (b) Notch filter spectrum (c) Noise pattern in spatial domain (d) Resultant image. (Deep Illumination, depth = 1 mm, $\mu'_{\text{eff}} = 4.7 \text{ cm}^{-1}$)	165
Figure 5-15. Imaging results after homomorphic processing. (Deep Illumination, depth = 1 mm, $\mu'_{\text{eff}} = 4.7 \text{ cm}^{-1}$)	166
Figure 5-16. (a) The original image without image processing. (b) The estimated background from previous processed image. (c) Result after background subtraction with contrast adjustment, from 204 μm phantom size to 51 μm . (Deep Illumination, depth = 1 mm, $\mu'_{\text{eff}} = 4.7 \text{ cm}^{-1}$).....	168
Figure 6-1. ADI system diagram in trans-illumination mode. The AFA must be designed with a sufficiently high aspect ratio, length (L) over opening width (W), to provide the small acceptance angle and filter scattered photons. Optional wedge prism can be used to estimate background noise to enhance the tomographic image.....	179
Figure 6-2. System for trans-illumination angular domain optical projection tomography system.....	182
Figure 6-3. System for fluorescent emission angular domain optical projection tomography (f-ADOPT).	184
Figure 6-4. Angular domain imaging with the L-shape resolution targets placed in various positions in a 5 cm optical cuvette with scattering medium ($\mu'_s = 0.8 \text{ cm}^{-1}$, $\mu_a = 0.01 \text{ cm}^{-1}$). (a) front position, 0 cm and closest to AFA, (b) middle position, 2.5 cm, and (c) back position, 5 cm and furthest from the AFA. The L-shape test structures had line thicknesses of 150, 200, 300, and 400 μm	188
Figure 6-5. Angular domain optical projection scans in trans-illumination mode (t-ADOPT). Sinogram scan of two 0.9 mm diameter graphite rods suspended in a 2 cm optical cell filled with (a) water, (b) 0.25% Intralipid™ with $\mu'_s = 2 \text{ cm}^{-1}$, $\mu_a = 0.01 \text{ cm}^{-1}$, (c) 0.3% Intralipid™ with μ'_s	

= 2.4 cm^{-1} , $\mu_a = 0.01 \text{ cm}^{-1}$, and (d) 0.35% Intralipid™ with $\mu'_s = 2.8 \text{ cm}^{-1}$, $\mu_a = 0.01 \text{ cm}^{-1}$. Each sinogram represents a 360° rotation with 200 steps. The field of view was approximately 13 mm. (e) Contrast enhanced t-ADOPT sinogram of (c) at the detection limit with 0.3% Intralipid™ 189

Figure 6-6. Reconstructed t-ADOPT images of two 0.9 mm diameter graphite rods suspended in a 2-cm optical cell filled with (a) water, (b) 0.25% Intralipid™ ($\mu'_s = 2 \text{ cm}^{-1}$, $\mu_a = 0.01 \text{ cm}^{-1}$), and (c) 0.3% Intralipid™ ($\mu'_s = 2.4 \text{ cm}^{-1}$, $\mu_a = 0.01 \text{ cm}^{-1}$). (d) Contrast-enhanced t-ADOPT images of (c) using the wedge subtraction process. 191

Figure 6-7. f-ADOPT sinogram images of a glass tube (ID: 1.13 mm) filled with 20 μM ICG in a 2-cm optical cell filled with (a) water and (b) 0.1% Intralipid™ ($\mu'_s = 0.8 \text{ cm}^{-1}$, $\mu_a = 0.01 \text{ cm}^{-1}$). (c) Reconstructed f-ADOPT image corresponding to (a). (d) Reconstructed f-ADOPT image corresponding to (b). 194

Figure 7-1. Principle and method for Angular domain fluorescent imaging. (a) Angular domain fluorescent imaging principle. (b) Silicon micro-machined angular filter array (bottom piece). (d) Diagram of glass capillary tubes used to contain fluorescent agents during phantom-based experiments (top). Schematic of imaging setups used to compare performance of ADFI system (bottom). (d) Optical imaging setup (Abbreviations: CCD, charge-coupled device; HRI, high rate imager; INT, intensifier; DG, delay generator; DM, dichroic mirror; AFA, angular filter array; and PD, photo diode). 204

Figure 7-2. Angular domain fluorescent imaging in turbid media. Targets were two glass tubes filled with 20 μM DTTC diluted in ethanol and placed at various depths ($D \leq 2 \text{ mm}$) from the detection surface of an optical cuvette ($5 \text{ cm} \times 5 \text{ cm} \times 2 \text{ cm}$) filled with 1% Intralipid™: (a) image from lens system focused ($f/\# 2$) to the surface of the sample (top), lens and pinhole system (acceptance angle = 1.15°) (middle), and ADFI using AFA (bottom). (b) Line profiles from the images in (a) for $D = 1 \text{ mm}$. (c) Spatial resolution analysis of the fluorescent targets as a function of depth. (d) Contrast ratio analysis of the fluorescent targets as a function of depth 207

Figure 7-3. Mouse ADFI bone imaging with comparison to X-Ray CT and conventional reflectance-based imaging. (a) Maximum intensity projection of five X-ray CT slices (b) showing three vertebrae of the spine of a hairless mouse. Images in (b) represent 0.625mm thick slices though the animal proceeding from shallowest (left) to deepest (right) in increments of 0.625 mm. (c) Angular domain fluorescent image of three vertebrae of the mouse spine corresponding to (a & b). Camera integration time was 2 s for each line scan. (d) Conventional reflectance-based image of three vertebrae of the mouse spine indicated in (a & b). Each image (a-d) represents a field of view of 1 cm wide by 1 cm high. (e) Fluorescence intensity line profiles corresponding to (c). (f) Fluorescence intensity line profiles corresponding (d). 209

Figure 8-1. (a) Transillumination ADI System Schematic (b) Line profile due to micro –channel array physical geometry.	218
Figure 8-2. ADI scan of sample including resolution target (L-shaped targets with lines and spaces of ~ 51 μm , 102 μm , 153 μm , and 204 μm) placed in the middle position of 2 cm thick optical cell filled (a) Water, (b) 0.25% Intralipid™ (MFP' = 5) , and (c) 0.3% Intralipid™ (MFP' = 6) using an 808 nm laser diode. The line profile of yellow bar corresponding to images from (a) to (c) is shown in (d) – (f) respectively. The blue curve is the extracted upper envelop for each profile.	220
Figure 8-3. Results of ADI Image artifact correction and contrast enhancement for Intralipid™ phantom in scattering level of 6 \times MFP' (shown in Figure 8-2), (a) original scan, (b) image reformed based on upper envelop extraction, (c) the spatially normalized image. The same process has been implemented for ADI scan of 5 mm chicken breast tissue: (a) original image (b) After envelop extraction (c) after spatial normalization (red bar is 1mm long)	221
Figure 8-4. Angular domain hyperspectral imaging diagram in transillumination mode: (a) top view, (b) side view.	228
Figure 8-5. Transformation of ADSI images from the CCD camera (top) to multiple 2D images of tissue sample at different wavelengths (5 mm fresh chicken breast tissue).....	229
Figure 8-6. Angular domain spectroscopic imaging results of a 5 mm fresh chicken breast tissue sample at 8 wavelength ranges.....	230
Figure 8-7. Transmission and absorption (normalized) characterization of 5 mm chicken breast tissue at different regions of interest: (a) projection image with regions of interest, (b) transmitted light intensity through sample in selected regions, (c) normalized absorption curve for selected regions of interest	231
Figure 8-8. Mouse ADFI bone imaging result (middle image) with comparison to X-Ray CT (right) and conventional reflectance-based imaging (left). (The ADFI artefacts are corrected based on the envelop detection method described in section 8.2.2.1).....	235

LIST OF TABLES

Table 1-1: Overview of medical imaging systems	3
Table 3-1. Summary of the contrast enhancement methods using ADI	90
Table 4-1. Estimation of effect of reflected light in different AFA sizes.....	114
Table 4-2. Effect of channel wall reflection reduction by using RTAFA in resulted ADI image contrast measurements, (through scattering medium with $\mu'_s / (MPF) = 6$)	122
Table 4-3. Summary of the ADI contrast experimental measurements for different AFA geometries, (through scattering medium with $\mu'_s / L_1 = 6$, $L_1 = 5$ mm).....	124
Table 4-4. Summary contrast ratio measurements using AFA-60-1 in ADI and TADI methods with wedge subtraction	129
Table 5-1. Performance comparison for several optical imaging methods in human tissue 1-201-223-141-38.	147

GLOSSARY

2D, 3D, 4D	Two, three, four dimensional
ADFI	Angular domain fluorescence imaging
ADI	Angular domain imaging
ADOPT	Angular domain optical projection tomography
ADSI	Angular domain spectroscopic imaging
AFA	Angular filter array
CCD	Charge-coupled device
cm	Centimetre
CT	Computed tomography
DOT	Diffuse optical tomography
DRIE	Deep Reactive Ion Etching
DTTC	3,3'-Diethylthiatricarbocyanine Iodide
HG	Henyey and Greenstein
ICCD	Intensified Charge-coupled device
ICG	Indocyanine green (Cardiogreen)
MCP	Microchannel Plate
MFP	Mean free path
MRI	Magnetic resonance imaging

NIR	Near infrared
OCT	Optical coherence tomography
OPT	Optical projection tomography
PADI	Polarized angular domain imaging
PET	Positron-emission tomography
RT	Radiation transport
RTE	Radiation transport equation
SMCA	Silicon micromachined collimating array
SPECT	Single photon-emission CT
SR	Scattering ratio
TADI	Time angular domain imaging
TD	Time domain

1: INTRODUCTION

1.1 Background

Medical imaging modalities can be classified by various criteria such as the energy used to derive visual information (Gamma rays, X-Rays, photons, microwaves, and sound waves), the spatial resolution (microscopic, mesoscopic or macroscopic), and the delivered information type (anatomical, physiological, cellular or molecular). Macroscopic imaging systems like Computed Tomography (CT), magnetic resonance imaging (MRI) and Ultrasound (US) can offer anatomical and physiological information and already used in clinical and preclinical settings. Medical imaging systems like positron-emission tomography (PET), single photon-emission CT (SPECT), fluorescence imaging, Confocal and multiphoton microscopy can provide molecular information and have also been adopted widely.

Until now, projection X-ray imaging has been the most widespread modality used in radiological imaging. In this method, an x-ray beam is used to create a two dimensional anatomical transmission image of a target area of a patient. The x-ray radiation during the exposure is attenuated by absorption and scattering (very small in tissue) within the body and recorded by a detector to form an x-ray shadowgram. Many applications of this method were recognized very quickly and ultimately led to X-ray CT, which was a series of shadowgrams and image reconstruction to image a slice through the body. However, while

widely used, ionizing image techniques disrupt and destroy the chemical structure of living tissue causing tissue damage and increase cancer risk proportionate to the cumulative dose of radiation applied. Recently, there has been more awareness of the risk of radiation exposure to patients undergoing X-ray CT, SPECT and PET perfusion imaging [1-1, 1-2]. However, the radiation-related cancer risk from CT scans has not been sufficiently appreciated yet. For instance, recent studies [1-1,1-2] estimated that 72 million CT scans were performed in 2007 that will lead to approximately 29,000 excess cause of cancer resulting in 15,000 deaths in the next 20 to 30 years.

The attractive alternative of imaging with non-ionizing radiation has consequently been of high interest, resulting in such techniques as ultrasound (acoustic wavelengths), MRI (radio wavelengths), and optical imaging (visible and infrared light). MRI provides excellent soft tissue contrast, but requires expensive dedicated equipment. Video rate imaging is achievable with ultrasound, but the US image contrast is relatively poor compared to other modalities. Optical imaging modalities offer inherently lower cost and molecular contrast, but suffer from poor depth penetration and low resolution. Table 1-1 summarized the spatial resolution, depth penetration, imaging time, and cost of available systems [1-3, 1-4].

Optical absorption, scattering, and fluorescence in living tissues and blood in different wavelengths can give significant information about the structure and physiological content of the living bodies. Light in tissues and bioliquids experiences low absorption but high scattering [1-1] within the visible and

infrared spectra. The foundation of scattering in tissue is the refractive index mismatch between sub-cellular organelles and the surrounding cytoplasm, which defines tissue as a heterogeneously turbid medium.

Table 1-1: Overview of medical imaging systems

<i>Technique</i>	<i>MRI</i>	<i>CT</i>	<i>Ultrasound</i>	<i>PET/SPECT</i>	<i>Confocal/ Multiphoton microscopy</i>	<i>Fluorescence/ optical Imaging</i>
Ionizing	No	Yes	No	Yes	No	No
Resolution	10-100 μm	50 μm	50 μm	1-2 mm	1 μm	2-3 mm
Depth	No-limit	No-limit	Several centimetres	No-limit	< 1mm	<1 cm
Time	Minutes to hours	Minutes	Seconds to minutes	Minutes to hours	Seconds to hours	Seconds to minutes
Target	Anatomical, physiological, molecular	Anatomical, physiological	Anatomical, physiological	physiological, molecular	Anatomical, physiological, molecular	physiological, molecular
Cost	\$\$\$	\$\$	\$\$	\$\$\$/\$\$	\$\$\$	\$
Clinical use	Yes	Yes	Yes	Yes	In progress	Yes
Soft tissue contrast	Excellent	Poor	Good	Good	Excellent	Excellent

Optical imaging is the result of these interactions on light input to generate a composite effect that can be measured and reconstructed as the “image”.

However, imaging the contents and/or structure within tissue can be an extremely challenging problem. Furthermore, scattering in a medium is

exponentially related to the depth, and consequently, scattering levels can reach extremely high levels for many applications. For tissue thickness beyond 5 mm scattered photons are many orders of magnitude higher levels compared to non-scattered ones. The high scattering level can entirely obscure the contents of the medium when viewed from outside. Therefore, in most cases scattered photons are considered as a source of noise for imaging purposes. However, there have been many techniques to bypass or reduce the scattering effect. With recent developments in micro-scale light source delivery and sensor fabrication, both illumination and detection can happen inside the body using fibre optics based micro-endoscopy [1-5] or wireless transmitters by Wireless Capsule Endoscopy (WCE) technology [1-6]. These minimally invasive technologies provide images of internal organs of human body for disease diagnostics.

From another point of view, stable mesoscopic optical imaging of intact, unprocessed tissue with high resolution (sub millimetre) and large field of view (1-3 cm) is not currently possible to our knowledge. In this thesis, we sought to develop methods that take advantage of new micro-fabrication techniques to make such imaging possible.

One of the key strategies for successful optical imaging is to clearly understand the behaviour of light transportation in tissue. The following section briefly describes photon transport in a tissue-like medium, with emphasis on models and approximations used in imaging through turbid media.

1.2 Light-tissue interactions

When light travels into a scattering medium, its trajectory can be changed in several ways. Figure 1-1 presents four cases for a photon traveling through a tissue for which three cases result in a photon that can be recorded outside of the medium. The first case describes a photon that travels through the medium along its original trajectory with absolutely no scattering. This photon is called a *ballistic photon* (1). The second case describes a photon that undergoes a minimal amount of scattering resulting in minimal alteration of the photon path through the medium and its exit angle. This photon is termed *quasi-ballistic* or *snake photon* (2) because of the similar behaviour to the ballistic photon. Many optical imaging methods use both ballistic and quasi-ballistic photons since they follow a straight path through the scattering medium. In this thesis, the term “ballistic and quasi-ballistic photons” and “unscattered photons” are used interchangeably.

A third case that is the absorbed photon. The *absorbed photon* (3) dies within the medium and never exits. The fourth case is that of the scattered photon, which experiences a random walk-like path through the medium. The *scattered photon* (4) is considered to be a source of noise in most optical imaging techniques (excluding Diffuse Optical Tomography) because it does not follow a clear path through the medium and can exit the medium at any location and angle.

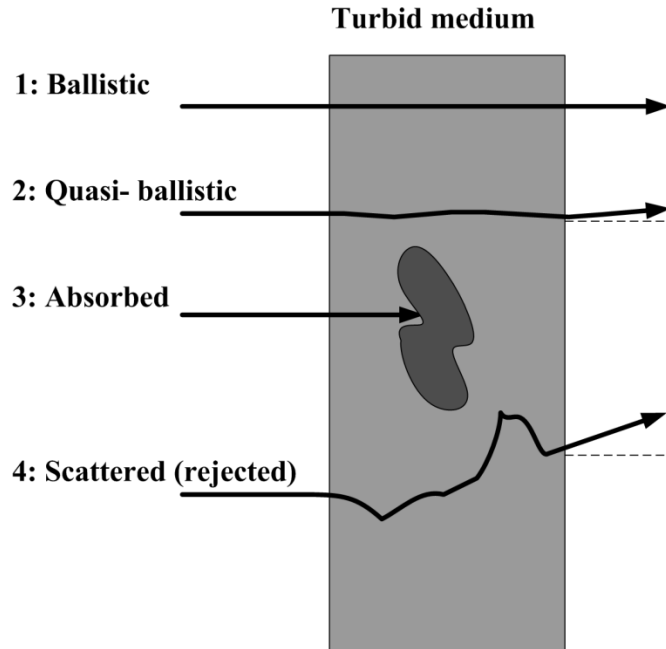


Figure 1-1: Photon transmission through a scattering medium.

Many optical imaging methods fall within the category of ballistic imaging, which extract an image of the internal structure of an object from the unscattered light while rejecting the scattered light. Ballistic and quasi-ballistic photons are information-bearing photons since they pass through a straight path all the way through the medium. Therefore unscattered light can indicate the optical transparency along that path in the turbid medium. A two-dimensional projection shadowgram of the medium can as a result be resolved using the ballistic and quasi-ballistic light that is captured. However, scattered light is considered as image noise and must be rejected in this technique.

1.2.1 The radiation transport model

A comprehensive theoretical behaviour of light propagation in turbid media is complex since the electromagnetic equations can only be solved for

straightforward conditions. As a result, simplifications are essential for solving real-world problems. The Boltzmann Radiative Transport equation (RT) is the fundamental simplification to model steady-state scattering of monochromatic light in a homogenous medium. The RT model is rooted in an energy balance on photons entering and exiting a photon beam in each particular direction. [1-1,1-8,1-9] As illustrated in Figure 1-2, taking into consideration a radiance of light, $I(r, s, t)$, defined by its position, $r(t)$, and direction of s . As it propagates in space over the time interval dt , the radiance drops energy due to the absorption and scattering out of s , but accumulate energy from light scattered into the s direction from other directions (e.g. s') and from any local source of the light at $r(t)$.

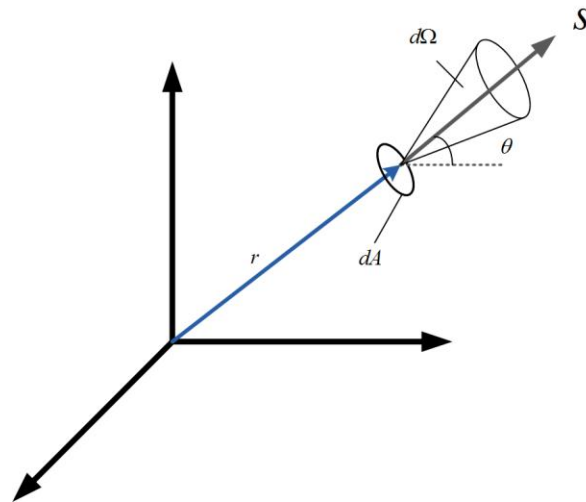


Figure 1-2: The light energy passing through a surface element (dA) inside a cone of $d\Omega$ directed to the vector s .

The progression can be formulated by an integro-differential equation recognized as the radiation transport relation:

$$\frac{1}{c_m} \frac{d}{dt} I(r, s, t) = -(\mu_a + \mu_s) I(r, s, t) + \frac{\mu_a + \mu_s}{4\pi} \int p(s \cdot s') I(r, s, t) d\Omega' + Q(r, s, t). \quad 1-1$$

where $I(r, s, t)$ is identified as the radiance which specifies the angular dependence of the flow of optical power at position r . $Q(r, s, t)$ is the source intensity, c_m is the speed of light in the medium, $\mu_a [m^{-1}]$ is the absorption coefficient, $\mu_s [m^{-1}]$ is the scattering coefficient, $\mu_t [m^{-1}]$ is the attenuation coefficient (extinction coefficient) which can be derived from:

$$\mu_t = \mu_a + \mu_s \quad 1-2$$

A parameter known as the albedo is defined to describe the diffusivity of the medium.

$$albedo = \frac{\mu_s}{\mu_a + \mu_s} \quad 1-3$$

In equation 1-1, the $p(s \cdot s')$ is the phase function which describes the angular distribution of a photon for a single scattering event. The phase function is normally assumed to be a function of the angle between s and s' . The $p(s \cdot s')$ can be defined as the probability density function for scattering from direction s' to direction s where the integral of phase function is normalized to unity. Usually the phase function is related to a g parameter through the relation:

$$g = \int_{4\pi} p(s \cdot s')(s \cdot s') d\Omega' \quad 1-4$$

The g parameter is also named the anisotropy coefficient. It shows the asymmetry of a single scattering pattern; g approaching 0, 1, -1 describes isotropic, extremely forward, and extremely backward scattering orientation, respectively.

Calculation of light distribution based on the RT model necessitates knowledge of μ_a , μ_s , and the phase function. However, in order to derive these parameters, a solution of the RT equation has to be calculated as well. Because of the complexity of solving the RT equation, some to the radiance and/or the phase functions have to be made. Here I present some of the approximations used to simplify the RT model.

1.2.2 Scattering phase function approximation

In order to model the phase function, an analytical model has been developed by Henyey and Greenstein (named as HG-function) to describe the angular dependence of light scattered by small particles, which they used to investigate diffuse radiation from interstellar dust clouds in galaxy as the following [1-10]:

$$p_{HG}(s \cdot s') = p_{HG}(g, \cos \theta) = \frac{1}{4\pi} \frac{1 - g^2}{(1 + g^2 - 2g \cos \theta)^{3/2}} \quad 1-5$$

Jacques et al. have found [1-11] that the equation 1-5 accurately describes the scattering of light in biological tissues. The important parameter of this phase function is the g factor which is described in equation 1-4. For tissues, g ranges from 0.4 to 0.99 [1-7], such values signify that scattering is strongly in the forward direction. For instance, for $g = 0.6$ or 0.99 , approximately 90% of the scattered energy is within the 90° or 5° of the forward direction, respectively.

1.2.3 Diffusion approximation

The RT equation is complicated to solve since it has six independent variables which are $x, y, z, \theta, \varphi,$ and t where θ and φ are the polar and azimuthal angles of s . In a high albedo medium when absorption is relatively low compared to scattering, penetration of light into the medium is due largely to scattering. For this limiting case, photon transport can be modelled with a few anisotropic movements followed by a series of steps of random length, but each equally likely to be taken in any direction isotropically. The number of anisotropic scattering steps can be estimated as $m = \frac{1}{1-g}$ after which the angular distribution turns isotropic. For instance, for $g = 0.75$, it takes an average of four anisotropic scattering events for the population of photons to scatter isotropically. This isotropic scattering is described by the reduced scattering coefficient μ'_s , which is related to the g factor parameter as follows:

$$\mu'_s = \mu_s(1-g) \quad 1-6$$

By including the effect of absorption during photon transport, the total attenuation coefficient can be expressed as:

$$\mu_t' = \mu_a + \mu_s(1 - g) \quad 1-7$$

The reciprocal of μ_t' in equation 1-7 is referred to as the transport mean free path (MFP'), l_t' . In the diffusion approximation, radiance I is approximated as a function of fluence Φ and current density J . [1-12]

$$I(r, s) = \frac{1}{4\pi} \phi(r) + \frac{3}{4\pi} J(r) \cdot s \quad 1-8$$

In order to derive the diffusion equation from the RTE model, two approximations are made: 1) the radiance is assumed to be nearly isotropic owing to directional broadening therefore the expansion of the radiance is limited to first order spherical harmonics, and 2) the partial change in the current density (J) in one transport mean free path is much less than unity. These two conditions can be interpreted to a single condition $\mu_s' \gg \mu_a$, because all of the photons must have sustained a sufficient number of scattering events before being absorbed. Additionally, it is also required that the detection point be sufficiently far from any source and boundaries.

The diffusion equation resulting from application of the mentioned approximations to the RTE can be expressed as:

$$\frac{\partial \Phi(r,t)}{c_m \partial t} = -\mu_a \Phi(r,t) + D \nabla^2 \Phi(r,t) + S(r,t) \quad 1-9$$

where $\Phi(r,t)$ is defined as the fluence rate which is the energy flow per unit area per unit time regardless of the flow direction. $S(r,t)$ is the source term and D is the diffusion coefficient as follows:

$$D = \frac{1}{3(\mu_a + \mu_s(1-g))} \quad 1-10$$

Theoretical details are presented in [1-13,1-14]. The diffusion equation is a simplified version of RT model since it has 4 instead of 6 degrees of freedom. In addition, the diffusion equation does not depend on μ_s and g factor by themselves but on their combination of reduced scattering coefficient μ'_s .

1.2.4 Collimated transmission through turbid media

By assuming an infinite, isotropic, homogeneous medium with no sources, a collimated beam of light attenuates exponentially along its path through a tissue layer of thickness d in accordance with the Beer-Lambert law [1-7,1-14]:

$$I(d) = I_o \exp[-(\mu_s + \mu_a)d], \quad 1-11$$

where $I(d)$ is the intensity of transmitted light measured using a distance photo detector with a small aperture, and I_o is the input light intensity. The collimated (or ballistic) portion of the transmitted light can be captured by a photo detector

placed after two apertures aligned and placed at a distance to each other to create an angular filter as shown in Figure 1-3.

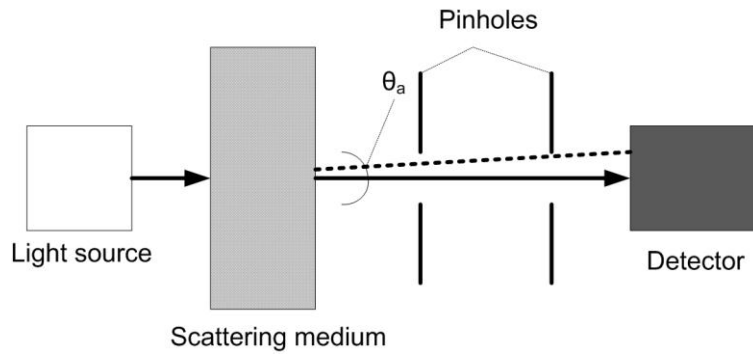


Figure 1-3: The collimated transmission method.

The ballistic transmittance T of the scattering medium is defined as:

$$T = \frac{I(d)}{I_0} \quad 1-12$$

We can also obtain the extinction coefficient of the sample as:

$$\mu_t = -\frac{1}{d} \ln T \quad 1-13$$

An important assumption in equation 1-13 is that the detected scattered light is much weaker than the detected ballistic light. Three factors affect this assumption: (1) the scattering optical depth of the sample $\mu_s d$, (2) the acceptance angle of detection θ_a , and (3) the scattering phase function.

The optical properties of turbid media can be expressed in different ways. The attenuation level can be stated using absorption and reduced scattering coefficients (μ_a, μ_s'), which includes the phase function of turbid medium. Alternatively, It can be expressed as optical depth, τ , which is the product of sample thickness and total attenuation coefficient. Optical depth also expresses the number of mean free paths (or reduced mean free paths) that photons must travel to exit the medium. Another metric used to describe the scattering level of a medium is termed the Scattering Ratio, SR , which is defined as the number of photons that are scattered for every non-scattered photon that passes through the medium (with the condition of $\mu_a \sim 0$) For a given T value of a specific scattering medium, the SR value is given as,

$$SR = \frac{\text{proportion of scattered photons}}{\text{proportion of non - scattered photons}} = \frac{1-T}{T} \quad 1-14$$

where “non-scattered” photons are defined to include both ballistic and quasi-ballistic photons. The SR value can be also proportional to $\exp[(\mu_s' + \mu_a)d]$ or $\exp[\tau']$ for a certain optical depth range while equation 1-11 is valid.

For biological tissue, a typical value of scattering coefficient is 100 cm^{-1} meaning that on average photons get scattered every $100 \mu\text{m}$ [1-7]. For instance, by assuming g factor equal to 0.90, the reduced scattering coefficient will decrease to 10 cm^{-1} which allows the photons to travel 1 mm without being scattered.

At tissue thickness beyond a few millimetres, quasi-ballistic photons will represent the greatest population of informative photons since they maintain a highly directional angular distribution. Optical imaging methods can target capturing ballistic/ quasi-ballistic or scattered photons as a source of information to reconstruct an image of internal structures. However, as scattering level increases the informative photons available for detection shifts from ballistic, to quasi-ballistic, and finally to scattered, which result in lower spatial resolution, but higher detection depth.

In the following section, a summary of optical imaging methods which can provide from mesoscopic to macroscopic spatial resolution is briefly described.

1.3 Overview of prior works in optical imaging

Optical imaging is based on illuminating the tissue with visible/ near infrared light and measuring of the light coming back out. Unscattered photons can be distinguished based on differences in their path length, because of the fact that scattered photons travel a longer distance in the medium as compared to unscattered photons, which travel almost straight through the tissue. Both Time Domain (TD) tomography [1-16-1-19], and Optical Coherence Tomography (OCT) [1-20, 1-21] use this principle. The difference between them relies on the fact that the TD tomography is based on measuring the transmitted light generated by fs/ps laser pulses into a scattering medium and looks for the earliest arriving photons, whereas, in order to avoid such high speed systems, OCT employs the concept that with a coherent optical source, differences in path length also create differences in the phase of the light.

Another technique is Diffuse Optical Tomography (DOT) [1-22-1-24] which treats the imaging of a scattering medium as an inverse problem, and uses multiple measurements of the medium with sources and detectors at various positions to develop and parameterize a three-dimensional model that describes the contents of the medium. Besides these technologies, hybrid detection techniques like photoacoustic imaging can be utilized to bypass the scattering problem present for pure optical imaging systems. In addition, we introduced the Angular Domain Imaging as an alternative optical imaging method, which is the principal for the proposed imaging technique in this thesis. In the following subsections, further details of these optical imaging techniques have been reviewed.

1.3.1 Time domain optical imaging

In Time Domain (TD) measurement, a short pulse of light illuminates the scattering medium and an ultra-fast imager records a time course of the illumination response. The high-speed imager is used to select the early arriving light and to reject the late arriving scattered photons [1-19]. A TD sample imaging setup, presented in [1-19] is shown in Figure 1-4. The light source was a Ti:Sapphire laser operated in femto-mode at a wavelength of 800 nm. The detection system included an ultra high speed shutter and imager to capture the early arriving photons. A small portion of the laser beam was deflected by a quartz plate to a fast photodiode, which generated a trigger signal for the imager. The turbid medium was mounted on a translation stage used to actuate relative movement between the light path and the object. A PC served as a central

controlling and data acquisition unit. TD optical imaging systems have been used for several applications. For example, breast cancer imaging using a Ti-Sapphire pulsed laser with a spectral range of 750nm- 850 nm has been performed [1-25]. A TD system for functional imaging of the adult brain has been developed as well [1-26].

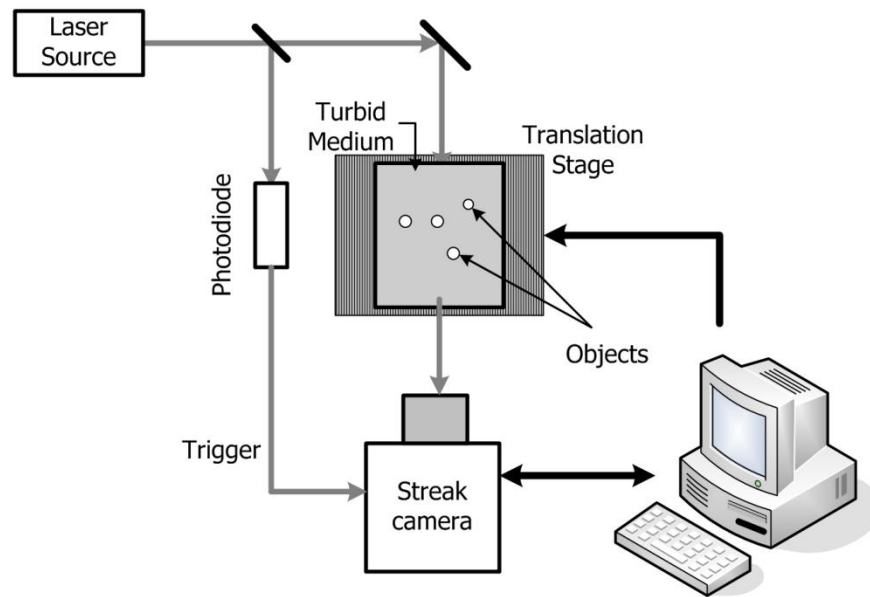


Figure 1-4: Time domain imaging setup using a streak camera to capture ballistic and quasiballistic photons [1-19].

The time domain optical tomography has two major drawbacks. First, in order to gate the incoming light, very short laser pulses (pico- to femto-second range) and fast camera detectors (nanosecond range) are needed, which makes this method expensive and dependent on high-performance equipment. Second, the signal at the detector consists only of an exponentially small portion of the

total number of photons emitted by the light source. Consequently, the signal-to-noise ratio is inherently low and scan time can be very long.

1.3.2 Optical coherence tomography

OCT principle is based on the fact that the coherence property of the backscattered light contains time-of-flight information that can be used to determine the longitudinal locations of reflective boundaries and sub-surface sites in the tissue. Early OCT systems have been based on low coherence interferometry, which splits a low coherence light source into two beams: a sample beam and a reference beam as shown in Figure 1-5. These two beams are then used to form an interferometer. The sampling or measurement beam hits and penetrates the tissue under observation [1-20]. The measurement beam is reflected or scattered from the sample, bringing information about the reflecting positions from the surface and the subsurface of the sample. The reference beam reflects from a reference reflector, such as a mirror. The reference reflected beam either moves or is designed such that the reflection happens at different distances from the beam splitting point and returns at a different point in time or in space, which in fact signifies the depth of scan. The return time for the reference beam corresponds to a specific depth of diffusion of tissue by the sampling beam [1-20]. A detector senses the interference from two reflected beams, that is the reference arm, and the coherently scattered photons back-reflected from certain depth within the sample with equal time delay. Whereas, multiply scattered photons are out of phase and incoherent with the reference beam [1-20, 1-21].

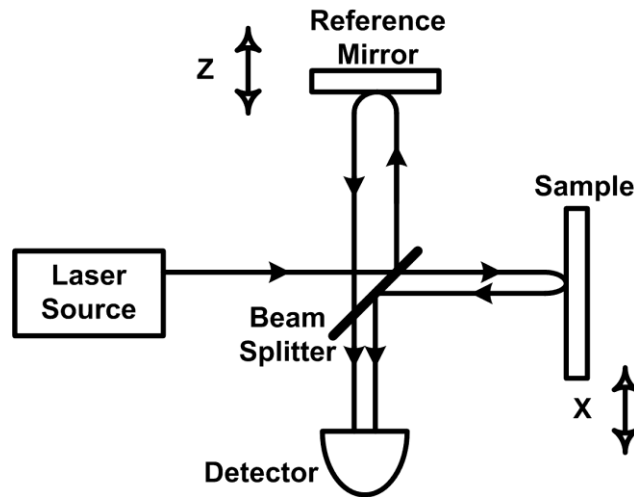


Figure 1-5: OCT system measures the echo time delay of reflected light beam by low-coherence interferometry. Longitudinal scan can be done by moving the reference mirror and transverse scan can be done by moving the sample [1-21].

Although, the main disadvantage of OCT compared to alternative imaging modalities is its limited penetration depth in scattering media, OCT is quite successful in ophthalmology because of the high transmittance of ocular media. Ultra-high-resolution OCT imaging utilizing a femtosecond Titanium–sapphire laser light source has been demonstrated with axial resolution of 1–3 μm in non-transparent and transparent tissue, enabling unprecedented in vivo imaging of intra-retinal sub-cellular structures [1-27]. OCT results are promising in gastroenterology and dermatology [1-28, 1-29]. In terms of a light source, coherency of the light source is an important issue where temporal coherence, correlation between the electric fields at one location but different times, determines depth resolution. The spatial coherence, correlation (fixed phase

relationship) between the electric fields at different locations, plays a role in both lateral resolution and depth resolution of OCT.

1.3.3 Diffuse optical tomography

The basic methodology of DOT imaging is to illuminate the tissue with light sources and to measure the light leaving the tissue with an array of detectors (Figure 1-6). For the specific source location, detectors record the light intensity reaching from other sources. A model of the propagation of light in tissue is developed and parameterized in terms of the unknown scattering and/or absorption as a function of position in the tissue. In most situations of interest, where the system size is larger than the transport scattering mean free path, the diffusion equation for light provides a reasonably good description. Then, using the model together with the ensemble of images over all the sources, one attempt to invert the propagation model to recover the parameters of interest, or, in other words, to estimate the scattering and/or absorption parameters out of the data, using the model. The application of DOT has many applications in medical structural or functional imaging including: brain functional imaging [1-30], breast imaging [1-31], muscle imaging [1-32] and imaging of joint inflammation [1-33]. However, its acceptance has been limited in scope because DOT requires intensive, and in most cases, time consuming, computations.

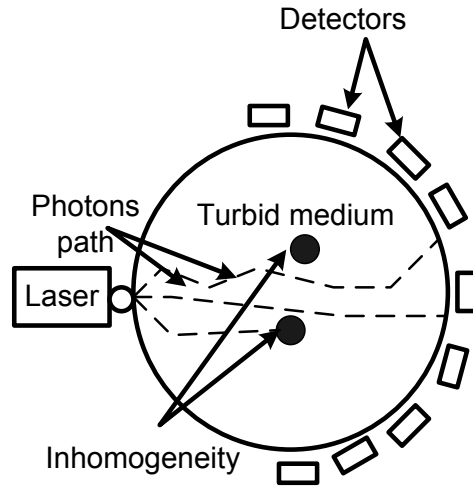


Figure 1-6: Diffuse Optical Tomography system diagram including multiple detectors, and light source.

The use of the diffusion model assumes that the number of scattered photons is much larger than the number of absorbed photons. Therefore, the signals received by detectors are less sensitive to absorptive structures ($\sim 1\text{cm}$) within the turbid medium, which results in low-resolution images. Furthermore, due to the physics of the propagation, the inverse problem is ill-posed [1-24]; in other words, relatively large changes in the parameters of interest tend to result in relatively small changes in the measurements. Thus, inverse solutions must amplify these small differences; as a consequence measurement noise and model error will be amplified as well, causing inverse solutions to be wildly erratic and nonphysical unless constrained by additional a priori assumptions and solutions which are not typically numerically unique [1-24].

1.3.4 Photoacoustic tomography

Pure optical imaging techniques, as described before, suffer from either shallow penetration depth (below 1 mm) in high-resolution imaging or limited resolution like DOT (~ 1 cm) to image in larger depth. Both limitations are a consequence of strong scattering of tissues. Therefore, an imaging technique that can provide optical contrast but is insensitive to scattering is highly desirable. Photoacoustic tomography is a promising candidate since the optical contrast recognition is encoded as sound waves. The principle of photoacoustic imaging is based on four steps: 1) a short pulse light source (~ ns duration) illuminates the tissue sample, 2) a small temperature rise results from optically absorbing structures due to energy to heat conversion, 3) the rapid heating due to short pulse results in thermoelastic expansion, followed by a pressure change, and 4) the pressure change is measurable as an acoustic wave that propagates outward and can be recognized by ultrasound detectors as shown in Figure 1-7.

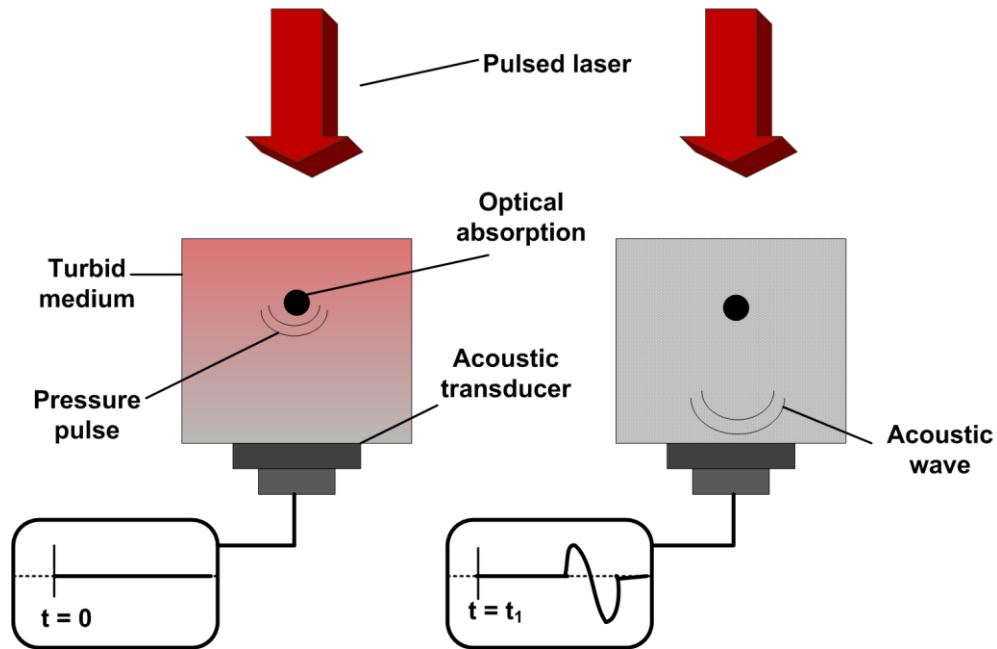


Figure 1-7: Stages of photoacoustic process.

Photoacoustic imaging can provide wide range of imaging applications from microscopic to macroscopic level with larger imaging depths than pur optical imaging approaches. For instance, Wang et al reported the PAT images of cortical vessels and functional imaging in the rat brain [1-34]. In their imaging system at the optical depths of 1 mm to 5 mm, a spatial resolution of 200 μm was achieved with an acquisition time of 13 min. On the other hand, another system by Alexander Oraevsky's research group has shown promising results for breast imaging application [1-35]. Their system can provide 2 cm optical penetration with 500- μm spatial resolution with 1-10 frame-rates per second.

Although, the PAT system cost is relatively high due to light source requirements (high power pulse laser), and the initial cost for acoustic transducers and electronics to acquire the data. Current efforts are focusing on

the acquisition of quantitative images [1-36]. Finally, PAT requires an extensive scanning steps or computational intensive reconstruction methods to create the 3D images [1-37].

1.3.5 Optical imaging modalities review

All of the above optical imaging methods are being studied to achieve high contrast and useful images mainly for biomedical uses. The lower cost, stability, and portability of the optical systems are a major benefit of these systems. However, optical imaging methods suffering from problems, which has limited there commercial success, except for very specific applications. For example, although TD imaging provide a wealth of information with the aim of mapping the optical properties of tissue, it suffers from a low proportion of informative photons when applied to thick tissues that leads to long data acquisition times compared to CW techniques. OCT provides high-resolution images but only for shallow depths or clear tissues. It has been recognized as ideal imaging method for studying the human eye. However, OCT is not sensitive to the absorption and fluorescence optical probes. Both TD and OCT methods require expensive and sensitively calibrated setups. TD methods require expensive and sophisticated fast laser sources (femtosecond range pulses) and fast detectors (picoseconds range) while Phase Coherence methods require a complex and expensive setup that is difficult to maintain over long distances to split the laser beam into a reference beam path and a path through the tissue. On the other hand, DOT application is limited by its poor spatial resolution; potentially long computation times for the recovery of a three dimensional image; and instability and non-

uniqueness of the image reconstruction problem. However, as a non-invasive and non-ionizing imaging technique, DOT with its high sensitivity and good depth penetration has proven to be useful as a technique for breast imaging.

Photoacoustic imaging needs more improvement in terms of scanning time versus resolution tradeoffs.

1.4 Angular domain imaging

A simple alternative method of eliminating almost all scattered light, which blurs the image of an object in turbid medium, is based on accepting, by means of a collimator, only photons propagating within a narrow solid angle with reference to the incident light direction. These photons participate in no or very few small-angle scattering events, which permits the photons to maintain their original propagation direction and contribute to the development of a faithful image of an object within a turbid medium. This modality is referred to as angular domain imaging (ADI).

ADI employs silicon micro-machined angular filter arrays. Angular filters are designed to extract non-scattered photons that arrive at a detector within very small acceptance angles in the presence of scattered photon levels many orders of magnitude greater. Angular filtration enables the imaging and characterization of optical contrast (absorption or fluorescence) in highly scattering media by extracting meaningful quasi-ballistic photons preferentially over background noise caused by scattered photons.

An angular filter consists of high-aspect ratio micro-channel called collimators to create pathways through which unscattered photons can pass without attenuating. Unscattered photons arrive within an allowable acceptance angle with respect to the longitudinal axis of each micro-channel aligned with the collimated beam. However, photons that arrive with incident angles beyond the acceptance angle (with large angular deviations) will strike the channel sides and be attenuated.

By variation of aperture size and micro-channel length, an acceptance angle range of 0.1° - 0.5° can be easily achieved. As shown in Figure 1-8, if a photon emerges from a scattering medium with an angle that is more than the acceptance angle, then it either fails to enter the collimator or gets absorbed within it (dashed lines). The assumption made here is that the scattered light has random exit angles and hence only the minimally deviated ballistic and quasi-ballistic photon will be detected. Monte-Carlo simulations [1-50] support this assumption by showing that most photons with small angular deviations undergo the shortest path length through a scattering medium.

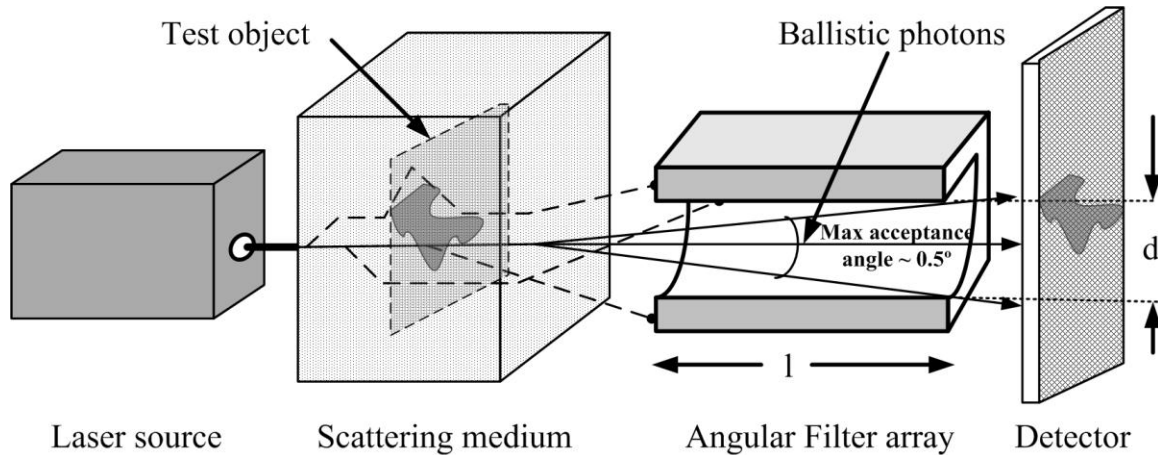


Figure 1-8: Typical setup for Angular Domain Imaging using high aspect ratio collimators

A conventional method for producing such high-aspect-ratio collimating structures is by using silicon bulk micromachining (Same technology used in the fabrication methods of Integrated Circuit to create mechanical and optical structures in micron dimensions). For instance, an early design of a linear collimating array was created using a silicon wafer patterned with the 51 μm diameter channels spaced 102 μm apart over an area of 20x20 mm (See Figure 1-9). The channels were created using chemical isotropic etchant. Early work referred to the device as a Silicon Micromachined Collimating Array (SMCA). Newer work refers to the device as an Angular Filter Array (AFA).

1.4.1 Overview of ADI methodology

Since the AFA has a limited vertical field of view, a scanning procedure has to be implemented to create a 2D shadowgram of the test object. Tests of the vertical and horizontal spatial resolution were performed initially using a glass slide with L-shaped metal test structures patterned onto the slide. Each L-

shaped test structure was made up by lines of 204 μm , 153 μm , 102 μm , or 51 μm in width, as shown below in Figure 1-10 (a).

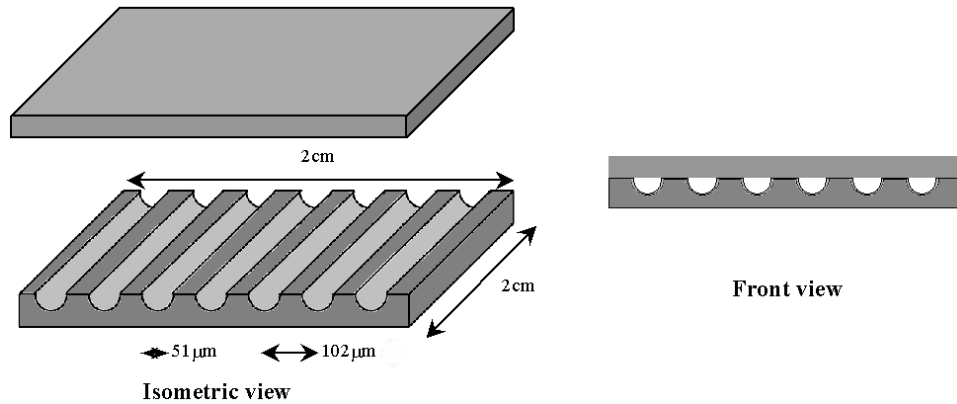


Figure 1-9: Silicon Micro-machined Collimating Array (SMCA) [1-47]

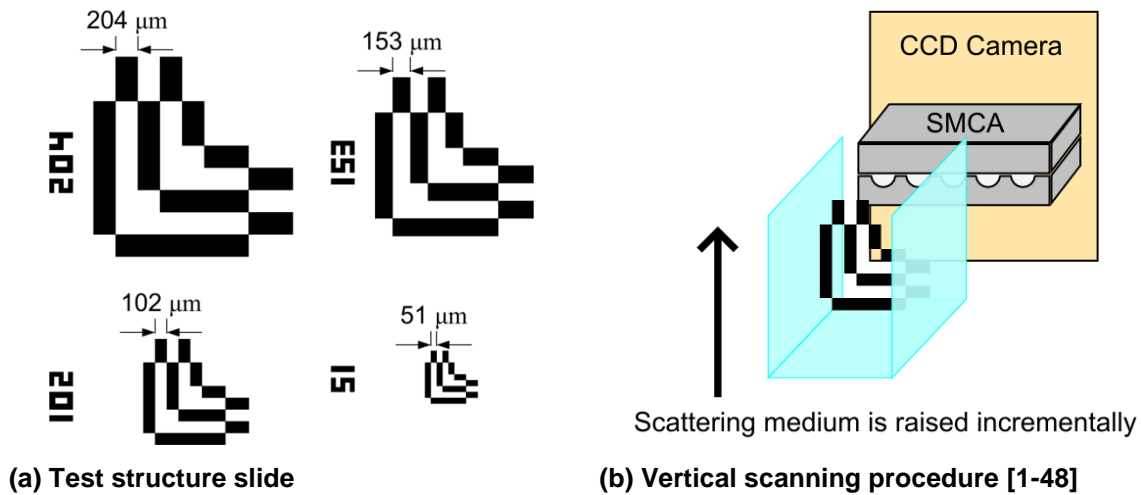


Figure 1-10: Scanning details for ADI experiments.

As illustrated in Figure 1-10 (b), image scans are taken one horizontal line at a time through the AFA. A computer controlled z-axis stage raises the sample

by a fixed step size before the next line is imaged, and the process is repeated to build up a 2D shadowgram.

1.5 Angular filter array fabrication

The first step is the growth of Silicon dioxide (SiO_2) as a masking layer approximately $0.5 \mu\text{m}$ thick on the silicon wafer. The oxidation process is performed in a furnace for several hours at temperatures in the range of 1100°C in the presence of gaseous H_2O (this is known as “wet” oxidation). Once this oxide is grown, an organic photoresist layer can be spun on top of the wafer, and a mask pattern can be transferred onto this photoresist layer using UV-light photolithography process (see Figure 1-11(a)). The pattern in the photoresist can then be transferred to the underlying oxide layer using SiO_2 etchant while leaving the photoresist largely intact. The photoresist layer can then be stripped away using acetone, leaving only the patterned oxide on the silicon wafer (see Figure 1-11(b)).

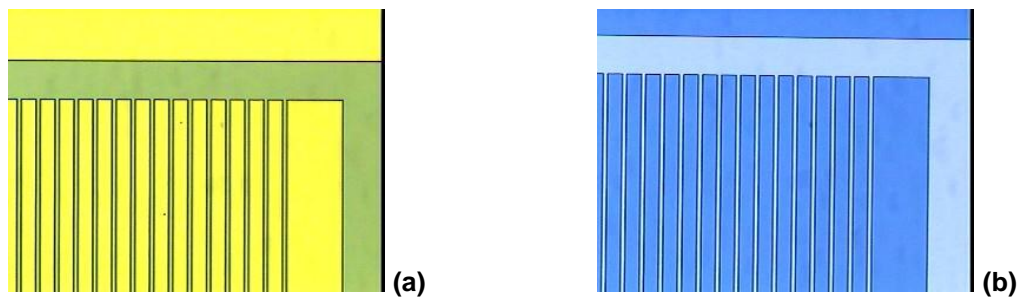


Figure 1-11: Microscope images of patterned photoresist and oxide layers on a silicon wafer, (a) Photoresist layer – (5x magnification) (b) Oxide layer – (5x magnification)

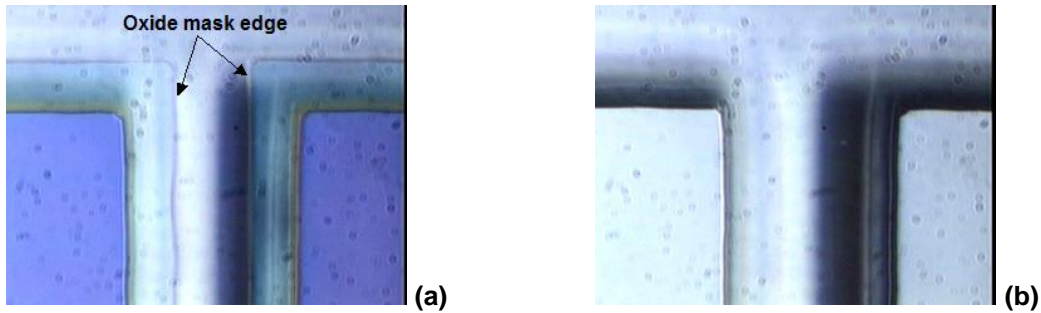


Figure 1-12: Microscope images of etched silicon tunnels with and without the oxide mask. (a) Oxide mask with etched tunnels– (80x magnification) (b) Silicon tunnels – (5x magnification)

The patterned oxide layer can then be used as a mask to etch the underlying silicon wafer. In order to fabricate semi-circular micro-channel arrays, isotropic etchant solution was used to etch tunnels into the silicon underneath the oxide mask, yielding the results shown in Figure 1-12 (a). The oxide layer can then be stripped away, with only the etched silicon tunnels remaining, as shown in Figure 1-12 (b). The AFA pieces were cut from the silicon wafer using a dicer before they can be used. The finished etched wafer (before scribing) and a scanning electron microscope (SEM) image of a tunnel are shown in Figure 1-13 and Figure 1-14 respectively. More details on semi-circular shape AFA fabrication details have been described in [1-40-1-42].

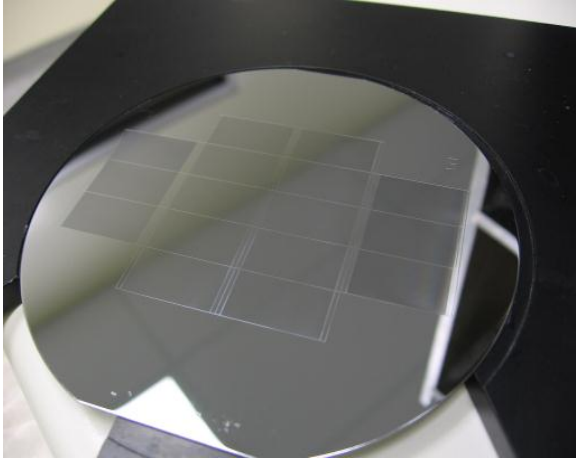


Figure 1-13– Completed silicon wafer with AFA devices.

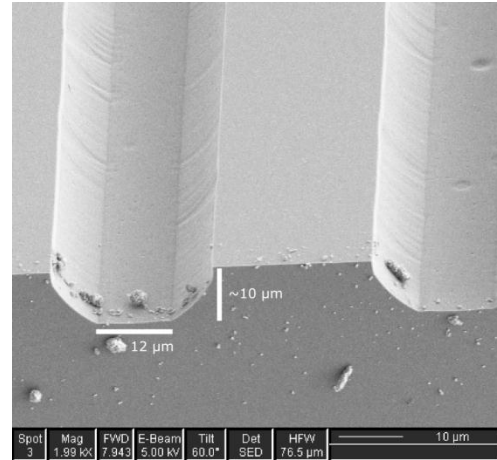


Figure 1-14– SEM picture of AFA channel [1-40].

1.6 Prior work in ADI

Angular domain optical imaging has a long history of investigation with different terminologies such as collimator, spatial filter, and lens and pinhole. A simple angular filter array (also called spatial filters) can be employed with an array of aligned pinholes with the detector at the output of pinholes [1-43]. Shimizu et al [1-44] employed angular filters (called collimator) using pinholes and fibre optics combined with time gating techniques to image through tissue mimicking samples as well as a murine model. Another Fibre optic based collimator for CT type imaging was presented as CW and frequency domain imaging systems by P. van der Zee et al [1-45]. Most of the research studies employ angular filter in combination of time or frequency domain system to get the maximum rejection of scattered light. Yet, the collimators had large geometries, which can be used only in point detection or arrays with large hole separations [1-46]. Use of optical fibres is not optimal since fibres also have

either large acceptance angle (multi-mode) or limited spectral range operation (single-mode) and thick outer layer for fibres protection preventing close spacing.

Early results for Angular Domain Imaging (ADI) in a highly scattering medium using a Silicon Micromachined Collimator Array (SMCA) were published by Tank and Chapman in the Canadian Journal of Electrical and Computer Engineering in January 2000 [1-49]. The results showed successful detection of a knife edge in front of a $SR=5\times 10^6:1$ scattering medium along with successful resolution of $180\mu\text{m}$ lines and spaces in a $SR=5\times 10^4:1$ scattering medium. The SMCA consisted of 50 micron wide etched semi-circular channels with 100 micron spacing over a 10 mm width of silicon to achieve a very high aspect ratio (200:1). It was shown that if the SMCA was precisely aligned to the collimated light source, then the unscattered photons exiting from turbid sample could pass directly through the channels to the CCD, while the channel walls absorbed the scattered light that had an angle greater than 0.29 degrees. The rationale behind SMCA fabrication compared to other angular filters was mainly based on their high angular selectivity, wavelength independence over the visible and near infrared range, relatively small separations with compact design, and high precision and low manufacturing cost. Dr. Chapman continued his work by publishing more comprehensive analysis of an ADI system in transillumination along with Monte Carlo simulation in 2003 [1-50]. Monte-Carlo simulation programs designed to test the ADI concept showed that the collimator detects the shortest path length photons [1-53]. Consequently, the collimator acts as an optical filter to remove scattered light while preserving the image resolution.

Simulations suggested that smaller channels and longer arrays could enhance detection by >100 in the condition that they do not violate diffraction and Raleigh range limitations [1-50]. Since the AFA has a limited vertical field of view, full illumination of a turbid sample is not efficient. Light that is not in the field of view of AFA results in increased background noise. Consequently, restricting the illumination to only the aperture of the AFA provides increased image contrast by reducing the amount of background noise due to the scattered light. This has been done by inserting horizontal slits [1-51] or in improved versions by using Cylindrical-Spherical-Cylindrical (CSC) lens beam expanders/shrinkers to form a wide collimated line of light of small thickness aligned to the collimator array [1-52].

ADI is an appealing technology for manufacturing compact and simple optical imaging systems for biomedical imaging. Angular domain imaging possesses superior advantages as an optical imaging method: *i)* detection is not wavelength dependent, which allows for broadband light sources or fluorescence detection; *ii)* there is no need for coherent sources nor ultra-fast pulse lasers, and therefore, incandescent lamps or LEDs can be used, which can ultimately lead to a low-power, low-footprint, portable imaging system. However many potential applications in ADI such as multispectral/hyperspectral imaging, fluorescence detection, tomography, and reflective measurement were untouched and needed to be explored.

1.7 Thesis objective and scope

The objective of the work presented in this thesis was to improve the performance of ADI with the aim of bringing ADI closer to real world with applications such as real biological tissue imaging. The ADI performance developments fall under two categories:

- 1- **Technological advancements**: Contrast and resolution enhancement by implementing various approaches such as fabricating new AFA designs, estimation and subtraction of background scattered noise, and using combination of polarization gating and/or time gating.
- 2- **Application development**: Study of different modes of operation such as multispectral/ hyperspectral, reflection, and fluorescence to recognize the feasibility and challenges of using AFAs compared with other available technologies.

1.8 Research approach

In order to achieve the thesis objective, several design modifications to the structure of the angular filter array device and optical system arrangements have been implemented. In terms of the thesis organization, six journal papers from chapter 2 to chapter 7 are presented encapsulating the accomplished advancements in ADI during my PhD studies. The order of journal articles are based on the coherency of the thesis stream, which is explained in more detail below:

Chapter 2 describes the article “Multi-spectral angular domain optical imaging in biological tissues using diode laser sources” which presents one of the most important properties of ADI imaging, which is the wavelength independence of this imaging technique. The manuscript describes conventional trans-illumination ADI with semi-circular micro channels at various wavelengths in the near infrared spectrum. Proof of concept experimental results showed that multi-spectral ADI measurements could be obtained and light intensity attenuation can be fitted with high accuracy to a $5\times$ MFP’ scattering level in the near infrared spectrum. This information provides confidence in the success of multispectral ADI for soft tissues up to 5 mm. ADI measurements of chicken breast, our first real biological sample, demonstrated that ADI revealed sub-millimetre resolution targets behind tissue sample. This helped us identify problems in imaging real tissues, i.e. heterogeneous scattering media, with ADI.

Chapter 3 presents the article “Image contrast enhancement in angular domain optical imaging of turbid media” which compares different contrast enhancement techniques in ADI. In general, at high scattering levels, ADI image contrast declines due to the non-uniform scattered background light fraction still within the acceptance angle of the angular filter array. The paper describes a method to correct for this problem using ADI and polarization gating. The paper also describes a second correction method that employs the capture and subtraction of scattered photons using a wedge prism. Improved image contrast by experimental measurements of background scatter is analyzed using a wedge prism and image processing algorithms.

Chapter 4 presents the article “Angular domain trans-illumination imaging optimization with an ultra-fast gated camera”. The article shows an experimental characterization of the angular distribution of photons exiting turbid media to determine the optimum range of acceptance angles of the angular filter array. The article also shows performance analysis for different AFA fabrication geometries to minimize the photon reflections within the micro-channels. The paper also describes the combination of ADI with time domain detection using a pulsed laser and ultra fast camera. Experimental results in tissue-mimicking phantoms showed that the combination of complimentary techniques like time and angular filtration further enhance the performance of scattered photon rejection and made it possible to image thick biological specimens with higher contrast while maintaining sub-millimetre resolution.

Chapter 5 presents the article “An Optical Imaging Technique Using Deep Illumination in the Angular Domain” which describes a novel optical imaging method enabling the optical detection of sub-millimetre targets within highly scattering media in a reflection detection arrangement. So called “Deep illumination ADI” uses collimation detection capabilities of angular filter arrays to extract image-forming photons emitted from the scattered light created by a laser source aimed deep (3 mm) beneath the surface of a turbid medium. The article reports the imaging results from tissue-like phantoms as a proof of concept and a biological tissue sample as a final result. This new optical imaging modality is significant for two reasons. First, the technique is able to capture optical images

to depths up to 3 mm in the reflection mode. Second, it employs simple and inexpensive optical components compared to other competing modalities.

Chapter 6 presents the article “Transmission and Fluorescence Angular Domain Optical Projection Tomography of Turbid Media” which extended the two dimensional capture of projection images to tomographic image with the use of computed tomography techniques. By collecting images at various angles and using a filtered backprojection algorithm, we could establish the depth of internal structures hidden in a turbid medium. The tomographic system was capable of sub-mm resolution when imaging through thick (> 5 mm) biological specimens. The tomography system was also able to collect fluorescent signals in a dark field illumination setup, resulting in a tomographic map of fluorescent targets in a tissue mimicking phantom.

Chapter 7 presents the article “Angular Domain Fluorescence Imaging for Small Animal Research”, which describes a novel macroscopic fluorescent imaging technique called Angular Domain Fluorescence Imaging (ADFI). ADFI is capable of detecting fluorophores embedded in biological tissues in reflection mode. The method exploits the collimation detection capabilities of an angular filter array (AFA) for fluorescent imaging in both tissue-mimicking phantoms and murine model. ADFI was used to collect images of a hairless mouse injected with a fluorescent bone marker. Structural and morphometric data of vertebrae collected using ADFI in correlation with data derived from volumetric X-ray CT and other conventional optical imaging systems was presented.

Finally in Chapter 8, the summary of accomplishments from previous chapters is presented, current developments are described, and directions for future work are proposed. The discussion sections are arranged by subject rather than chronologically to tie the different chapters together conceptually and present a consistent discussion for each specific topic. The summary is organized to mirror the initial objectives of the thesis.

1.9 Reference list

- 1-1. R. Smith-Bindman, J. Lipson, R. Marcus et al. Radiation dose associated with common computed tomography examinations and the associated lifetime attributable risk of cancer. *Arch Intern Med*, vol. 169, p.2078-86 (2009)
- 1-2. R.F. Redberg, "Cancer risks and radiation exposure from computed tomographic scans: How can we be sure that the benefits outweigh the risks". *Arch Intern Med*, Vol. 169 p.2049-50 (2009)
- 1-3. J. V. Frangioni, "New Technologies for Human Cancer Imaging", *J Clin Oncol*, Vol. 26: 4012-402 (2008)
- 1-4. D. A. Benaron, "The Future of Cancer Imaging", *Cancer and Metastasis Reviews*, Vol. 21(1): 45-78 (2002)
- 1-5. R. A. Natalin & J. Landman, "Where next for the endoscope?", *Nature Reviews Urology* 6, 622-628 (2009)
- 1-6. J. C. Saurin, "Capsule endoscopy," *Endoscopy* 39, 986–991 (2007)
- 1-7. Tuan Vo-Dinh, Ed., "Biomedical Photonics Handbook," Publisher: CRC, (2003)
- 1-8. E. Profio, "Light Transport in Tissue," *Appl. Opt.*, vol 28, no. 12, pp. 2216-2222 (1989)
- 1-9. M. R. Arnfield, J. Tulip, and M. S. McPhee, "Optical propagation in tissue with anisotropic scattering," *IEEE Trans. Biomed. Eng.*, vol. 35, pp. 372-381 (1988)
- 1-10. Henyey, L. and Greenstein, J. L., "Diffuse radiation in the galaxy", *Astrophys. J*, 93, 70, (1940)
- 1-11. Jacques SL, Alter CA, Prael SA, "Angular Dependence of HeNe laser Light Scattering by Human Dermis", *Laser Life Sci.* 1, pp.309-333 (1987).

- 1-12. L. V. Wang, and H.I Wu, "biomedical optics principles and imaging" John Wiley & Sons, Inc., Hoboken, New Jersey (2007)
- 1-13. M. R. Arnfield, J. Tulip, and M. S. McPhee, "Optical propagation in tissue with anisotropic scattering," IEEE Trans. Biomed. Eng. 35, 372–381 (1988).
- 1-14. W. F. Cheong, "A review of the optical properties of biological tissues," IEEE J. Quantum Electron. 26, pp. 2166-2185 (1990).
- 1-15. HG van Staveren, CJM Moes, J van Marle, SA Prahl, MJC van Gemert, "Light scattering in Intralipid-10% in the wavelength range of 400-1100 nanometers," Appl. Opt. 30, 4507-4514, (1991).
- 1-16. B. B. Das, "Time-resolved fluorescence and photon migration studies in biomedical and model random media," Reports on Progress in Physics, vol. 60, pp. 227-92, 1997.
- 1-17. J.C. Hebden and D.T. Delpy, "Enhanced time-resolved imaging with a diffusion model of photon transport," Opt.Lett., vol. 19, pp. 311-13, 03/01. 1994.
- 1-18. B.B. Das, K.M. Yoo and R.R. Alfano, "Ultrafast time-gated imaging in thick tissues: a step toward optical mammography," Opt.Lett., vol. 18, pp. 1092-4, 07/01. 1993.
- 1-19. Chen, Kun ; et al., "Optical computed tomography in a turbid media," US Patent Application 2003/0065268, April 3, 2003.
- 1-20. F. Fercher , "Optical coherence tomography-principles and applications," Reports on Progress in Physics, vol. 66, 239-303, 2003.
- 1-21. J. G. Fujimoto , "Optical coherence tomography," Comptes Rendus De l'Academie Des Sciences, Serie IV (Physique, Astrophysique), vol. 2, 1099-111, 2001.
- 1-22. D. A. Boas, D. H. Brooks, E. L. Miller, C. A. DiMarzio, M. Kilmer, R. J. Gaudette and Quan Zhang, "Imaging the body with diffuse optical tomography," IEEE Signal Process. Mag., vol. 18, pp. 57-75, 11/. 2001.
- 1-23. M.A. O'Leary, D.A. Boas, B. Chance and A.G. Yodh, "Experimental images of heterogeneous turbid media by frequency-domain diffusing-photon tomography," Opt.Lett., vol. 20, pp. 426-8, 03/01. 1995.
- 1-24. Tikhonov and V. Arsenin, Solution of Ill-Posed Problems. Washington, DC: Winston, 1977.

- 1-25. X. Intes, S. Djeziri, Z. Ichalalene, N. Mincu, Yong Wang, P. St-Jean, F. Lesage, D. Hall, D. A. Boas and M. Polyzos, "Time-domain optical mammography Softscan® Initial results on detection and characterization of breast tumors," in Photonics North 2004: Photonic Applications in Astronomy, Biomedicine, Imaging, Materials Processing, and Education, 2004, 2004, pp. 188-97.
- 1-26. J. Selb, D. K. Joseph and D. A. Boas, "Time-gated optical system for depth-resolved functional brain imaging," *J. Biomed. Opt.*, vol. 11, pp. 44008-1, 07/. 2006.
- 1-27. R. K. Ghanta, W. Drexler, U. Morgner, F. Kartner, E. P. Ippen, J. G. Fujimoto, J. S. Schuman, A. Clermont and S. Bursell, "Ultrahigh resolution retinal imaging with optical coherence tomography," in Conference on Lasers and Electro-Optics (CLEO 2000). Technical Digest. Postconference Edition. TOPS Vol.39, 7-12 may 2000, 2000, pp. 506-8.
- 1-28. J. A. Izatt, M. D. Kulkarni, Hsing-Wen Wang, K. Kobayashi and M. V. Sivak Jr, "Optical coherence tomography and microscopy in gastrointestinal tissues," *IEEE Journal of Selected Topics in Quantum Electronics*, vol. 2, pp. 1017-28, 12/. 1996.
- 1-29. N. Gladkova, "In vivo optical coherence tomography imaging of human skin: norm and pathology," *Skin Research and Technology*, Vol. 6, pp. 6-16(2000)
- 1-30. B. Chance, E. Anday, S. Nioka, Shuoming Zhou, Long Hong, K. Worden, C. Li, T. Murray, Y. Ovetsky, D. Pidikiti and R. Thomas, "A novel method for fast imaging of brain function, non-invasively, with light," *Optics Express*, vol. 2, 05/11. (1998)
- 1-31. B.W. Pogue, S.P. Poplack, T.O. McBride, W.A. Wells, K.S. Osterman, U.L. Osterberg and K.D. Paulsen, "Quantitative hemoglobin tomography with diffuse near-infrared spectroscopy: pilot results in the breast," *Radiology*, vol. 218, pp. 261-6, 01/. (2001)
- 1-32. E.M.C. Hillmanl, J.C. Hebden, M. Schweiger, H. Dehghani, F.E.W. Schmidt, D.T. Delpy and S.R. Arridge, "Time resolved optical tomography of the human forearm," *Phys.Med.Biol.*, vol. 46, pp. 1117-30, 04/. (2001)
- 1-33. Y. Xu, "Imaging of in vitro and in vivo bones and joints with continuous-wave diffuse optical tomography," *Optics Express*, vol. 8, pp. 447-451. (2001)
- 1-34. X. Wang, Y. Pang, G. Ku, X. Xie, G. Stoica, and L. V. Wang, "Noninvasive laser-induced photoacoustic tomography for structural and functional in vivo imaging of the brain", *Nat. Biotechnol.* 21, 803 (2003).

- 1-35. S. Ermilov, A. Stein, A. Conjusteau, R. Gharieb, R. Lacewell, T. Miller, S. Thompson, P. Otto, B. McCorvey, T. Khamapirad, M. Leonard, and A. Oraevsky, "Detection and noninvasive diagnostics of breast cancer with 2-color laser optoacoustic imaging system," in *Photons Plus Ultrasound: Imaging and Sensing 2007: The Eighth Conference on Biomedical Thermoacoustics, Optoacoustics, and Acousto-optics*(SPIE, San Jose, CA, USA, 2007), 6437, pp. 643703-643711.
- 1-36. Benjamin T. Cox, Simon R. Arridge, Kornel P. Köstli, and Paul C. Beard, "Two-dimensional quantitative photoacoustic image reconstruction of absorption distributions in scattering media by use of a simple iterative method," *Appl. Opt.* **45**, 1866-1875 (2006)
- 1-37. Ephrat, P., Keenliside, L., Seabrook, A., Prato, F.S., & J.J.L. Carson. Three-dimensional photoacoustic imaging by sparse-array detection and iterative image reconstruction. *J. Biomed. Opt.* **13**(5): (2008)
- 1-38. Alfano R. R. et al, "Time-Resolved Optical Backscattering Tomographic Image Reconstruction in Scattering Turbid Media" U.S. patent, US6205353, March 20, 2001.
- 1-39. H Inaba, "Coherent Detection Imaging for Medical Laser Tomography", SPIE IS11, 317-347, 1993.
- 1-40. P. Chan, "Angular Filters for Angular Domain Imaging Optical Tomography in Highly Scattering Media" M.A.Sc. thesis, Simon Fraser University, Burnaby, BC, Canada, 2008.
- 1-41. P. Chan, "Exploring the Limits of Silicon Micromachined Collimating Array Assisted Optical Tomography" B.A.Sc. thesis, Simon Fraser University, Burnaby, BC, Canada, 2005.
- 1-42. M. Tank, "Development of a Silicon Micromachined Collimator Array to Detect Objects within Highly Scattering Mediums," M.A.Sc. thesis, Simon Fraser University, Burnaby, BC, Canada, 2001.
- 1-43. J. Beuthan, O. Minet, G. Muller, V. Prapavat, "IR-diaphanoscopy in medicine", in *Medical Optical Tomography: Functional Imaging and Monitoring* (G. Muller, B. Chance, R. Alfano et al. eds.), 263-282(1993).
- 1-44. K. Shimizu and M. Kitama, "Fundamental study of near-axis scattered light and its application to optical computed tomography," *Opt. Rev.* **7**, 383-388 (2000).
- 1-45. P. van der Zee, R. Khalaf, L. Dixon, A. Davies, R. Roy, "Optical medical tomography for the localisation of oxygenation in the limb", SPIE proceeding, 3196, 61-70 (1998).

- 1-46. P. van der Zee et al., "Methods for measuring the optical properties of tissue samples in visible and near infrared wavelength range," in Medical Optical Tomography: Functional Imaging and Monitoring, SPIE IS11, G. Muler et al., Eds., 1993, pp. 166–192.
- 1-47. N. Pfeiffer, B. Wai, and G.H. Chapman, "Angular Domain Imaging of phantom objects within highly scattering mediums" Proc. SPIE Photonics West: Laser Interaction with Tissue and Cells XV, v 5319, San Jose, CA pp. 135-145 (2004)
- 1-48. P. Chan, "Angular Filters for Angular Domain Imaging Optical Tomography in Highly Scattering Media" M.A.Sc. thesis, Simon Fraser University, Burnaby, BC, Canada, 2008.
- 1-49. M. Tank and G.H. Chapman, "Micromachined Silicon Collimating Detector Array to View Objects in Highly Scattering Medium", Can Jour Elec. & Comp. Eng, .25, no. 1, 13-18 (2000)
- 1-50. G. H. Chapman, M. Trinh, N. Pfeiffer, G. Chu and D. Lee, "Angular Domain Imaging of Objects Within Highly Scattering Media Using Silicon Micromachined Collimating Arrays", IEEE J. Special Topics on Quantum Electronics, v9, no. 2, 257-266 (2003)
- 1-51. G.H. Chapman, M. Trinh, G. Chou, N. Pfeiffer and D. Lee, "Optical imaging objects within highly scattering material using Silicon Micromachined Collimating Arrays", SPIE Photonics West, Optical Tomography and Spectroscopy of Tissue V, San Jose, (BIOS) v4955, pg 464-473, Jan. 2003.
- 1-52. G.H. Chapman, P.K.Y. Chan, J. Dudas, J. Rao and N. Pfeiffer, "Angular Domain Image Detectability with Changing Turbid Medium Scattering Coefficients", Proc. SPIE Photonics West: Laser Interaction with Tissue and Cells XVI, v, 5695, pg 160-171, San Jose, CA, Jan. 2005.
- 1-53. N. Pfeiffer, "Imaging of turbid media using trajectory filter methods" Ph.D. thesis, Simon Fraser University, Burnaby, BC, Canada, 2009

2: MULTI-SPECTRAL ANGULAR DOMAIN OPTICAL IMAGING IN BIOLOGICAL TISSUES USING DIODE LASER SOURCES¹

2.1 Abstract

Angular Domain Imaging (ADI) employs micro-machined angular filter to detect non-scattered photons that pass through the micro-scale tunnels unattenuated while scattered photons are rejected. This paper describes the construction of an ADI system utilizing diode lasers at three different wavelengths in the range of the red and near infrared spectrum. Experiments are performed to verify the feasibility of ADI at multi-wavelengths. ADI results of chicken breast as a biological scattering medium are presented for different thicknesses. A spatial resolution of <0.5 mm is achieved with 5 mm thick chicken breast using a 975 nm diode laser source.

2.2 Introduction

Optical imaging systems are highly desirable in medical imaging since optical methods are inherently non-ionizing. Also, tissue characteristics are wavelength dependent, allowing unique information to be gained at different wavelengths. For example, these methods offer the potential to measure blood content and oxygenation, which are surrogates for angiogenesis and hypermetabolism, respectively [2-1]. The basis for these measurements is the

¹ The following chapter has been published in Optics Express, 16, 14456-14468 (2008) under the co-authorship of Bozena Kaminska, Paulman K. Y. Chan, and Glenn H. Chapman.

strong optical absorption of hemoglobin in blood and its associated oxygen-dependent spectral changes [2-2]. However, optical methods suffer from optical scatter, a serious limitation that prevents features below the surface from being visualized at high resolutions. For instance, confocal microscopy fails to provide high resolution images when imaging is deeper than a few hundred micrometers.

To overcome the limitation of optical scatter, several approaches have been investigated, including time-domain imaging, and spatial filtering. Time-domain imaging, which observes the first arriving photons which have shorter path lengths than the scattered light, is a technique that was first shown to be applicable to small animal imaging more than a decade ago [2-3], but has suffered from lengthy image acquisition times due to hardware inadequacies. Moreover, there has been much interest in developing a sub-millimeter resolution optical imaging method with wavelength independency, which can be useful for multispectral or hyperspectral imaging.

Another way of rejecting multiple scattered photons can be achieved by employing collimated detection by spatial filtering, which uses a lens to create the Fourier spectrum of the spatial distribution of light on the exit surface of a transilluminated object and then removes high-order frequencies using a small aperture placed at the focal point of the lens [2-4]. Through spatial filtering, an image can be formed using only the small angle deviated light emitted from the exit surface of the object. Image contrast deteriorates as the scattering level of the medium is increased due to the decreasing proportion of non-scattered light, which is a limiting factor to this method's use in real tissue imaging applications.

Moreover, the lens and aperture system has a spectral bandwidth limitation due to the diffraction dependency of multiple wavelengths sources, which makes it more difficult to use in multispectral/hyperspectral imaging systems.

Angular domain imaging [2-5] using a micro-tunnel array is a good candidate for such multi-spectral imaging since it is independent of the wavelength and coherency of the source. In fact, the ADI optical method can ultimately be useful not only for detection of absorbing targets in the scattering medium but also for bioluminescence and fluorescence imaging of biological tissue, such as in whole animal scanning of genetic reporters and molecular contrast agents. In this paper we are exploring angular domain imaging beginning with test phantoms using homogenous scattering fluids of μ_s' in the range of 0.8 to 4 cm^{-1} with the thicknesses decreasing from 5 cm to 1 cm respectively. These will be compared to tests with chicken breast tissue, an inhomogeneous muscle tissue with a higher μ_s' in the range of 5 – 8 cm^{-1} , and thicknesses up to 5 mm. This should be a good first test for the complexities of dense tissue biomedical imaging. All these experiments are using transmission of illumination through the test samples. ADI can be applicable for observing optical properties which can help histologists to test thicker tissue samples with a relatively larger field of view. Small animal imaging e.g. mouse pup ($\mu_s' = 5 - 15 \text{ cm}^{-1}$) [2-11] is within the capabilities of angular domain imaging is one of the major goals of the authors.

In this paper, an explanation of the angular behaviour of photons in tissue and an overview of the angular domain imaging principle are given, followed by

an investigation into the multispectral feasibility of angular domain imaging. Experimental results are provided to confirm sub-millimetre spatial resolution for chicken breast tissue samples at different wavelengths.

2.3 Light tissue interaction

Within the last thirty years, a better understanding of light distribution in turbid media has been attained, providing an accurate prediction of light-tissue interaction. The fundamental mechanism of light transport in absorbing and scattering media was adapted from nuclear physics, where Chandrasekar calculated the fluencies of neutrons through different materials [2-6]. Hence, in most medical laser applications, light is regarded as a particle and not as a wave. The integro-differential equation describing the stationary photon transport for monochromatic light is given by the diffusion theory as follows [2-7, 2-8]:

$$\Omega \cdot \nabla I(x, \Omega) = -(\mu_a + \mu_s)I(x, \Omega) + \mu_s \int_{4\pi} I(x, \Omega') S(\Omega' \rightarrow \Omega) d\Omega' + S(x, \Omega) \quad 2-1$$

where $I(x, \Omega)$ is the angular energy flux density at position x and angle Ω in $\text{Wm}^{-2}\text{sr}^{-1}$ and $S(\Omega' \rightarrow \Omega)$ denotes the angular distribution of light scattered from angle Ω' to Ω . In addition, μ_a in cm^{-1} denotes the absorption coefficient and μ_s in cm^{-1} denotes the scattering coefficient.

$S(\Omega' \rightarrow \Omega)$ also represents the scattering phase function and is normalized to unity when integrated over a 4π solid angle. The net anisotropy of scattering for an arbitrary phase function is named the g -factor, which is defined as follows:

$$g = \langle \cos \theta \rangle = 2\pi \int_0^\pi S(\Omega' \rightarrow \Omega) \cos \theta \sin \theta d\theta \quad 2-2$$

A phase function $S(\Omega' \rightarrow \Omega)$ that describes the experimentally observed distribution of scattering angles of photons after a single scattering event is the Henyey-Greenstein (HG) function [2-9]:

$$S(\Omega' \rightarrow \Omega) = \frac{1}{4\pi} \frac{1 - g^2}{(1 + g^2 - 2g \cos \theta)^{3/2}} \quad 2-3$$

It has been found by Jacques et al. [2-10] that the HG function $S(\theta)$ also accurately describes the scattering of light in biological tissue. The important parameter of this phase function is the g -factor. Many common biological tissues have a high degree of forward scattering, with g values ranging from 0.79 to 0.98 for 633 nm wavelength illumination [2-11]. This forward scattering result in a much lower effective scattering quantity that can be calculated for tissue, known as the reduced scattering anisotropic coefficient, μ'_s . This reduced scattering coefficient takes into account the so-called “quasi-ballistic” or “snake photons” (i.e. photons which follow paths close to that of ballistic photons), and is defined according to the formula:

$$\mu'_s = \mu_s(1 - g) \quad 2-4$$

Described simply, a collimated beam of light decays exponentially along its path through a tissue layer of thickness d in accordance with the Beer-Lambert law [2-12]:

$$I(d) = I_o \exp[-(\mu'_s + \mu_a)d] \quad 2-5$$

where $I(d)$ is the intensity of transmitted light measured using a distance photodetector with a small aperture, I_o , is the incident light intensity.

While the reduced scattering coefficient μ'_s characterizes a material for a given thickness of medium it is useful to recognize the relative levels of scattered light and information carrying photons. In order to quantify the scattering level compatible with ADI method, a metric used in this paper to describe the scattering level of a medium is termed the Scattering Ratio, SR . The SR value is defined as the number of photons that are scattered for every non-scattered photon that passes through the medium as the following.

$$SR = \frac{\text{proportion of fully scattered photons}}{\text{proportion of ballistic + quasi ballistic photons}} \quad 2-6$$

For example, for $SR = 10^6:1$, we have 10^6 photons that are scattered in the medium for every ballistic and quasi-ballistic (information carrying) photon that passes through the medium. Our measurement results in section 4 shows the SR value can be fitted to the exponential trend to get approximation for scattering coefficient of our test samples.

2.4 Angular domain imaging principle

It can be assumed that quasi-ballistic photons are closely confined within a small angle of their initial light source trajectory (i.e. they have a forward directed distribution) due to the anisotropy factor in tissue. However, highly

scattered light, which has undergone numerous scatterings, has a nearly uniform or isotropic angular distribution. A Monte Carlo model of steady-state light transport in multi-layered tissues (MCML) by Jacques et al. [2-13] has demonstrated through simulation that non-scattered photons exit an ideal isotropic scattering medium with very small angular deviations from their initial entry trajectories. Extending this work, we have previously [2-5] used Monte Carlo simulations to show that exiting scattered photons with small angular deviations also follow the shortest path, and hence are quasi-ballistic in nature. Hence, a detection system using angular filtration with a small acceptance angle and an aligned, collimated source of light that is passing through a turbid media can be a practical method to reject most of the uniformly distributed scattered light while accepting quasi-ballistic photons with small angular deviations.

In conditions where the scattering of light within a medium is not too large, many researchers report filtering non-scattered photons by employing a collimator as an angular filter aligned co-axially with an incident beam of light. Jarry et al [2-14] in 1984 designed a scanning collimated transillumination system to image small metal objects embedded in 1.5 cm thick mammalian tissue. A more sophisticated computerized tomographic device described by Wist et al in 1993 [2-15] has been investigated employing thin collimated light beams (1.5 mm cross section) synchronized with a similarly collimated detector to increase contrast in lesions normally lost due to the detection of diffuse light. The study demonstrates that detection of a 1.5 mm wide target is possible in phantoms simulating breast tissues 6 mm thick, regardless of depth. Wang et al in 1993 [2-

16] have investigated a similar technique that employs a lens and aperture system to produce the Fourier spectrum of the spatial distribution of light on the exit surface of a transilluminated object. In this technique, an image can be produced using only the light emitted at angles close to the normal to the exit surface of the object with a maximum 0.2° angular deviation.

The angular domain imaging method, introduced previously by the authors [2-5], operates by filtering out highly scattered light in a medium based on the observation that light tends to scatter in a nearly uniform angular distribution, while non-scattered ballistic and quasi-ballistic light remain closely confined within a small angle of the initial light source. In the implementation described in this paper ADI utilizes the creation of a micro-tunnel array with a sufficiently high aspect ratio, as determined by tunnel length over width and height, to form the basis of angular discrimination.

Figure 2-1 illustrates a basic experiment setup for ADI in transillumination mode, consisting of a laser source, a scattering medium with resolution target, the angular filter micro-tunnels with a small acceptance angle, 0.29° , and an image sensor. The angular filter (see Figure 2-2) constructed for ADI experiments at high scattering ratios ($SR \geq 10^6:1$) consists of a parallel array of tunnels, 51 microns wide on 102 micron centers passing along a 1 cm long plate to obtain an aspect ratios of approximately 200:1. The tunnel size was selected to match an even number of pixels in the detector for best imaging, while the aspect ratio was around the limit for alignment of the system with the current setup. Because the tunnels are semicircular in geometry, there exists an angular

acceptance angle variation from 0.11° to 0.29° . The angular filter acceptance angle must be tolerant enough to collect quasi-ballistic photons, which are believed to deviate by up to 0.2° [2-25]. The standard configuration for the angular filter (see Figure 2-2) is a 2 cm wide linear array consisting of 1 cm long tunnels with widths of $51\ \mu\text{m}$, an approximate depth of $20\ \mu\text{m}$, and a pitch spacing of $102\ \mu\text{m}$. The micro-tunnel cross-sectional area is large enough such that each tunnel illuminates a consistent number of image sensor pixels. Current angular filter array do not collect the photons that hit the wall areas between the tunnels. This area represents a loss of approximately 60%. Switching to square cross section collimators would reduce this but create other complications. For example making the tunnel spacing narrower will allow overlapping of the accepted light from adjacent tunnel. This is being studied in other experiments underway. Also it is important to confine the light to the micro-tunnel line so as not to waste photons in areas not collected.

The linear array of micro-tunnels has a limited vertical field of view. Therefore, the scattering sample and test phantoms are incrementally raised by a computer controlled precision z-axis stage (with $0.05\ \mu\text{m}$ repeatability). As the test sample is raised, one horizontal section of the sample is imaged through the angular filter at each step, and a final image is assembled using all the horizontal sections from each step. Hence, an entire region of the sample can be passed through the angular filter's field of view and imaged.

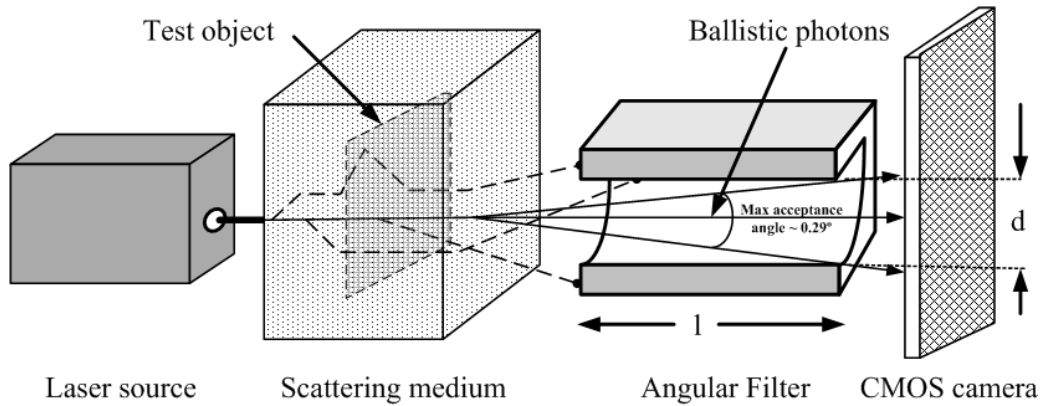


Figure 2-1. Basic ADI experiment setup in transillumination mode.

To test the spatial resolution of our scans, resolution targets consisting of L-shaped patterned aluminum thin film on a glass slide, as shown in Figure 2-3, have been fabricated for imaging. The resolution target is placed either within the scattering medium or at the front (i.e. closest to the laser). To test the resolution performance of our imaging technique, we have two sets of differently sized resolution targets, with each target composed of lines and spaces of equal width.

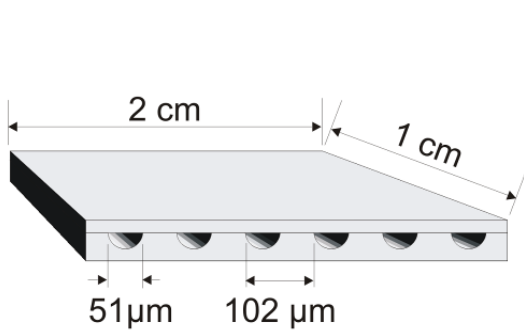


Figure 2-2. Angular filter array.

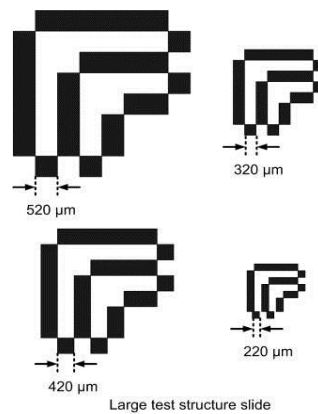


Figure 2-3. Resolution target to measure the spatial resolution of ADI.

The small resolution target slide with line and space widths of 200 μm , 150 μm , 100 μm , and 50 μm is used in our homogeneous scattering medium (e.g. milk/water solution) experiments, while the large resolution target slide with the line and space widths of 520 μm , 420 μm , 320 μm , and 220 μm is used in our heterogeneous scattering medium (e.g. chicken breast) experiments.

One important limitation of angular domain imaging is that near the detection limits a fraction of the highly scattered photons creates a background noise in the image. As highly scattered light is nearly uniformly distributed across all angles, there will be a small fraction that happens to exit the tissue within the micro-tunnel acceptance angle in addition to the ballistic and quasi-ballistic photons. This results in “background scattered light” that reduces the effective image contrast. Figure 2-4 shows two ADI images using an 808 nm laser. As the scattering level of the medium is increased from a modest $\text{SR}=10^3:1$ (Figure 2-4(a)) to a high $\text{SR}=10^7:1$ (Figure 2-4(b)), the fraction of the light that is ballistic or quasi-ballistic decreases significantly (by almost 10^4), while the background scattered light stays nearly constant. This results in a decrease in the signal relative to the background noise. As a result, image contrast decreases (Figure 2-4(b) has less contrast compared to Figure 2-4(a)) as the scattering level increases to the point where the object patterns are submerged in the background scattered light level.

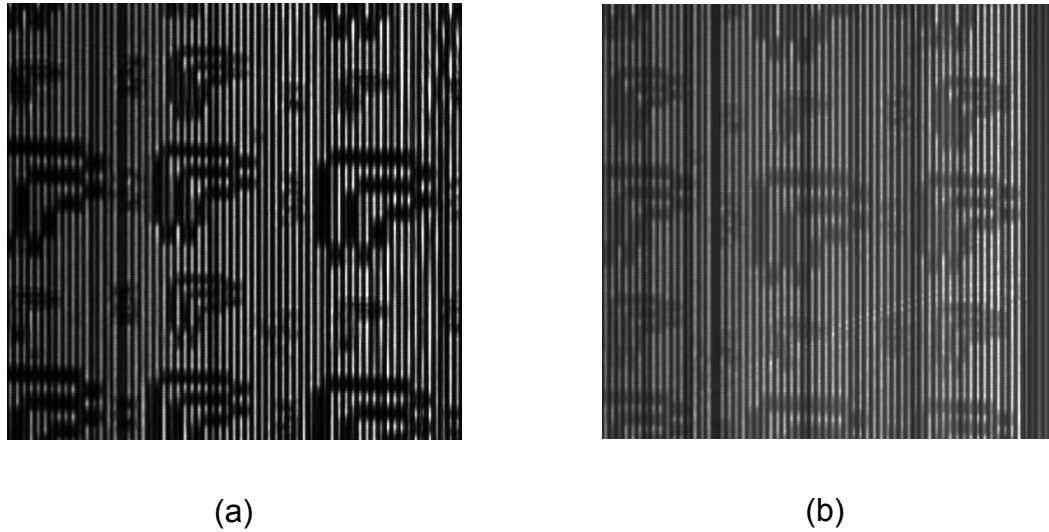


Figure 2-4. Image of small resolution targets placed in a 2 cm optical cell filled with homogenous scattering milk/water solution using an 808 nm laser diode at (a) $SR \approx 10^3:1$ [$\mu'_s = 1 \text{ cm}^{-1}$, $\mu'_a = 0.01 \text{ cm}^{-1}$] and (b) $SR \approx 10^7:1$ [$\mu'_s = 2.5 \text{ cm}^{-1}$, $\mu'_a = 0.01 \text{ cm}^{-1}$]. (Total scan area is 6.6 mm by 6.5 mm)

Most recently other authors have been exploring areas related to this ADI work. K. Shimizui et al in 2000 [2-18] reported employing collimators with a 0.57° acceptance angle to capture so-called “Near Axis Scattered Light” (NASL) using an optical computer tomography (CT) technique. With this technique, 1 cm thick samples can be detected within a 5 cm thick container filled with an aqueous solution of non-fat milk as the scattering medium ($\mu'_s = 0.44 \text{ mm}^{-1}$).

The ADI technique works successfully in the transmission geometry, where the laser source is aligned to the angular filter to trans-illuminate the turbid medium from front to back (Figure 2-1). ADI can also be employed using an illumination source on the same side as the angular filter to capture non-scattered photons generated deep from within the scattering medium. In this geometry, collimated light is injected into the turbid medium, thus generating a

ball of illumination from inside the medium and behind the imaging target object. This newly formed light source in the scattering medium emits non-scattered and scattered light relative to the angular filter array micro-tunnels. When these back reflected photons pass an imaging target and reach the angular filter, the relative non-scattered photons are accepted through the micro-tunnels and reach the camera, whereas scattered photons are rejected by the filter. Reflection geometry ADI has been thoroughly investigated in [2-24] by the authors.

In the present paper, transmission geometry ADI is investigated to achieve multi-spectral sub-millimetre resolution optical imaging for relatively thick scattering media as compared to other high resolution optical imaging methods. The long term goal of this work is to allow imaging through moderately thick samples around 2- 3 cm in thickness of biological tissue with sub-millimetre spatial resolution, thus enabling imaging through a small animal target.

Although the authors have been investigating [2-26] how to improve image contrast in ADI, discussion about such contrast enhancement techniques is outside the scope of this paper, which instead focuses on the multi-spectral feasibility of the ADI technique.

2.5 Methodology

The basic ADI setup used in previous research by the authors [2-5, 2-21] involves using a large-frame 488-514 nm Argon ion laser source due to the very high quality beam characteristics of that system. In our new experiments, three sets of experiments using several diode lasers with a collimation lens system

have been employed in place of the Argon laser, thus allowing us to utilize longer wavelength diode sources in the red and near infrared spectrum. Figure 2-5 shows our experiment setup with a scattering sample and submerged resolution targets resting on a computer-controlled vertical linear stage (with $\pm 0.05\mu\text{m}$ resolution), where it is illuminated by a collimated line of light and imaged through the angular filter array by a CMOS camera detector.

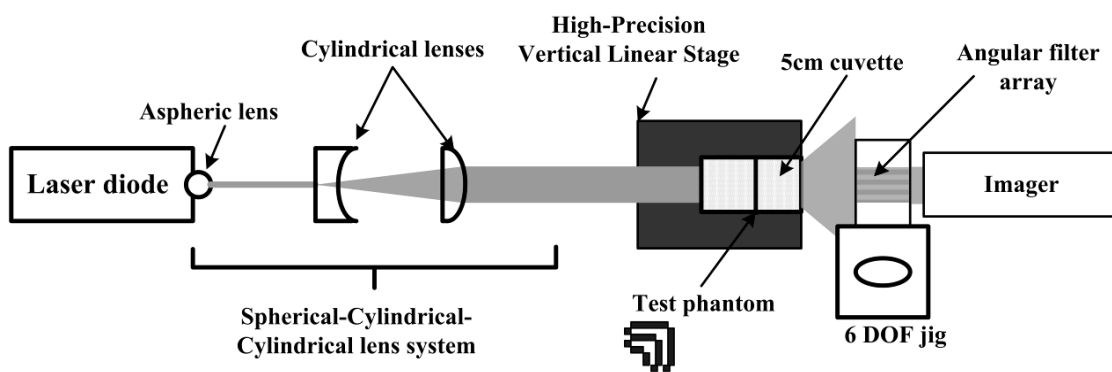


Figure 2-5. ADI setup with diode laser and a collimation system.

Diode lasers are available in many visible to near infrared wavelengths, take much less space, have lower power supply requirements, and much lower costs compared to large frame lasers. However collimation is an area that presents challenges for diode lasers due to their small and asymmetric emission areas (on the order of one micron along the vertical axis by tens or hundreds of microns along the horizontal axis). As a result, the beam diverges rapidly along the horizontal axis and even more rapidly along the vertical axis. However, this asymmetric divergence can be corrected using an aspheric/cylindrical lens

system, (shown in Figure 2-5) that bends the light with a different power along each axis, and is thus able to shape the beam into a collimated line of light. The collimated beam then passes through an iris approximately 8 mm wide (slightly larger than the image sensor width) to restrict the width of the beam before it illuminates the sample. Although the 808 nm and 975 nm laser diodes have different beam divergences, the same experiment setup is used for both except with modification to the beam collimation optics, where the positions of the aspheric lens followed by two cylindrical lenses have been slightly changed to achieve proper beam collimation. The diode laser coherence length is much shorter (few mm) than the Argon laser (23 m). However, this is not a problem for ADI since a coherent source is not required.

A resolution target slide can be inserted at any position along the 5 cm cuvette, ranging from the front position (5 cm) facing the laser, to the back position (0 cm) facing the angular filter and camera. The angular filter is placed in front of a high-resolution (1280×1024 pixel) CMOS detector with a square pixel size ($5.2 \mu\text{m} \times 5.2 \mu\text{m}$) and is mounted on a 6 degree-of-freedom jig that provides alignment to the laser source. Because the angular filter is a linear array of tunnels, only one horizontal line of the sample can be imaged through the angular filter at a given time. Thus, a two-dimensional image is captured by scanning line-by-line as the scattering medium is moved vertically while the illumination and detection equipment are kept stationary.

Calibrated scattering samples were prepared for ADI experiments made from 2% fat partially skimmed milk diluted in water. Milk was chosen as a

scattering element because it exhibits similar properties to tissue and is highly scattering but with a low absorption coefficient.

The scattering level of the solution is measured by a collimated transmission measurement with a small acceptance angle. A collimated laser beam (1 mm diameter) is passed through a 1 cm thick glass cell filled with the milk/water solution. After this, the collimated transmittance is filtered through two 1 mm pinholes with an approximately 50 cm apart from each other, creating an angular filter with an approximately 0.11° acceptance angle and allowing straight or slightly deviated photons to pass through the pinholes and reach the photodetector.

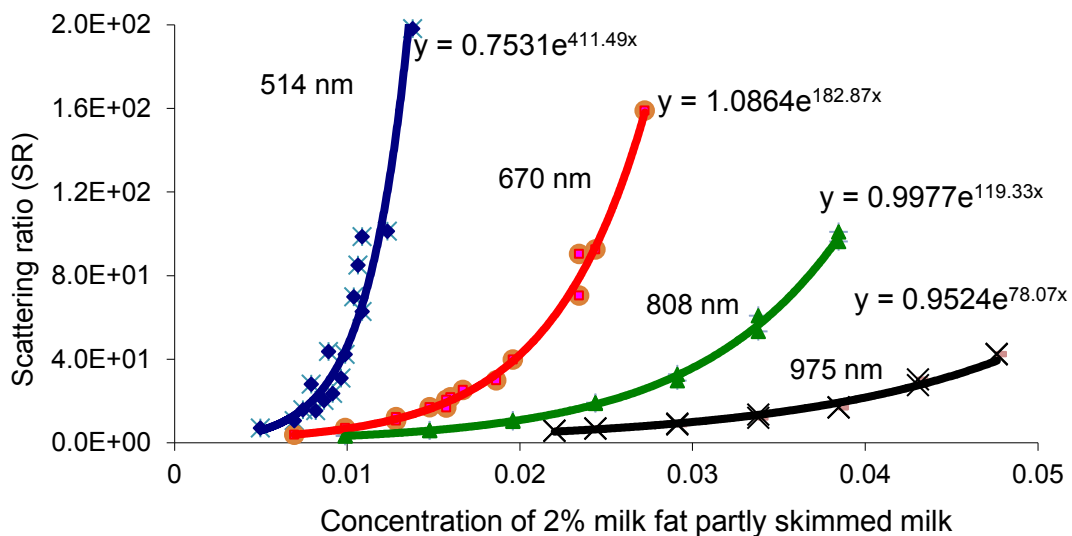


Figure 2-6. Collimated transmission measurement results; Scattering ratio versus concentration of 2% fat partly skimmed milk (in percentage) diluted by water in 1 cm container.

We have chosen this method of scattering sample measurement since it employs the same angular filtration concept as ADI with micromachined tunnels.

Transmitted light from the medium is attenuated by the small acceptance angle formed by the pinholes and also by the reflection and refraction that occurs due to refractive index mismatch between the sample, glass, and air. These two effects may explain why the measured light intensity is lower than other collimated transmission measurements in the literature [2-17, 2-18]. Figure 2-6 plots out the relationship between the scattering ratio and the concentration of 2% fat partly skimmed milk in water (in percentage) for a 1 cm deep solution. Because the scattering coefficient for milk decreases at higher wavelengths, a higher concentration of milk at higher wavelengths is required to achieve the same level of scattering compared to the lower wavelengths. Exponential trends for all four wavelengths are visible in the graph across a broad range of SR values, where the 514 nm line [$\mu'_s \sim 115.2 \text{ cm}^{-1}$] has an exponential coefficient 2.3 times that of the 670 nm diode laser line [$\mu'_s \sim 50 \text{ cm}^{-1}$], 3.6 times that of the 808 nm line [$\mu'_s \sim 32 \text{ cm}^{-1}$], and roughly 5.5 times that of 975 nm line [$\mu'_s \sim 21 \text{ cm}^{-1}$].

Scattering ratios were measured based on the collimated transmission measurement through chicken breast samples sandwiched between two microscopic glass slides. These experiments allow us to investigate the behavior of attenuated light through real tissue at red and near infrared wavelengths. The transmittance light intensity to the detector is measured using the same setup as for the milk/water solutions. Figure 2-7 shows different scattering ratio measurements at three different wavelengths with a vertical log scale and at different chicken breast sample thicknesses.

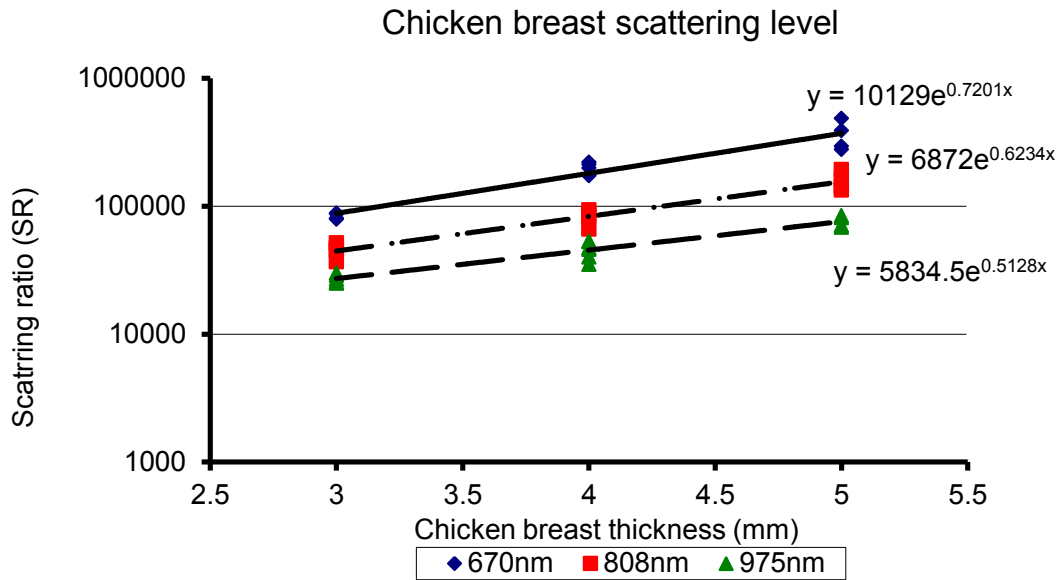


Figure 2-7. Chicken breast scattering ratio measurement results with vertical log scale.

As shown in Figure 2-7, total light attenuation decreases as wavelength is increased. This is anticipated from previous research works [2-26, 2-28].

Figure 2-7 shows the measured data fit to the exponential trend, which is in agreement with the Beer-Lambert law. Our extracted values for reduced scattering coefficient (μ'_s) of chicken breast tissue are 7.2 cm^{-1} for 670 nm, 6.2 cm^{-1} for 808 nm, and 5.1 cm^{-1} for 975 nm, assuming the absorption coefficient is much less than the reduced scattering coefficient [2-26, 2-28].

2.6 Results and discussions

Expanding the operating wavelength of our ADI experiments from an Argon ion (488- 514 nm) laser to longer wavelengths (670, 808 and 975 nm) is an important step towards imaging biological tissues, which exhibit lower scattering coefficients at NIR wavelengths. Furthermore, utilizing laser sources of

differing wavelengths confirms that ADI is capable of multi-spectral imaging and is not dependent on a particular wavelength for operation.

An imaging performance comparison has been previously made between the 670 nm wavelength diode laser source and the Argon laser in [2-23]. Results with all the diode lasers (see Figure 2-8) are similar up to higher scattering ratios such as $SR \sim 10^6:1$ ($\mu'_s = 0.8 \text{ cm}^{-1}$, $\mu'_a = 0.01 \text{ cm}^{-1}$) with imaging results consistent with water, but with increasingly degraded image contrast as SR is increased. The 200, 150 and 100 micron line/space targets in this readily identified. These results appear to be on par with or better than previous imaging results with the Argon laser source, as shown in [2-23]. Figure 2-8 shows scans at all three wavelengths, each for a sample at $SR \sim 10^6:1$, with test patterns at the middle and front positions after image processing using histogram equalization and gamma curve correction. Improvement in scans for the 670 nm diode laser may be attributed to a better shaped and collimated beam produced by the collimation optics system, as compared with the 808 nm and 975 nm laser beams.

In order to progress from imaging synthetic/organic scattering samples (e.g. milk solutions) towards being able to image human tissues, it is useful to experiment with other biological tissues (e.g. chicken breast). Tissue samples were prepared from commercially available fresh chicken breast meat. Sections of tissue were cut out using a scalpel and then compressed by hand with firm pressure and secured between two glass microscope slides. Compression appears to reduce the thickness of the chicken sample on the order of a millimeter, only. Scans were conducted using the 670 nm, 808 nm, and 975 nm

diode laser sources with an aspheric/cylindrical lens collimation system (shown in Figure 2-5) for compressed chicken samples of different thicknesses.

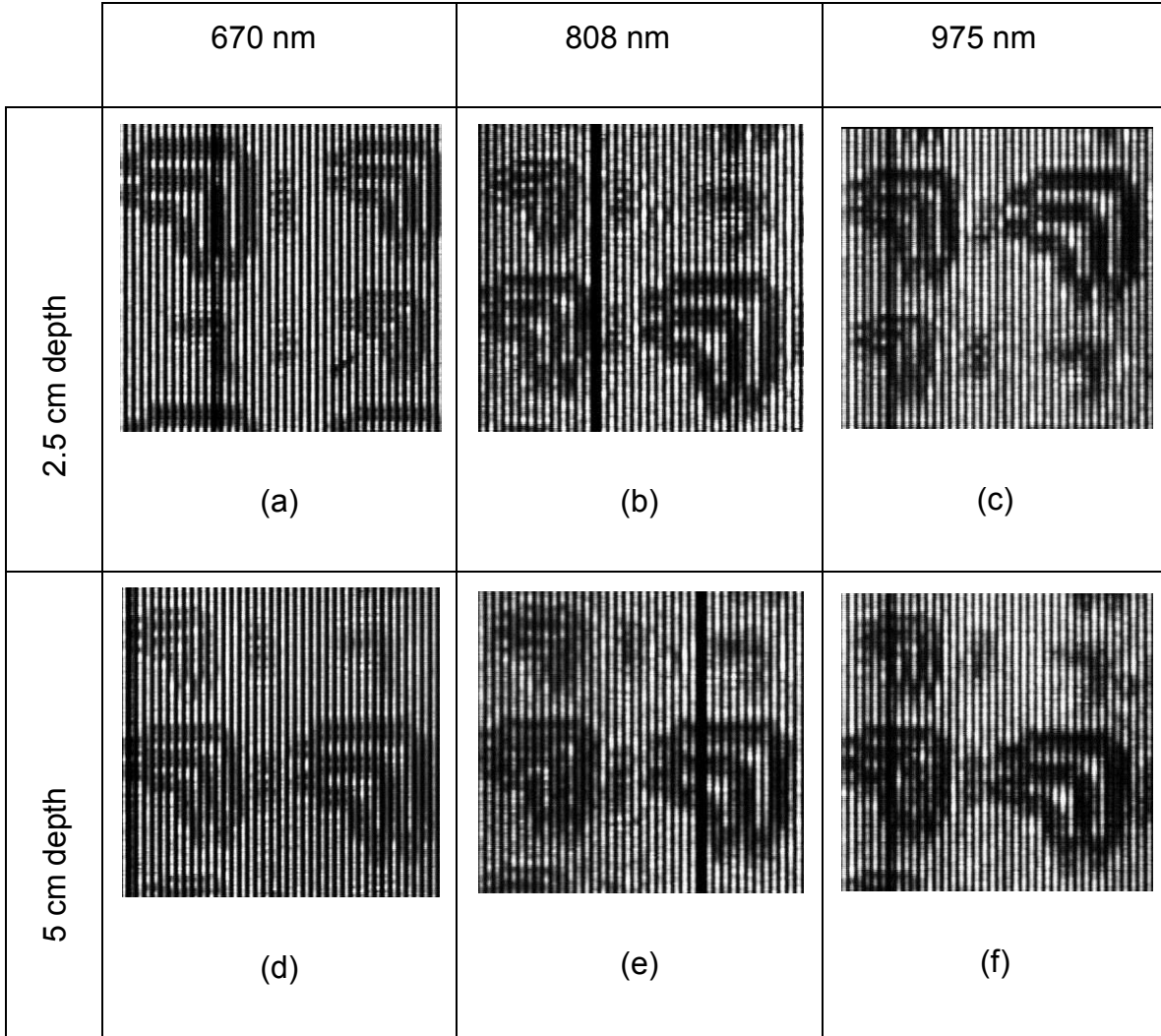


Figure 2-8. Resolution targets placed in diluted milk sample with SR $\sim 10^6$:1 scattering media [$\mu'_s = 0.8 \text{ cm}^{-1}$, $\mu'_a = 0.01 \text{ cm}^{-1}$]: at 2.5 cm depth in a 5 cm optical path cuvette with the (a) 670 nm, (b) 808 nm, or (c) 975 nm diode laser system; and at 5 cm depth with the (d) 670 nm, (e) 808 nm, or (f) 975 nm diode laser system. (All images are histogram equalized and gamma curve corrected)

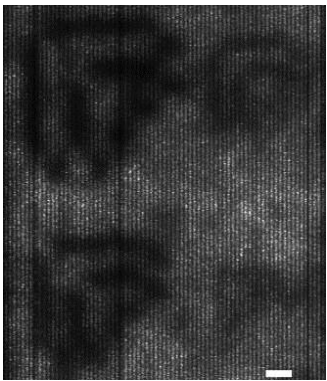
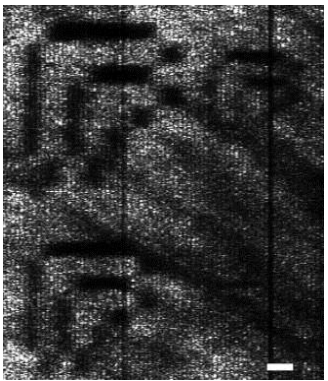
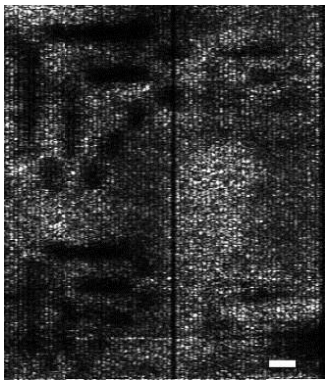
	670 nm	808 nm	975 nm
2.2 ± 0.2 mm thick			
	(a)	(b)	(c)

Figure 2-9. Large resolution target slide in front of 2.2 ± 0.2 mm chicken breast with the (a) 670 nm, (b) 808 nm, or (c) 975 nm diode laser system. (Total scan area is approximately 7.8 mm × 8.8 mm; white scale bar is 500 μm)

Scans of the large resolution target slide placed in front of the 2.2 ± 0.2 mm chicken breast sample (closest to the laser source) at all three wavelengths are presented in Figure 2-9. The scattering ratio measurement for the three wavelengths are $SR = 4.9 \times 10^3:1$ for 670 nm, $2.7 \times 10^3:1$ for 808 nm, and $1.8 \times 10^3:1$ for 975 nm as taken from Figure 2-7. These SR values are well below the detection limit (around $10^7:1$) reached in previous milk sample experiments. These scans indicate that the tissue samples are quite heterogeneous (especially when compared to the milk solution scans), with many uneven illuminations due to features in the image intrinsic to the tissue itself. These non-uniformities make it more difficult to distinguish the small resolution targets introduced in front of the sample for imaging.

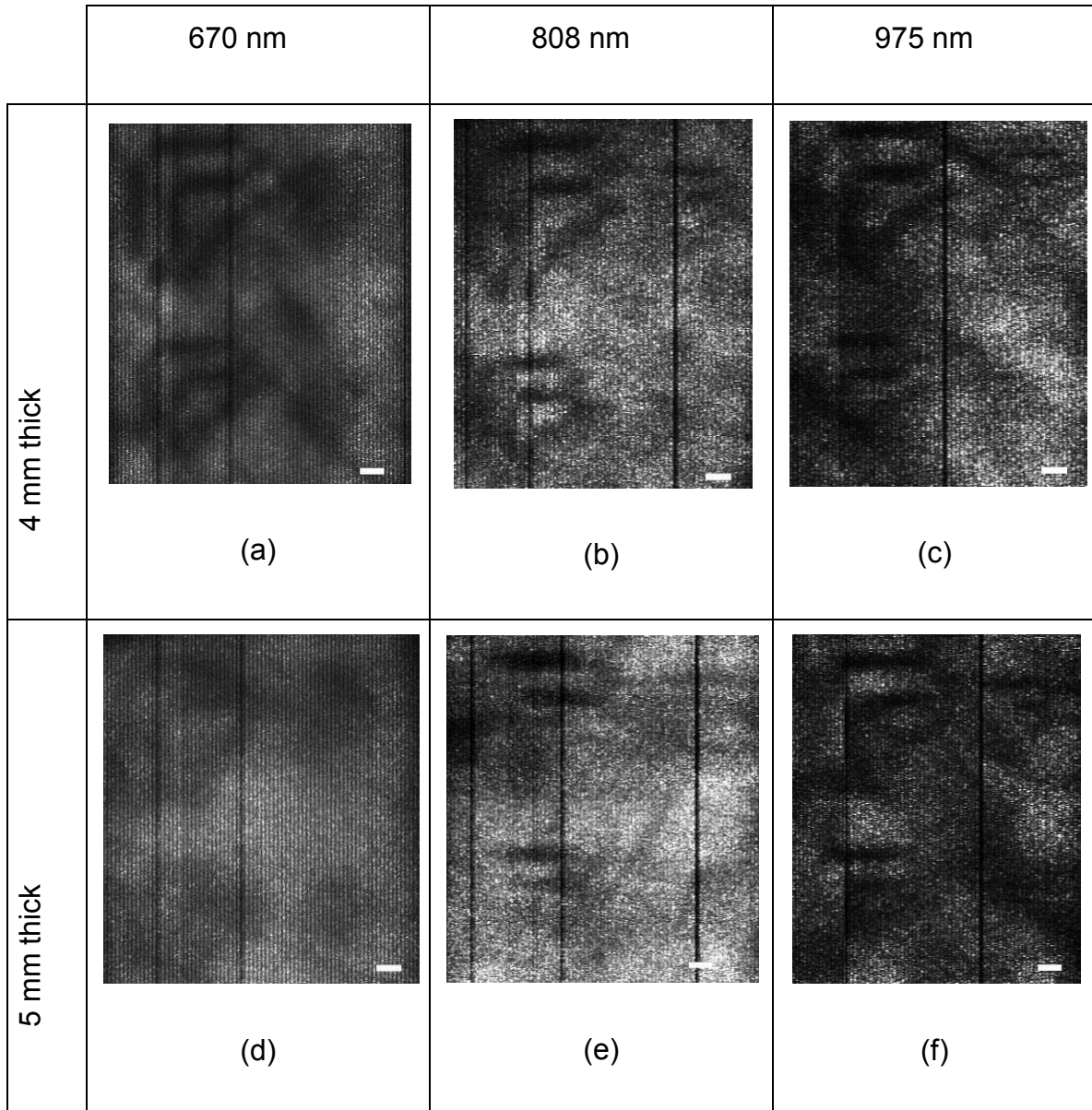


Figure 2-10. Large resolution targets in front of a chicken breast sample of 4 mm thickness with the (a) 670 nm, (b) 808 nm, or (c) 975 nm diode laser system, and for 5 mm thick chicken breast with the (d) 670 nm, (e) 808 nm, or (f) 975 nm diode laser system. (Total scan area is approximately 7.8 mm × 8.8 mm; white scale bar is 500 μm)

For all three wavelengths in Figure 2-9, the three largest resolution targets (composed of 520, 420, or 320 μm wide lines and spaces) are resolvable in the image with their lines and spaces distinguishable. The 220 μm resolution target is

only faintly detectable in the 670 nm image, and is not visible at the longer two wavelengths. These results demonstrate sub-millimetre resolution performance (320 μm or better) with the ADI system at all three wavelengths for a 2.2 mm thick chicken sample.

Figure 2-10 shows scans at all three wavelengths of thicker chicken breast samples of approximately 4 mm and 5 mm. According to the measurements shown in Figure 2-7, SR values of $\text{SR} = 1.8 \times 10^4:1$, $8.3 \times 10^3:1$, and $4.5 \times 10^3:1$ for the 4 mm thick chicken breast sample and $\text{SR} = 3.7 \times 10^4:1$, $1.5 \times 10^4:1$, and $7.5 \times 10^3:1$ for the 5 mm thick chicken breast sample were measured for 670, 808, and 975 nm wavelengths, respectively. Again, these SR values are well below the detection limit (around $10^7:1$) reached in previous milk sample experiments. Both samples exhibit better uniformity in the image, as compared to the 2.2 mm sample. For the 4 mm thick sample (Figure 2-10(a) –(c)), only the two largest resolution targets (520 μm and 420 μm) are resolvable, while the smallest two resolution targets (320 μm and 220 μm) are not clearly visible. For the 5 mm thick sample (Figure 2-10(d) – (f)), the largest resolution target (520 μm) is resolvable at 808 nm and 975 nm, but is barely distinguishable at 670 nm. The second largest target (420 μm) is no longer clearly detectable at 670 nm and is only partially resolvable at the 808 nm and 975 nm wavelengths. The two smallest resolution targets are not visible for the 5 mm thick scans. These results demonstrate sub-millimetre resolution for all three wavelengths in 4 mm thick chicken tissue and for 808 nm and 975 nm in 5 mm thick chicken tissue, with the largest resolution target visible but not clearly resolvable at 670 nm. In addition,

these scans demonstrate that image contrast and detectability is improved as wavelength is increased from 670 nm to 808 nm and 975 nm. This trend is expected since Figure 2-7 shows that light undergoes less scattering as wavelengths are increased from 670 nm to 975 nm.

Various image processing techniques can be employed to improve ADI results. The following image processing techniques are based on previous image processing work [2-24]. One operation that can be performed is to fill in the missing image information that is lost due to the approximate 51 μm gap between the angular filter tunnels. The approach taken to accomplish this involves vertically scanning the chicken tissue and resolution target slide followed by a second scan with the entire sample shifted laterally by 50 μm . The reconstruction process involves comparing the mean intensity value for a particular column from both the normal and laterally shifted images, and then selecting the column with the highest value and inserting it into the new reconstructed image.

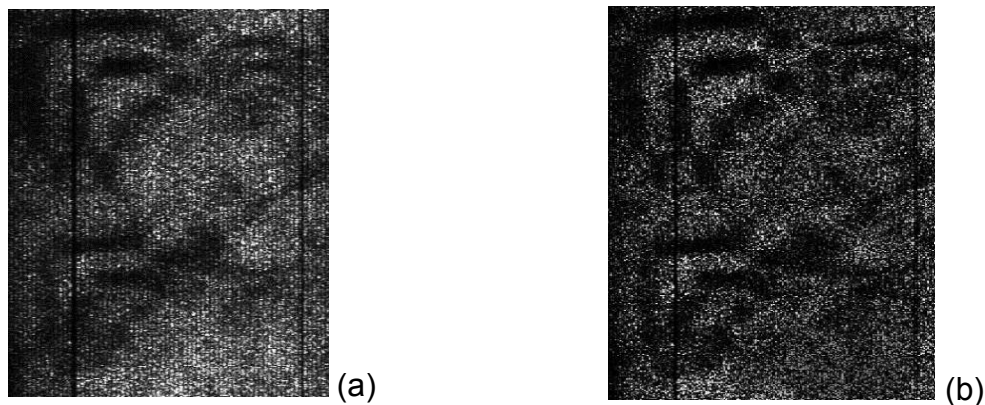


Figure 2-11. Large resolution targets in front of 3 mm chicken breast (a) without digital image processing, and (b) after digital image processing. (Total scan area is approximately 7.8 mm \times 8.8 mm)

In order to enhance the definition, contrast, and detectability of the resolution targets, homomorphic filtering background subtraction using morphological opening and adaptive histogram equalization have been employed. The digital image processing details have been investigated in further details in [2-24]. As an example, this image processing has been performed on a 3 mm chicken breast sample ADI scan using the 808 nm diode laser system. The original scan (Figure 2-11(a)) is processed and the final image (Figure 2-11(b)) shows some improvement in contrast and detectability of the resolution target lines and spaces, especially for the 320 μm resolution target slide (top right in both images). Further exploration into different parameters and additional techniques for image processing should be conducted in order to further improve ADI scan results.

2.7 Conclusion

ADI with an angular filter array has been shown to be successful at multiple wavelengths with sub-millimetre resolution or better using different laser sources ranging from a 670 nm to a 975 nm diode laser. Note that the same micro-collimator angular filter worked over this wide wavelength range. Performance with the 670, 808, and 975 nm diode lasers is on par with or better than previous results with an Argon ion (488 – 514 nm) laser source for calibrated milk scattering solutions. Chicken breast tissue samples with a compressed thickness ranging from approximately 2 mm to 5 mm were imaged using 670, 808, and 975 nm wavelengths with 520 μm resolution or better. Resolution target lines and spaces of 520 μm were successfully resolved when

imaged in front of 5 mm thick chicken breast tissue. Enhancement of the angular filter tunnels to improve scattered noise rejection and imaging performance can be investigated in future research, along with alternate designs for the angular filter array (e.g. new tunnel dimensions and aspect ratios). Since angular filter arrays are wavelength independent, different wavelength diode lasers can be introduced to create a true hyperspectral imaging, along with improved shaping of the beam into a thinner line of collimated light to enhance the signal to noise ratio.

2.8 Reference list

- 2-1 H. Hielscher, "Optical tomographic imaging of small animals," *Current Opinion in Biotechnology*, vol. 16, pp. 79-88, 2 (2005).
- 2-2 Roggan, M. Friebel, K. Dorschel, A. Hahn, and G. Muller, "Optical Properties of Circulating Human Blood in the Wavelength Range 400--2500 nm," *J. Biomed. Opt.* 4, 36-46 (1999).
- 2-3 D.A. Benaron and D.K. Stevenson, "Optical time-of-flight and absorbance imaging of biologic media" *Science* 259, pp. 1463–1466 (1993).
- 2-4 Nick Pfeiffer, Paulman Chan, Glenn H. Chapman, Fartash Vasefi, and Bozena Kaminska, "Optical imaging of structures within highly scattering material using a lens and aperture to form a spatiofrequency filter" *Proc. SPIE* 6854, 68541D (2008).
- 2-5 G. H. Chapman, M. Trinh, N. Pfeiffer, G. Chu and D. Lee, "Angular domain imaging of objects within highly scattering media using silicon micromachined collimating arrays," *IEEE J. Sel. Top. Quantum Electron.* 9, pp. 257-66, 03 (2003).
- 2-6 S. Chandrasekhar: *Radiative Transfer*, Oxford University Press, London, 1950. Ishimaru: *Wave Propagation and Scattering in Random Media: Single Scattering and Transport Theory*, Academic Press, NY (1978).
- 2-7 M. R. Arnfield, J. Tulip, and M. S. McPhee, "Optical propagation in tissue with anisotropic scattering," *IEEE Trans. Biomed. Eng.* 35, 372–381 (1988).
- 2-8 W. F. Cheong, "A review of the optical properties of biological tissues," *IEEE J. Quantum Electron.* 26, pp. 2166-2185 (1990).

- 2-9 Henyey, L. and Greenstein, J. L., "Diffuse radiation in the galaxy", *Astrophys. J*, 93, 70, (1940)
- 2-10 Jacques SL, Alter CA, Prahl SA, "Angular Dependence of HeNe laser Light Scattering by Human Dermis", *Laser Life Sci.* 1, pp.309-333 (1987).
- 2-11 Tuan Vo-Dinh, Ed., *Biomedical Photonics Handbook*. Publisher: CRC (2003).
- 2-12 H. C. van de Hulst, *Multiple Light Scattering*, 2. New York: Academic, 1980.
- 2-13 L. Wang, S. L. Jacques and L. Zheng, "MCML—Monte Carlo modeling of light transport in multi-layered tissues," *Computer Methods and Programs in Biomedicine*, 47, pp. 131-146, 7 (1995).
- 2-14 G. Jarry, S. Ghesquiere, J. M. Maarek, F. Fraysse, S. Debray, M.H. Bui and D. Laurent, "Imaging mammalian tissues and organs using laser collimated transillumination" *J. Biomed. Eng.* 6 70–4 (1984).
- 2-15 O. Wist, P.P. Fatouros and S. L. Herr, "Increased spatial resolution in transillumination using collimated light" *IEEE Trans. Med. Imaging* 12 751–7 (1993).
- 2-16 Q. Z. Wang, X. Liang, L. Wang, P. P. Ho, and R. R. Alfano, "Fourier spatial filter acts as a temporal gate for light propagating through a turbid medium," *Opt. Lett.* 20, 1498–1500 (1995).
- 2-17 Cheong, W.F., Prahl, S.A. & Welch, A.J. A review of the optical properties of biological tissues. *IEEE J. Quantum Electron.* 26, 2166–2185 (1990).
- 2-18 Koichi Shimizu and Masataka Kitama, "Fundamental study on near-axis scattered light and its application to optical computed tomography," *Opt. Rev.* 7, 383 (2000).
- 2-19 G. H. Chapman, M. Trinh, D. Lee, N. Pfeiffer and G. Chu, "Angular domain optical imaging of structures within highly scattering material using silicon micromachined collimating arrays," *Proc. SPIE* 4955, 462 (2003).
- 2-20 M. S. Tank and G. H. Chapman, "Micromachined silicon collimating detector array to view objects in a highly scattering medium," *Canadian J. of Elec. and Comp. Eng.*, vol. 25, pp. 13-18, 01 (2000).
- 2-21 G.H. Chapman, J. Rao, T. Liu, P.K.Y. Chan, F. Vasefi, B. Kaminska, and N. Pfeiffer, "Enhanced Angular Domain Imaging in Turbid Media using Gaussian Line Illumination", *Proc. SPIE* 6084. (2006).
- 2-22 F. Vasefi, P. K. Y. Chan, B. Kaminska, and G. H. Chapman, "Deep illumination angular domain imaging within highly scattering media enhanced by image processing", *Proc. SPIE* 6380 (2006).

- 2-23 P.K. Chan, F. Vasefi, G.H. Chapman, B. Kaminska, N. Pfeiffer. Angular Domain Optical Tomography in Scattering Media with Multi-spectral Diode, Proc. SPIE 6435 (2007).
- 2-24 F. Vasefi, P.K.Y. Chan, B. Kaminska, G. H. Chapman, N. Pfeiffer, "An Optical Imaging Technique Using Deep Illumination in the Angular Domain," IEEE J. Sel. Top. Quantum Electron. 13, pp. 1610-1620 (2007).
- 2-25 L. Wang, P. P. Ho, and R. R. Alfano, "Time-resolved Fourier spectrum and imaging in highly scattering media," Appl. Opt. 32, 5043- (1993)
- 2-26 F. Vasefi, G. H. Chapman, P. K. Y.Chan, B. Kaminska, N. Pfeiffer, "Enhanced angular domain optical imaging by background scattered light subtraction from a deviated laser source", Proc. SPIE Vol. 6854 (2008).
- 2-27 G. Marquez, B.S. Lihong Wang, Shao-Pow Lin, S. L. Jacques, F. K. Tittel, S. L. Thomsen and J. Schwartz, "Measurement of absorption and scattering spectra of chicken breast with oblique incidence reflectometry," in Biomedical Sensing, Imaging, and Tracking Technologies II, pp. 306-17 (1997).
- 2-28 G. Marquez, L. V. Wang, Shao-Pow Lin, J. A. Schwartz and S. L. Thomsen, "Anisotropy in the absorption and scattering spectra of chicken breast tissue," Appl. Opt., vol. 37, pp. 798-804, 02/01 (1998).
- 2-29 G. Ku, X. Wang, X. Xie, G. Stoica and L. V. Wang, "Deep penetrating photoacoustic tomography in biological tissues," in Photons Plus Ultrasound: Imaging and Sensing x: The Sixth Conference on Biomedical Thermoacoustics, Optoacoustics, and Acousto-Optics, pp. 117-26 (2005).

3: IMAGE CONTRAST ENHANCEMENT IN ANGULAR DOMAIN OPTICAL IMAGING OF TURBID MEDIA ²

3.1 Abstract

Imaging structures within a turbid medium using Angular Domain Imaging (ADI) employs an angular filter array to separate weakly scattered photons from those that are highly scattered. At high scattering coefficients, ADI contrast declines due to the large fraction of non-uniform background scattered light still within the acceptance angle. This paper demonstrates various methods to enhance the image contrast in ADI. Experiments where a wedge prism was used to deviate the laser source so that scattered photons could be imaged and subtracted from the image obtained by standard ADI provided the greatest improvement in image contrast.

3.2 Introduction

Optical tissue characteristics are wavelength dependent, which allows physiological and functional information to be gained from wavelength-dependent measurements [3-1]. For example, blood content and oxygenation, which are respective surrogates for angiogenesis and hypermetabolism, can be deduced by spectral measurements [3-2]. The basis for this technique is the strong optical absorption of hemoglobin in blood and its associated oxygen-dependent spectral changes [3-2]. However, optical methods suffer from optical scatter, a serious

² The following chapter has been published in Optics Express, 16, 21492-21504 (2008) under the co-authorship of Bozena Kaminska, Glenn H. Chapman, and Jeffrey J. Carson.

limitation that prevents features below the surface from being visualized at high resolutions. For instance, confocal microscopy or Optical Coherence Tomography (OCT) fails to provide high resolution images deeper than a few hundred micrometers [3-3]-[3-5]. Fluorescence and luminescence techniques have become popular for whole animal scanning of genetic reporters and molecular contrast agents; however, they too are hampered by the degrading effects of optical scatter and cannot provide high resolution images of internal structures.

To overcome the limitations to tissue imaging imposed by optical scatter, several approaches have been investigated, including time domain, spatial filtering and angular domain. Time-domain optical imaging is a technique that was first shown to be applicable to imaging tissues more than a decade ago [3-6,3-7]. The time-domain method separates the early arriving (and image forming) ballistic and quasi-ballistic photons from the late arriving scattered photons (non-image forming). This technique has not been adopted widely likely on account of the lengthy acquisition time resultant from hardware inadequacies. Spatial filtering techniques have been studied as a means to reject scattered light and preserve the image forming photons. The technique uses a lens to create the Fourier transform of the spatial distribution of light on the exit surface of a trans-illuminated object and then removes high-order frequencies using a small aperture placed at the focal point of the lens. Several groups have successfully used this method to image resolution targets, but the approach suffers from insufficient rejection of scattered light, loss of resolution due to the small

aperture, and has yet to be shown applicable to imaging thick tissues on its own. Our group has been studying angular domain optical imaging (ADI), which uses a micro-machined silicon angular filter (collimator) to filter unwanted scattered photons and pass the image forming quasi-ballistic photons. This technique has been successfully applied to imaging resolution targets as small as 150 μm suspended in turbid solutions of milk and Intralipid™ [3-8,3-9,3-10]. The objective of the present work was to characterize and compare three methods for improving image contrast in ADI. The first method involved the introduction of a wedge prism into the light path of the ADI scanner to quantify the degree of highly scattered light. The second method introduced a pair of polarizers into the ADI light path as a means to quantify the scattered light. The third method combined the wedge and polarizer techniques. In all cases, the images representative of the scattered light were used to correct the quasi-ballistic photon-weighted images.

In preparation for describing image contrast enhancement in ADI, this paper reviews the light-tissue interactions relevant to ADI, the practical implementation of ADI for imaging turbid media, and mechanisms responsible for the degradation of ADI image contrast. The paper then goes on to describe the three approaches to improving image contrast in ADI and their relative performance compared to ADI alone.

3.3 Light-tissue interaction

The fundamental mechanism of light transport in absorbing and scattering media was adapted from nuclear physics where Chandrasekar calculated the

fluence of neutrons through different materials [3-11]. Hence, in most medical laser applications light is regarded as a particle and not as a wave. The integro-differential equation describing the stationary photon transport for monochromatic light is given by the diffusion theory as follows [3-12, 3-13]:

$$\begin{aligned} \Omega \cdot \nabla I(x, \Omega) = & \\ -(\mu_a + \mu_s)I(x, \Omega) + \mu_s \int_{4\pi} I(x, \Omega') S(\Omega' \rightarrow \Omega) d\Omega' + Q(x, \Omega) & \end{aligned} \quad 3-1$$

where $I(x, \Omega)$ is the angular energy flux density at position x and angle Ω in $\text{Wm}^{-2}\text{sr}^{-1}$ and $S(\Omega' \rightarrow \Omega)$ denotes the angular distribution of light scattered from angle Ω' to Ω . $Q(x, \Omega)$ represents the distributed source density. Here, μ_a in cm^{-1} is the absorption coefficient, and μ_s in cm^{-1} is the scattering coefficient.

$S(\Omega' \rightarrow \Omega)$ also represents the scattering phase function and is normalized to unity when integrated over a 4π solid angle. When the phase function is independent of angle, the scattering is said to be isotropic. For anisotropic scattering, the phase function depends only on θ , the angle between the incident and scattered radiation. The net anisotropy of scattering for an arbitrary phase function is named the g -factor which is summarized as follows.

$$g = \langle \cos \theta \rangle = 2\pi \int_0^\pi S(\Omega' \rightarrow \Omega) \cos \theta \sin \theta d\theta \quad 3-2$$

The phase function $S(\Omega' \rightarrow \Omega)$ that describes the experimentally observed distribution of scattering angles of photons is the Heneye-Greenstein (HG) function 2-9:

$$S(\Omega' \rightarrow \Omega) = \frac{1}{4\pi} \frac{1 - g^2}{(1 + g^2 - 2g \cos \theta)^{3/2}} \quad 3-3$$

It has been found by Jacques et al. [2-10] that the HG function $S(\theta)$ also accurately describes the scattering of light in biological tissue. Many common biological tissues have a high degree of forward scattering, with g values ranging from 0.79 to 0.95 in the red and near infrared spectrum range [3-16]. The scattering coefficient decreases to the reduced scattering coefficient, μ'_s , for the so-called “quasi-ballistic or snake photons” (i.e. photons which follow paths close to that of ballistic photons) as

$$\mu'_s = \mu_s (1 - g) \quad 3-4$$

For instance, measurements of skin and underlying tissue at 633 nm [3-17] have determined $\mu_s = 70.7 \text{ cm}^{-1}$ and $g = 0.8$. By eq. 3-4, μ'_s will be about 5 times lower and equal to $\mu'_s = 11.4 \text{ cm}^{-1}$. It can be assumed that quasi-ballistic photons are closely confined within a small angle of their initial trajectory (i.e. they have a forward directed distribution) due to the anisotropy factor in tissue. A Monte Carlo model of steady-state light transport in multi-layered tissues (MCML) by Jacques et al. [3-18] demonstrated that quasi-ballistic photons exit an ideal isotropic scattering medium with very small angular deviations from their initial trajectories. Extending this work, we used Monte Carlo simulations to show that

scattered photons exiting with small angular deviations also follow the shortest path, and hence are quasi-ballistic in nature [3-9]. Therefore, a detection system that uses angular filtration with a small acceptance angle and an aligned, collimated source of light that passes through a turbid media can be a practical method to reject most of the uniformly distributed scattered light while accepting quasi-ballistic photons with small angular deviations. This is the basis of ADI.

3.4 Angular domain imaging

3.4.1 Principle of operation

The ADI method operates by selecting ballistic and quasi-ballistic light closely confined within a small angle of the incoming photon trajectory while filtering out highly scattered light. This follows from the observation that highly scattered light tends to have a nearly uniform angular distribution while image forming quasi-ballistic light is highly directional [3-9,3-10]. As shown in Figure 3-1, the Angular Filter Array (AFA) employs high-aspect ratio micro-tunnels to create extended apertures through which photons can pass if they arrive within the allowable acceptance angle with respect to the longitudinal axis of each micro-tunnel. Photons that arrive with incident angles beyond the acceptance angle will strike the micro-tunnel sides and be attenuated. The performance of ADI is largely dependent on the design of the array of angular filter micro-tunnels. The AFA must be designed with a high aspect ratio, length (l) over diameter (d), to provide sufficiently strict angular filtering of scattered photons.

The ADI technique works successfully in transmission geometry, where the laser source is aligned to the angular filter to trans-illuminate the turbid medium from front to back, ADI can also be employed using an illumination source on the same side as the angular filter to capture quasi-ballistic photons generated deep from within the scattering medium. In the reflective geometry, collimated light is injected into the turbid medium, thus generating a source of illumination from inside the medium and behind the imaging target object. This newly formed light source in the scattering medium emits non-scattered and scattered light relative to the AFA micro-tunnels. When these back reflected photons pass an imaging target, which can be either absorbing or fluorescent material, and reach the AFA, the relative non-scattered photons are accepted through the micro-tunnels and reach the camera, whereas scattered photons are rejected by the filter. Reflection geometry ADI has been investigated previously [3-19].

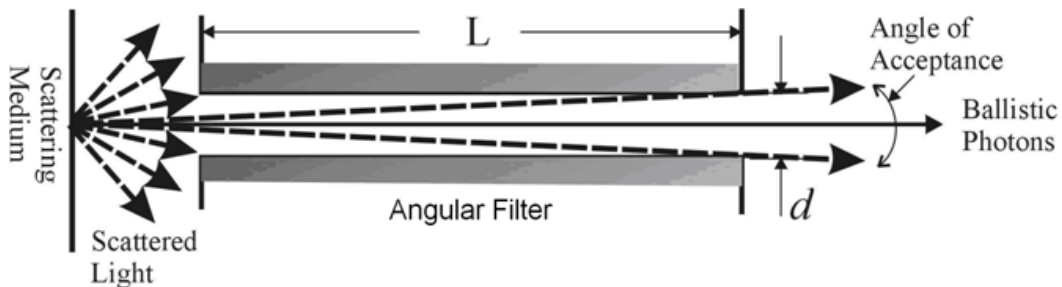


Figure 3-1. Angular domain imaging in transillumination mode.

Recently, we investigated a new design for the angular filter array (see Figure 3-2), which consisted of a parallel array of square-shaped micro-tunnels,

60 microns wide and tall along a 1 cm long plate to obtain aspect ratios of approximately 167:1. The square shape with small spacing had higher performance compared to our previous semi-circular micro-tunnels. Compared to the semi-circular geometry, the square geometry employed smaller spacing between micro-tunnels with a larger cross-sectional area for a given nominal acceptance angle; therefore, it was more efficient at accepting the informative quasi-ballistic photons exiting the turbid sample. The aspect ratio and micro-tunnel size for the square geometry reported above was observed to provide optimal image contrast compared to other filter geometries (data will be presented in [3-20]). Because the micro-tunnels were square in geometry, there existed an angular acceptance angle variation from 0.34° (wall to wall) to 0.48° (corner to corner). This design was selective enough to collect quasi-ballistic photons that provided at least $200\ \mu\text{m}$ spatial resolution through turbid media. The main part of the AFA is an array of long channels etched into a silicon substrate as shown in Figure 3-2, forming the bottom section. For the complete AFA a flat silicon wafer added on top of these etched channels to create enclosed tunnels. The new AFA fabrication decreased the power loss due to the larger opening size compared to the previously tested semi-circular shapes. This feature could be used to reduce the time required to capture one image or reduce the light power for delicate samples.

The one dimensional linear array of micro-tunnels has a limited field of view as shown in Figure 3-3. This can create two limiting issues. First, light from all illuminated regions of the sample that are not in the area being imaged will be

scattered into the region of the AFA and a small portion will be within the acceptance angle of the channels, thus reaching the sensor. This result in a background signals at each pixel location and reduces image contrast. This effect can be suppressed somewhat by reducing the amount of unnecessary illumination of the sample using a collimated line source coincident with the AFA [3-10]. Second, the limited vertical field of view of the AFA necessitates a scanning system for capture of 2D images. We have employed a computer-controlled z-axis stage (with 0.05 μm repeatability) to incrementally raise the scattering sample between scans. One horizontal line image of the sample is taken through the angular filter at each step and a final 2D image is assembled from the stacked line images. Hence, an entire region of the sample can be passed through the angular filter's field of view and imaged.

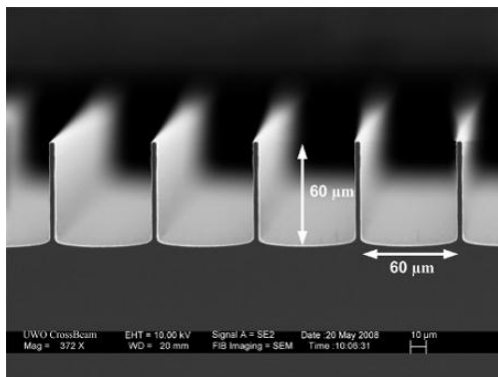


Figure 3-2. Silicon micromachined angular filter array (etched bottom section).

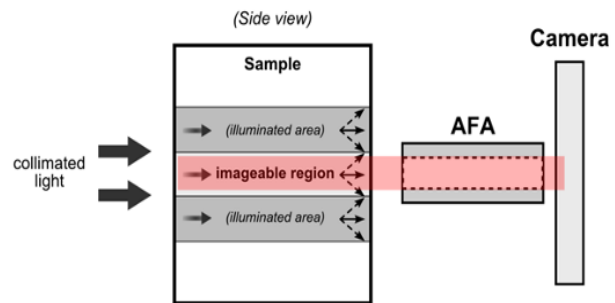


Figure 3-3. Illustration of limited field of view in one dimensional AFA.

Angular domain imaging possesses multiple benefits as an optical imaging method. These include: *i)* wavelength independence, which allows for

broadband or multi-spectral light sources [3-10]; *ii*) non-coherent source compatibility, which implies that ADI can be performed with inexpensive light sources, and *iii*) multimodal capability, that is ADI is useful not only for detection of absorbing targets in a turbid medium, but also for fluorescence targets, which has promise for imaging genetic reporters and molecular contrast agents in biological tissue.

3.4.2 Mechanisms of loss of image contrast in ADI

As noted one important limitation of ADI relates to a loss of image contrast as the scattering level of the sample increases. The fraction of the highly scattered photons increases and creates background noise in the image. Inherently, highly scattered light has a nearly uniform angular distribution; hence, a small fraction of the scattered light happens to exit the sample within the micro-tunnel acceptance angle, which biases the ballistic and quasi-ballistic photons accepted by the filter. This results in *background scattered light* that reduces the effective image contrast. Figure 3-4 shows ADI scans using an 808 nm laser diode at three levels of scattering. As the scattering level of the medium is increased from modest (Figure 3-4(b)) to high scattering levels (Figure 3-4(c)), the fraction of light that is ballistic or quasi-ballistic decreases significantly, while the *background scattered light* increases. This results in a decrease in contrast between the target and the background. Image contrast decreases as the scattering level increases to the point where the object patterns are obscured by the *background scattered light*. That is, ADI is unable to distinguish between filtered non-scattered light from *background scattered light*.

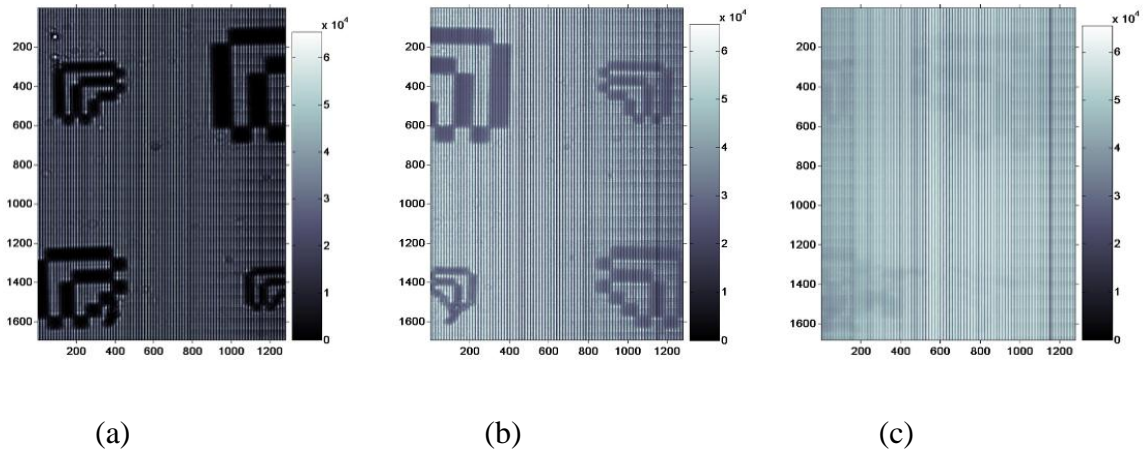


Figure 3-4. ADI scan of sample including resolution target (L-shaped targets with lines and spaces of 150 μm , 200 μm , 300 μm , and 400 μm) placed in the middle position of 1 cm thick optical cell filled (a) Water, (b) 0.6% Intralipid™ ($\mu's = 4.8 \text{ cm}^{-1}$, $\mu_a = 0.01 \text{ cm}^{-1}$), and (c) 0.75% Intralipid™ ($\mu's = 6 \text{ cm}^{-1}$, $\mu_a = 0.01 \text{ cm}^{-1}$) using an 808 nm laser diode.

The image exposure time by the detector is dependent on the scattering level, laser power, and camera exposure time. For instance, in order to form an ADI scan in water (Figure 3-4 (a)) each scan line was acquired with a laser diode power of 2.4 mW and an exposure time equal to 0.012 ms (the full 2D image was formed from 330 line scans). At 0.6% Intralipid™ (Figure 3-4 (b)), the laser power was increased to 350 mW and the camera exposure time for each scan line was lengthened to 10 ms. However, in the practical implementation, several other processes (data communication, computer software and stage translation) increase the time for one line scan to approximately one second; therefore, the whole scan shown in Figure 3-4(b) took approximately 5 min. At 0.75% Intralipid™ as shown in Figure 3-4(c), each line scan was captured at a laser

power equal to 350 mW with a 25 ms camera exposure time. The full 2D image was acquired in approximately 5 min.

To quantify this effect, we employ a geometric analysis. As a first approximation, scattered photons will exit the medium with a uniform distribution of angles. Of these randomly scattered photons, a small proportion will be in the acceptance range of the angular filter and contribute to the gray background in the image. The amount of scattered light leaked through the angular filter is related to the solid angle subtended by the micro-tunnel. The solid angle of a rectangular field of view (symmetrical with respect to the axis of observation) of width a , height b , and length of d is:

$$\Omega = 4 \arcsin \frac{ab}{\sqrt{(4d^2 + a^2)(4d^2 + b^2)}} \quad [sr] \quad 3-5$$

In our case, $60\mu\text{m} \times 60\mu\text{m}$ square-shaped micro-tunnels with a length of 1cm subtend a solid angle of $3.6 \times 10^{-5} \text{ sr}$. The solid angle, Ω , can be imagined as the fractional surface area at the opening of the micro-tunnel. Hence, the fraction of light collected by one micro-tunnel of the angular filter is $\Omega/4\pi$. Finally, the number of total scattered photons for every scattered photon within the solid angle of the micro-tunnel (SR_{max}) is:

$$SR_{\text{max}} = \frac{4\pi}{\Omega} = 3.5 \times 10^5 \quad 3-6$$

Therefore, two populations of photons contribute to the ADI image: 1) Scattered photons, which are distributed as a sphere of light in all directions.

From this scattered light, a small portion passes through the angular filter array and forms the *background scattered light* component of the image that degrades image contrast. 2) Forward-directed ballistic and quasi-ballistic photons within the acceptance angle of the filter that contribute to the informative component of the image that provides contrast. It is important to note that this second component decreases as SR_{max} increases.

Another challenge of ADI implemented with an angular filter array is related to the partially reflective nature of the silicon micro-tunnel sidewalls. Ideally, scattered light that collides with the micro-tunnel sidewalls would be fully absorbed and prevented from passing through the micro-tunnel and reaching the detector. However, silicon is a semiconductor with a very wavelength dependent complex index of refraction of $n = 3.72 + i0.013$ reflecting ~34% reflective to normally incident light. At very shallow angles Fresnel reflection substantially increases this. Using the Fresnel reflection formulae for reflection of angled light, the reflectance for parallel and perpendicular polarized light can be calculated for shallow angles of incidence. For a 0.3° (i.e. 89.7° relative to the normal) angle of incidence that is likely to be present in an ADI experiment, the reflectance is expected to be 92.5% - 99.4% for silicon, depending on polarization and the wavelength. Therefore, instead of being fully attenuated, a fraction of the scattered light at very shallow angles collides with the micro-tunnel sidewalls is reflected within the micro-tunnel several times and reaches the detector, where it combines with non-scattered light to form the image. In practice as light is absorbed at each reflection only the scattered light with 2 or 3 times the

acceptance angle makes it through to the detector. This scattered light acts as an additional source of bias in the image that leads to a loss of image contrast.

We devised three methods to account for the *background scattered light* in ADI and use the information to improve image contrast. The first approach attempts to better understand the effect of polarization discrimination during ADI. The approach takes advantage of the fact that the orientation of linearly polarized light is randomized by scattering during propagation through turbid media. The experiments were conducted in transmission mode where photons propagated through a cuvette containing Intralipid™ and were detected on the backside of the sample. The second approach employed a wedge prism to deviate the laser source where it entered the medium by an angle slightly larger than the AFA acceptance angle. This created a second image consisting of highly scattered photons with the filtration characteristics of the angular filter, and a pixel by pixel correspondence to the fully scattered illumination emitted from the medium. The third method combined the polarizers with the wedge prism.

3.5 Methodology

3.5.1 Experimental setup (ADI)

Due to the benefits of the longer wavelengths in NIR range, the experiment setup employed an 808 nm laser diode (Thorlabs, L808P1WJ multi mode laser diode). The laser beam was shaped and collimated into a line of light by an aspheric and cylindrical lens based collimation system (see Figure 3-5). The beam divergence for the laser diode was high along the vertical axis while

significantly lower along the horizontal axis; therefore, a two-axis collimation system was implemented using one aspheric lens followed by two cylindrical lenses. This lens collimation system produced a line of light with approximately 3 cm wide by 1 mm tall. This beam then passed through an iris diaphragm approximately 8 mm wide to restrict the width of the beam before it illuminated the sample. This was necessary to ensure that the line of light had a uniform light intensity profile before hitting the sample. Previous work at high scattering levels [3-21] showed that due to the very small acceptance angle, the exiting light included many internal shallow angle reflections due to the micro-tunnel walls of the AFA. This light exited at higher angles from the micro-tunnels and degraded both the signal to noise ratio and the spatial resolution. At these shallow angles, $\sim 0.48^\circ$, absorbing films or anti-reflection coatings are known to be not effective [3-22]. Therefore, we chose to use a Keplerian lens system to accept the parallel light exiting the micro-tunnels and reject the majority of the diffracted photons caused by internal reflections. In addition, with the lens system in place, an increase in the scanned area compared to previous work was possible.

Turbid samples with an embedded resolution target rested on a computer-controlled z-axis stage, where they were illuminated by the collimated light source and imaged through the angular filter array by a CMOS camera. Resolution targets could be inserted at any position along the test container, ranging from the front position facing the laser to the back position facing the angular filter and camera as shown in Figure 3-5. The AFA was placed in front of a high-resolution (1280 x 1024 pixel) CMOS detector with a square pixel size (5.2

$\mu\text{m} \times 5.2 \mu\text{m}$) that was smaller than the dimensions of each AFA micro-tunnel and was mounted on a 6 degree-of-freedom (DOF) jig that provided alignment to the laser source. As noted earlier, due to the design of the AFA only one horizontal projection through the sample could be imaged with AFA at a time. Thus, the sample was incrementally raised by a computer controlled z-axis stage so that an entire region of the sample passed through the field of view of the AFA. The default vertical step size used was $26 \mu\text{m}$, which was equivalent to 5 rows of pixels in the CMOS detector. As the test sample was raised, one horizontal projection of the sample was captured at each step, and a final image was assembled by combining the horizontal projections.

3.5.2 Phantoms

For all experiments, we used an aqueous suspension of Intralipid™. Intralipid™, a phospholipid emulsion used usually as an intravenous nutrient, is a practical phantom medium for light dosimetry studies since, like tissue, it is turbid at visible and near infrared wavelengths. Additionally, Intralipid™ lacks strong absorption bands in the visible and near infrared region of the spectrum [3-23]. As a scattering medium, the optical properties of Intralipid™ have been well characterized [3-23]. To test the spatial resolution of our scans, resolution targets were fabricated as L-shaped patterned aluminum thin films on a glass slide. The resolution target was placed either within the scattering medium or at the front (i.e. closest to the laser). In our experiments the resolution target had L-shaped lines and spaces varying from $150 \mu\text{m}$, $200 \mu\text{m}$, $300 \mu\text{m}$, and $400 \mu\text{m}$.

The L-shape geometry provided a means to test the spatial resolution of our imaging setup in both x and y -axis.

3.5.3 Estimation of background scattered light using polarization discrimination (PADI & PADI-CS)

In principle, ballistic photons maintain their polarization memory while scattered photons start to become randomly polarized within the sample. Hence, when the axes of two polarizers are parallel, ballistic light will be passed and some scattered light will be attenuated. The experimental arrangement for the polarized angular domain imaging (PADI) measurements is shown in Figure 3-5 and described in Table 3-1. The collimated line beam was passed through a linear polarizer to grant linear polarity to the incoming light to the sample. The second polarizer was set with their polarization axis parallel to the first. The camera was focused on the surface of AFA using the Keplerian lens system. The measurements were performed on an aqueous suspension of Intralipid™.

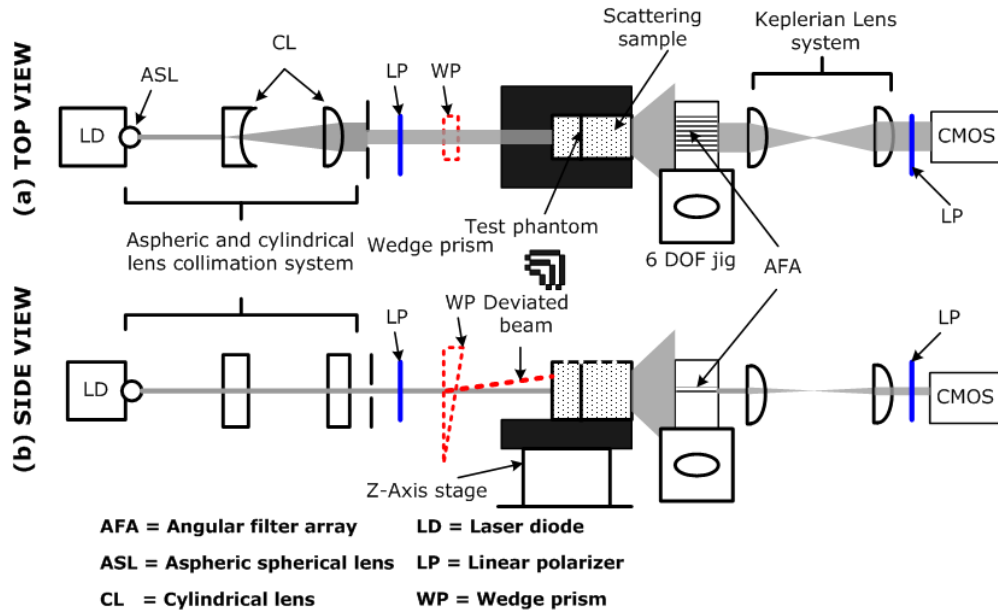


Figure 3-5. ADI setup with 808 nm laser diode and aspheric and cylindrical lens collimation system. (a) Top view (b) Side view.

Alternatively, when the axis of one polarizer is rotated by 90° relative to another (crossed), the ballistic light, which maintains its polarization, will be rejected and the scattered light will be transmitted. Therefore, ADI can be used with a pair of crossed polarizers to estimate the background scattered light. The second image collected with crossed polarizers contains multiply scattered light with pixel by pixel correspondence to the ADI scan with parallel polarity configuration (i.e. PADI). The technique of PADI with crossed subtraction (PADI-CS; Table 3-1) utilizes digital image subtraction of the PADI scan obtained with the crossed polarizers from the PADI scan collected with the parallel polarizers. This technique provides a way to enhance the image contrast by subtracting the background scattered *light* and potentially correct for its degrading effect on image contrast in ADI.

3.5.4 Estimation of background scattered light using deviated light (ADI-WS)

In principle, most scattered photons are assumed to be eliminated while exiting the turbid medium with an angle greater than the acceptance angle of the AFA (e.g. 0.48°). However, as discussed earlier in this paper, a small proportion of scattered photons leak through the AFA giving rise to background scattered light. Experiments show that a slight deviation of the collimated laser beam prior to striking the face of the sample ($\sim 2\times$ of angular filter's acceptance angle) results in a loss of detected ballistic and quasi-ballistic photons, but a preservation of the detected background scattered light. Therefore, the ADI image resultant from the deviated light source provides a pixel by pixel estimate of the background scattered light present in a corresponding ADI image where the light sources is aligned with the AFA. Digital image processing is then used to subtract the background scattered light image from the original ADI image (i.e. wedge subtraction), thus enhancing contrast on a pixel by pixel basis. In our system, we used a wedge prism to deviate the light source slightly beyond the angular filter acceptance angle (~ 1 degree in our experiments). We define this method as angular domain imaging with wedge subtraction (ADI-WS; Table 3-1). It is important to note that scattered light is affected by many factors such as the individual micro-tunnel geometry, illumination uniformity, and the test structure pattern. Capture of the background scattered light image by the wedge technique provides a more accurate pixel by pixel estimates of the scattered light distribution than digital image processing techniques applied globally to the original ADI image.

3.5.5 Combined approach (PADI-WS)

In this setup, parallel polarization measurements with angular domain imaging (PADI) filters the light from scattering medium based on polarization and small acceptance angle provided by AFA. Estimation of *background scattered light* is also feasible by employing the wedge prism. We define the combined technique as polarized angular domain imaging with wedge subtraction (PADI-WS; Table 3-1).

Table 3-1. Summary of the contrast enhancement methods using ADI

<i>Methods</i>	<i>Description</i>
PADI	Polarized angular domain imaging using two parallel polarizers
ADI-WS	Angular domain imaging with <i>background scattered light</i> subtraction using wedge prism
PADI-WS	Polarized angular domain imaging using two parallel polarizers with <i>background scattered light</i> subtraction using a wedge prism
PADI-CS	Polarized angular domain imaging using two parallel polarizers with <i>background scattered light</i> subtraction using two polarizers with cross polarity

In this technique, light passes through two polarizers with axes parallel to obtain an image which includes quasi-ballistic light and a small fraction of scattered light. Then the wedge prism is inserted, which causes the quasi-ballistic light to be deviated out of the field of view of the AFA, hence only scattered light will be detected by camera through the AFA. Using the same principle as ADI-WS, the second image can be subtracted from the original to

correct for the *background scattered light*. Table 3-1 summarizes all the methods employed to enhance the image contrast.

3.6 Results and discussion

3.6.1 Detection limit imposed by sample thickness and Intralipid™ concentration

When the concentration of Intralipid™ was increased, the detection limit of ADI depended inversely on the thickness of the sample. For instance, a resolution target was detectable with ADI in a 5 cm thick optical cell filled with 0.14% Intralipid™, a 2 cm thick optical cell filled with 0.3% Intralipid™, and a 1 cm thick optical cell filled with 0.7% Intralipid™. This confirmed that the product of the reduced scatter coefficient (proportional to Intralipid™ concentration) and the thickness was a predictor of the detection performance of ADI. Based on these findings, we chose 0.25% and 0.3% Intralipid™ in a 2 cm optical cell to study the performance of ADI at scattering levels below and in the range of the detection limit. The experiments used the 808 nm laser diode as the source of illumination. According to Mie theory [3-24], the reduced scattering coefficient, μ'_s for 0.25% and 0.3% Intralipid™ solutions is approximately 2 cm^{-1} and 2.4 cm^{-1} , respectively. However, the effective scattering level at the angular filter array was higher due to the refractive index mismatch between the Intralipid™-glass, and glass-air boundaries.

3.6.2 Image contrast enhancement by wedge-based subtraction (ADI-WS)

The results of the ADI-WS image contrast enhancement techniques are shown in Figure 3-6(a)-(c). Without the wedge in place (Figure 3-6(a)), the

resolution target was discernable, but the contrast was poor. With the wedge prism inserted into the light path, the resolution target could not be visualized (Figure 3-6 (b)). This was to be expected since the quasi-ballistic photons were directed out of field of view of the AFA, which left only scattered light to leak through the AFA and reach the camera.

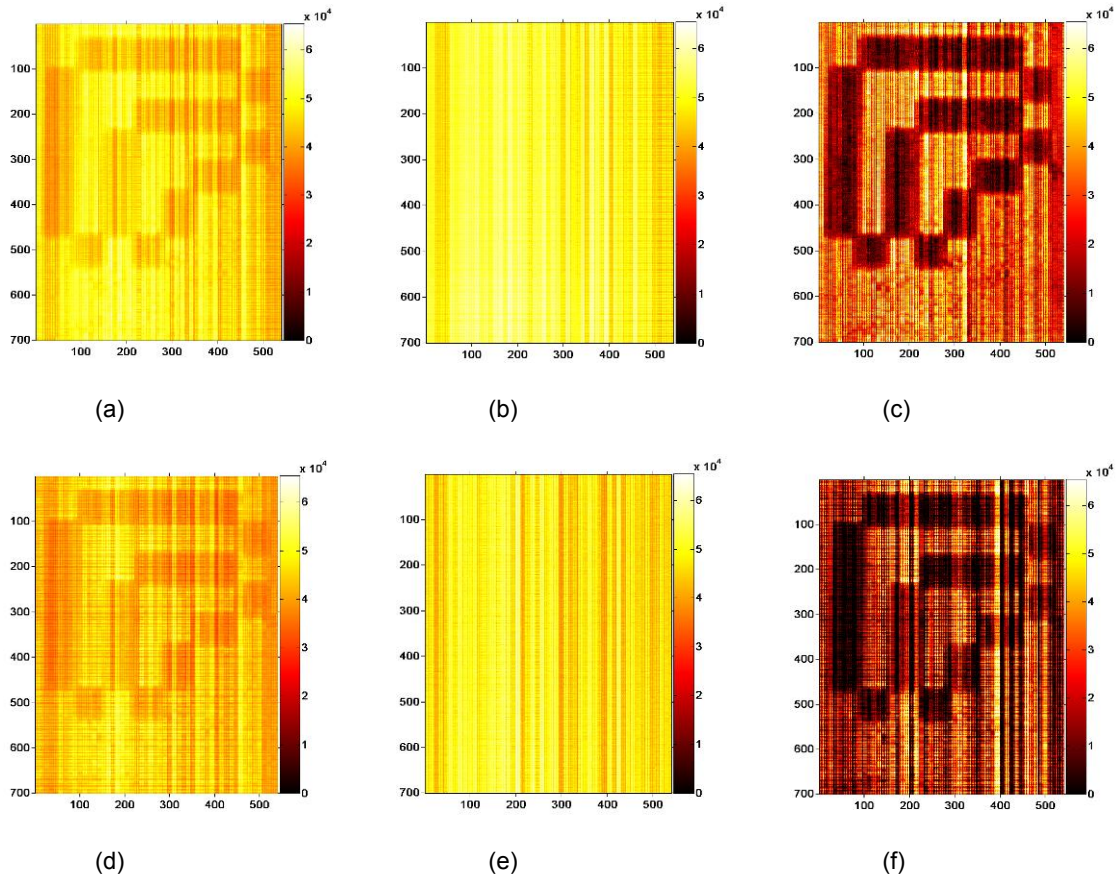


Figure 3-6. Contrast enhancement of ADI scan of L-shape target (line and space width of $400\ \mu\text{m}$) at 808nm for a scattering medium composed of 0.3% Intralipid™ in a 2 cm thick optical cell. (a) Original ADI scan, (b) Wedge inserted ADI scan (c) Wedge subtraction image (d) Parallel polarized ADI scan (PADI) (e) cross polarized ADI scan (f) subtraction result of parallel and cross orientation (PADI-CS).

Digital image subtraction of the two images revealed an image of the resolution target with better contrast compared to ADI without the wedge (i.e.

compare Figure 3-6(c) to Figure 3-6(a)). The superior image contrast of the subtracted image as shown in Figure 3-6(c) was due to the removal of the majority of the *background scattered light*.

As described earlier, the *background scattered light* becomes more dominant in ADI scans as the scattering level of the sample increases. This was evident in Figure 3-6(a) where there was poor contrast between the resolution target and background for the 2 cm thick optical cell filled with 0.3% Intralipid™. Based on our previous work [2-26], digital image processing techniques could be used to increase the visibility of the lines and spaces to some degree, but the *background scattered light* image subtraction method (Figure 3-6(c)) shows much better contrast compared to image processing alone.

3.6.3 Image contrast enhancement by polarization-based subtraction (PADI)

Figure 3-6 (d)-(e) show the results of the polarized ADI images with the linear polarizers oriented with axes parallel (Figure 3-6(d)) and axes perpendicular (Figure 3-6(e)). Digital image subtraction of the two images revealed an image of the resolution target with better contrast compared to ADI with the polarizers in the parallel orientation (i.e. compare Figure 3-6(f) to Figure 3-6(d)). However, it was evident that the contrast enhancement was qualitatively not as good as the ADI-WS technique (i.e. compare Figure 3-6(c) to Figure 3-6(f)). Although it was assumed that the perpendicular polarization measurement did not include quasi-ballistic light, it was likely that some quasi-ballistic photons suffered random changes in their polarization and leaked

through the cross polarizers. This leakage added to the estimated *background scattered light* and degrade image contrast.

3.6.4 Image contrast enhancement by combined use of wedge and polarization-based subtraction (PADI-WS)

Comparing the image contrast between ADI and PADI, parallel polarization measurements do not appear to increase the image contrast significantly, only a small improvement is observed. This was likely due to some informative quasi-ballistic photons losing their initial polarization followed by attenuation by the second polarizer in a similar manner to randomly scattered light. Our experiment at the lower scattering level (0.25% Intralipid™ in the 2 cm optical cell) showed that with crossed polarized ADI measurements, the L-shape targets were still faintly observable (not discernable in presented image), which indicated that some of the informative signal changed polarization and passed through the cross polarizer. Hence, cross polarized ADI cannot be effective as a pure *background scattered light* correction method like ADI-WS. The following section will compare all the presented methods in a more quantitative manner.

3.6.5 Comparison of image contrast enhancement methods

In order to compare the results of wedge, polarization, and combined subtraction procedures in terms of image contrast enhancement, the contrast of the contrast-enhanced images was calculated based on the following formula:

$$\text{Contrast Ratio} = \frac{\text{mean}(I_{\max}) - \text{mean}(I_{\min})}{\text{mean}(I_{\max}) + \text{mean}(I_{\min})} \quad 3-7$$

where I_{min} is the average light intensity corresponding to shadowed region (i.e. due to the shadow of the L-shape target within the phantom) and I_{max} is the average light intensity corresponding to the unshadowed local area near the structure.

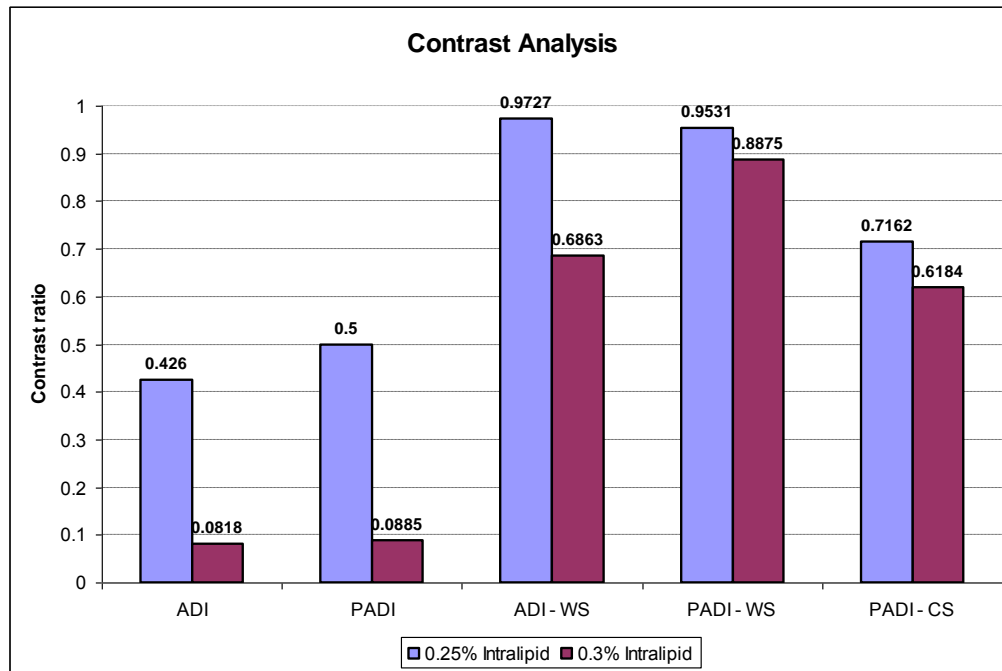


Figure 3-7. Comparison of image contrast enhancement using polarization contrast enhancement and wedge subtraction methods in different scattering ratio levels.

Figure 3-7 shows the image contrast computed from eq. 3-7 for the results collected at two scattering levels of the sample. For standard ADI, the image contrast declined from 0.4 to 0.08 when the scattering level of the sample increased due to an increase in concentration of Intralipid™ from 0.25% to 0.3%. As Figure 3-7 shows, addition of the linear polarizers to ADI (PADI) improved the image contrast by only a minor amount compared to ADI alone. This was likely due to the poor discrimination of the polarizers between quasi-ballistic and

scattered photons. On the other hand, estimation of the *background scattered light* by the wedge prism technique with subsequent image subtraction (ADI-WS) resulted in improved image contrast compared to ADI alone. A similar result was observed for the combination of the wedge subtraction technique with polarized angular domain imaging (PADI-WS). The combined technique provided the highest level of image contrast improvement at the detection limit of ADI (i.e. 0.3% Intralipid™). The subtraction of the cross polarizer measurements from the parallel polarizer measurements (PADI-CS) provided an intermediate level of improvement in image contrast, and was inferior to the ADI-WS and PADI-WS techniques.

3.7 Conclusion

Although ADI is proving to be a powerful technique for imaging turbid samples, methods for contrast enhancement in ADI are likely needed if the technique is to be applied to imaging biological systems. Here we reported significant improvements in ADI image contrast by placement of readily available optical components into the light path combined with digital image subtraction. These methods captured pixel by pixel estimates of the *background scattered light* levels without compromising optical alignment of the setup. This significant side benefit ensured that contrast enhancement during transillumination ADI could be facilitated without disturbing the highly aligned collimated light source and AFA. For turbid samples where the scattering level was low enough for ADI to detect targets easily, the wedge subtraction technique (i.e. ADI-WS) had the greatest impact on improving image contrast with a greater than 2-fold

improvement over ADI alone. For turbid samples where the scattering was at a level beyond which ADI could reliably detect embedded objects, the combination of the wedge and polarizer-based subtraction techniques (i.e. PADI-WS) gave the greatest improvement in image contrast. This suggested that although the use of polarizers in ADI was not as good at improving image contrast as the wedge-based ADI method, the combination of the two was superior to either technique alone. Further improvements to ADI image contrast may be possible by replacing the camera with one of higher bit precision and lower noise so that contrast differences below 0.08% can be distinguished. These approaches will likely push the capabilities of ADI into the realm of high resolution imaging of highly scattering (equivalent to 1% Intralipid™ and beyond) biological specimens up to 1 cm in thickness, which would enable multispectral imaging for tissue characterization and functional studies at a spatial resolution exceeding 200 μm. These capabilities could prove useful for histological analysis of thicker tissue specimens over a larger field of view compared to current optical methods. This might find a direct application in optical analysis of entire biopsy specimens rather than selected sections as is currently the case.

3.8 Reference list

- 3-1 H. Hielscher, "Optical tomographic imaging of small animals," *Curr. Opin. Biotechnol.* 16, 79-88 (2005).
- 3-2 Roggan, M. Friebel, K. Dorschel, A. Hahn, and G. Muller, "Optical Properties of Circulating Human Blood in the Wavelength Range 400--2500 nm," *J. Biomed. Opt.* 4, 36-46 (1999).
- 3-3 T. Wilson, ed., *Confocal Microscopy* (Academic, London, 1990).

- 3-4 F. Fercher, "Optical coherence tomography-principles and applications," Rep. Prog. Phys., 66, 239-303 (2003).
- 3-5 J. G. Fujimoto, "Optical coherence tomography," Comptes Rendus De l'Academie Des Sciences, Serie IV (Physique, Astrophysique), 2, 1099-111 (2001).
- 3-6 L. M. Wang, P. P. Ho, C. Liu, G. Zhang, and R. R. Alfano, "Ballistic 2-D imaging through scattering walls using an ultrafast optical Kerr gate," Science, 253, 769-771 (1991).
- 3-7 D.A. Benaron and D.K. Stevenson, "Optical time-of-flight and absorbance imaging of biologic media" Science, 259, 1463–1466 (1993).
- 3-8 N. Pfeiffer, P. Chan, G. H. Chapman, F. Vasefi, and B. Kaminska, "Optical imaging of structures within highly scattering material using a lens and aperture to form a spatiofrequency filter", Proc. SPIE, 6854 (2008).
- 3-9 G.H. Chapman, M. Trinh, N. Pfeiffer, G. Chu, and D. Lee, "Angular Domain Imaging of Objects Within Highly Scattering Media Using Silicon Micromachined Collimating Arrays", IEEE J. Sel. Top. Quantum Electron., 9, 257-266, (2003).
- 3-10 F. Vasefi, B. Kaminska, P. K. Y. Chan, and G. H. Chapman, "Multi-spectral angular domain optical imaging in biological tissues using diode laser sources," Opt. Express 16, 14456-14468 (2008)
- 3-11 S. Chandrasekhar, "Radiative Transfer", Oxford University Press, London, (1950).
- 3-12 M. R. Arnfield, J. Tulip, and M. S. McPhee, "Optical propagation in tissue with anisotropic scattering," IEEE Trans. Biomed. Eng. 35, 372–381 (1988).
- 3-13 W. F. Cheong, "A review of the optical properties of biological tissues," IEEE J. Quantum Electron., 26, 2166-2185 (1990).
- 3-14 Henyey, L. and Greenstein, J. L., "Diffuse radiation in the galaxy", Astrophysics. J., 93, 70 (1940).
- 3-15 Jacques SL, Alter CA, Prael SA, "Angular Dependence of HeNe laser Light Scattering by Human Dermis", Laser Life Sci, 1, 309-333 (1987).
- 3-16 Tuan Vo-Dinh, Ed., Biomedical Photonics Handbook. Publisher: CRC (2003).
- 3-17 V. V. Tuchin, "Fundamentals of low-intensity laser radiation interaction with biotissues: dosimetry and diagnostical aspects Bull. Russ. Acad. Sci., Phys. Ser. 59 120–143, (1995).

- 3-18 L. Wang, S. L. Jacques and L. Zheng, "MCML—Monte Carlo modeling of light transport in multi-layered tissues," *Comput. Methods Programs Biomed.*, 47, 131-146, 7 (1995).
- 3-19 F. Vasefi, P.K.Y. Chan, B. Kaminska, G. H. Chapman, N. Pfeiffer, "An Optical Imaging Technique Using Deep Illumination in the Angular Domain," *IEEE J. Sel. Top. Quantum Electron.* 13, 1610-1620 (2007).
- 3-20 F. Vasefi, B. Kaminska,, G. H. Chapman,, J. J.L. Carson, "Angular distribution of quasi-ballistic light measured through turbid media using angular domain optical imaging", Submitted to *SPIE Photonics West: Optical Interactions with Tissue and Cells XX*, (2009).
- 3-21 F. Vasefi, B. Kaminska, G. H. Chapman, "Angular Domain Optical Imaging Using a Micromachined Tunnel Array and a Keplerian Lens System" in 30th *IEEE EMBS Annual International Conference*, 3730-3734 (2008) .
- 3-22 P.K. Chan, F. Vasefi, G.H. Chapman, B. Kaminska, N. Pfeiffer. *Angular Domain Optical Tomography in Scattering Media with Multi-spectral Diode*, *Proc. SPIE* 6435 (2007).
- 3-23 S. Jacques, Optical properties of "Intralipid™", an aqueous suspension of lipid droplets, <http://omlc.org/spectra/intralipid/index.html> .
- 3-24 HG van Staveren, CJM Moes, J van Marle, SA Prahl, MJC van Gemert, "Light scattering in Intralipid-10% in the wavelength range of 400-1100 nanometers," *Appl. Opt.* 30, 4507-4514, (1991).
- 3-25 F. Vasefi, G. H. Chapman, P. K. Y.Chan, B. Kaminska, N. Pfeiffer, "Enhanced angular domain optical imaging by background scattered light subtraction from a deviated laser source", *Proc. SPIE Vol.* 6854 (2008)

4: ANGULAR DOMAIN TRANS-ILLUMINATION IMAGING OPTIMIZATION WITH AN ULTRA-FAST GATED CAMERA³

4.1 Abstract

By employing high aspect ratio parallel micro-channels as an angular filter, quasi-ballistic photons sensitive to internal structures in a turbid medium can be captured. Scattered photons exiting the turbid medium typically exhibit trajectories with random angles compared to the initial trajectory and are mostly rejected by the filter. However, AFAs cannot differentiate between quasi-ballistic photons (early arriving) and photons that happen to attain a scattered trajectory that is within the acceptance angle (late arriving). Therefore, this work had two objectives: (i) to experimentally characterize the angular distribution and proportion of minimally deviated quasi-ballistic photons and multiply scattered photons in a turbid medium; and (ii) to combine time and angular gating principles so that early and late arriving photons could be distinguished. From the angular distribution data, the angular filter with angular acceptance about 0.4° yielded the highest image contrast for trans-illumination images. The use of ADI with time-gating enabled visualization of sub-millimetre absorbing objects with approximately seven times higher image contrast compared to ADI in turbid medium with a scattering level of six times the reduced mean free path.

³ The following chapter is published in Journal of Biomedical Optics, Vol. 15, No. 6, 061710 (2010) under the co-authorship of Mohamadreza Najiminaini, Eldon Ng, Bozena Kaminska, Glenn H. Chapman, and Jeffery J.L. Carson.

4.2 Introduction

4.2.1 Background and motivation

Several applications in biomedical optics and optical remote sensing involve imaging through a turbid medium. In optical bio-imaging methods, illumination and detection can be performed either on the same side of the medium for reflective imaging, or on opposite sides of the medium for trans-illumination imaging. Reflectance imaging methods [4-1] like optical coherence tomography [1-204-2, 4-3] and enhanced backscattering spectroscopy [4-4], where photons are either coherently or diffusely reflected by the scattering properties of the medium, are more developed but suffer from limited light penetration into tissue. Trans-illumination imaging methods can image through thicker samples (since the photon path is not folded compared to reflectance methods) and have found application for small animal imaging [4-5, 4-6]. However, the challenges associated with the strong scattering properties of tissue places an effective limit on the detection of ballistic photons for tissues no greater than 3-4 mm in thickness [4-7]. With recent improvements, trans-illumination imaging has found new applications, i.e. biometric authentication using vein patterns of a finger or palm [4-8], and histopathological characterization and high resolution margin delineation of sectioned tissue samples [4-9,4-10].

When imaging thick tissue samples by trans-illumination methods, image forming signal is largely affected by scatter, and less so by attenuation. The scattering coefficient is on the order of $\mu_s \approx 100 \text{ cm}^{-1}$, being about four orders of

magnitude larger than absorption and thus leading to a total mean free path of only 0.1 mm. Therefore, for trans-illumination imaging of tissue samples up to a centimetre in thickness, the amount of ballistic light passing through the tissue sample is negligible. Only quasi-ballistic and scattered photons are present in large enough quantities to provide image forming signal. Since there is no clear borderline between quasi-ballistic and scattered light, K. Shimizu et al. [4-11, 4-12] redefined non-ballistic light into three categories: near-axis scattered light, weakly scattered light, and strongly diffused light. These categories were based on the concepts of deviation of photon trajectory from the original path and transit time taken to traverse the optical path. For a trans-illumination imaging system, photons in each category contribute differently to the spatial resolution of the resultant projection image. For instance, an imaging system that captures only near-axis scattered light provides higher spatial resolution compared to an imaging system that captures only weakly scattered light [4-11, 4-12].

By using the dissimilarities of scattering characteristics on time, angle, and polarization, different imaging techniques have been explored to select ballistic and quasi-ballistic photons. In time domain, the snake and diffuse photons are usually differentiated by photon travel times. Techniques based on the capture of snake photons with time gating alone [4-13, 4-14] suffer from low sensitivity. Alternatives to time gating are polarization-gating [4-15, 4-16] and angle-gating [4-17, 4-18]. In certain experiments, combinations of more than one method were used for higher efficiency in imaging [4-19, 4-20- 4-23]. Time and coherence domain imaging systems usually require expensive and complicated

instrumentation including fast pulsed lasers and detectors although polarization and angular gating can be less expensive solutions.

Our previous work [4-23] showed that quasi-ballistic photons passing through a turbid medium quickly lost their initial polarization and so could not be selected using polarization based filtration. Angle filtration of exiting photons was more efficient compared to the polarization filtration scheme. Angular Domain Imaging (ADI) utilizes a passive optical device to filter out highly scattered photons and is based on the principle that scattered photons tend to exit a turbid medium with a nearly uniform angular distribution while non-scattered ballistic and quasi-ballistic photons exit with a trajectory that remains close to the initial trajectory with minimal angular deviation [4-24]. Hence, by rejecting scattered light by ADI, internal absorption or scattering targets appear as shadows from outside of the turbid sample.

4.2.2 Angular domain imaging principle

The simplest implementation of Angular Domain Imaging (ADI) involves the use of a converging lens and pinhole aperture. When the aperture is located at the back focal plane of the lens, the arrangement forms a spatiofrequency filter (SFF) and is capable of blocking incoming photons with trajectories outside the angular acceptance of the SFF [4-25,4-26]. Therefore, when used to view a trans-illuminated turbid sample, minimally-scattered image forming photons are preferentially selected to produce a projection image of the sample contents. An alternative design for ADI involves an array of high aspect ratio micro-channels known as an Angular Filter Array (AFA) [4-23, 4-24]. The AFA approach has the

advantage that distortions and aberrations common to the lens/pinhole arrangement are avoided. As shown in Figure 4-1, the AFA provides a means to reject highly scattered photons preferentially compared to quasi-ballistic photons, so that the projection image can be formed on the detector. Recently, a series of ADI studies analyzed silicon micro-machined AFA performance for detection of information-bearing diffusely reflected photons [4-27] and fluorescence targets [4-28]. The experiment results demonstrated that ADI performed better than standard reflectance methods and could measure deeper structures more accurately.

4.2.3 Improvement of ADI by new AFA designs and time-gating

Although AFA devices have been shown to reject scattered photons for turbid samples with thicknesses of up to 6 times the reduced mean free path, beyond this thickness background scattered light dominates. Background scattered light arises due to photons that leak through the AFA due to internal reflections and/or multiply scattered photons that attain acceptable trajectories and leak through the AFA to the detector [4-23]. One potential solution to reject photons that leak due to internal reflections is to introduce surface features into the micro-channel walls that attenuate photons through the principle of reflection loss [4-29]. We hypothesized that by introducing rectangular features into micro-channel walls, photons will be reflection trapped and the effect of photon leakage due to wall reflections will be suppressed greatly. A potential solution to the problem of leakage of multiply scattered photons relates to path length differences between quasi-ballistic and multiply scattered photons. Due to their

longer trajectory, photons representative of background scattered light take longer to reach the detector than quasi-ballistic photons.

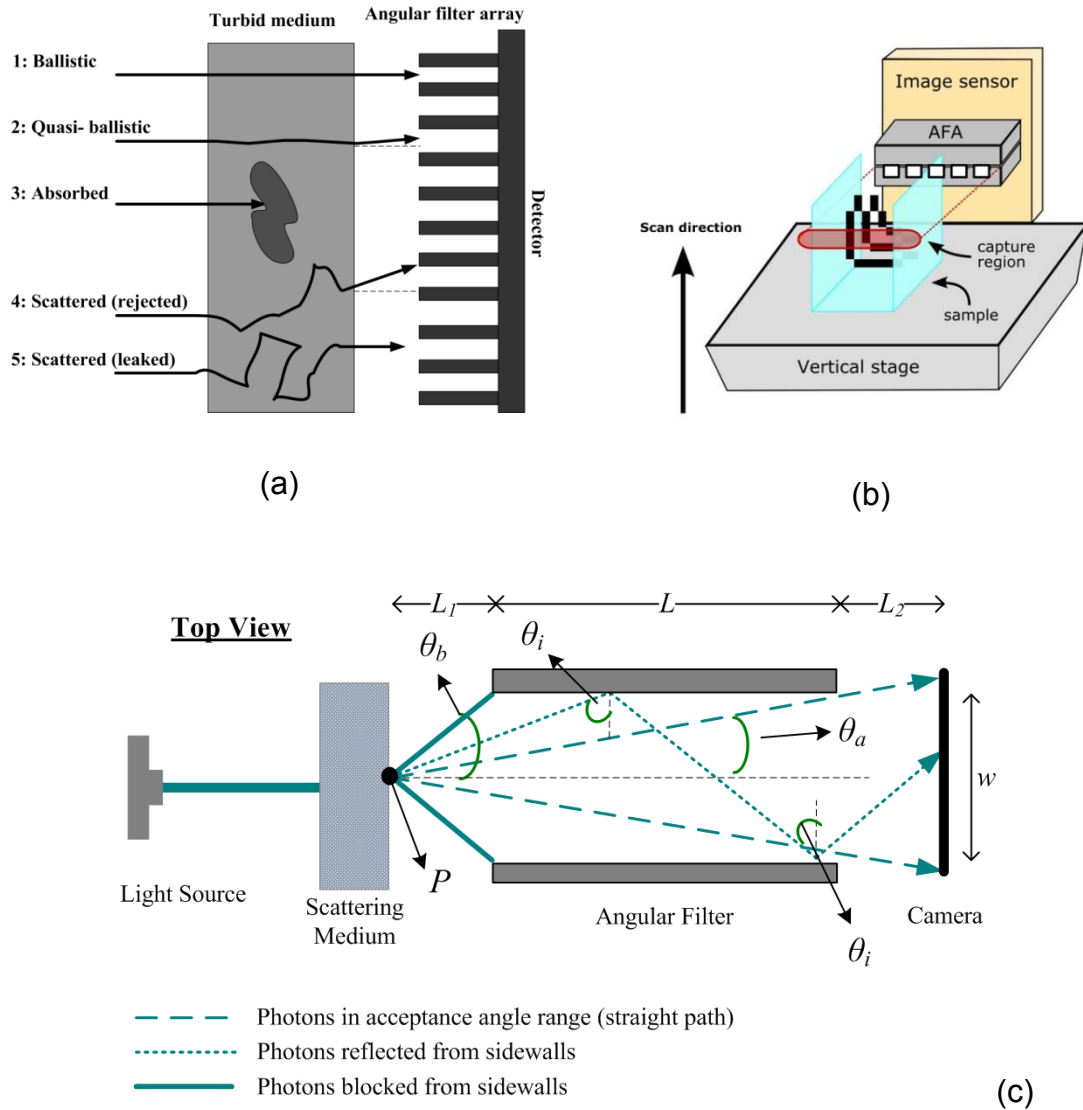


Figure 4-1. (a) Photon trajectories through a turbid medium. (b) ADI scanning procedure of an L-shape resolution target in a turbid used to collect a 2D projection image. (c) Possible photon reflections due to channel walls. (θ_a : acceptance angle, θ_b : blocking angle, θ_i : incident angle)

Therefore, we hypothesized that time-gated detection of the early arriving photons will provide a means to suppress background scattered light during ADI. This is based on the fundamental difference between path length gating (as employed by time-domain) and trajectory angle filtration. As the path length gate is decreased, photons with path lengths exceeding the filter cut-off are excluded. While as the trajectory angle gate is decreased, only the average path length of accepted photons is decreased. Images comprised of trajectory-filtered photons will always include a contingent of well-scattered photons resulting in reduced contrast and degraded resolution. However, by combining both trajectory angular filtration and time gating, complimentary improvements in AFA scattered light leakage can be realized and push the detection limit of ADI beyond current levels.

4.2.4 Objective and approach

Reflections off of the micro-channel walls and background light leakage are two processes that limit the performance of ADI when imaging through thick turbid media. Therefore, to enhance our understanding of how these processes impact ADI so that ultimately sample thickness can be increased, the work presented here had four objectives. First, we sought to model micro-channel wall reflections and their dependence on incidence angle of photons entering the AFA. Second, we wanted to compare the modeling results to measurements obtained with AFAs of increasing acceptance angle. Third, we tested a new AFA design for suppressing channel wall reflections and compared its performance to

conventional AFA designs. Last, we designed an alternative strategy for suppression of background light leakage and compared to established methods. Our approach to modeling was to apply the Fresnel Law to the micro-channel geometry to predict the transmitted light through the AFA as a function of incident angle. Our approach to reducing channel wall reflections was to optimize the design parameters of the AFA. AFAs of various acceptance angle and channel wall design (flat Vs patterned) were fabricated and employed in trans-illumination ADI. We then evaluated the efficiency of the different AFAs at capturing quasi-ballistic photons and rejecting highly scattered photons and compared the results to the output of our modeling. Our approach to reducing background light leakage was to devise a new ADI design that combined angular domain imaging (using an AFA) with time domain technology in the form of a picosecond pulsed laser for illumination and an ultra fast gated CCD camera for detection. We then tested the new ADI design on its ability to improve image contrast by rejection of the late arriving photons that contributed to background light leakage. We then compared the results to those from wedge subtraction, which provided an independent means to correct for background light leakage.

4.3 Methods

4.3.1 Fabrication of tissue mimicking phantoms

In the following experiments, an aqueous suspension of Intralipid™ was employed to model the high scattering properties of biological tissue samples. Intralipid™ is a practical and widespread phantom medium for light dosimetry studies because, like tissue, it is turbid and has low optical absorption at near

infrared wavelengths. As a scattering medium, the optical properties of Intralipid™ have been well described [4-30, 4-31]. Within each phantom we placed a resolution target at the midpoint of the optical cuvette. The resolution target consisted of a collection of L-shaped patterns (optical thick film of aluminum) on a glass slide to evaluate the horizontal and vertical spatial resolution of image; see Figure 4-1(b). The L-shaped lines and spaces had various sub-millimetre sizes.

Results from earlier work [4-23] demonstrated that the detection limit of ADI in trans-illumination mode depended both on the thickness of the sample and its scattering level, which is dependent of Intralipid™ concentration. For instance, a 150 μm line and spacing target was detectable with ADI at the midpoint of a 5 cm thick (l) optical cuvette filled with 0.14% Intralipid™ as well as a $l = 2$ cm thick optical cell filled with 0.3% Intralipid™, and a $l = 1$ cm thick optical cell filled with 0.7% Intralipid™. This confirmed that the product of the reduced scatter coefficient (proportional to Intralipid™ concentration) and the thickness was a predictor of the detection performance of ADI. As described in [4-30, 4-31], considering the forward scattering property ($g = 0.75$) common in tissue-mimicking phantoms, the reduced scattering coefficient for 1% Intralipid™ is roughly 8-10 cm^{-1} in the near infrared, while the absorption coefficient is about 0.1-0.01 cm^{-1} which is two to three orders of magnitude smaller. The reciprocal value of reduced scattering coefficients yields the reduced mean free path (MFP'). Therefore, for the resolvable 150 μm line targets, the effective resolution

of ADI was 3 line pairs per millimetre (lp/mm) at a scattering level of $6 \times \text{MFP}'$ about the detection limit.

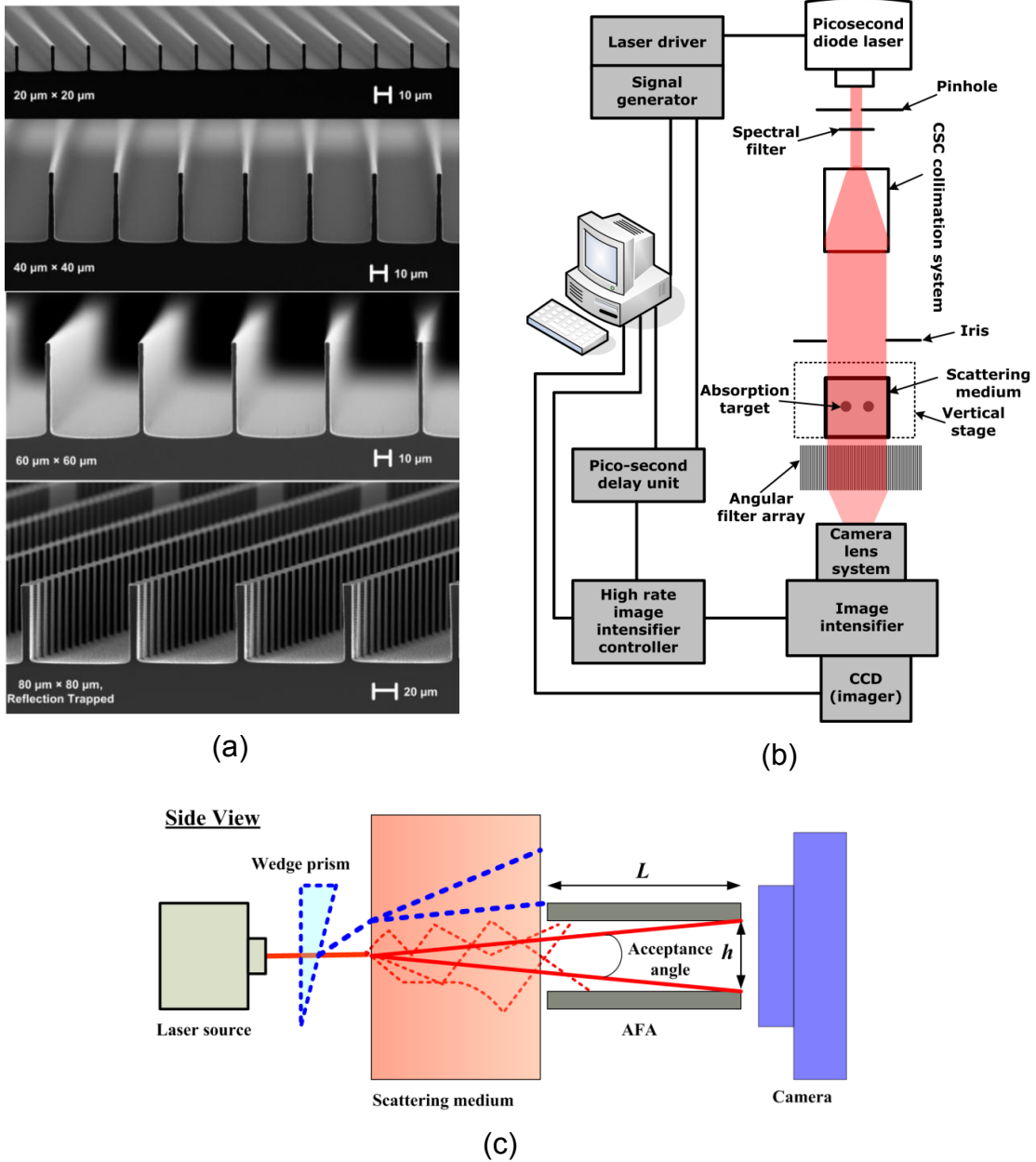


Figure 4-2. Experimental setup for the proposed techniques, (a) Different AFA geometries (b) Diagram of the Time Angular Domain Imaging (TADI) system. (c) Diagram describing wedge subtraction method where images were collected with and without a wedge prism so that the contributions from image forming quasi-ballistic photons and background scattered photons could be estimated.

4.3.2 Conventional angular filter arrays

Monte-Carlo simulation programs designed to test the ADI concept showed that the collimator detects the shortest path length photons [4-24]. Consequently, the collimator acts as an optical filter to remove scattered light while preserving the ballistic and quasi-ballistic light. Simulations suggested that smaller channels and longer arrays could enhance detection by >100 in the condition that they do not violate diffraction and Raleigh range limitations [4-24]. In this manuscript, we report the experimentally determined effect of AFA geometry on ADI performance.

Four AFAs were fabricated using silicon micro-machining techniques. Each had unique properties related to the micro-channel aperture size, acceptance angle, and micro-channel wall pattern. More description about fabrication of square-shape AFAs has been described in [4-32]. During testing of the AFAs, a standardized ADI system (i.e. same light source, turbid sample, and camera used for all AFAs) was used to enable accurate comparisons between AFA geometries. The consistency of the ADI setup was critical since the resultant image contrast and resolution in ADI is known to be directly affected by the collimation quality, illumination shape (large field circular or line) [4-33], wavelength of the light source [4-18], AFA alignment, sample scattering level, and camera pixel size. As shown in Figure 4-2(a), the conventional AFAs were fabricated with a parallel array of square-shaped micro-channels that varied in aperture size from $20\ \mu\text{m} \times 20\ \mu\text{m}$, $40\ \mu\text{m} \times 40\ \mu\text{m}$, to $60\ \mu\text{m} \times 60\ \mu\text{m}$. The micro-channels of each AFA were 1 or 1.5 cm long to provide a complimentary

range of testable aspect ratios (i.e. same aspect ratio, but different micro-channel dimensions).

4.3.3 Reflection-trapped angular filter arrays

Even though the AFAs we tested in previous work [4-32] had small aspect ratios, internal reflections within the micro-channel led to apparent increases in the effective aspect ratio. For example, photons entering the micro-channel aperture at an angle greater than the acceptance angle can reflect internally. As we discussed previously, intrachannel reflected light acts as a source of background bias (noise) in the ADI scans, and various techniques can be employed to modify the channel walls in order to suppress it. Previous methods used to reduce the internal reflection of the channel include coating the channel wall with carbon and increasing the surface roughness [4-29, 4-34]. Although these methods reduced internal reflections, they did not completely eliminate reflected light from reaching the detector. We therefore devised an alternative design called a reflection trapped AFA (RTAFA; last design in Figure 4-2(a)) that had patterned channel walls to trap reflected photons. In the RTAFA device, the channel walls were patterned with square vertical ridges $2.5\ \mu\text{m}$ (at least twice the wavelength) at a periodicity of $20\ \mu\text{m}$. More fabrication details are presented in [4-35].

In order to distinguish between individual AFAs, we employed a naming convention for the AFA design based on either regular (AFA) or reflection trapped (RTAFA) with the first number denoting the aperture size and the second number denoting the channel length. For example, RTAFA-80-1.5 represents a

reflection trapped AFA with an $80\mu\text{m}\times 80\mu\text{m}$ micro-channel aperture and a channel length of 1.5 cm.

4.3.4 Ray trace analysis of AFA geometries

For AFAs with flat channel walls, photons with trajectories outside the acceptance angle range of the AFA can potentially pass through the AFA due to the high reflectivity of the silicon at shallow angles. Silicon (index of refraction, $n = 3.65$ in near infrared) can be up to 40% reflective to perpendicularly incident light, and much more so at shallower angles. Figure 4-1(c) shows the top view of one micro-channel of an AFA in trans-illumination model, where L_1 is the distance between the scattering medium and the opening of the channel; L_2 is the distance from the end of the channel to the detector camera; and L and w are the length and the width of the channel, respectively. The angular parameters of the filter include θ_a , and θ_b . The acceptant angle, θ_a , of the channel is defined as the maximum angle for light to arrive at the detector camera without experiencing any reflection with the channel wall while θ_b is defined as the minimum angle for photons to be blocked by the filter channel. The reflected angle, θ_r , is the angle between θ_a and θ_b . Incident light at θ_r tends to reflect with the channel wall before it reaches the detector camera. Using the Fresnel reflection formulae for reflection of angled light, the reflectances R_p (for parallel polarized light) and R_s (perpendicular) are given by [4-36]:

$$R_s = \left[\frac{n_1 \cos(\theta_i) - n_2 \sqrt{1 - \left(\frac{n_1}{n_2} \sin(\theta_i)\right)^2}}{n_1 \cos(\theta_i) + n_2 \sqrt{1 - \left(\frac{n_1}{n_2} \sin(\theta_i)\right)^2}} \right]^2 \quad 4-1$$

$$R_p = \left[\frac{n_1 \sqrt{1 - \left(\frac{n_1}{n_2} \sin(\theta_i)\right)^2} - n_2 \cos(\theta_i)}{n_1 \sqrt{1 - \left(\frac{n_1}{n_2} \sin(\theta_i)\right)^2} + n_2 \cos(\theta_i)} \right]^2 \quad 4-2$$

where θ_i is the angle between the incident light to the normal of the refracted plane and equivalent to $90^\circ - (\theta_r/2)$, and n_1 and n_2 are the index of refraction for the incident light medium and the refracted light medium, respectively. In the case of the AFA for near infrared light, $n_1 = 1$ for air and $n_2 = 3.5$ for silicon. For a randomly polarized beam, both reflectance values can be averaged. Thus, instead of being fully attenuated, scattered photons that collide with the channel wall can be reflected (perhaps multiple times) and reach the detector, where it combines with quasi-ballistic light to form the image.

To simulate the performance of the AFA designs to photons outside the acceptance angle, we performed a simple optical ray trace analysis. The reflectance from the AFA micro-channel walls was calculated using the Fresnel Law (Eq. 4-1 and Eq. 4-2) and reported in Figure 4-3. Scattered light exiting the turbid medium at a point was modeled as a point source with isotropic emission. The point source is shown as “P” in Figure 4-1(c).

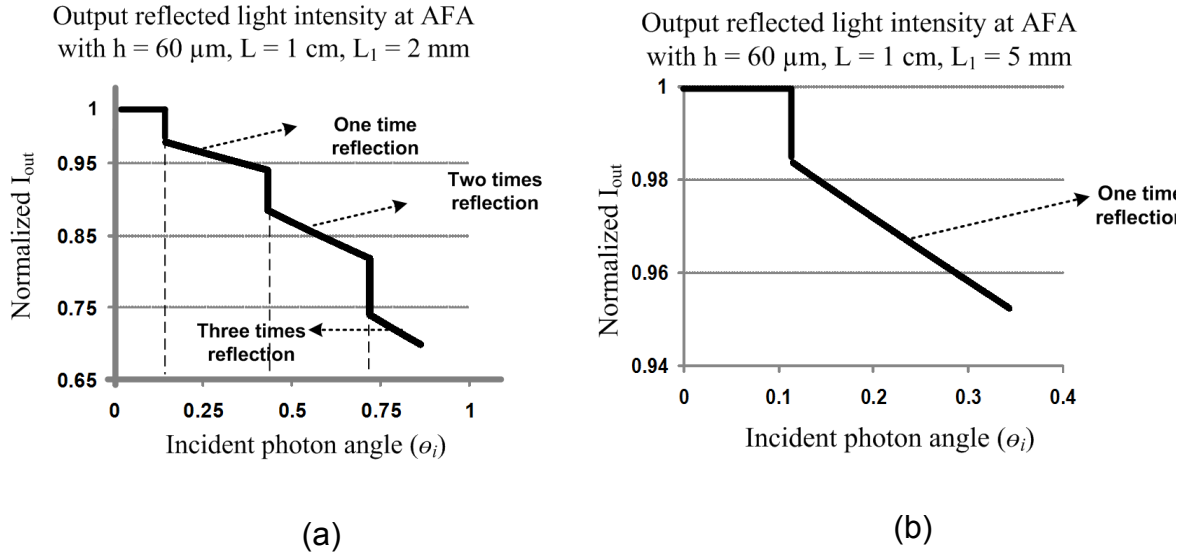


Figure 4-3. Reflected light intensity using AFA-60-1 placed at two different distances from a point source with uniform angular distribution.

Table 4-1. Estimation of effect of reflected light in different AFA sizes

	$L_1 = 2 \text{ mm}$					$L_1 = 5 \text{ mm}$				
	θ_a	θ_b	R_a	R_b	η	θ_a	θ_b	R_a	R_b	η
AFA-20-1	0.095°	0.573°	0.993	0.885	82.6	0.076°	0.229°	0.994	0.984	66.4
AFA-40-1	0.191°	1.146°	0.986	0.786	81.9	0.153°	0.458°	0.989	0.968	66.2
AFA-60-1	0.287°	1.719°	0.980	0.701	81.3	0.229°	0.688°	0.984	0.952	65.9

θ_a : acceptance angle

θ_b : blocking angle, ($\theta_a < \theta_i(\text{incident light}) < \theta_b$)

R_a = Reflected light intensity at an angle right after θ_a

R_b = Reflected light intensity at an angle right before θ_b

η = Proportion of reflected light intensity to total input light

The normalized transmittance and effect of multiple reflections versus the incident photon angle (θ_i) was calculated for a single micro-channel of the AFA (AFA-60-1) with the central axis of the entrance aperture placed 2 mm or 5 mm from the source. An ideal detector was assumed (i.e. sensitivity assumed independent of position and angle of incidence).

4.3.5 Wedge subtraction method

In principle, most scattered photons are assumed to be rejected since they exit the turbid medium with an angle greater than the acceptance angle of the AFA. Yet, as discussed earlier in this paper, there is always a group of multiply scattered photons with trajectories that are within the acceptance angle of the AFA, because of the spherically uniform distribution of scattered photons in the turbid media (see trajectory #5 in Figure 4-1(a)). The analytical descriptions of the leaked scattered photons are described in [4-23]. Experiments have shown that by slight deviation of the laser beam (shown in Figure 4-2(c)) by $\sim 2 - 3\times$ the AFA acceptance angle, approximately the same amount of scattered light can pass through the AFA while the ballistic and quasi-ballistic photons will be rejected by the micro-channels [4-23]. Consequently, an ADI image collected using a deviated light source will contain mostly scattered photons with good pixel by pixel correspondence with the original scan collected without the wedge prism. Deviation of the source beam can be implemented by introducing an optical wedge prism into the light path prior entering the sample. This methodology enabled us to estimate the proportion of quasi-ballistic photons that provided the image building signal to the proportion of scattered photons that

represented the background leakage for each of the AFA designs. A wedge prism with a 1° deviation specification was used to redirect the collimated line of light out of the plane of the AFA. Wedge subtracted images were computed by subtracting the background scattered light image (with wedge prism inserted in to the light path) from the image of the same sample collected without the wedge prism. The resultant wedge subtracted image had enhanced contrast on a pixel by pixel basis.

4.3.6 Angular domain imaging (CW) setup

To test the different AFA designs, a continuous wave ADI system was constructed based on earlier work [4-18, 4-29]. Briefly, an 808 nm laser diode housed in a 9 mm package (L808P1WJ, Thorlabs, NJ, USA) was used for illumination. The emission area of the laser diode was $100\ \mu\text{m}$ wide and approximately $1\ \mu\text{m}$ tall. The emitted laser beam had asymmetry and high angular divergence along both axes. The beam was transformed into a collimated thin line of light using a beam shaping system with the ability to correct the strong divergence. It consisted of an aspheric-cylindrical lens system to correct both horizontal and vertical divergence [4-18, 4-29]. Each AFA was precisely aligned to the collimated line of light from the laser source using a 6-axis positioner. A high resolution CMOS camera (1280×1024 pixel) with square pixels ($5.2\ \mu\text{m} \times 5.2\ \mu\text{m}$; i.e. smaller than the micro-channel aperture) was positioned directly behind the AFA. As shown in Figure 4-1 (b), the ADI system was used to image a turbid sample that contained a resolution target. The sample was placed on a computer-controlled vertical z-axis stage between the

output of the beam shaping system and the AFA. Repeated ADI scans at a sequential series of sample heights provided a 2D image of the turbid sample.

4.3.7 Time-angular domain imaging system setup

To test the effect of time-gating in combination with an AFA, a time-angular domain imaging (TADI) system was designed and assembled. The optical layout was similar to the CW ADI system, but the TADI system included a pulsed laser for illumination and a gated camera for detection (Figure 4-2(b)). The laser emitted pulses at 780 nm with a pulse duration of 100 ps (FWHM) and a repetition rate of 80 MHz (PicoTA, PicoQuant GmbH and TOPTICA Photonics). A spectral filter [$\lambda=780\pm 5$ nm] was used to block the background emission caused by the laser amplifier system. The beam was shaped into a uniform line of light using a cylindrical-spherical-cylindrical lens collimation system [4-33]. While the majority of existing time-domain systems utilize a Kerr gate or a streak camera [4-13], we had available an ultra-fast gated camera (PicoStar HR, LaVision) for image capture. The camera incorporated a micro-channel plate (MCP) controlled via a high rate imager (HRI, Kentech Instruments, Oxfordshire, UK). Gating of the MCP was achieved by applying a pulsed negative voltage across a photocathode in front of the MCP. The gate width was controlled using an ultra-short pulse generated by the HRI, with nominal gate width settings from 200 to 1000 ps. The output of the MCP was coupled to a 12-bit CCD camera (1370 × 1040 pixels). The MCP operated as a very fast shutter that was synchronized to the incoming laser pulses. Synchronization was facilitated by an electronic delay unit (Delay Unit, LaVision, Germany) between the output

synchronization signal from the PicoTA laser controller and the input trigger on the HRI. The delay time (T_d) on the delay unit could be adjusted with a resolution of 5 ps. With the MCP operating in “comb” mode, a sequence of gated transmission images accumulated on the CCD during each camera exposure (typically 0.1 – 10 s depending on transmitted light intensity). Overall camera operation including the setup of the delay time, camera exposure time, and image capture and display was performed using camera acquisition software (DaVis, LaVision). The system enabled a parallel and temporally resolved detection of the light emitted from all micro-channels of the AFA. To record the Temporal Point Spread Function (TPSF) of the detected photons from sample, the delay was scanned electronically, typically in 15-ps steps.

Since the laser pulse duration was of similar to the camera gate width, we evaluated the effect of laser pulse width on the performance of the TADI system. Results from the ps TADI system were compared to preliminary findings from a femtosecond TADI system assembled with a fiber-based pulsed laser (Femtolite Ultra CX-20, IMRA America, Inc.). Since the fiber-based system had much shorter pulse duration of 100 fs (pulse repetition rate of 50 MHz and average power of 20 mW), the effects of laser pulse duration did not convolve with the camera response function. A more detailed description of the fs TADI system is presented in a recent proceedings article [4-1].

4.3.8 Image analysis

The image contrast of specific ADI scans was quantified using an image contrast ratio metric based on the following formula:

$$\text{Contrast Ratio } [\%] = \frac{\text{mean}(I_{\max}) - \text{mean}(I_{\min})}{\text{mean}(I_{\max}) + \text{mean}(I_{\min})} \times 100 \quad 4-3$$

where I_{\min} was the average light intensity corresponding to the shadowed region (i.e. due to the shadow of the L-shape target within the phantom) and I_{\max} was the average light intensity corresponding to a non-shadowed area nearby the L-shaped structure.

4.4 Results and discussion

4.4.1 Ray trace analysis of AFA geometries

The results of the simple optical ray trace analysis based on the Fresnel Law (Eq. 4-1 and Eq. 4-2) are reported in Figure 4-3. For the source nearby (2 mm) the entrance aperture of the AFA (AFA-60-1), the normalized transmittance decreased in a stepwise manner as the trajectory of the incoming photons deviated from the central axis of the micro-channel (see Figure 4-3(a)). The stepwise response was due to the occurrence of reflections off of the micro-channel walls before the photons exited the AFA. When the source was far (5 mm) from the entrance aperture of the AFA, the acceptance angle of the AFA provided for, at most, a single reflection off of the micro-channel side walls before the photon exited the AFA (Figure 4-3(b)) and hence only a single step was observed. For both source positions, the normalized transmittance was not constant between steps, but decreased monotonically in accordance with the Fresnel Law as the incident angle increased. Table 4-1 summarizes the reflected light intensity parameters for three different AFA geometries for the acceptance angle (θ_a), where the first reflection occurs and the blocking angle

(θ_b), above which the AFA is 100% effective (for this simplified model off-axis sources are not considered). Even though the AFA-20-1 placed 2 mm from the point source had the smallest acceptance angle it could still accept photons with trajectories up to 5× the acceptance angle, which included photons that experienced one or more channel wall reflections. The normalized transmitted light intensity near the acceptance angle was about 0.993 due to a single reflection off of the silicon micro-channel wall at the shallowest angle of incidence. The normalized transmitted light intensity was reduced to 0.885 when the trajectories of photons were near the blocking angle. The proportion of photons experiencing one or more reflections was 82.6% of the total number of photons entering the AFA micro-channel aperture. When the AFA-20-1 was placed 5 mm from the source, both the acceptance angle (θ_a) and blocking angle (θ_b) decreased resulting in shallower angles of incidence for reflected photons and overall lower reflection loss. The improved transmission characteristics for the AFA-20-1 observing the distant source were also due in part to the smaller proportion of reflected photons for a given number of photons entering the micro-channel (66.4%). This overall behaviour was also observed for the AFA-40-1 and AFA-60-1 devices, but the proportion of photons experiencing at least one reflection decreased only minimally as the micro-channel aperture increased. Therefore, a large portion of photons with trajectory angles greater than the acceptance angle of the AFA are expected to leak through the AFA to the detector for all devices with smooth micro-channel walls. Therefore, improvements in AFA performance can only be realized by minimizing micro-

channel wall reflections to ensure that all photons exiting the AFA have been angularly filtered according to the AFA geometry.

4.4.2 Micro-channel wall reflection suppression with reflection-trapped AFAs

In an independent set of experiments, we tested 4 AFA devices with square-shaped openings each with a different combination of aspect ratio and micro-channel wall patterning. We used the trans-illumination ADI (CW) to collect scans of a 2-cm path length optical cuvette filled with 0.3% Intralipid™ (diode laser with $\lambda = 780$ nm). An L-shaped resolution target placed at the midpoint to the cuvette and image analysis as described in the methods was used to assess image contrast. For the conventional AFA devices, an increase in image contrast ratio from 16% (AFA-60-1) to 20% (AFA-60-1.5) was measured as the aspect ratio increased. As shown in Table 4-2, a similar relative improvement in contrast ratio was observed for the reflection trapped AFAs, i.e. RTAFA-60-1.5 to RTAFA-80-1.5. However, the RTAFAs had considerably better performance in terms of contrast ratio than the conventional AFAs for a constant aspect ratio. For example, the contrast ratio for images obtained with the RTAFA-60-1.5 was 31% compared to only 20% for the AFA-60-1.5. Regardless of AFA type, the highest image contrast ratio (34%) was observed for the RTAFA-80-1.5 device, which had an acceptance angle of $\{0.30^\circ - 0.42^\circ\}$. These results suggest that by employing RTAFA, the effective angular acceptance of each micro-channel approaches the acceptance angle related to the physical geometry of channel opening and the channel length, which leads to improved performance compared

to a conventional AFA of similar dimensions, where the channel walls are reflective, leading to higher effective acceptance angles and poorer performance due to transmission of a greater number of unwanted scattered photons.

4.4.3 Background suppression by wedge subtraction for various AFA geometries

Figure 4-4 shows ADI scans obtained with four AFA devices each of unique geometry. The turbid sample was used for testing and consisted of a 1 cm path length optical cuvette filled with 0.7% Intralipid™ (diode laser with $\lambda = 808$ nm). With the L-shape resolution target placed at the midpoint along the optical path. The ADI scans in Figure 4-4 (a) – (d) show the intrinsic image contrast differences when the acceptance angle ranged from 0.11° to 0.48° . It is qualitatively apparent that the ADI scans suffered from low image contrast due to the fact that the images were formed by both quasi-ballistic light and background scattered light. As discussed in our previous work [4-23], one way to account for the background scattered light leakage through the AFA is to deviate the light source out of the acceptance angle of the AFA.

Table 4-2. Effect of channel wall reflection reduction by using RTAFA in resulted ADI image contrast measurements, (through scattering medium with $\mu'_s l (MPF) = 6$)

	<i>AFA channel wall</i>	<i>Aspect ratio</i>	<i>CR (ADI)</i>
AFA-60-1	Not-pattered	167:1	16%
AFA-60-1.5	Not-pattered	250:1	20%
RTAFA-60-1.5	Patterned	250:1	31%
RTAFA-80-1.5	Patterned	187:1	34%

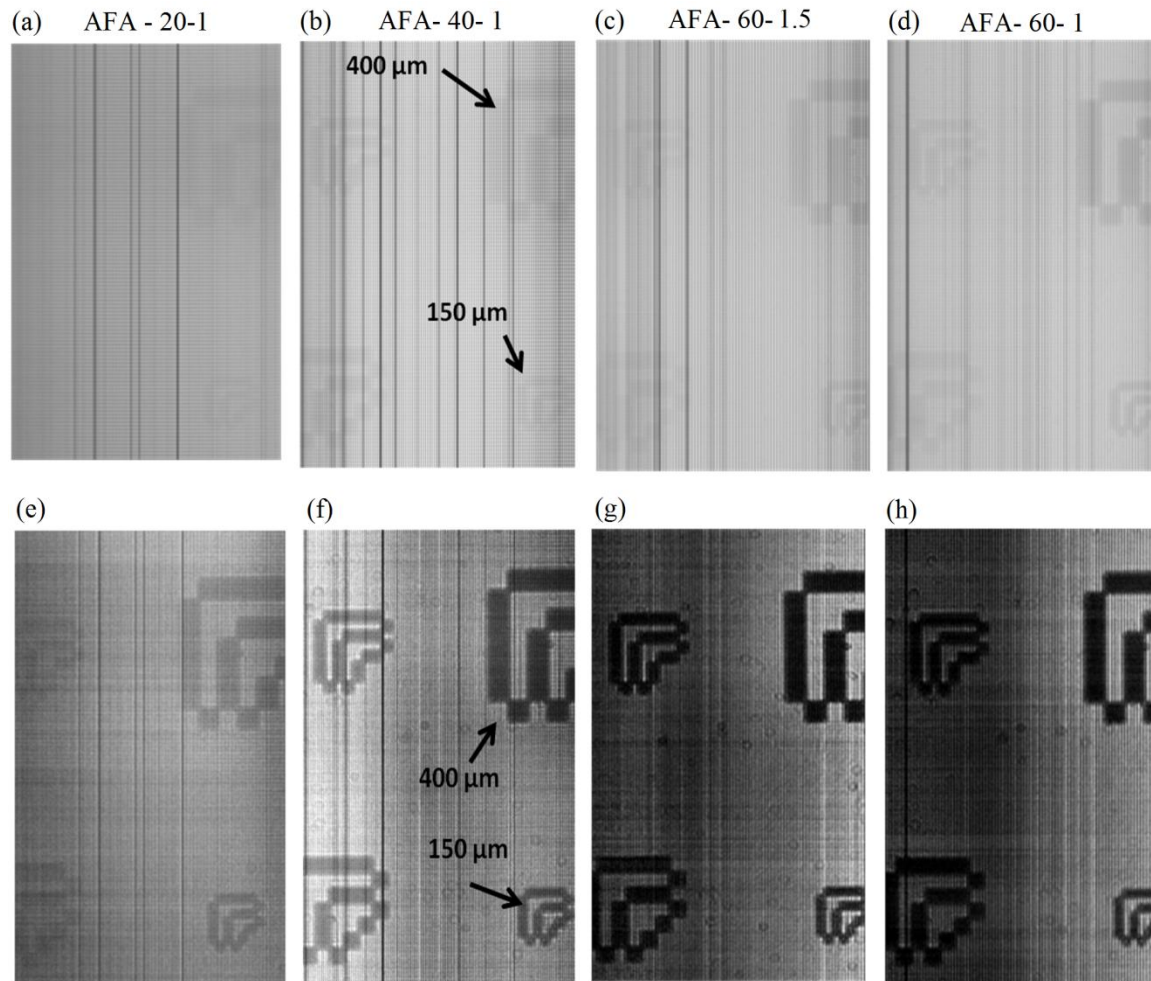


Figure 4-4. ADI scan results in turbid media (Intralipid™) with $\mu'_s/l = 7$ using four different AFA geometries (a) – (d). Contrast-enhanced images using the wedge technique for background scattered light estimation and subtraction (e)- (h).

With this method, the background scattered light can be estimated and subtracted on a pixel by pixel basis from the ADI scan with collimated light. Applying this method to the images in Figure 4-4(a) - (d), we estimated and subtracted the background scattered light for each ADI image. The resultant images are shown in Figure 4-4 (e) – (h) and had much improved image contrast

(compare the ADI scans of Figure 4-4 (e) – (h) to Figure 4-4 (a) – (d), respectively).

Table 4-3. Summary of the ADI contrast experimental measurements for different AFA geometries, (through scattering medium with $\mu'_s l = 6$, $L_1 = 5$ mm)

	<i>Acceptance angle (α)</i>	<i>CR%_(ADI)</i>	<i>CR%_(ADI-WS)</i>	<i>CR%_(ADI-WS)/CR%_(ADI)</i>
AFA-20-1	{0.11° - 0.16°}	4.1	19	4.5
AFA-40-1	{0.22° - 0.32°}	8.3	73	8.9
AFA-60-1.5	{0.22° - 0.32°}	8.3	83	10
AFA-60-1	{0.34° - 0.48°}	12	83	6.7

Quantitative contrast estimates from the ADI scans supported the qualitative analysis. The contrast estimates corresponding to Figure 4-4 are presented in Table 4-3. The poorest contrast (~4.0%) was obtained from the ADI scan where the AFA (AFA-20-1) with an acceptance angle range of {0.11° - 0.16°} was used. The image contrast increased (up to ~ 8.3%) for ADI scans collected with the AFA devices AFA-40-1 and AFA-60-1.5, which had an intermediate acceptance angle {0.22° - 0.32°}. ADI scans collected with the AFA-60-1 device that had the highest acceptance angle {0.34° - 0.48°} had the highest image contrast (~12.3%).

The wedge-subtracted ADI images shown in Figure 4-4(e) – (h) show an image contrast improvement of about 4.5 times for the device with an acceptance angle of {0.11° - 0.16°}, 8.8-10 times for the two devices with acceptance angles of {0.22° - 0.32°}, and about 6.7 times for the device with the highest acceptance angle {0.36° - 0.48°}. Since we were using a wedge prism with angular deviation

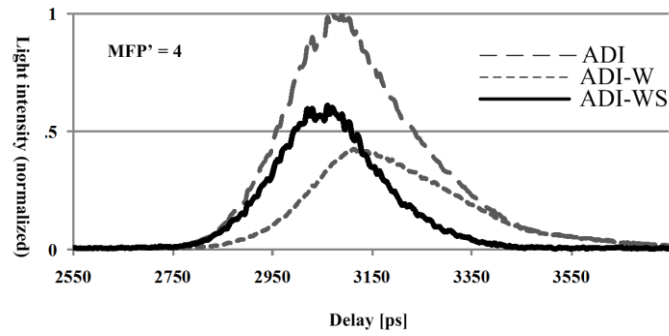
of 1° , it may not be optimal for the AFA-60-1 device, where the acceptance angle permitted quasi-ballistic photons to leak through to the detector.

The experimental results indicated that the larger aperture size from 20 μm to 60 μm allowed higher numbers of quasi-ballistic photons to be accepted by AFA, which resulted in higher contrast ratios. Also, longer arrays resulted in increased image contrast. In the context of our modeling analysis, this was expected since photons outside the acceptance angle experienced a greater number of reflections and hence they were attenuated to a larger degree before reaching the detector. A similar improvement in image contrast was observed for longer RTAFAs as shown in Table 4-2.

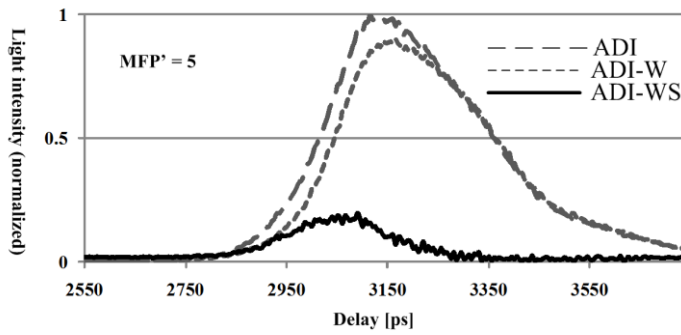
From the Monte Carlo analysis on the AFA geometry, it has been shown that the AFA operates more effectively when the the channel opening size is decreased and the channel length is increased (with the caveat that the the geometry does not introduce diffraction issues). Consistent with the Monte Carlo analysis, we observed experimentally that longer micro-channels improve the ADI image contrast. However, the experimental analysis showed that larger AFA opening sizes (until 80 μm) resulted in better image contrast, which was inconsistent with the Monte Carlo results. Although one might consider using even larger channel openings, the spatial resolution (3 lppm; $\sim 160 \mu\text{m}$ line and space widths) begins to degrade for openings larger than 80 μm . The channel opening also should be chosen to compensate for experimental limitations such as low light intensities due to source limitations and permissible exposure limits.

4.4.4 Background suppression by time-angular domain imaging

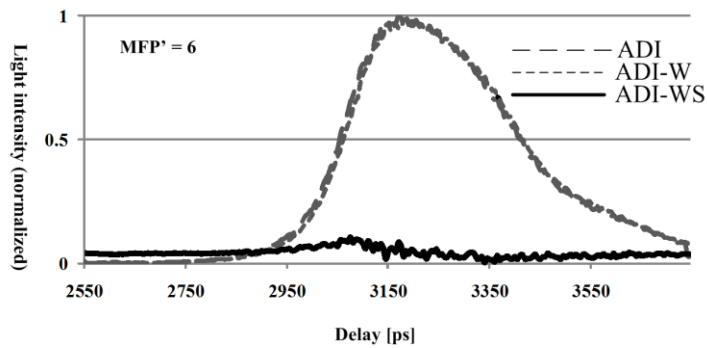
Figure 4-5 shows time-resolved measurements from the TADI system using the AFA-60-1 device with and without wedge prism (ADI-W and ADI) at different scattering levels. The measured temporal response in each case was broadened due to the presence of late arriving scattered photons. This was in contrast to the temporal response computed by the wedge subtraction method, which was primarily confined to early arrival times representative of quasi-ballistic photons. As shown in Figure 4-5, the proportion of ballistic/quasi-ballistic photons relative to the total photons detected through the AFA was measurable by the temporal profile peak intensity of ADI with wedge subtraction (ADI-WS) compared to ADI case. At lower scattering levels such as $\mu'_s l = 4$ more than 60% of the detected photons were quasi-ballistic. The contribution of quasi-ballistic photons diminished to 20% at $\mu'_s l = 5$ and less than 10% at the detection limit ($\mu'_s l = 6$).



(a)



(b)



(c)

Figure 4-5. Temporal profiles of transmitted light obtained in time-resolved measurements using Picostar camera (250 ps temporal gate width): (a) through scattering medium with 2 cm optical cuvette filled with 0.2% Intralipid™ at $\lambda = 780$ nm, (b) 0.25% Intralipid™, and (c) 0.3% Intralipid™.

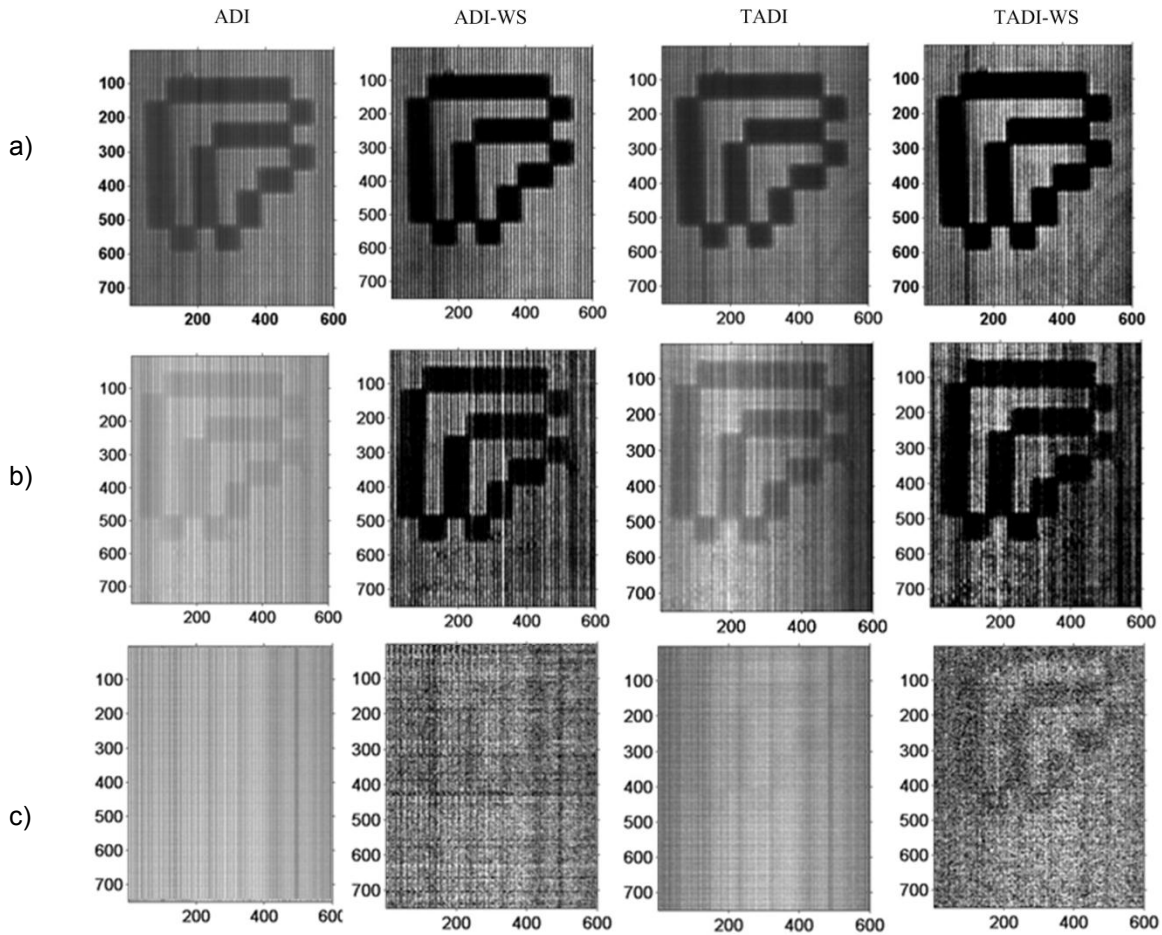


Figure 4-6. ADI and TADI scanning results (using AFA-60-1) of a 350 μm L-shape resolution target at the middle of a turbid medium with and without wedge subtraction procedure at different scattering levels: (a) through scattering medium with 2 cm optical cuvette filled with 0.25% Intralipid™ at $\lambda = 780 \text{ nm}$, (b) 0.3% Intralipid™, and (c) 0.35% Intralipid™.

In an attempt to push the ADI detection limit beyond $\mu'_s l = 6$, the ultrafast gated CCD camera with temporal gate width of 250 ps was used for temporal discrimination of photons exiting the AFA. Figure 4-6 shows the image results for TADI versus ADI with and without the wedge subtraction method. The images are of an L-shaped resolution target with lines and spaces of 350 μm placed at the mid-point of a 2 cm optical path length cuvette filled with Intralipid™ solution

at scattering levels from $\mu'_s l = 5$ to $\mu'_s l = 7$. The range of scattering levels was chosen to bracket the scattering level representative of the ADI detection limit. Scattered light rejection was evaluated using the wedge subtraction method for both angular (ADI-WS) and time-angular (TADI-WS) filtration. The image contrast values computed for the images in Figure 4-6 are tabulated for each scattering level (Table 4-4). Our measurements indicated that the image contrast ratio increased by 10-15% for TADI alone, which was less than the image contrast increases observed with ADI wedge subtraction method. However both time gating and wedge subtraction provided resulted in detectable contrast beyond the ADI detection limit to $\mu'_s l = 7$ with an image contrast ratio of 25%. At the 250 ps time gate width, non-scattered light can travel up to 5.5 cm, which is much greater than the sample thickness of 2 cm. Therefore, image contrast with TADI under these conditions is expected to be sub-optimal since scattered photons with paths up to 5.5 cm will be accepted by the camera. A faster camera, such as a streak camera with a gate width of 50 ps could lead to more efficient time-gated filtration compared to the PicoStar camera.

Table 4-4. Summary contrast ratio measurements using AFA-60-1 in ADI and TADI methods with wedge subtraction

Intralipid™ concentrations	<i>CR%</i> (ADI)	<i>CR%</i> (ADI-WS)	<i>CR%</i> (TADI)	<i>CR%</i> (TADI-WS)
0.25%	45.16	92.98	57.89	93.55
0.30%	12.34	81.43	23.61	84.62
0.35%	N/A	10.15	5.26	25

We also investigated TADI implemented with a fs pulsed laser (Femtolite Ultra CX-20, IMRA America, Inc.) and compared performance to ADI alone. More description of the system setup can be found in [4-37].

Figure 4-7 shows the temporal scan of the trans-illuminated signal from a 2 cm optical path cuvette as a function of the scattering level of the medium using TADI. The temporal gate width of the camera system was 250 ps. We discovered that the beam from the Femtolite had poorer far field collimation properties compared to the ps pulsed laser (PicoTA), which had a negative impact on ADI performance. However, the image contrast improvement by the combination of time and angular gating was noticeable. Figure 4-7 shows the image contrast variation of TADI system as a function of the camera gate width. The image contrast analysis was conducted at two scattering levels; 0.25% Intralipid™ with $\mu'_s = 2.5 \text{ cm}^{-1}$, and $\mu_a = 0.01 \text{ cm}^{-1}$ ($\text{MFP}' = 5$) which was below the detection limit of ADI and 0.3% Intralipid™ solution with $\mu'_s = 3 \text{ cm}^{-1}$, and $\mu_a = 0.01 \text{ cm}^{-1}$ in a 2 cm optical length sample ($\text{MFP}' = 6$). For the 0.25% Intralipid™ solution, the image contrast increased from 24% in ADI measurements up to 68% in TADI at the earliest possible time gate measurement using a gate width of 250 ps. While for the 0.3% Intralipid™ solution, the image contrast increased from 3% (about the noise level) in ADI measurements up to 34% at the earliest possible time gate measurement. Hence, the time-resolved ADI measurement showed an image contrast enhancement from 4% to 34% compared to TADI at 0.3% Intralipid™ solution, which represents a greater than 8 times improvement in image contrast compared to ADI alone.

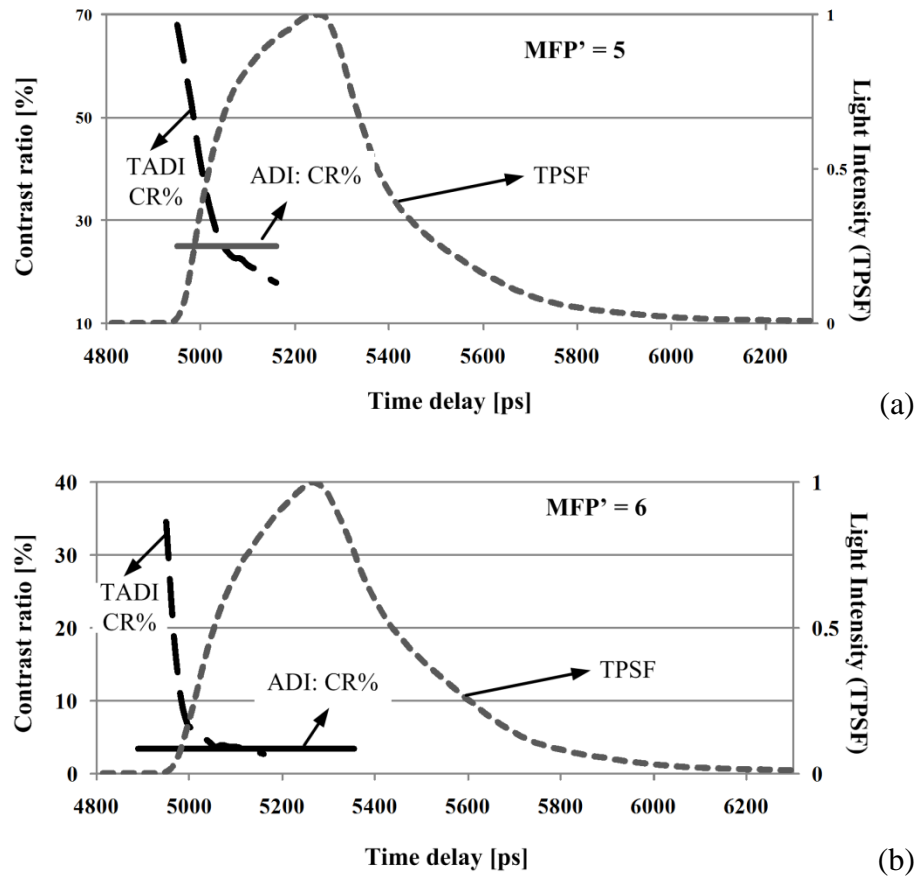


Figure 4-7. TADI image contrast as a function of gate delay and scattering level of (a) through scattering medium with 2 cm optical cuvette filled with 0.25% Intralipid™ at $\lambda = 780$ nm, (b) 0.3% Intralipid™, using femtosecond pulsed laser.

4.4.5 Implications of scattering level to scan time

Since the AFA devices had a limited vertical field of view and required vertical scanning to acquire 2-dimensional images, acquisition time was lengthy. The scanning procedure was mainly limited by the camera exposure time and the communication between the computer and translation stage. The camera exposure time was dependent on the scattering level, and laser power. For instance, in order to form an ADI scan at scattering level of equivalent to six

times reduced mean free path (Figure 4-4 (a)-(d)), the laser power was increased to 350 mW (collimation reduced the effective power that reached the sample) and the camera exposure time for each scan line was lengthened to 30 ms, 15 ms, and 10 ms while employing the AFAs with the opening size of $20\ \mu\text{m} \times 20\ \mu\text{m}$, $40\ \mu\text{m} \times 40\ \mu\text{m}$, and $60\ \mu\text{m} \times 60\ \mu\text{m}$, respectively. However, in the practical implementation, data communication increased the time for one line scan to approximately one second, resulting in ADI scans as shown in Figure 4-4 that took approximately 5 min (300 steps) to collect. Therefore, in the limiting case where data transfer from camera to computer is minimized, lower laser power and/or faster scanning times will be achieved by using an AFA with a larger acceptance angle.

4.5 Conclusion

In this paper, we experimentally characterized the angular distribution and proportion of minimally deviated quasi-ballistic photons versus multiply scattered photons in a turbid medium. The measurements were made using an angular domain imaging system in trans-illumination mode that employed different design of silicon micro-machined angular filter arrays each with a different range of acceptance angles. The balance between quasi-ballistic photons and unwanted multiply scattered photons accepted by the micro-machined angular filters was measured in order to determine the optimum range of acceptance angles for the system.

A reflection trapped angular filter array design was fabricated, tested, and compared to a conventional angular filter array design. The RTAFA resulted in a

50% increase in ADI image contrast compared to the non-reflection trapped AFA design. The effect of time-gating on the angular domain imaging method was also investigated. Time-resolved ADI scans of targets within turbid samples were captured with an ultra fast gated ICCD camera system. The scan results indicated that TADI with a 250 ps temporal gate width provided some image contrast improvement compared to ADI alone. The effect of wedge subtraction method in combination with TADI on image contrast was examined. TADI with wedge subtraction gave the greatest improvement in image contrast which was more than seven times larger than the result obtained with ADI alone for $\mu'_s l = 6$. The enhancements to ADI offered by RTAFA devices, time-gating, and wedge subtraction methodology have lead to measurable and significant improvements in image contrast for targets at depth in turbid samples. These enhancements provide flexibility when performing ADI imaging. They can either be utilized to reduce ADI scan time to achieve an image contrast comparable to standard ADI methodology, or they can be implemented alone or in combination to improve image contrast well beyond standard ADI methodology.

In conclusion, the angular filter method offered efficient scattered light suppression with moderate levels of scattering (i.e. ~5-6 mm soft tissue thickness). One interesting possibility for future work is to employ the filtration properties of the AFA to hyperspectral imaging (i.e. pushbroom setup) to provide a means to display differences in image contrast between different tissues based on their optical absorption/scattering differences in the near infrared spectral band.

4.6 Acknowledgment

This project was funded by grants from the Natural Sciences and Engineering Research Council of Canada (NSERC) to B. Kaminska and J. J. L. Carson and by a Small Grant for Cancer Research and Training from the London Regional Cancer Program (LRCP) to K. Jordan, J. J. L. Carson and B. Kaminska. F. Vasefi was supported by a LRCP Translational Breast Cancer Research Trainee Studentship.

4.7 References

- 4-1 F. Fabbri, M. A. Franceschini, and S. Fantini, "Characterization of spatial and temporal variations in the optical properties of tissuelike media with diffuse reflectance imaging," *Appl. Opt.*, 42(16), 3063-3072 (2003).
- 4-2 F. Fercher, "Optical coherence tomography-principles and applications," *Reports on Progress in Physics*, 66, 239-303 (2003).
- 4-3 J. G. Fujimoto, "Optical coherence tomography," *Comptes Rendus De l'Academie Des Sciences, Serie IV (Physique, Astrophysique)*, 2, 1099-111 (2001).
- 4-4 O. L. Muskens, A. Lagendijk, "Broadband enhanced backscattering spectroscopy of strongly scattering media," *Opt. Express*, 16(2), 1222-1231 (2008).
- 4-5 D. A. Benaron and D. K. Stevenson, "Optical time-of-flight and absorbance imaging in biologic media," *Science* 259, 1463–1466 (1993).
- 4-6 V. Ntziachristos, J. Ripoll, L. V. Wang, and R. Weissleder, "Looking and listening to light: the evolution of whole-body photonic imaging," *Nat. Biotechnol.* 23, 313-320 (2005).
- 4-7 L. Wang, P. P. Ho, C. Liu, G. Zhang, and R. R. Alfano, "Ballistic 2-D imaging through scattering wall using an ultrafast Kerr gate," *Science* 253, 769–771 (1991).
- 4-8 M. Kono, H. Ueki, and S. Umemura, "Near-infrared finger vein patterns for personal authentication," *Appl. Opt.* 41, 7429–7434 (2002).

- 4-9 W. H. Yong, P. V. Butte, B. K. Pikul, J. A. Jo, Q. Fang, T. Papaioannou, K. Black, and L. Marcu, "Distinction of brain tissue, low grade and high grade glioma with time-resolved fluorescence spectroscopy," *Front. Biosci.* 11, 1255–1263 (2006).
- 4-10 S. K. Gayen, M. Alrubaiee, M. E. Zevallos, and R. R. Alfano, "Temporally and spectrally resolved optical imaging of normal and cancerous human breast tissues" *Proceedings of Inter-Institute Workshop on In Vivo Optical Imaging at the NIH*, 142–147 (2000).
- 4-11 K. Takagi, Y. Kato, and K. Shimizu, "Extraction of near-axis scattered light for transillumination imaging," *Appl. Opt.* 48, D36-D44 (2009)
- 4-12 K. Takagi, H. Kakinuma, Y. Kato, and Koichi Shimizu, "CW transillumination imaging by extracting weakly scattered light from strongly diffused light," *Opt. Express* 17, 8332-8342 (2009)
- 4-13 K. M. Yoo, B. B. Das, and R. R. Alfano, "Imaging of a translucent object hidden in a highly scattering medium from the early portion of the diffuse component of a transmitted ultrafast laser pulse" *Opt. Lett.* 17, 958 (1992).
- 4-14 L. Wang, X. Liang, P. Galland, P. P. Ho, and R. R. Alfano, "True scattering coefficients of turbid matter measured by early-time gating," *Opt. Lett.* 20, 913 (1995).
- 4-15 H. Wang, C. Sun, Y. Wang, Y. Kiang, and C. C. Yang, "Determination of the depth of a scattering target in a turbid medium with polarization discrimination of transmitted signals," *Opt. Lett.* 28, 25-27 (2003)
- 4-16 H. Horinaka, K. Hashimoto, K. Wada, Y. Cho, and M. Osawa, "Extraction of quasi-straightforward-propagating photons from diffused light transmitting through a scattering medium by polarization modulation," *Opt. Lett.* 20, 1501-1503 (1995)
- 4-17 S. P. Schilders, X. S. Gan, and M. Gu, "Microscopic imaging through a turbid medium by use of annular objectives for angle gating," *Appl. Opt.* 37, 5320 (1998).
- 4-18 F. Vasefi, B. Kaminska, P. K. Y. Chan, and G. H. Chapman, "Multi-spectral angular domain optical imaging in biological tissues using diode laser sources," *Opt. Express* 16, 14456-14468 (2008)
- 4-19 L. Wang, P. P. Ho, and R. R. Alfano, "Time-resolved Fourier spectrum and imaging in highly scattering media," *Appl. Opt.* 32, 5043 (1993).
- 4-20 X. Liang, L. Wang, P. P. Ho, and R. R. Alfano, "Time-resolved polarization shadowgrams in turbid media," *Appl. Opt.* 36, 2984-2989 (1997)

- 4-21 C. Yang, Chia-Wei Sun, Cheng-Kuan Lee, Chih-Wei Lu, Meng-Tsan Tsai, C. Yang, and Yean-Woei Kiang, "Comparisons of the transmitted signals of time, aperture, and angle gating in biological tissues and a phantom," *Opt. Express* 12, 1157-1168 (2004)
- 4-22 X. Gan, S. Schilders, and M. Gu, "Combination of annular aperture and polarization gating methods for efficient microscopic imaging through a turbid medium: theoretical analysis," *Microsc. Microanal.* 3, 495–503 (1997).
- 4-23 F. Vasefi, B. Kaminska, G. H. Chapman, and J. J. Carson, "Image contrast enhancement in angular domain optical imaging of turbid media," *Opt. Express* 16, 21492-21504 (2008)
- 4-24 G. H. Chapman, M. Trinh, N. Pfeiffer, G. Chu, and D. Lee, "Angular Domain Imaging of Objects Within Highly Scattering Media Using Silicon Micromachined Collimating Arrays," *IEEE J. Sel. Top. Quantum Electron.* 9, 257-266 (2003).
- 4-25 N. Pfeiffer, P.K.Y. Chan, G. H. Chapman, F. Vasefi, and B. Kaminska, "Optical imaging of structures within highly scattering material using a lens and aperture to form a spatiofrequency filter" *Proceedings of SPIE* , 6854, 68541D (2008).
- 4-26 L. V. Wang, H. Wu, "Biomedical Optics: Principles and Imaging", Ch. 8, John Wiley and Sons, Hoboken, NJ (2007).
- 4-27 F. Vasefi, P.K.Y. Chan, B. Kaminska, G. H. Chapman, N. Pfeiffer, "An Optical Imaging Technique Using Deep Illumination in the Angular Domain," *IEEE J. Sel. Top. Quantum Electron.* 13, 1610-1620 (2007).
- 4-28 F. Vasefi, M. Belton, B. Kaminska, G. H. Chapman, and J. J. L. Carson, "Angular domain fluorescence imaging for small animal research", *J. Biomed. Opt.* 15, 016023 (2010)
- 4-29 P. K. Y. Chan, F. Vasefi, G. H. Chapman, B. Kaminska, N. Pfeiffer, "Multispectral angular domain optical tomography in scattering media with argon and diode laser sources" *Proceedings of SPIE Vol. 6435*, 64350M. (2007)
- 4-30 S.T. Flock, S.L. Jacques, B.C. Wilson, W.M. Star, M.J.C. van Gemert, "Optical Properties of Intralipid: A phantom medium for light propagation studies," *Lasers in Surgery and Medicine* 12, 510-519 (1992).
- 4-31 H.G. van Staveren, C.J.M. Moes, J. Marle, S.A. Prahl, M.J.C. van Gemert, "Light scattering in Intralipid-10% in the wavelength range of 400-1100 nanometers," *Applied Optics* , 30, 4507-4514 (1991).

- 4-32 F. Vasefi, B. Kaminska, G.H. Chapman, J.J.L. Carson, "Angular distribution of quasi-ballistic light measured through media using angular domain optical imaging", Proc. of SPIE Vol. 7175 (2009).
- 4-33 G. H. Chapman, J. Rao, T. C. K. Liu, P. K. Y. Chan, F. Vasefi, B. Kaminska, and N. Pfeiffer, "Enhanced angular domain imaging in turbid media using Gaussian line illumination" in Proceedings of SPIE Vol. 6084, 60841D (2006).
- 4-34 F. Vasefi, P. K. Y. Chan, B. Kaminska, G. H. Chapman, "Subsurface Bioimaging using Angular Domain Optical Backscattering Illumination," 28th Annual International Conference of the IEEE Engineering in Medicine and Biology Society, EMBS 2006. 1932-1936. (2006)
- 4-35 F. Vasefi, B.S.L. Hung, B. Kaminska, G.H. Chapman, J.J.L. Carson, "Angular domain optical imaging of turbid media using enhanced micro-tunnel filter arrays" in Proceedings of SPIE 7369, 73691N (2009).
- 4-36 E. Hecht, Optics. ,4th ed .San Francisco ; London: Addison-Wesley, pp. 698 (2002).
- 4-37 F. Vasefi, E. Ng, B. Kaminska, G. H. Chapman, J. J. L. Carson, "Effect of time gating and polarization discrimination of propagating light in turbid media during angular domain imaging (ADI)" in Proceedings of SPIE 7182, 718217 (2009).

5: AN OPTICAL IMAGING TECHNIQUE USING DEEP ILLUMINATION IN THE ANGULAR DOMAIN⁴

5.1 Abstract

This paper describes a novel optical imaging method, deep illumination Angular Domain Imaging (ADI), for detecting micron-scale objects within highly scattering media. The new optical imaging is a much simpler and less expensive solution compared to other available optical imaging techniques. In principle, deep illumination ADI uses collimation detection capabilities of small acceptance angle devices to extract photons emitted from the scattered light created by a laser source aimed deep beneath the turbid medium surface. The laser source forms an illumination-ball within the medium that emits scattered light in all directions and illuminates objects near the surface from behind. Consequently, when photons from this illumination-ball pass an object and reach the angular filter, light that is not subsequently scattered passes through to a camera detector, whereas scattered photons are rejected by the filter. Image results obtained are recorded for different phantom locations, phantom sizes, and medium scattering levels. Our images clearly display sub-204 μm phantoms when placed three millimetres deep within a test scattering medium with total effective attenuation coefficient (μ'_{eff}) up to 5.8 cm^{-1} or 2.5 mm deep in chicken

⁴ The following chapter has been published in IEEE Journal of Selected Topics in Quantum Electronics. 13(6): 1610-1620 (2007) under the co-authorship of P.K.Y. Chan, B. Kaminska, G.H. Chapman, and N. Pfeiffer.

tissue tests. Preliminary digital image processing shows the image contrast enhancement and the definition improvement.

5.2 Introduction

Medical imaging is focused on obtaining the internal structure of living subjects. The most often used is X-ray imaging which gave rise to Computerized Axial Tomography (CAT), a method which uses a series of images to reconstruct a 3D cross-section of the subject. However, X-ray imaging has some limitations, which include disruption of the chemical structure of living tissues, causing tissue damage and increasing cancer risks proportionate to the cumulative dose of radiation applied [5-1]. The attractive alternative of non-ionizing radiation imaging has consequently been of high interest, including such modalities as ultrasound (acoustic wavelengths), Magnetic Resonance Imaging (MRI - radio wavelengths), and optical imaging (visible and infrared light).

The optical methods are of interest because biological tissues with irregular physiological activities have different tissue compositions, which may present themselves in the form of differing optical absorption and scattering characteristics [5-1]. In general, this difference in optical property occurs far earlier than the other macro-indications, such as tissue mechanical properties.

Other researchers have found that the average scattering size between tumorigenic cells and nontumorigenic cells induces different tissue scattering properties [5-2, 5-3]. Currently, the optical properties and differences of oxygenated and de-oxygenated blood are appropriately characterized by light in

the red and near infrared spectrum. In addition, an increase in blood supply can be a major indication of the rapid cancer cell growth [5-4]. Also, malignant tissue usually has larger absorption coefficient than normal tissue due to its higher blood content [5-5]. Consequently, optical detection of the abnormalities can be considered sensitive enough for early detection of various kinds of cancers.

A major challenge faced by optical imaging in biological tissue is tissue's high level of scattering. In highly scattering media, the majority of the photons follow random-walk trajectories. This makes image-carrying photon detection more difficult than most other medical imaging modalities such as X-ray, in which the photons penetrate the tissue in a ballistic trajectory [5-1].

In this paper, an optical method is introduced using angular domain imaging using illumination created deep in the tissue from the light that enters the front surface of the medium. The obtained images are enhanced by digital image processing techniques.

5.3 Light-tissue Interaction

For light in the visible and near infrared spectra (500 nm – 1300 nm), tissues and bioliquids have low light absorption levels while acting as highly scattering media. The scattering properties describe the spectral and angular characteristics of light interacting with living material, as well as its penetration depth. Migrating photons in a turbid medium can be divided into three major groups: 1) Ballistic or quasi-ballistic photons; 2) Absorbed photons; and 3) Scattered photons. The ballistic and quasi-ballistic photons are those which

travel the shortest path, as shown in Figure 5-1, while the scattered photons are those that traverse a longer path as a result of numerous scattering events in the turbid medium [5-10].

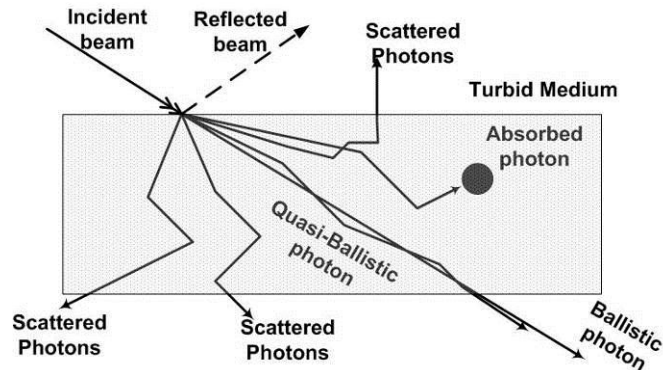


Figure 5-1. Light interaction in the turbid medium [5-10].

Described simply, a collimated beam of light decays exponentially along its path through a tissue layer of thickness d in accordance with the Beer-Lambert law [5-6]:

$$I(d) = I_o \exp[-\mu'_{eff} d] \quad 5-1$$

where $I(d)$ is the intensity of transmitted light measured using a distance photodetector with a small aperture, I_o , is the incident light intensity, and μ'_{eff} (cm^{-1}) is the total effective attenuation coefficient. The total effective attenuation coefficient is characterized by the absorption coefficient, μ_a (cm^{-1}), the scattering coefficient, μ_s (cm^{-1}), and finally the anisotropy factor, g , as follows:

$$\mu'_{eff} = \mu_a + (1-g)\mu_s = \mu_a + \mu'_s \quad 5-2$$

Henye and Greenstein have developed the g factor to describe the angular dependence of light scattering by small particles, which they used to study diffuse radiation from interstellar dust clouds in the galaxy [5-7]. A phase function $S(\theta)$ that describes the experimentally observed distribution of scattering angles of photons developed by Henye and Greenstein as the Henye-Greenstein (HG) function is [5-8]:

$$S(\theta) = \frac{1}{4\pi} \frac{1-g^2}{(1+g^2-2g\cos\theta)^{3/2}} \quad \text{where:} \quad 5-3$$

$$\int_0^\pi S(\theta) 2\pi \sin\theta d\theta = 1$$

$$\int_0^\pi S(\theta) \cos\theta 2\pi \sin\theta d\theta = g$$

It has been found by Jacques et al [5-8] that the Henye-Greenstein phase function $S(\theta)$ also accurately describes the scattering of light in biological tissue. The g factor is defined as the cosine weighted average of the scattering, which is a measure of scatter retained in the forward direction following a scattering event [5-9]. The reduced scattering coefficient, μ'_s , is defined as the product between $(1-g)$ and the scattering coefficient, μ_s , in order to represent aforementioned forward scattering effect. All the optical parameters are highly dependent on the tissue type and the wavelength of light. As an example, from the wavelength of 750 nm to 830 nm, the reduced scattering coefficient varies

from 8.7 ± 2.2 to 8.3 ± 2.0 (cm^{-1}), while the absorption coefficient unchanged at 0.047 (cm^{-1}) and the g factor remains in the range of $0.88 - 0.95$ [5-6].

In the following sections, we briefly introduce current works in optical imaging. Subsequently, we introduce our new technique as deep illumination angular domain imaging, followed by the imaging results.

5.4 Current works in optical imaging

Optical imaging is a technique for revealing objects and structures within highly scattering media by extracting information from unscattered photons that travel through the medium. Two techniques, Time Domain (TD) tomography [5-10, 5-11] and Optical Coherence Tomography (OCT) [5-12, 5-13] distinguish between unscattered and scattered photons based on differences between their path lengths.

Time Domain Optical Tomography: In Time Domain (TD) measurement, a short pulse of light illuminates the scattering medium and ultra-fast imager records a time course of the illumination response. The high-speed imager is used to select the early arriving light and to get rid of the late arriving scattered photons [5-11]. The time domain optical imaging system has been used for several applications, such as breast cancer screening and diagnosis using a Ti-Sapphire pulse laser (with spectrum range of 750 nm - 850 nm), as presented in [5-23], and functional imaging of the adult brain, as has been shown in [5-24].

TD optical tomography has two major drawbacks. First, in order to gate the incoming light, very short laser pulses (pico- to femtosecond range) and fast

camera detectors (sub-nanosecond range) are employed, which makes this method expensive and high-performance equipment dependent [5-10]. Second, the signal at the detector consists only of an exponentially small portion of the total number of photons emitted by the light source. Consequently, the signal-to-noise ratio is inherently low and exceedingly sensitive [5-10].

Optical Coherence Tomography (OCT): OCT is based on the principle that the coherence property of the backscattered light contains time-of-flight information and can be used to determine the longitudinal locations of reflective boundaries and sub-surface sites in the tissue [5-12, 5-13]. Although, the main disadvantage of OCT compared to alternative imaging modalities is its limited penetration depth (less than 2 mm) in scattering media, OCT is quite successful in ophthalmology because of the high transmittance of ocular media. Ultra-high-resolution OCT imaging utilizing a femtosecond Titanium–sapphire laser light source has been demonstrated with axial resolution of 1–3 μm in non-transparent and transparent tissue, enabling unprecedented *in vivo* imaging of intra-retinal sub-cellular structures [5-25].

Diffuse Optical Tomography (DOT): The basic idea of DOT imaging is to illuminate the tissue with light sources and to measure the light leaving the tissue with an array of detectors. For the specific source location, the detector array records an image of the light reaching it from that source. A model of the propagation of light in tissue is developed and parameterized in terms of the unknown scattering and/or absorption as a function of position in the tissue. Then, using the model together with the ensemble of images over all the

sources, an attempt is made to obtain the “inverse” of the propagation model to recover the parameters of interest, or, in other words, to estimate the scattering and/or absorption parameters [5-14, 5-15].

The applications of DOT have expanded into wide medical imaging fields: brain functional imaging [5-26], breast imaging [5-27], muscle imaging [5-28] and imaging of joint inflammation [5-29]. However, its application is limited in scope because it requires intensive, and in most cases, time consuming, computations. In most situations of interest, where the system size is larger than the transport scattering mean free path, the diffusion equation for light provides a reasonably good description. However, the diffusion method only uses diffusive photons which have undergone many scattering events. Therefore, the signals received by detectors are less sensitive to changes in the structure of the turbid medium, which makes it difficult to obtain high-resolution image reconstruction [5-15].

To summarize, the optical imaging methods discussed in this section are compared in terms of imaging depth, lateral resolution, and technology requirements, as shown in Table 5-1. All of these optical imaging methods are being widely studied with the goal of enabling high contrast imaging within tissue. Also, the fact that these optical methods can operate at varying wavelengths and that tissue has many characteristics that vary with wavelength allows them to provide additional information not available from other techniques such as ionizing X-Ray based imaging methods.

5.5 Angular domain imaging (ADI)

The Angular Domain Imaging (ADI) method operates by filtering out highly scattered light based on the observation that light tends to scatter in a nearly uniform angular distribution while non-scattered ballistic and quasi-ballistic light remains closely confined within a small angle of the initial light source. Thus, highly scattered light can be filtered out based on angles by using high aspect ratio angular filter collimating tunnels (see Figure 5-2) that reject scattered photons while allowing ballistic and quasi-ballistic light within the angular filter's acceptance angle to pass through to the detector.

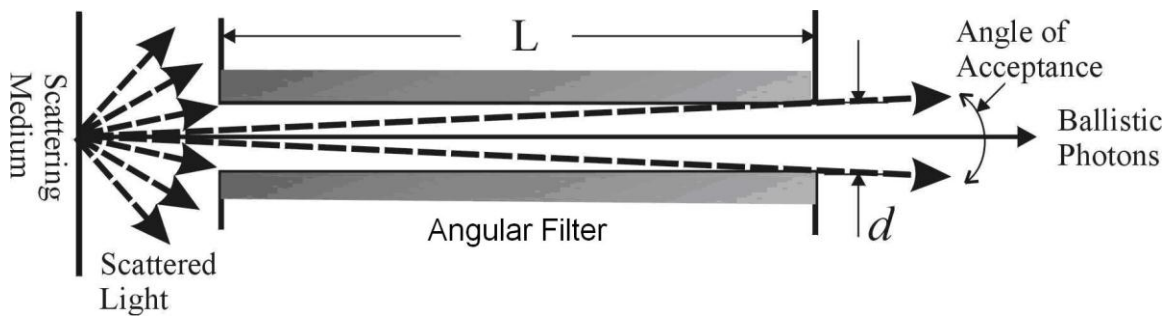


Figure 5-2. High aspect ratio micro-channel proving angular filters.

Monte Carlo simulation methods [5-19] demonstrate that ballistic and quasi-ballistic photons exit from an ideal isotropic scattering medium with unchanged or very small angular deviations from their initial entry trajectories, respectively. The angular filter will operate under any conditions where the signal being detected consists of ballistic or quasi-ballistic photons arriving within the allowed acceptance angle, and can be employed to reject all other photons

arriving at the source outside of the acceptance angle, thus making it possible to separate the signal from the background scattered noise. Consequently, the said angular filters enable the extraction of a meaningful image from this signal amidst unintelligible background noise in a highly scattering medium.

Table 5-1. Performance comparison for several optical imaging methods in human tissue 1-201-223-141-38.

	Imaging depth	Lateral resolution	Technology requirements
TD	1 cm	1 mm	Ultra-fast laser source and detector
OCT	1-2 mm (retina)	10-20 μ m	Interferometry
DOT	1.5 cm	1 mm -1 cm	Multiple detectors, inverse algorithms

As shown in Figure 5-2, the angular filter employs high-aspect ratio channels to create pathways through which photons can pass through if they arrive within the allowable acceptance angle with respect to the longitudinal axis of each channel. Photons that arrive with incident angles beyond the acceptance angle will strike the channel sides and be absorbed [5-16-5-22]. The performance of ADI is largely dependent on the design of the array of angular filter microchannels. These microchannels must be designed with a sufficiently high aspect ratio, length (l) over diameter (d), to provide the angular filtering of scattered photons.

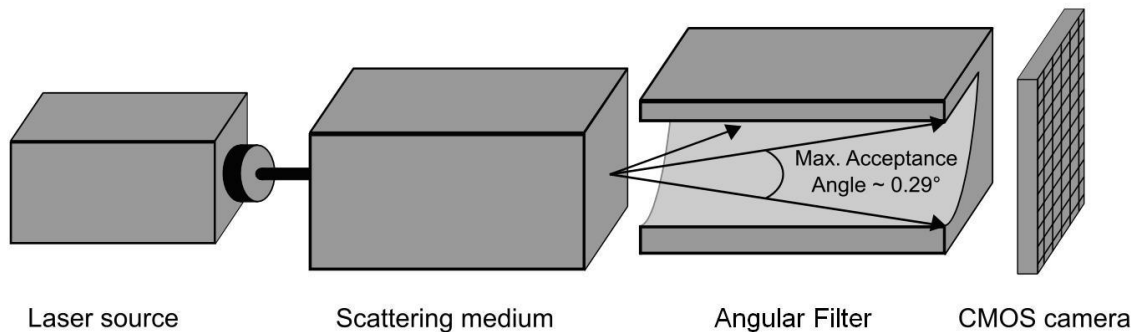


Figure 5-3. Experimental setup for Angular domain imaging in transillumination mode.

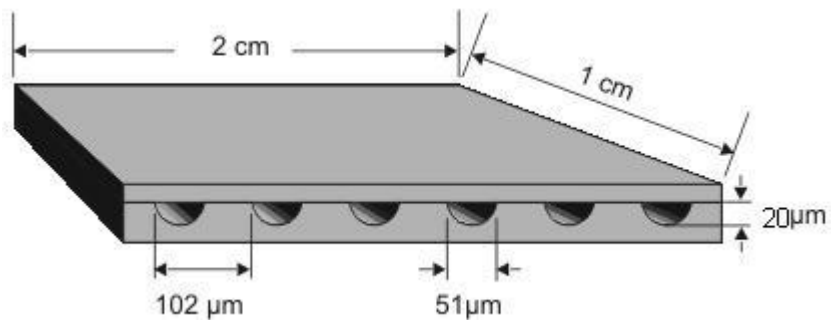


Figure 5-4. Silicon micro-machined angular filter array.

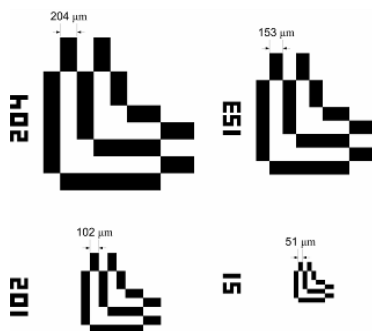


Figure 5-5. Two-dimensional phantom test structures ranging from 204 μm line width and spacing down to 51 μm .

ADI in transillumination mode includes the light source and the detector, which are aligned in front of each other, while the scattering medium is placed in between, as shown in Figure 5-3. Angular domain imaging possesses multiple advantages as an optical imaging method: i) detection is not wavelength dependent, which allows for broadband light sources without being restricted to narrowband laser lights; ii) there is no need for coherent sources nor ultra-fast pulse lasers, and therefore, LED's can be used which can ultimately lead to a low-power, low-footprint imaging system.

5.5.1 Angular filter and test phantom fabrication process

In order to produce high resolution images, an angular filter array must have relatively small openings with small spacing between them. In the design of the silicon micromachined angular filter array, as shown in Figure 5-4, we chose 51 μm wide tunnels with 102 μm spacing to produce a parallel array of collimating channels with the length of 10 mm to obtain an acceptance angle of 0.29° [5-19]. For these initial experiments, only a linear angular filter array was created.

First, a furnace oxidation process grows a silicon oxide (SiO_2) layer (0.5 μm thick) on a silicon wafer. The oxide layer is then patterned by photolithography and etched with a buffered oxide etchant to create an oxide masking layer for the angular filter array grooves. Using the patterned oxide as a mask, the silicon is etched using a wet HNA etchant solution (HNO_3 , CH_3COOH , and HF solution in the ratio of 75:35:9) to produce a groove width of 51 μm after

isotropic etching, with a 20 μm deep channel. The oxide can then be stripped, leaving grooved micro-channels etched in the silicon.

In order to determine the resolution of the objects being imaged at various scattering levels, a standard resolution test structure consisting of lines and spaces in both X and Y directions was fabricated (Figure 5-5). The mask for these test structures is designed to show 51, 102, 153 and 204 μm line and space widths in both the X and Y directions. This design was chosen in the expectation that the 204 μm would be clearly visible with the angular filter array's 102 μm hole spacing, the 102 and 153 μm would be near the limits of detectability, and the 51 μm would be below the detectable limit. These test patterns were fabricated from thin films (100 nm) of aluminium deposited on thin glass slides and then patterned photolithographically and etched to produce the structures.

Previous ADI work in transillumination setup [5-22] has been successful at imaging objects 153 μm in size or smaller for a 5 cm thick scattering medium with a scattering ratio of $8 \times 10^9:1$ scattered photons to ballistic/quasi-ballistic photons. These results were obtained with the use of a cylindrical-spherical-cylindrical lens beam shaping system to produce a thin line of light, along with a vertical slit (1 mm wide). Using only a simple 10x spherical beam expander to illuminate the sample, successful ADI results are obtainable at a SR of $10^6:1$.

In the next section, we present a new technique based on ADI principles and angular filters, called deep illumination ADI, which allows for imaging where the tissue is as thick that transillumination may not be possible. This new

technique provides high-resolution images of the micro-scale phantoms in highly scattering media with the light source and detector placed on the same side of the scattering medium, without requiring a carefully aligned or collimated illumination source.

5.6 Deep illumination technique in angular domain

Deep illumination ADI applies angular domain imaging by creating a glow ball of illumination deep within the tissue to detect structures near the surface. This technique differs from previous backscattering techniques, which use all the light scattered back to the detector and apply time or wavelength filtration to that light. In the following subsection, we introduce the deep illumination ADI technique in detail.

5.6.1 The methodology

As noted in section 3.2, Previous ADI experiments [5-16-5-22] have focused on using a laser source aligned to the angular filter to transilluminate the turbid medium from front to back (transillumination), as shown in Figure 5-6. However, Angular Domain Imaging can also be employed using an illumination source that is not aligned to the angular filter, though for much shallower imaging depths compared to transillumination ADI. In the deep illumination approach, objects can be detected at moderately shallow depths even when providing illumination from the same side as the detector [5-16, 5-17].

The principle of this imaging technique is that by injecting light into the turbid medium at an angle, a ball of illumination is generated at a depth below

the surface, as shown in Figure 5-6. Note it is important that the light enter the medium both at an angle and displaced from angular filter array. The deep illumination glow ball emits light in all directions uniformly, with a fraction of the emitted light being aligned to the angular filter. Most of that aligned light is in turn scattered before it emerges from the medium, and thus is rejected by angular filter array. However, a small fraction is not scattered, or is only slightly scattered, and thus can be considered as ballistic or quasi-ballistic light that originates from the glow ball and is passed by the angular filter. In addition, a tiny fraction of the scattered light emitted by the glow ball will emerge from the scattering medium within the acceptance angle of the angular filter, and will contribute to scattered background noise at the detector.

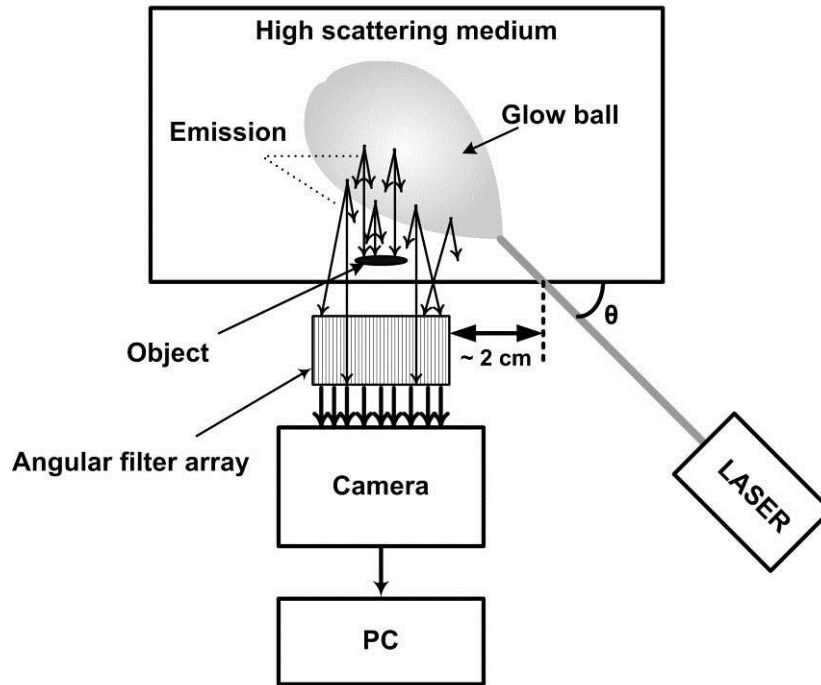


Figure 5-6. Deep illumination and angular filtering system overview.

Light from the glow ball that falls within the angular filter acceptance angle and is not blocked by a test object will pass through to the camera detector, while scattered light, along with light that encounters a test object, will fail to reach the detector. The test structures can be distinguished in the image as high absorption (dark) areas over the bright background. Scattering is exponentially related to depth; thus, scattering media with scattering levels comparable to human tissues can be imaged using the deep illumination ADI technique when phantoms are placed at relatively shallow depths from the surface.

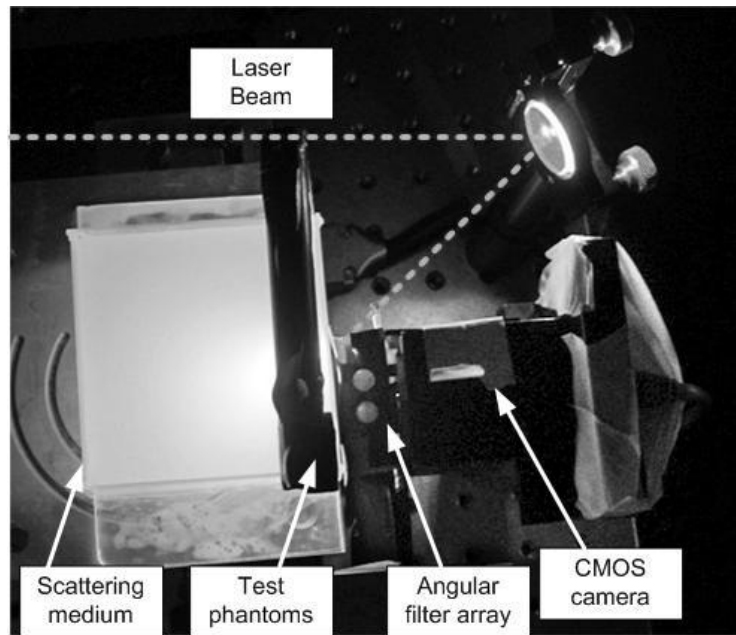


Figure 5-7. Deep illumination ADI experimental setup.

5.6.2 Experimental setup

The deep illumination ADI experimental setup (see Figure 5-7) utilizes an Argon ion laser running in the TEM_{00} mode, with 2.3 mm $1/e^2$ beam radius of nearly Gaussian profile, to illuminate the high scattering medium glass container. The Argon ion laser was chosen only for its optical laser characteristics and would not be used if actual tissue were being scanned, as its green light (514 nm) would be too heavily scattered. During operation, other background illumination was almost fully removed to leave the laser as the only light source. The whole system was mounted on a vibration isolation table so that the measured drift of the laser alignment was $< 0.007^\circ$ per day.

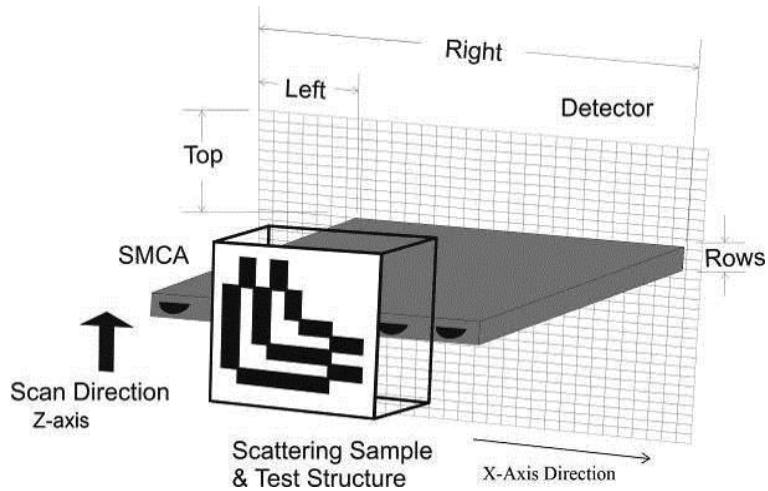


Figure 5-8. Scan of sample medium across angular filter array.

The scanning system (Figure 5-8) requires an angular filter array aligned with the CMOS imager. The angular filter was mounted to give X, Y, Z translation and 3 axes of rotation control. For alignment, the imager was put in a real time imaging mode, and the angular filter array adjusted using the rotations until the laser light was seen illuminating the filter holes in the images. The angular filter was then rotated so the holes formed a straight line across the detector with less than one pixel spacing error across the full array. The angular filter vertical (Z) position was adjusted so the holes fit within the minimum spacing. Once aligned this setup was stable. The detector used was an Electrim Corp. EDC-3000D with a 1280×1024 pixel count, resulting in a 6.7 mm detection width with the pixel size of $5.2 \times 5.2 \mu\text{m}$. The detector output could be displayed in real time or captured under computer control. An Electrim Corp. image capture board allowed full control over the imager parameters such as gain and exposure time.

During the experiments, a computer program would capture the image, then move the glass cell up an integer number of pixel spacings (typically 26 μm , or 5 pixels), using a Z axis table, before taking the next image. The program would also select the 10 pixel rows containing the image, and assemble all the rows of images to form a complete scanned image of the test object. In typical operations, 200 images were assembled per scan to image a 6.7 mm by 5.2 mm area. Depending on the imager exposure, scanning times would typically take from 2 to 5 minutes.

To create an easily controllable scattering medium, a solution is created by mixing specific amounts of 2% partially skimmed milk with water to achieve a desired scattering level. Milk is chosen because it has properties similar to tissue and exhibits good scattering characteristics as well as a low absorption coefficient [5-31]. Before each experiment, the scattering level was calibrated by first using the unexpanded laser beam and measuring the transmitted unscattered light through a 1 cm thick glass cell filled with water. The illumination was measured with a silicon power meter placed at a distance of around 1 meter from the cell, thus, giving the total transmitted light when no scattering occurs. with the measurement was then repeated with the cell filled with the scattering medium (milk/water solution). 3 mm diameter iris was placed at the output side of the cell to prevent scattered light exiting the medium from reaching the detector, while allowing the unscattered ballistic and quasi-ballistic light to pass.

Thus, the total attenuation coefficient can be calculated for each scattering medium, according to the Beer-Lambert law in equation 5-1, by relating the

fraction of transmitted unscattered light detected through the medium with the total transmitted light detected through the water-filled cell (i.e. no scattering). For example, by adding 0.26 mL milk to 20 mL water, the measured transillumination through 1 cm decreases from 89.5 μW (for water) to 6.81 μW (for the milk/water solution), which equates to a scattering ratio of $2.63 \times 10^5:1$ for an equivalent 5 cm thick scattering medium.

5.7 Experimental results

In the experiments introduced in this section, the test phantom slide is placed at a distance of 1, 2, and 3 mm back from the surface. A 2 mm diameter laser beam forms an angle of 54° with respect to the camera and illuminates a highly scattering medium; earlier experiments demonstrate that imaging is also possible with alternate beam angles or side illumination, as shown in [5-22]. The 2 mm diameter beam enters the scattering medium approximately 2 cm to the right of L-shape phantoms placed within the medium (Figure 5-7). As the light penetrates into the medium, scattering will occur from the beam's point of entry at the surface until it forms a ball-like region of deep illumination behind the sample.

Figure 5-9 presents images of the L-shape test phantoms captured at different depths in scattering media with measured total effective attenuation coefficients of $\mu'_{eff} = 4.7 \text{ cm}^{-1}$ and 5.8 cm^{-1} . For the $\mu'_{eff} = 4.7 \text{ cm}^{-1}$ results at a 1 mm depth, all four test structures are visible, and lines and spaces as small as 102 μm can be resolved (Figure 5-9 (a) and (b)) . At 2 mm, the 153 μm lines and

spaces are both visible and resolvable (Figure 5-9(c) and (d)). As the depth increases to 3 mm, image contrast and definition degrade. However, the 204 μm wide lines and spaces can still be resolved (Figure 5-9 (e) and (f)).

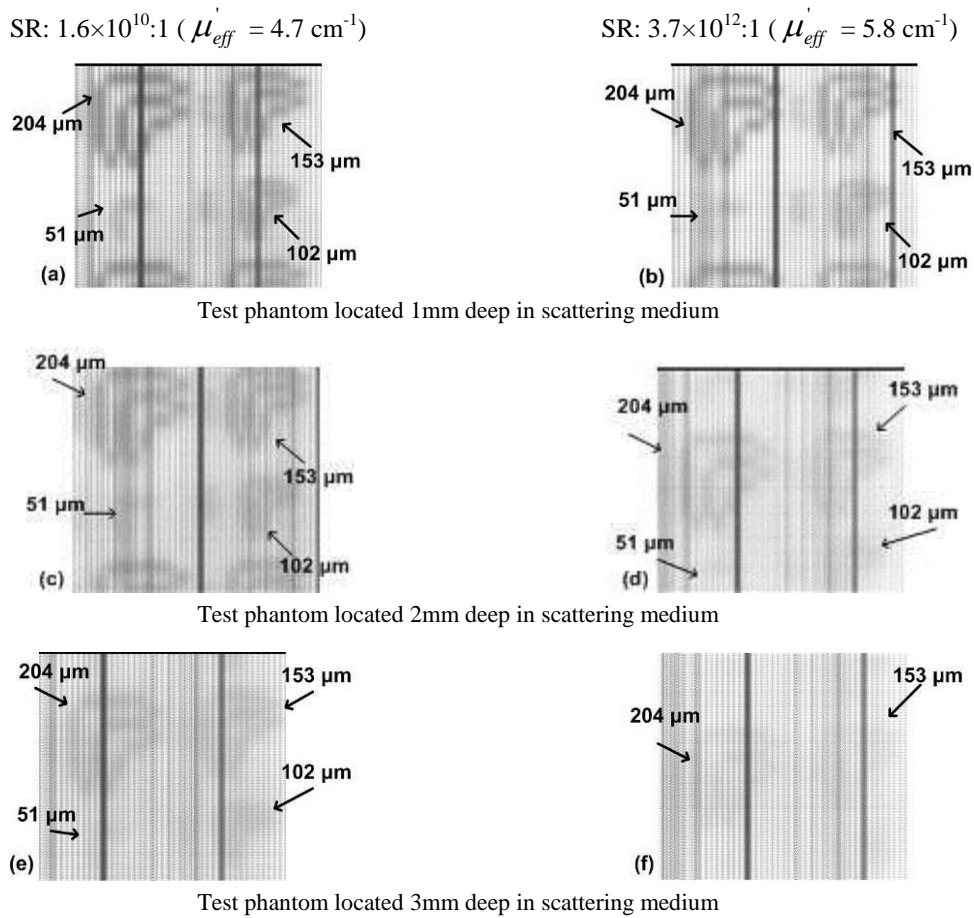


Figure 5-9. Images captured by Deep Illumination ADI at $\mu'_{eff} = 4.7$ and 5.8 cm^{-1} and depths of 1 - 3 mm.

Results at $\mu'_{eff} = 5.8 \text{ cm}^{-1}$ are similar to those at $\mu'_{eff} = 4.7 \text{ cm}^{-1}$, but with poorer image contrast and definition. For $\mu'_{eff} = 5.8 \text{ cm}^{-1}$, the 1 mm depth images show the 153 μm lines and larger as visible (Figure 5-9 (b)). At 2 mm, the 153 μm lines are only faintly detectable, while the 204 μm lines are more clearly

visible (Figure 5-9 (d)). At 3 mm, the 204 μm lines are no longer clearly visible (Figure 5-9 (c)). However, these results demonstrate that subsurface deep illumination imaging of structures at depths up to 3 mm is possible with better than 0.2 mm resolution at highly scattering conditions up to $\mu'_{\text{eff}} = 5.7 \text{ [cm}^{-1}\text{]}$, which is in the range of some typical tissue scattering levels previously discussed in this paper.

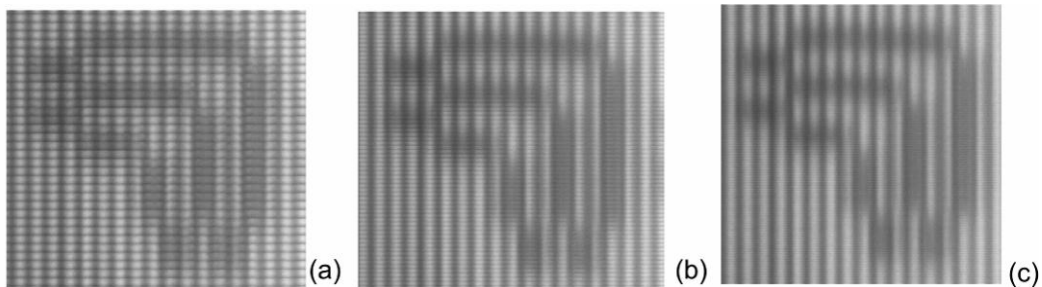


Figure 5-10. Scan results for the deep illumination method, with (a) 52 μm , (b) 26 μm , and (c) 13 μm vertical step size. (phantom size = 153 μm , depth = 1 mm, $\mu'_{\text{eff}} = 4.7 \text{ cm}^{-1}$)

Images with the angular filter array are taken one horizontal line at a time, with the sample raised vertically after each line scan by a specific vertical step. This horizontal line is centered about the middle of the tunnels, and has a height that is equal to the step size. The default step size used between scans is approximately 52 μm . However, the actual vertical height of the collimator tunnels is only in the range of approximately 20 μm , and thus, scanning with a step size

of 52 μm results in an under-sampling of the image that can lead to aliasing of small features in the image.

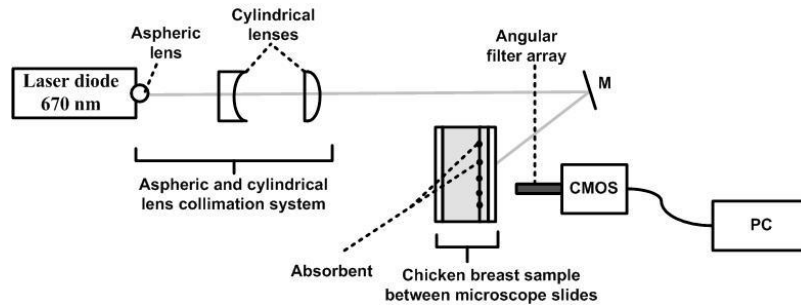


Figure 5-11. Deep illumination ADI of biological tissue diagram using 670nm laser diode.

Figure 5-10 presents scans taken of the 153 μm -wide line test structure at a 1 mm depth from the surface, with vertical step sizes of 52 μm , 26 μm , and 13 μm . Because the size of the 153 μm lines and gaps is larger than all of the vertical step sizes, aliasing is not a concern. However, with the largest step size of 52 μm , we can still see that the test structure is being sampled with a relatively low spatial sampling frequency, resulting in poorer definition of the test structure. Moving to finer step sizes results in each test structure line being sampled more frequently over the same given area, which allows for increases in image definition. Note the test structures are reversed in the following scans from previous sections.

5.8 Deep illumination ADI with biological tissue

This section presents preliminary deep illumination ADI experiments with biological tissues. Tissue samples were prepared from commercially available fresh chicken breast meat. Sections of tissue were cut out by scalpel and then

compressed by hand with firm pressure to a thickness of approximately 1.3 cm and secured between two glass microscope slides. Compression appears to reduce the thickness of the chicken sample only on the order of a millimeter. Scans were conducted using the 670 nm diode laser source with its aspheric/cylindrical lens collimation system to produce a line of light (1 cm x 2 mm) that is redirected into the tissue sample, as shown in Figure 5-11.

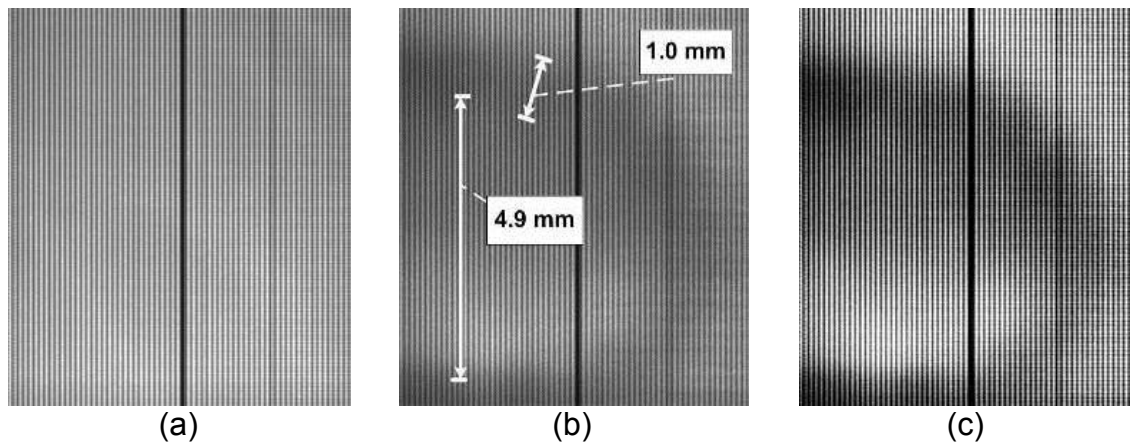


Figure 5-12. (a) Deep illumination ADI scan of the chicken breast sample, (b) the 1 mm thick paper clip, 2.5 mm deep inside the tissue, and (c) the histogram equalized version of (b).

The collimated line of light illuminates the tissue sample at an angle of 54° and 12 mm above the scan line of the angular filter array. The sample, located 1 cm from the angular filter array, was incrementally raised by the Z axis table during scanning with the illumination source held stationary. Figure 5-12 presents scans of the chicken tissue sample with and without a 1.10 mm thick paper clip, inserted 2.5 mm deep into the 13 mm thick sample. The total scan area in each image is 6.7 mm by 7.8 mm.

Figure 5-12 (a) shows the chicken breast sample alone. In Figure 5-12(b), a loop of the inserted paper clip, 2.5 mm below the surface, is shown, while Figure 5-12(c) presents a histogram-equalized version of the scan that shows the paper clip shape more clearly. Measurement bars indicate that the paper clip appears with an approximate thickness of $1 \text{ mm} \pm 0.2 \text{ mm}$ in the image, versus a physically measured value of 1.10 mm, and a gap width of $4.9 \text{ mm} \pm 0.2 \text{ mm}$, compared to a physically measured value of 4.90 mm. These results demonstrate that with deep illumination ADI, objects on the order of 1 mm can not only be detected in tissue, but also imaged with accuracy in size. In addition, preliminary scans with cylindrical rods in tissue detected objects 500 μm in size. Future experiments will further explore depth and resolution limits for deep illumination ADI.

5.9 Digital image processing for deep illumination ADI

The ADI scan results shown previously suffer from a low signal to noise ratio at deeper test phantom positions. One problem is the dark vertical lines in the image caused by the gaps between channels. These dark lines make image contrast enhancement and edge detection techniques more difficult to perform and degrade the horizontal spatial resolution in our scans. Also, the image is composed of periodic squarish patterns with bright centers surrounded by dark corners. These non-uniformities, which are a product of the collimator shape and scanning procedure, deteriorate the image quality.

Various digital image processing techniques can be employed to overcome these problems. We investigate multiple possible techniques in the following subsections.

5.9.1 Full image reconstruction

As explained previously in this paper, deep illumination photons from the turbid medium are passed through an angular filter array, depicted previously in Figure 5-4, which consists of approximately 51 μm wide channels and gaps. These spaces between channels lead to dark vertical lines in the image scans. One potential solution to this problem is fabricating two-dimensional angular filters with one array of tunnels above the other, but with one array shifted horizontally so as to eliminate the gaps between the lower arrays of tunnels during imaging. However, a simpler solution is to take two scans, where one scan is taken normally, while the other is taken after shifting the test sample horizontally by 50 μm and then using both scans to reconstruct a full image without dark vertical gaps between the tunnels, which should significantly improve horizontal image resolution. This reconstruction process involved comparing a column of pixels from one image with the corresponding column in the second image, and inserting the brighter of the two columns into the new reconstructed image. This is done for all columns, from left to right, thus forming the new reconstructed image.

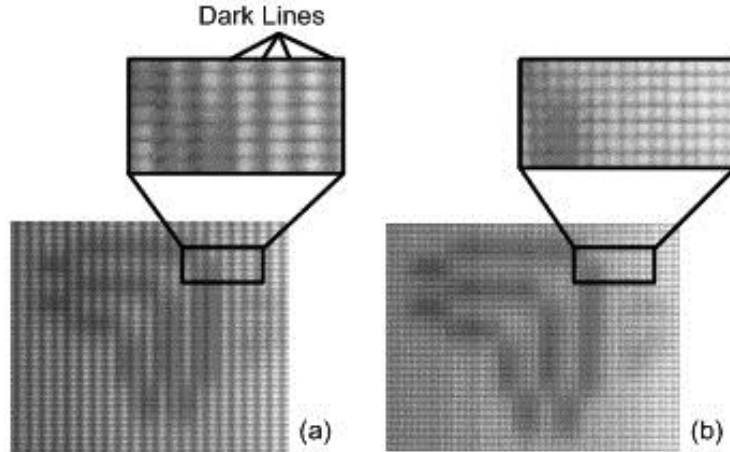


Figure 5-13. Full image reconstruction using two different scans that differ by a 50 μm horizontal shift. (a) Original image result with dark vertical lines. (b) Full image after reconstruction. (Deep Illumination, phantom size = 153 μm , depth = 1 mm, $\mu'_{\text{eff}} = 4.7 \text{ cm}^{-1}$)

As shown in Figure 5-13, the spatial resolution in horizontal axes has improved when compared with the original image. Also, this new reconstructed image makes the use of further image enhancement techniques easier and more effective, since dark gaps have been eliminated and substituted with additional image information.

5.9.2 Periodic noise removal

After image reconstruction, the image result shown previously in Figure 5-13(b) still contains squarish-shaped areas of illumination surrounded by darker areas. These patterns are frequently repeated both horizontally and vertically with a constant period. In order to remove the darkened areas surrounding the areas of illumination, periodic noise removal in the frequency domain can be employed. Transferring the image to the Fourier domain, the periodic noise can be distinguished from the desired image, as shown below in

Figure 5-14(a). The frequency domain spectrum of the image shows that most of the periodic noise is laid out on the horizontal and vertical axes, as shown in Figure 5-14(b) and also in Figure 5-14(c), which shows the noise pattern in the spatial domain.

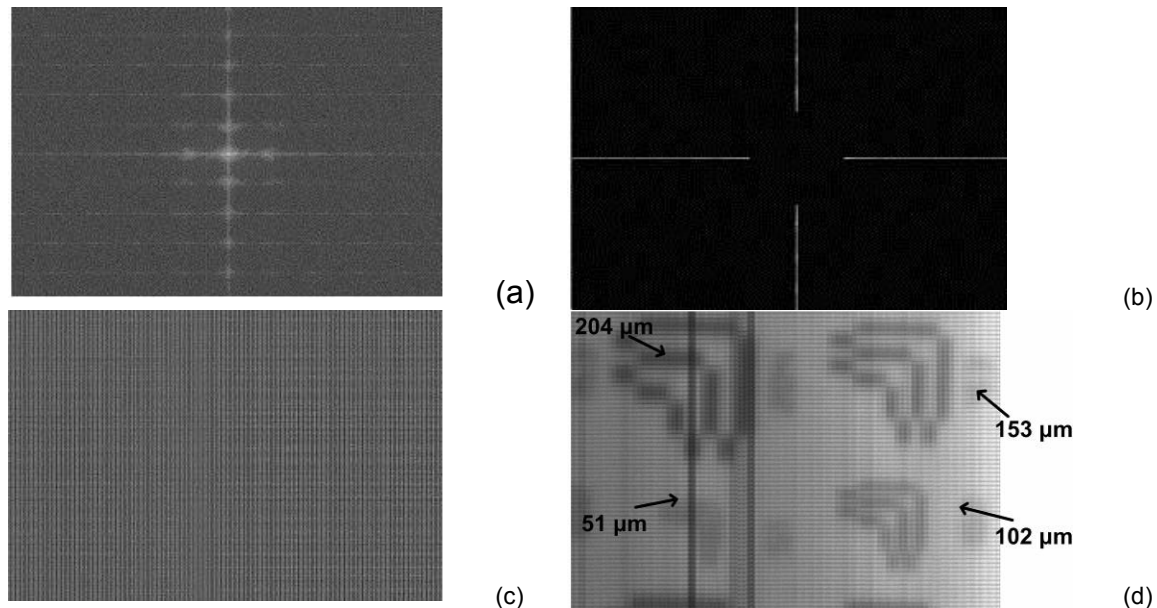


Figure 5-14. Stages in the periodic noise removal procedure. (a) Fourier transform (b) Notch filter spectrum (c) Noise pattern in spatial domain (d) Resultant image. (Deep Illumination, depth = 1 mm, $\mu_{eff} = 4.7 \text{ cm}^{-1}$)

By subtracting the noise pattern from the image in the Fourier domain, we observe less periodic noise in the background of resulted image as presented in Figure 5-14(d). Before applying any contrast enhancement process, noise in the image should be suppressed in order to avoid any noise amplification during further image processing.

5.9.3 Contrast enhancement

It can be observed that the image in deep illumination ADI is much brighter in intensity on one side and diminishes in intensity towards the other side (horizontally). This is because the deep illumination source enters the scattering medium at an angle from the side that is brighter in the image and travels deeper into the medium as it crosses horizontally to the other side of the image, thus resulting in a non-uniform background intensity which makes image content extraction more difficult [5-32]. The background illumination variation for example in Figure 5-14(d) is about 50% of the total dynamic range starting from bright background from the right and start darkening toward the left. The contrast enhancement process has two steps. 1) Homomorphic processing; and 2) Background estimation and subtraction by morphological opening.

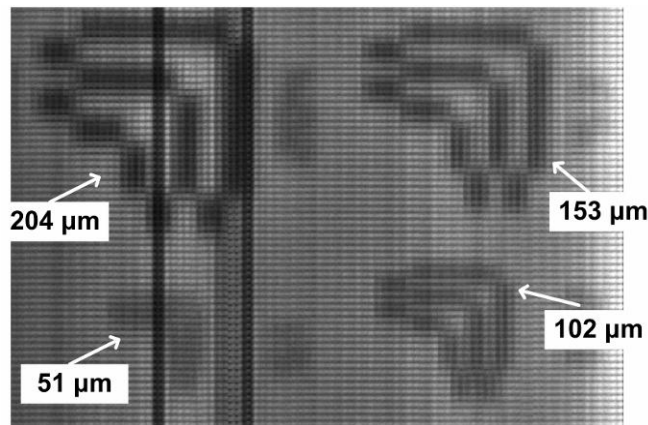


Figure 5-15. Imaging results after homomorphic processing. (Deep Illumination, depth = 1 mm, $\mu_{eff}^i = 4.7 \text{ cm}^{-1}$)

In homomorphic processing, the image with spatially varying background illumination can be described by the illumination–reflection model [5-32], which can be expressed as:

$$z(x, y) = i(x, y)r(x, y) \quad 5-4$$

where $z(x, y)$ represent as a model for the image, $i(x, y)$ is the varying illumination component and $r(x, y)$ is the test object shadow which contains the informative signal. Homomorphic processing can be used to develop a frequency domain procedure for improving the appearance of an image through simultaneous gray-level range compression and contrast enhancement. By taking the natural logarithm of equation 5-4, multiplication converts to a summation operation as follows:

$$\left\{ \begin{array}{l} \ln[z(x, y)] = \ln[i(x, y)] + \ln[r(x, y)] \\ z'(x, y) = i'(x, y) + r'(x, y) \end{array} \right\} \quad 5-5$$

where $z'(x, y)$ can be separated by the two independent random variables, $i'(x, y)$ and $r'(x, y)$. We believe that the background variation takes place at a low frequency and that by passing $z'(x, y)$ through a homomorphic high pass filter, we can diminish the illumination non-uniformity in the background as follows:

$$\left\{ \begin{array}{l} F\{z'(x, y)\} = F\{i'(x, y)\} + F\{r'(x, y)\} \\ Z(u, v) = I(u, v) + R(u, v) \end{array} \right\} \quad 5-6$$

where $I(u, v)$ and $R(u, v)$ are Fourier transforms of $i'(x, y)$ and $r'(x, y)$, respectively. If we process $Z(u, v)$ by means of a filter function $H(u, v)$, then it forms:

$$G(u, v) = H(u, v)I(u, v) + H(u, v)R(u, v). \quad 5-7$$

After taking the inverse Fourier transform of $G(u, v)$, and using the exponential operation, the desired enhanced image after homomorphic processing is yielded, as shown in Figure 5-15.

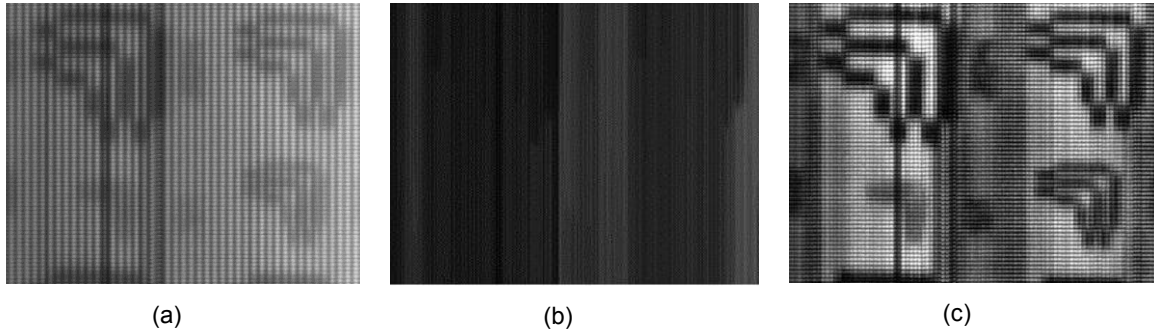


Figure 5-16. (a) The original image without image processing. (b) The estimated background from previous processed image. (c) Result after background subtraction with contrast adjustment, from 204 μm phantom size to 51 μm . (Deep Illumination, depth = 1 mm, $\mu_{eff}' = 4.7 \text{ cm}^{-1}$)

The last step to enhance contrast is to detect the background using a morphological line shape element and background subtraction in order to increase the contrast and signal-to-noise ratio. This processing involves creating a more uniform background in the image by first estimating the value of background pixels. The process uses a morphological opening operation to estimate the background illumination. Morphological opening involves erosion followed by dilation, using the same structuring element for both operations [5-33]. The opening operation has the effect of removing objects that cannot completely contain the line-shape structuring element. Figure 5-16(b) shows the morphologically estimated background from the previous processed

(homomorphic) image, followed by the result after background subtraction with contrast adjustment (Figure 5-16 (c)).

5.10 Conclusion

Deep illumination ADI was introduced and demonstrated to be successful using illumination from the same side as the detector. Deep illumination ADI can be performed using a non-collimated and unaligned light source, which generates a randomly scattering source of deep illumination within the medium. As a result, however, the proportion of unscattered to scattered light at the deep illumination source is many orders of magnitude lower for deep illumination ADI than for transillumination ADI, which is a severe detriment to signal-to-noise ratio. However, because scattering is exponentially related to depth, deep illumination ADI can be successful at high scattering levels when objects are positioned at relatively shallow depths, as compared to transillumination ADI. The deep illumination experiments were conducted using a laser beam angle of 54° to illuminate the sample. Two dimensional phantom test structures have been successfully detected in scattering media up to 3 mm deep with total effective attenuation coefficient (μ'_{eff}) up to 4.7 cm^{-1} , and up to 2 mm deep with μ'_{eff} up to 5.8 cm^{-1} . These total effective attenuation coefficients are comparable to some typical tissues. Image resolution under such conditions is better than 0.2 mm. Resolution is improved by reducing the vertical step size between line scans as well as employing digital image processing techniques.

The results show that deep illumination ADI has some unique advantages compared to other backscattering optical imaging methods (e.g. TD and OCT), such as it requires little to no alignment precision in the sample illumination. It can be easily adaptable to laser diodes, which have lower power consumption and portable-device compatibility, and finally, it can be used for a vast range of biomedical applications, which have spatial resolution requirements of only a few microns at a depth of a few millimetres in tissue.

In future work, longer or near-IR wavelength illumination sources will be employed to perform multi-wavelength imaging experiments. With multiple light sources, we can employ both deep illumination and transillumination ADI in order to obtain more information from different sides of our scanning sample. In addition, to be explored will be scans of biological samples, along with angular filter tunnel enhancements in order to increase the attenuation of scattered light by the tunnels.

5.11 Reference list

- 5-1 V. V. Tuchin, Ed., Handbook of Optical Biomedical Diagnostics. Bellingham: SPIE Press, 2002.
- 5-2 Mourant JR, Bigio IJ, Boyer J, Conn RL, Johnson T and Shimada T, "Spectroscopic diagnosis of bladder cancer with elastic light scattering," Lasers in Surgery and Medicine. vol. 17, pp. 350, 01/01. 1995.
- 5-3 Mourant JR, Hielscher AH, Eick AA, Johnson TM and Freyer JP, "Evidence of intrinsic differences in the light scattering properties of tumorigenic and nontumorigenic cells," Cancer, vol. 84, pp. 366, 12/25. 1998.
- 5-4 Santinelli A, Baccarini M, Colanzi P and Fabris G, "Microvessel quantitation in intraductal and early invasive breast carcinomas," Analytical and Quantitative Cytology and Histology, vol. 22, pp. 277, 08/01. 2000.

- 5-5 Cerussi A E, Berger A J, Bevilacqua F, Shah N, Jakubowski D, Butler J, Holcombe R F and Tromberg B J "Sources of absorption and scattering contrast for near-infrared optical mammography" *Acad. Radiol.* 8 211–8
- 5-6 Tuan Vo-Dinh, Ed., *Biomedical Photonics Handbook*. Publisher: CRC, 2003.
- 5-7 L. G. Henyey and J. L. Greenstein, "Diffuse Radiation in the Galaxy," *Astrophys. J.*, 93, 70-83 (1941).
- 5-8 Jacques SL, Alter CA, Prael SA., "Angular Dependence of HeNe laser Light Scattering by Human Dermis", *Laser Life Sci*, Vol 1, 1987, pp.309-333.
- 5-9 J. Beuthan, O. Minet, G. Muller, and V. Prapavat, "IR-Diaphanoscopy in medicine," in *Medical Optical Tomography: Functional Imaging Monitoring*, IS11, G. Muller, Ed, Bellingham: SPIE, 1993, pp. 263–282.
- 5-10 B. B. Das "Time-resolved fluorescence and photon migration studies in biomedical and model random media," *Reports on Progress in Physics*, vol. 60, pp. 227-92, 1997.
- 5-11 Chen, Kun, Perelman, Lev T. , Zhang, Qingguo Dasari, Ramachandra R., Feld, Michael S. ., "Optical computed tomography in a turbid media," U. S. Patent Application 2003/0065268, April 3, 2003.
- 5-12 F. Fercher, "Optical coherence tomography-principles and applications," *Reports on Progress in Physics*, vol. 66, pp. 239-303, 2003.
- 5-13 J. G. Fujimoto, "Optical coherence tomography," *Comptes Rendus De l'Academie Des Sciences, Serie IV (Physique, Astrophysique)*, vol. 2, pp. 1099-111, 2001.
- 5-14 D. A. Boas, D. H. Brooks, E. L. Miller, C. A. DiMarzio, M. Kilmer, R. J. Gaudette and Quan Zhang, "Imaging the body with diffuse optical tomography," *IEEE Signal Process. Mag.*, vol. 18, pp. 57-75, 11/. 2001.
- 5-15 Tikhonov , V. Arsenin, *Solution of Ill-Posed Problems*. Washington, DC: Winston, 1977.
- 5-16 F. Vasefi, P. K.Y. Chan , B. Kaminska, G. H. Chapman, "Subsurface Bio-imaging Using Angular Domain Optical Backscattering Illumination", *The 28th Annual International Conference of IEEE EMBS*, August 30-Sept. 3, 2006.
- 5-17 F. Vasefi, P. K. Y. Chan, B. Kaminska, and G. H. Chapman, "Deep illumination angular domain imaging within highly scattering media enhanced by image processing", *Proc. SPIE Int. Soc. Opt. Eng.* 6380, 63800Q (2006)

- 5-18 G. H. Chapman, M.S. Tank, G. Chou and M. Trinh, "Angular Domain Optical Imaging of Structures Within Highly Scattering Material Using Silicon Micromachined Collimating Arrays", Proceedings of SPIE Vol. 4955, pp. 462-473, Jan. 2003.
- 5-19 G.H. Chapman, M. Trinh, N. Pfeiffer, G. Chu, and D. Lee, "Angular Domain Imaging of Objects Within Highly Scattering Media Using Silicon Micromachined Collimating Arrays", IEEE J. Special Topics on Quantum Electronics, V9, No. 2, pp. 257-266, 2003.
- 5-20 N. Pfeiffer, B. Wai, and G.H. Chapman," Angular Domain Imaging of phantom objects within highly scattering mediums", Proceedings of SPIE Vol. 5319, pp. 135-145, Jan. 2004
- 5-21 M.S. Tank, G.H. Chapman, "Micromachined Silicon Collimating Detector Array to View Objects in Highly Scattering Medium", Can Jour Elec. & Comp. Eng, .25, no. 1, 13-18, Jan. 2000.
- 5-22 G. H. Chapman J. Rao, T. Liu, P. K.Y. Chan, F. Vasefi, B. Kaminska, and N. Pfeiffer, "Enhanced Angular Domain Imaging in Turbid Medium using Gaussian Line Illumination", Proceedings of SPIE Volume: 6084, Jan 2006.
- 5-23 X. Intes, S. Djeziri, Z. Ichalalene, N. Mincu, Yong Wang, P. St-Jean, F. Lesage, D. Hall, D. A. Boas and M. Polyzos, "Time-domain optical mammography Softscan: Initial results on detection and characterization of breast tumors," in Photonics North 2004: Photonic Applications in Astronomy, Biomedicine, Imaging, Materials Processing, and Education, 2004, 2004, pp. 188-97.
- 5-24 J. Selb, . K. Joseph and D. A. Boas, "Time-gated optical system for depth-resolved functional brain imaging," J. Biomed. Opt., vol. 11, pp. 44008-1, 07/. 2006.
- 5-25 R. K. Ghanta, , W. Drexler, U. Morgner, F. Kartner, E. P. Ippen, J. G. Fujimoto, J. S. Schuman, A. Clermont and S. Bursell, "Ultrahigh resolution retinal imaging with optical coherence tomography," in Conference on Lasers and Electro-Optics (CLEO 2000). Technical Digest. Postconference Edition. TOPS Vol.39, 7-12 may 2000, 2000, pp. 506-8.
- 5-26 Chance, , E. Anday, S. Nioka, Shuoming Zhou, Long Hong, K. Worden, C. Li, T. Murray, Y. Ovetsky, D. Pidikiti and R. Thomas. "A novel method for fast imaging of brain function, non-invasively, with light," Optics Express, vol. 2, 05/11. 1998.
- 5-27 B.W. Pogue, S. P. Poplack, T.O. McBride, W.A. Wells, K.S. Osterman, U.L. Osterberg and K.D. Paulsen, "Quantitative hemoglobin tomography with diffuse near-infrared spectroscopy: pilot results in the breast," Radiology, vol. 218, pp. 261-6, 01/. 2001.

- 5-28 E.M.C. Hillman, J.C. Hebden, M. Schweiger, H. Dehghani, F.E.W. Schmidt, D.T. Delpy and S.R. Arridge, "Time resolved optical tomography of the human forearm," *Phys.Med.Biol.*, vol. 46, pp. 1117-30, 04/. 2001.
- 5-29 Y. Xu "Imaging of in vitro and in vivo bones and joints with continuous-wave diffuse optical tomography," *Optics Express*, vol. 8, pp. 447-451, 2001.
- 5-30 Alfano R. R., Wei Cai, Melvin Lax, "Time-Resolved Optical Backscattering Tomographic Image Reconstruction in Scattering Turbid Media" U.S. patent, US6205353, March 20, 2001.
- 5-31 H Inaba, "Coherent Detection Imaging for Medical Laser Tomography", SPIE IS11, 317-347, 1993.
- 5-32 R. C. Gonzalez , R. E. Woods," *Digital Image Processing*", Upper Saddle River, N.J. : Prentice Hall, c2002.
- 5-33 MATLAB Digital Image Processing Toolbox user guide, v5.0,

6: TRANSMISSION AND FLUORESCENCE ANGULAR DOMAIN OPTICAL PROJECTION TOMOGRAPHY OF TURBID MEDIA⁵

6.1 Abstract

Background: When imaging through turbid media, objects are often blurred by scattered light. An optical collimator (i.e. angular filter array) improves images by accepting only photons propagating within a narrow solid angle about the direction of the incident light. These photons are expected to participate in a limited number of small-angle scattering events, maintaining their original propagation direction, and finally contributing to the development of a faithful image of an object within turbid medium. The collimation method, also referred to as Angular Domain Imaging (ADI), applies to a see-through configuration where the incident collimated light beam can be aligned with the collimator in a trans-illumination mode of operation. Objective: In this paper, we present Angular Domain Optical Projection Tomography (ADOPT), a method that can extract depth information of optical contrast in turbid media with high longitudinal resolution based on ADI technology. Materials and methods: The resolution of the ADI system has been tested over various depths in a 5 cm optical cuvette using a resolution target suspended in a homogeneous turbid medium. The ADOPT system reconstructed images from a series of angular domain

⁵ The following chapter has been published in Applied Optics, 48, 6448-6457 (2009) under the co-authorship of E. Ng, B. Kaminska, G.H. Chapman, K. Jordan, and J.J.L. Carson.

projections collected at angular intervals. The system was used to measure the attenuation of an absorbing target in transmission mode (t-ADOPT) and to measure the light emitting from a fluorescent target (f-ADOPT). Tissue-mimicking phantoms were used to validate the performance of the method. In the t-ADOPT configuration, a background scattered light estimation and subtraction methodology was introduced to improve the imaging contrast. A target consisting of two graphite rods (0.9 mm diameter) was suspended in the cuvette by a rotation stage. ICG-filled glass rod was used as an imaging target in f-ADOPT arrangement. The target was placed in a manner that the line of laser light was perpendicular to the longitudinal axis of the rods. Several projections were collected at increments of 1.8° and compiled into a sinogram. A transverse image was reconstructed from the sinogram using filtered backprojection and image contrast was improved by experimental scatter measurements using a wedge prism and an image processing algorithm. Results: The sub-millimeter target embedded in a 2 cm thick scattering medium (reduced scattering coefficient $\leq 2.4 \text{ cm}^{-1}$) was discernable in both the sinograms and the reconstructed images. In the f-ADOPT system, fluorescent line targets $< 1 \text{ mm}$ in diameter embedded in a 2-cm thick scattering medium (reduced scattering coefficient $\leq 0.8 \text{ cm}^{-1}$) were discernable in both the sinograms and the reconstructed images. Conclusion: The proposed method could be used as the basis to construct an optical tomographic scanner for simultaneous absorption and fluorescence based imaging of biological specimens (i.e. up to 7 mm across).

6.2 Introduction

6.2.1 Background and motivation

Optical Projection Tomography (OPT) is a noninvasive technique for observing the internal structure of objects under illumination by projection based image reconstruction methodology [6-1]. The technique has applicability to small animal imaging research and detection of tissue abnormalities during diagnostic screening [6-2]. However, OPT has been limited to small objects since optical scattering of incident and emitted light results in degraded image resolution and contrast [6-3]. That is, sub-millimeter OPT image resolution is not achievable for turbid objects more than a few millimeters in thickness when using purely optical approaches. For example, Sharpe et. Al. [6-4] described an OPT system capable of high resolution optical projection tomography of both fluorescent and absorbent optical contrast in biological specimens (e.g. mouse embryo), but the approach was limited to thin biological tissue specimens (i.e. the mouse embryo between the ages of 5 and 30 somites [6-5]). Furthermore, the method was limited to transparent specimens (i.e. by processing the tissue with an optical clearing method) as it was highly sensitive to optical scatter. Recently, advances in hybrid technologies such as phototacoustic microscopy have achieved sub-millimeter resolution at a depth of several millimeters [6-6], but the instrumentation is costly, complex, and the interpretation of image contrast as absorption is complicated by local variations in laser fluence and thermoelastic properties within the sample. Therefore, there is need to develop optical imaging systems that can provide tomographic and 3D capabilities in turbid samples of

greater thickness (i.e. up to 1 cm), without the need for optical clearing, but with sub-millimeter image resolution.

To overcome the limitation of optical scatter, several approaches have been investigated including frequency-domain [6-7], time gating [6-8, 6-9], and coherence gating [6-10] methods. Each of these approaches has employed complex instrumentation to filter out scattered photons from ballistic and quasi-ballistic photons using the principle that the latter follow the shortest path through the scattering medium. Continuous Wave (CW) [6-11, 6-12] methods utilize less costly instrumentation, have high signal to noise, and high sensitivity [6-13]; however, their application is limited in scope due to the intensive, and in most cases, time consuming computational requirements during image reconstruction [6-13]. Sub-millimeter resolution in CW measurements can be reached with the use of sub-millimeter source and detector arrays, which provide large data sets [6-14]. Several of the above approaches can be extended to perform fluorescence imaging by inserting spectral filters in front of the detector. CW [6-15], frequency domain [6-16, 6-17], or time domain (TD) pulsed excitations [6-18, 6-19] can be utilized to extract fluorescent emission signals of fluorescent molecules with specificity to cellular and molecular processes. Time domain fluorescence optical tomography technique can also extract lifetime information of the fluorophores in tissue [6-20].

Recently, Angular Filter Array (AFA) technology has been used to perform Angular Domain Imaging (ADI) through turbid phantoms and tissue samples with

thicknesses ranging from 6-9 mm with image resolution down to 150 μm [6-21] - [6-26].

6.2.2 Concept of angular domain imaging in transillumination

Trans-illumination ADI involves illuminating a scattering sample from one direction and imaging the emitted light that traverses the sample at the exact opposite end. Most of the emitted light has been randomly scattered within the medium. However, use of an angular filter aligned to the collimated light source can be used to reject the scattered light and accept ballistic and quasi-ballistic photons that emerge from the sample. The collected photons are captured by a CCD camera to form an image of internal structures in turbid sample (see Figure 6-1). The essence of trans-illumination is that the collimated source and angular filter must be carefully aligned. Previous work in ADI has utilized the trans-illumination technique for imaging a scattering medium [6-21] - [6-26]. Sub-millimeter resolution has been achieved using collimated illumination and an angular filter array (AFA) device and the measured effective penetration depth is approximately equal to six reduced mean free paths under the experimental conditions of an acceptance angle of less than 0.5 degree [6-21] - [6-26]. This method provides both scattered light filtration and high depth of field.

Fluorescence-based ADI has also been demonstrated and enables images of fluorescent targets at considerable depth within the turbid medium [6-27]. Since ADI provides a means to obtain optical projections of absorbing objects and fluorescent sources depending on the mode of operation, it is well-suited to OPT.

6.3 Objective and approach

The objective of this work was to evaluate a two-dimensional optical projection tomography method that could image optically absorbing and fluorescing targets embedded within turbid samples without prior optical clearing. The approach was to exploit the scatter rejection capabilities of ADI to obtain optical projections from the turbid sample in either transmission or fluorescence mode. Two imaging systems were constructed and tested. The transmission angular domain optical projection tomography (t-ADOPT) system combined an ADI system in transmission mode with the capability to rotate the sample and collect a series of ADI projections over a range of sample angles.

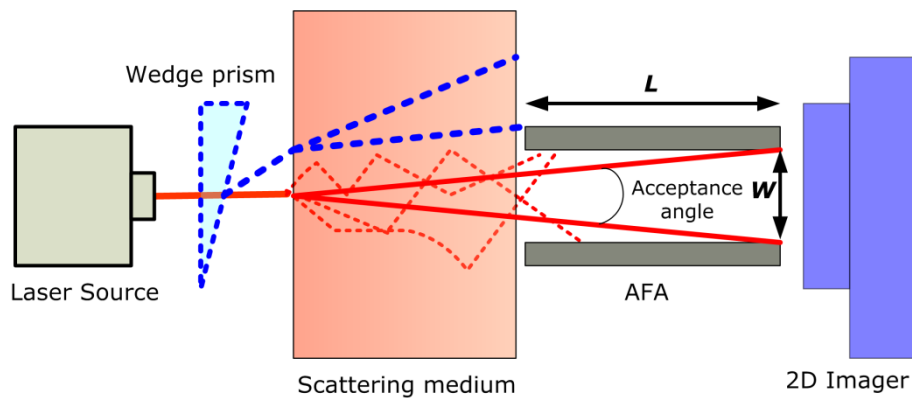


Figure 6-1. ADI system diagram in trans-illumination mode. The AFA must be designed with a sufficiently high aspect ratio, length (L) over opening width (W), to provide the small acceptance angle and filter scattered photons. Optional wedge prism can be used to estimate background noise to enhance the tomographic image.

The fluorescence angular domain optical projection tomography (f-ADOPT) system combined an ADI system in fluorescence mode with similar projection collection capabilities. The depth of field of the ADI system was studied to assess the quality of ADI projections as a function of depth of

absorbers within the turbid medium. The tomographic imaging capabilities of each ADOPT system was tested with tissue-like phantoms prepared from Intralipid™ and optically absorbing targets or targets containing the fluorescent dye indocyanine green (ICG). Contrast enhancement by the wedge subtraction method [6-24] was also evaluated.

6.4 Methods

6.4.1 Angular filter array

For this series of experiments, we employed a previously described AFA [6-26]. Each channel was square in shape with a width of 60 μm , height of 60 μm , length of 1 cm, and 5 μm spacing between channels. The channel geometry provided an aspect ratio of 167:1, but because the micro-channels were square in geometry the optical acceptance angle (θ_a) had a range from 0° (parallel to the channel length), to $\theta_a = 0.34^\circ$ (entrance wall to opposite exit wall) to $\theta_a = 0.48^\circ$ (entrance corner to opposite exit corner). This design was selective enough to collect quasi-ballistic photons that provided at least 200 μm spatial resolution through 7 mm of turbid media similar to tissue [6-26].

Another approach in angular filtration of scattered light can be implemented using a converging lens and pinhole aperture. When the aperture is located at the back focal plane of the lens, such an arrangement forms a SpatioFrequency Filter (SFF) [6-28]. Our previous work [6-28] showed that the image resulting from a lens and pinhole system has poorer spatial resolution compared to ADI since the SFF behaves as a spatial low-pass filter

6.4.2 Tissue mimicking phantom

Tissue-mimicking phantoms were prepared from aqueous suspensions of Intralipid™ contained in a glass cuvette. Intralipid™ is a phospholipid emulsion and a practical phantom medium for light dosimetry studies since it has turbidity and absorbance properties similar to tissue in the NIR [6-29], [6-30].

6.4.3 Sample rotation

Imaging targets were incrementally rotated 200 times in steps of 1.8° with a custom made rotation stage to achieve a complete 360° rotation. At each step, an ADI line scan was collected. In the trans-illumination mode, each ADI line scan provided an optical projection of the absorbing objects within sample. In fluorescence mode, each ADI line scan provided an optical projection of the fluorescent sources within the sample.

6.4.4 t-ADOPT

A functional outline of the t-ADOPT setup is shown in Figure 6-2. For illumination, a laser diode capable of emitting up to 1 W of 808 nm light was used (L808P1WJ, Thorlabs Inc., Newton, NJ). The emission area of the diode laser was 100 μm wide and approximately 1 micron tall. The emitted laser beam had asymmetry and high angular divergence along both axes, with a rated angular divergence of 8° horizontally and 35° vertically. The strong divergence was corrected to obtain a collimated line of light using a beam shaping system. The beam was collimated along the vertical axis with a converging aspheric lens ($f.l.$ = 4.5 mm) positioned one focal length away from the laser diode. A concave

cylindrical lens ($f.l. = -25$ mm) was used to diverge the beam along the horizontal axis. The beam was then collimated in the horizontal direction with a convex cylindrical lens ($f.l. = 100$ mm). The resultant collimated beam was restricted in width to approximately 1.3 cm using an adjustable iris placed before the sample. Trans-illumination ADOPT involved illuminating the turbid sample with the collimated beam perpendicular to the optical cell sidewall followed by detection of the optical projection directly opposite using the AFA and a CMOS camera (EDC-3000D, Electrim Corporation, Princeton, NJ). The camera was connected to a computer and custom software was used to capture and store the resultant images.

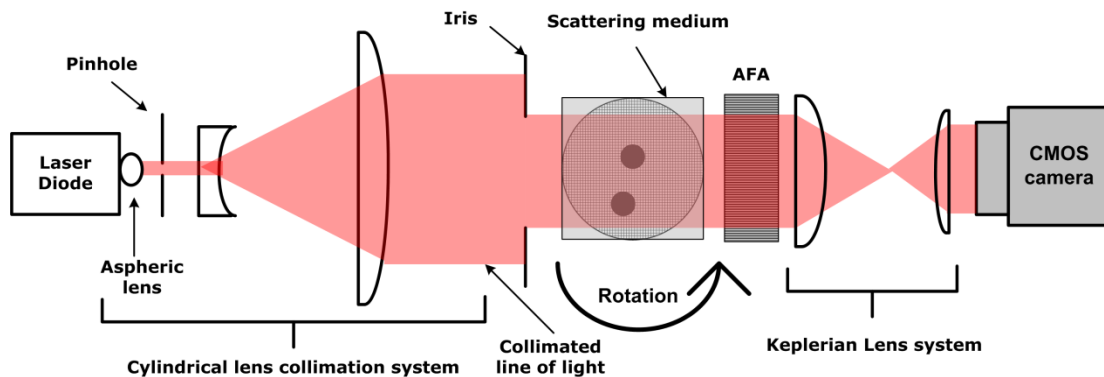


Figure 6-2. System for trans-illumination angular domain optical projection tomography system.

A phantom consisting of 0.25%, 0.30% or 0.35% Intralipid™ in a 2 cm optical cell was used to study the performance of t-ADOPT at scattering levels below and above the detection limit of ADI [6-24]. According to Mie theory, the reduced scattering coefficient for 0.25% Intralipid™ solution is approximately 2 cm^{-1} at 808 nm [6-29], [6-30]. Two graphite rods (0.9 mm diameter) were

attached to the rotation stage and suspended in the stationary Intralipid™ solution.

6.4.5 f-ADOPT

Figure 6-3 shows the ADOPT system for fluorescent emission detection (f-ADOPT). A pulsed laser (PicoTA, PicoQuant, 780nm, ~100 ps FWHM) was used to illuminate the sample. A collimation system similar to t-ADOPT was used to produce a collimated line of light at the sample. The AFA was mounted on a six degree-of-freedom jig to facilitate precise alignment of the micro-tunnel array with the plane of the collimated light. The fluorescent re-emitted photons were spectrally separated from the incident illumination by a short band-pass interference emission filter and 785nm laser line long-pass filter before reaching the AFA. A Keplerian lens system similar to that used for t-ADOPT was used to image the output of the AFA onto a gated camera (Picostar, LaVision, MCP, 12-bit CCD). A wide camera gate width (1000 ps) was selected to integrate the fluorescence due to the illuminating pulse. As a result, time gating was not used to improve images based on the time domain photon time of flight principle. Instead, the gated system served to minimize reflection artifacts. In addition, the gain feature of the MCP was used to amplify the weak fluorescence signal to enhance sensitivity.

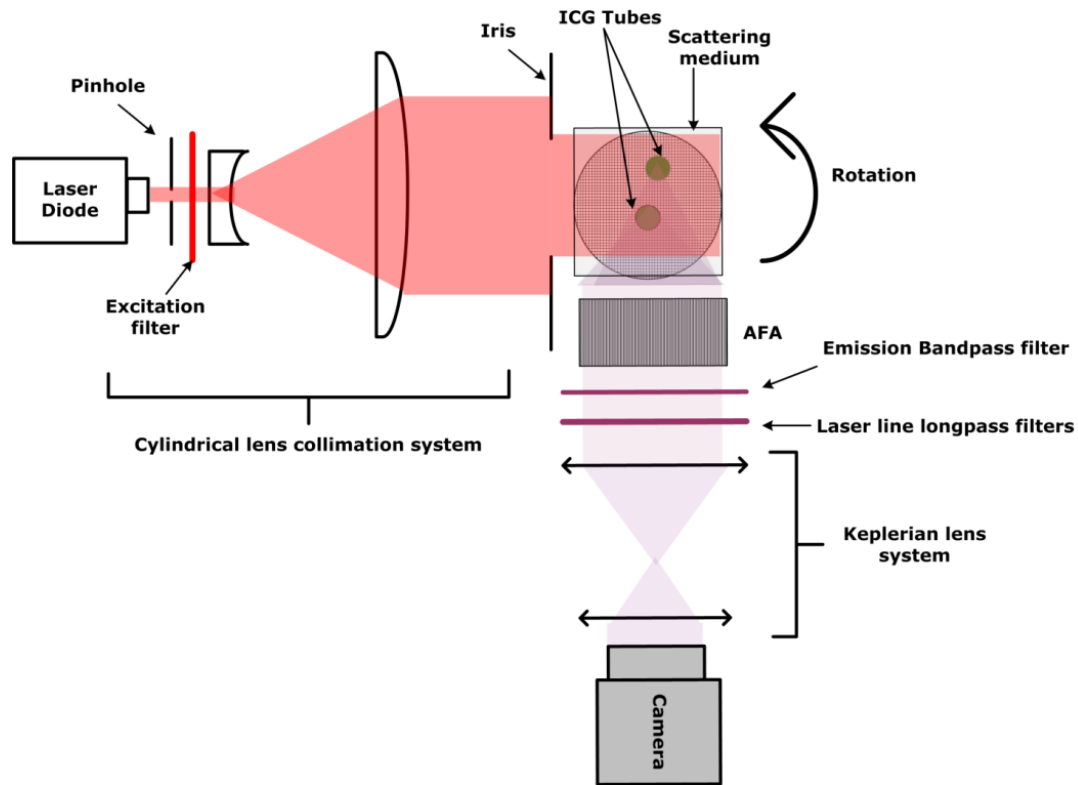


Figure 6-3. System for fluorescent emission angular domain optical projection tomography (f-ADOPT).

To test the contrast and spatial resolution of the f-ADOPT system, a clear glass tube (ID: 1.13mm, OD: 1.2 mm) filled with 20 μM indocyanine green (ICG) diluted with water was used. ICG was chosen as the excitation maximum was well-matched to the pulsed laser source (ICG @ 20 μM : $\lambda_{\text{ex.}} = 768 \text{ nm}$, $\lambda_{\text{em.}} = 807 \text{ nm}$). The tube was mounted to the rotation stage and suspended within the stationary Intralipid™ solution in a manner similar to the graphite rods used in the t-ADOPT experiments.

6.4.6 Depth of field analysis

The depth of field of the ADOPT system was characterized to determine if the resolution was dependent on depth. A glass slide with optically absorbing L-shaped targets [6-19] was suspended in 0.1% Intralipid™ ($\mu'_s = 0.8 \text{ cm}^{-1}$, $\mu_a = 0.01 \text{ cm}^{-1}$) at the front, middle or back positions of a 5 cm optical cuvette. This combination of depth and scattering level was similar to the experiments at higher scattering in the 2 cm cuvette, but the larger cuvette facilitated easier placement of the glass slide. At each glass slide position, the cuvette was incremented vertically in steps of 50 μm . At each step an ADI line scan was collected. The line scans were stacked to produce a 2D image. The image contrast and spatial resolution were determined from the smallest resolvable L-shaped target on the glass slide in the 2D ADI image.

6.4.7 Image reconstruction

From the t-ADOPT and f-ADOPT experiments, sequential line scans were stacked as sinograms and then reconstructed into an image representative of a transverse slice through the sample. Reconstruction was performed with a standard filtered back-projection algorithm (Inverse Radon transform) available in Matlab®. It should be noted that because all rays were approximately parallel, a cone beam reconstruction was not required.

6.4.8 Wedge subtraction and digital image processing

Although the AFA can reject most of the scattered light exiting from the turbid medium, a small portion of scattered light leaks through the AFA and

results in background image noise and reduced image contrast. Image contrast enhancement using digital image processing can be useful as long as the background scattered noise level can be estimated [6-23]. In principle, most scattered photons are assumed to be eliminated while exiting the turbid medium with an angle greater than the acceptance angle of the AFA. However, as discussed earlier in this paper, there are always a proportion of scattered photons which passes through the acceptance angle because of the spherically uniform distribution of scattered photons in turbid media. Experiments show that by slightly deviating the laser beam ($\sim 2X - 3X$ of AFA acceptance angle), approximately the same amount of scattered light can pass through the AFA while all the ballistic photons and most quasi-ballistic photons will be rejected by the micro-tunnels (see Figure 6-1). Therefore, the ADI image collected using a deviated light source will contain mostly scattered photons with good pixel by pixel correspondence with the original scan. Note though that scattered light varies due to many factors such as the individual AFA channel characteristics, illumination uniformity, and the test pattern used as the target. Nevertheless, the scattered background light image can be used as a more accurate method for scattered light correction than pure DSP approaches [20]. With the position of the light source and the angular filter array unchanged, a wedge prism ($\sim 1^\circ$) was inserted after the collimating optics before the sample to deviate the light source. Each image collected with the wedge was then subtracted from the non-wedge ADI image, thus enhancing image contrast on a pixel by pixel basis [6-20]. The

image contrast among the ADI scans was quantified using an image contrast ratio metric based on the following formula:

$$\text{Contrast Ratio [\%]} = \frac{\text{mean}(I_{\max}) - \text{mean}(I_{\min})}{\text{mean}(I_{\max}) + \text{mean}(I_{\min})} \times 100 \quad 6-1$$

where I_{\min} was the average light intensity corresponding to the shadowed region (i.e. due to the shadow of the absorbing target within the phantom) and I_{\max} was the average light intensity corresponding to a non-shadowed area nearby the absorbing target.

6.5 Results and discussion

Figure 6-4 shows ADI scans of L-shaped targets at different positions within the 5 cm optical cuvette. The test structures were clearly visible in images obtained for a scattering medium consisting of 0.1% Intralipid™. However, as the test structures were placed further from the camera (i.e. closer to the light source), the edges of the test structures became less defined, and the interior of the test structures became brighter. However, the experiments showed that at target distances between 1 to 5 cm from the AFA, image contrast varied by 15%. Therefore, image resolution and contrast did not degrade significantly as a function of position within the cuvette, which suggested that the ADI technique was suitable for optical projection tomography of thick turbid samples up to a reduced scattering coefficient-distance product of 4.

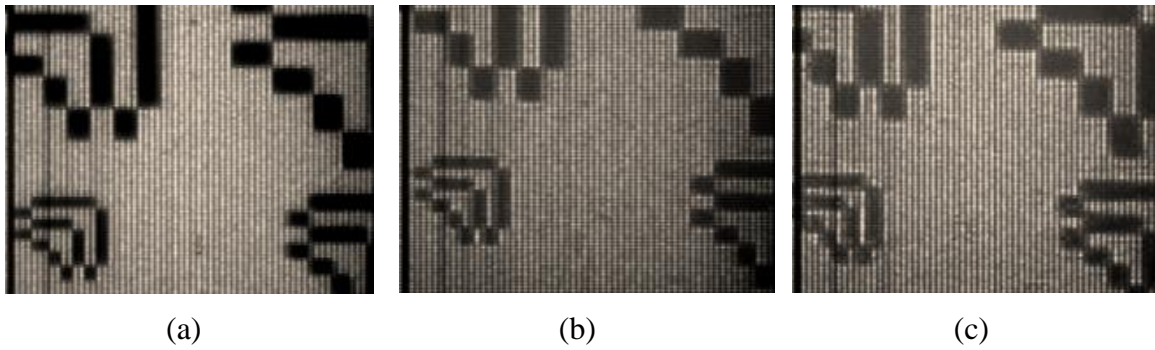


Figure 6-4. Angular domain imaging with the L-shape resolution targets placed in various positions in a 5 cm optical cuvette with scattering medium ($\mu'_s = 0.8 \text{ cm}^{-1}$, $\mu_a = 0.01 \text{ cm}^{-1}$). (a) front position, 0 cm and closest to AFA, (b) middle position, 2.5 cm, and (c) back position, 5 cm and furthest from the AFA. The L-shape test structures had line thicknesses of 150, 200, 300, and 400 μm .

Figure 6-5 shows transmission ADI sinograms collected by stacking line scans of the sample at each of the 200-1.8° rotation steps. The absorbing targets were suspended in water, 0.25%, 0.3% and 0.35% Intralipid™/water solution. This concentration range spanned and exceeded the detection capabilities of trans-illumination ADI (see Methods). The sinograms revealed high contrast projections for water and 0.25% Intralipid™ at all rotation angles. However, as the scattering level was increased to 0.3% Intralipid™, the contrast of the projections became degraded. At the highest scattering level (0.35% Intralipid™) projections were not visible in the sinogram. Therefore, t-ADOPT was limited to turbid samples having scattering coefficients up to and including 0.3% Intralipid™ equivalents or a reduced scattering coefficient-distance product ≤ 4.8 . This result was consistent with the depth of field findings in Figure 6-4. The light intensity on the detection side of the AFA had a sinusoidal pattern due to the periodic pattern of micro-channels and walls between them. As shown in Figure 6-4, the

sinusoidal pattern results in a dark vertical lines in sonograms and ring artifacts in tomographic image. Although not controlled for in this work, one potential way to reduce the ring artifacts by the sinusoidal patterns might be to use digital signal processing where the upper-limit envelope of the sinusoidal pattern can be calculated for each AFA line profile to interpolate the maximum light intensity due to each micro-channel.

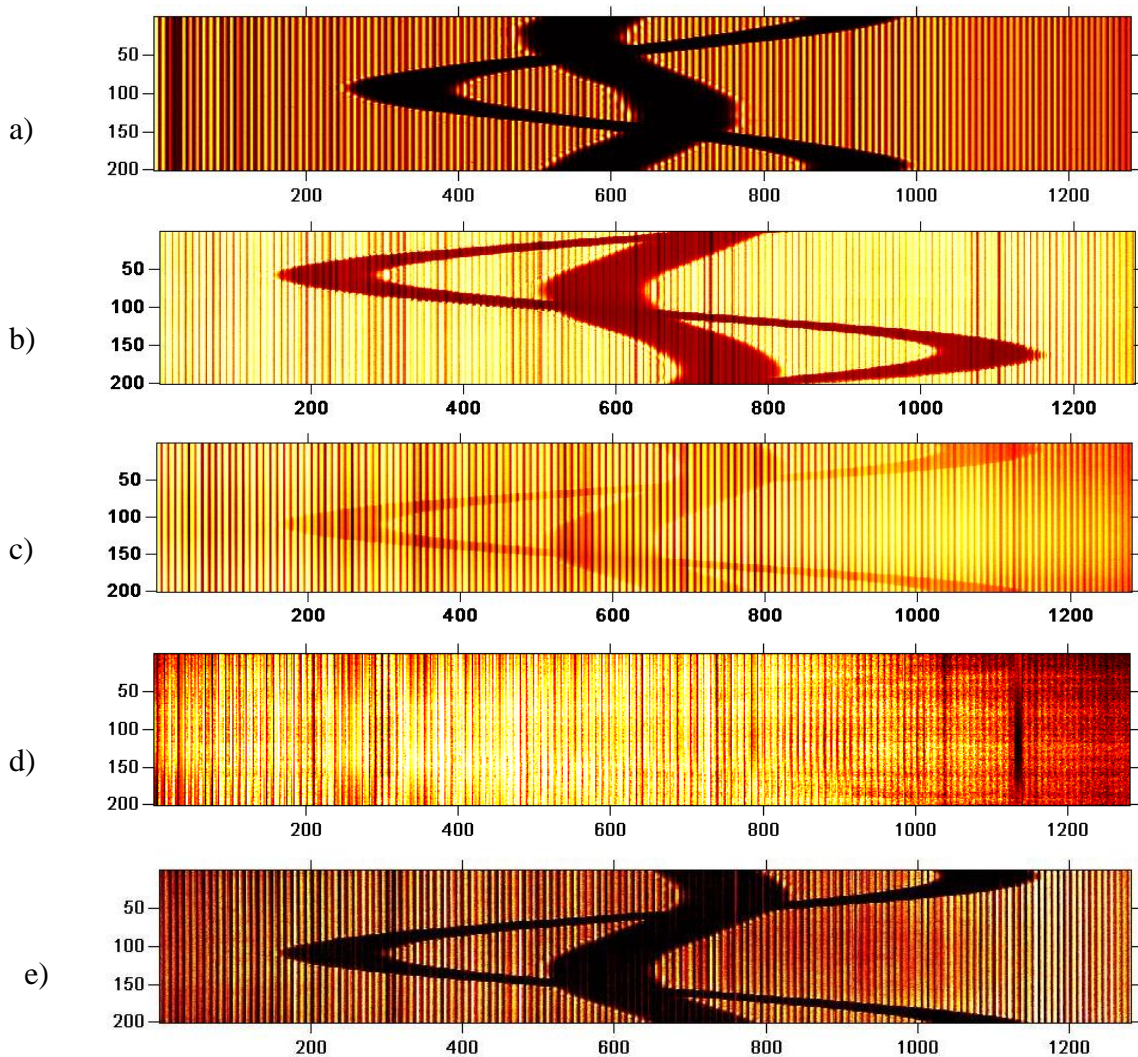


Figure 6-5. Angular domain optical projection scans in trans-illumination mode (t-ADOPT). Sinogram scan of two 0.9 mm diameter graphite rods suspended in a 2 cm optical cell filled with (a) water, (b) 0.25% Intralipid™ with $\mu'_s = 2 \text{ cm}^{-1}$, $\mu_a = 0.01 \text{ cm}^{-1}$, (c) 0.3% Intralipid™ with $\mu'_s = 2.4 \text{ cm}^{-1}$, $\mu_a = 0.01 \text{ cm}^{-1}$, and (d) 0.35%

Intralipid™ with $\mu'_s = 2.8 \text{ cm}^{-1}$, $\mu_a = 0.01 \text{ cm}^{-1}$. Each sinogram represents a 360° rotation with 200 steps. The field of view was approximately 13 mm. (e) Contrast enhanced t-ADOPT sinogram of (c) at the detection limit with 0.3% Intralipid™.

In addition, as the scattering level was increased, the transmitted light decreased and required that the laser power and camera exposure be optimized to fill the dynamic range of the camera. For instance, to collect a t-ADOPT scan in a 2 cm optical cell with 0.25% Intralipid™ (e.g. Figure 6-5(b)) each line scan was acquired with a laser diode power of 240 mW and an exposure time equal to 1 ms. At 0.3% Intralipid™ (i.e. Figure 6-5(c)), the laser power was increased to 350 mW and the camera exposure time for each scan line was lengthened to 10 ms to integrate sufficient signal. However, this increase in exposure had negligible impact on the time required for acquisition of each projection since several other processes (data communication, computer software and rotational stage translation) were much more time consuming and resulted in an ~1 s acquisition time for each projection. Therefore, even though the complete sinograms took ~200 seconds to acquire, there remains potential for significant increases in t-ADOPT imaging speed by reduction of the time for data communication, data processing, and sample rotation.

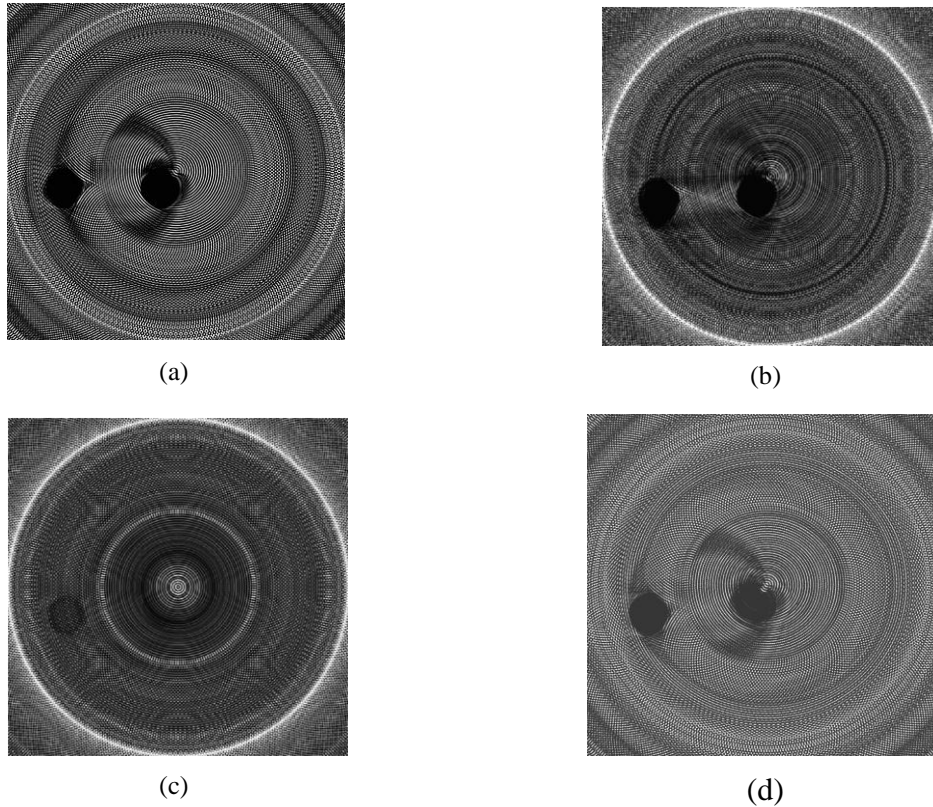


Figure 6-6. Reconstructed t-ADOPT images of two 0.9 mm diameter graphite rods suspended in a 2-cm optical cell filled with (a) water, (b) 0.25% Intralipid™ ($\mu'_s = 2 \text{ cm}^{-1}$, $\mu_a = 0.01 \text{ cm}^{-1}$), and (c) 0.3% Intralipid™ ($\mu'_s = 2.4 \text{ cm}^{-1}$, $\mu_a = 0.01 \text{ cm}^{-1}$). (d) Contrast-enhanced t-ADOPT images of (c) using the wedge subtraction process.

The transmission ADI sinograms were transformed to tomographic images representative of the transverse plane. As shown in Figure 6-6, the rod targets could be clearly identified in the reconstructed transverse images for all scans except at the highest scattering coefficient. Image contrast deteriorated between the 0.25% Intralipid™ sample (Figure 6-6(b)) and 0.3% Intralipid™ sample (Figure 6-6 (c)) in accordance with the respective sinograms (Figure 6-5). In Figure 6-6(b) and (c) bright concentric rings in the reconstruction plane were observed due to background scattered light reaching the detector. Improved

tomographic images were generated from sinograms where the background scattered light was estimated and removed by the wedge subtraction method. An example of the wedge subtraction method in Figure 6-5(e) shows the contrast enhanced t-ADOPT sinogram scanned over 2-cm optical cell filled with 0.3% Intralipid™. The reconstructed image of two absorbing targets using t-ADOPT, Figure 6-6(d), at the detection limit (0.3% Intralipid™) had higher contrast compared to Figure 6-6(c). The contrast ratio increased from 6% before the wedge subtraction (see Figure 6-6(c)) to 48% (~ 8 times) after background scattered light estimation and subtraction (Figure 6-6 (d)). In addition, the bright concentric rings observed in the original reconstructed images were less apparent after wedge subtraction contrast enhancement. Although the wedge subtraction contrast enhancement method resulted in increased image noise by up to a factor of 2, the 8-fold increase in image contrast provided in an overall improvement in contrast to noise ratio by a factor of 4.

Figure 6-7 (a) and (b) shows the fluorescent emission ADI sinograms for water and 0.3% Intralipid™ in a 2-cm optical cuvette. The rotational axis was aligned with the center long axis of the cuvette. A glass rod (1 mm diameter) filled with 20 μ M ICG in water was rotated in a circular path with a 2 mm radius. As with t-ADOPT, the complete scan consisted of 200 steps of 1.8° to cover 360° of rotation. In water, the detected light intensity was uniform as the fluorescent target was rotated (Figure 6-7(a)). However, in the scattering medium, the fluorescence intensity depended on target position (Figure 6-7 (b)). The highest detection intensity was recorded at step number 100th and the lowest light

intensity was recorded at the 200th rotation step. This phase-dependent variation in detected light intensity was due to two light transport effects. First, the fluence of light due to the excitation source was expected to depend in a complex manner on position with the highest fluence within the medium nearest the illumination surface due to backscatter with lower fluence as depth into the medium increased. Second, due to sample rotation, quasi-ballistic light emitted by the fluorescent target captured through the AFA travelled a range of distances from 7.5 mm to 12.5 mm through the scattering medium to reach the cuvette side wall nearest the AFA. Therefore, the detected fluorescence was expected to increase and decrease as the fluorescent target moved closer to and further from the AFA due to absorption and scattering. This effect was expected to be modulated by the excitation fluence which would be higher on one side of the cuvette than the side opposite and result in higher detected fluorescence on one side of the AFA compared to the other. The combination of these two effects resulted in the lowest detected fluorescence for the target in the quadrant furthest from the excitation and the AFA, the highest detected fluorescence for the target in the quadrant closest to the excitation (e.g. sinogram projections numbered 100 to 150) and the AFA and intermediate levels of detected fluorescence for the remaining two quadrants.

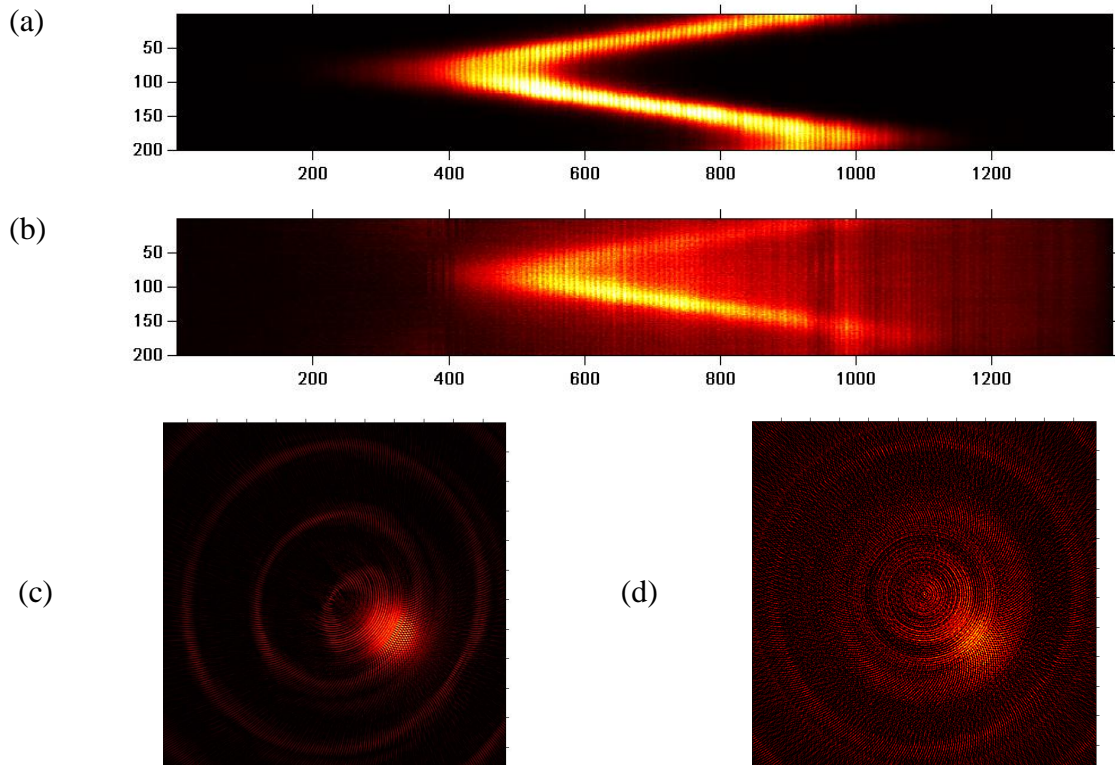


Figure 6-7. f-ADOPT sinogram images of a glass tube (ID: 1.13 mm) filled with 20 μM ICG in a 2-cm optical cell filled with (a) water and (b) 0.1% IntralipidTM ($\mu'_s = 0.8 \text{ cm}^{-1}$, $\mu_a = 0.01 \text{ cm}^{-1}$). (c) Reconstructed f-ADOPT image corresponding to (a). (d) Reconstructed f-ADOPT image corresponding to (b).

The reconstructed image of the f-ADOPT sinograms is shown in Figure 6-7(c) and (d) in non-scattering medium and at the detection limit - 0.1% IntralipidTM. The image contrast was directly affected by the sinogram image contrast. The detection limit of f-ADOPT was less than t-ADOPT. This result was expected as fluorescence emission was isotropic and only a small fraction of emitted photons proportional to the ratio of the solid angle subtended by the AFA to the solid angle subtended by a sphere would be detected. In addition, the quantum yield of ICG fluorescence further decreased the expected signal. The

signal decrease was partially compensated by an increase in laser power and camera integration time. In these experiments, the integration time for each rotation step of the scan was 160 ms and could be extended to improve the signal to noise in the images. In our setup, the image acquisition time was largely dependent on target rotation and electronic processing, so an increase in camera integration time would only lead to a minor increase in acquisition time.

In the future, it will be important to improve the performance of f-ADOPT by considering the complex dependence of signal detected through the AFA as a function of rotation angle of the target. It is anticipated that f-ADOPT images could be improved greatly by first estimating excitation fluence maps (e.g. by experimental measurements and/or Monte Carlo simulation) and then utilizing the maps to affect the tomographic image reconstruction. Further image improvement could be obtained by including a distance-dependent (i.e. distance from the object space to the AFA) weighting factor that accounts for the drop off in detected fluorescence as the target travels farther from the AFA during rotation. It is likely that these two improvements will require iterative image reconstruction approaches with longer computation times, but result in images with greater background uniformity and higher potential for quantitative analysis.

In addition, future efforts could evaluate the possibility of adapting both t-ADOPT and f-ADOPT to 3D tomographic imaging by stepping the sample perpendicular with respect to the long-axis of the AFA between each tomographic scan (i.e. in a similar manner to the depth of field experiment shown in Figure 6-4) . Modification of the current t-ADOPT and f-ADOPT systems with

a z-axis translation stage and modified control software would result in high resolution 3D images of turbid samples with reduced scattering coefficient-thickness products ≤ 4.8 and ≤ 1.6 , respectively. This simple modification for example could enable 3D imaging of tissue specimens up several millimeters in thickness at an image resolution of 200 μm

6.6 Conclusion

Angular domain optical projection tomography based on ADI projection imaging (i.e. t-ADOPT) was introduced and demonstrated for absorbing and fluorescent targets in turbid media. This was accomplished by rotating the sample and collecting many projections. The stacked projections resulted in a sinogram, which was reconstructed into a transverse image using a standard back-projection reconstruction algorithm. Tomographic images of two 0.9 mm diameter graphite rods in a tissue-like scattering medium had good qualitative contrast at a reduced scattering coefficient of up to 2 cm^{-1} . We also observed significant improvements in t-ADOPT image contrast by placement of readily available optical components into the light path combined with digital image subtraction. These methods captured pixel by pixel estimates of the background scattered light levels without compromising optical alignment of the setup. This significant side benefit ensured that contrast enhancement during t-ADOPT could be facilitated without disturbing the highly aligned collimated light source and AFA. We also described f-ADOPT a novel fluorescent optical projection tomography method capable of detecting fluorescent targets embedded in turbid media. The method exploited the collimation detection capabilities of the AFA to

extract photons emitted by a fluorophore embedded deep within a scattering medium. A laser source was used to excite the fluorophore within the medium. Photons emitted by the fluorophore that were not greatly scattered passed through the AFA and were detected by the camera. Scattered photons were rejected by the filter and did not pass through to the camera. By scanning the sample while the sample was rotating, a fluorescence emission sinogram could be generated. The back-projection reconstruction algorithm was used successfully for reconstruction of tomographic images from fluorescence ADI sinogram projections. In the future, These systems could be improved by accounting for light transport effects on excitation light and fluorescence emission during sample rotation, extended to 3D imaging by incremental vertical sample translation between each sinogram, and combining t-ADOPT and f-ADOPT into a hybrid modality for simultaneous detection and tomographic imaging of absorption and fluorescence from the same sample.

6.7 Reference list

- 6-1. J. Sharpe, "Optical projection tomography as a new tool for studying embryo anatomy," *Journal of Anatomy*, 202, pp. 175, (2003).
- 6-2. V. V. Tuchin, Ed., *Handbook of Optical Biomedical Diagnostics*. Bellingham: SPIE Press (2002).
- 6-3. G. Yoon, A. Welch, M. Motamedi, M. Gemert, "Development and application of three-dimensional light distribution model for laser irradiated tissue," *IEEE J. Quant. Electron.*, vol. 23, pp. 1721 (1987).
- 6-4. J. Sharpe, U. Ahlgren, P. Perry, B. Hill, A. Ross, J. Hecksher-Sorensen, R. Baldock, and D. Davidson, "Optical projection tomography as a tool for 3D microscopy and gene expression studies," *Science* 296, 541-545 (2002)

- 6-5. J. R. Walls, "Improving optical projection tomography for three-dimensional imaging of the embryonic mouse", Ph.D. dissertation, University of Toronto, Canada; Available from: <http://www.proquest.com>. Publication Number: AAT NR39864. (2008)
- 6-6. H. F. Zhang, K. Maslov, L. V. Wang, "In vivo imaging of subcutaneous structures using functional photoacoustic microscopy", *Nature Protocols* 2, - 797 - 804 (2007)
- 6-7. M. O'Leary, D. Boas, B. Chance, A. Yodh, "Experimental images of heterogeneous turbid media by frequency-domain diffusing-photon tomography," *Opt. Lett.* 20, 426-428(1995).
- 6-8. Kun Chen, Lev T. Perelman, Qingguo Zhang, Ramachandra R. Dasari, and Michael S. Feld, "Optical computed tomography in a turbid medium using early arriving photons" *J. Biomed. Opt.* 5, 144 (2000).
- 6-9. W. Cai, S. Gayen, M. Xu, M. Zevallos, M. Alrubaiee, M. Lax, R. Alfano, "Optical tomographic image reconstruction from ultrafast time-sliced transmission measurements," *Appl. Opt.* 38, 4237-4246(1999).
- 6-10. M. R. Hee , J. Izzat , J. Jacobson , J. G. Fujimoto , and E. A. Swanson , "Femtosecond transillumination optical coherence tomography , *Opt. Lett.* 18 , 950 952 (1993)
- 6-11. H. Jiang, Y. Xu, and N. Iftimia, "Experimental three-dimensional optical image reconstruction of heterogeneous turbid media from continuous-wave data," *Opt. Express* 7, 204-209 (2000)
- 6-12. S. B. Colak, D. G. Papaioannou, G. W. 't Hooft, M. B. van der Mark, H. Schomberg, J. C. J. Paasschens, J. B. M. Melissen, and N. A. A. J. van Asten, "Tomographic image reconstruction from optical projections in light-diffusing media," *Appl. Opt.* 36, 180-213 (1997)
- 6-13. V. Ntziachristos, J. Ripoll, L. V. Wang, R. Weissleder, "Looking and listening to light," *Nat. Biotechnol.* 23, 314 (2005).
- 6-14. E. E. Graves, J. Ripoll, R. Weissleder, and V. Ntziachristos, "A submillimeter resolution fluorescence molecular imaging system for small animal imaging," *Med. Phys.* 30, 901-911 (2003).
- 6-15. V. Ntziachristos and R. Weissleder, "Experimental three-dimensional fluorescence reconstruction of diffuse media by use of a normalized Born approximation," *Opt. Lett.* 26, 893-895 (2001)
- 6-16. M. A. O'Leary, D. A. Boas, X. D. Li, B. Chance, and A. G. Yodh, "Fluorescence lifetime imaging in turbid media," *Opt. Lett.* 21, 158- (1996)

- 6-17. Godavarty, M. J. Eppstein, C. Zhang, S. Theru, A. B. Thompson, M. Gurfinkel, E. M. Sevick-Muraca, "Fluorescence-enhanced optical imaging in large tissue volumes using a gain-modulated ICCD camera," *Phys. Med. Biol.* 48, 1701-1720 (2003).
- 6-18. M.E. Zevallos, S.K. Gayen, B. Baran Das, M. Alrubaiee, R.R. Alfano, "Picosecond electronic time-gated imaging of bones in tissues," *IEEE Journal of Selected Topics in Quantum Electronics*, 5, no.4, pp.916-922 (1999).
- 6-19. G. M. Turner, G. Zacharakis, A. Soubret, J. Ripoll, and V. Ntziachristos, "Complete-angle projection diffuse optical tomography by use of early photons," *Opt. Lett.* 30, 409-411 (2005)
- 6-20. T. N. Kumar, S. B. Raymond, B. J. Bacskai, and D. A. Boas, "Comparison of frequency-domain and time-domain fluorescence lifetime tomography," *Opt. Lett.* 33, 470-472 (2008)
- 6-21. G.H. Chapman, M. Trinh, N. Pfeiffer, G. Chu, and D. Lee, "Angular Domain Imaging of Objects Within Highly Scattering Media Using Silicon Micromachined Collimating Arrays", *IEEE J. Sel. Top. Quantum Electron.* 9, 257-266, (2003).
- 6-22. F. Vasefi, B. Kaminska, P. K. Y. Chan, and G. H. Chapman, "Multi-spectral angular domain optical imaging in biological tissues using diode laser sources," *Opt. Express* 16, 14456-14468 (2008)
- 6-23. F. Vasefi, G. H. Chapman, P. K. Y. Chan, B. Kaminska, N. Pfeiffer, "Enhanced angular domain optical imaging by background scattered light subtraction from a deviated laser source" *Proceedings of SPIE* 6854, 68541E (2008).
- 6-24. F. Vasefi, B. Kaminska, G. H. Chapman, and J. J.L. Carson, "Image contrast enhancement in angular domain optical imaging of turbid media," *Opt. Express* 16, 21492-21504 (2008)
- 6-25. F. Vasefi, P.K.Y. Chan, B. Kaminska, G. H. Chapman, N. Pfeiffer, "An Optical Imaging Technique Using Deep Illumination in the Angular Domain," *IEEE J. Sel. Top. Quantum Electron.* 13, 1610-1620 (2007).
- 6-26. F. Vasefi, B. Kaminska, G. H. Chapman, and J. J. L. Carson, "Angular distribution of quasi-ballistic light measured through turbid media using angular domain optical imaging," *Proceedings of SPIE* 7175, 717509 (2009).
- 6-27. F. Vasefi, E. Ng, B. Kaminska, G. H. Chapman, and J. J. L. Carson, "Angular domain fluorescent lifetime imaging in turbid media" *Proceedings of SPIE* 7183, 71830I (2009)

- 6-28. N. Pfeiffer, P. Chan, G. H. Chapman, F. Vasefi, B. Kaminska, "Optical imaging of structures within highly scattering material using a lens and aperture to form a spatiofrequency filter" Proceedings of SPIE 6854, 68541D (2008).
- 6-29. S. Jacques, Optical properties of "Intralipid™", an aqueous suspension of lipid droplets, <http://omlc.ogi.edu/spectra/intralipid/index.html> .
- 6-30. HG van Staveren, CJM Moes, J van Marle, SA Prahl, MJC van Gemert, "Light scattering in Intralipid-10% in the wavelength range of 400-1100 nanometers," Appl. Opt. 30, 4507-4514, (1991).

7: ANGULAR DOMAIN FLUORESCENCE IMAGING FOR SMALL ANIMAL RESEARCH⁶

7.1 Abstract

We describe a novel macroscopic fluorescent imaging technique called Angular Domain Fluorescence Imaging (ADFI) applicable to the detection of fluorophores embedded in biological tissues. The method exploits the collimation detection capabilities of an angular filter array (AFA). The AFA uses the principle of acceptance angle filtration to extract minimally scattered photons emitted from fluorophores deep within tissue. The goal of this paper was to develop ADFI system for imaging near infrared fluorescent markers for small animal imaging. According to the experimental results, the ADFI system offered higher resolution and contrast compared to a conventional lens and lens-pinhole fluorescent detection system. Furthermore, ADFI of a hairless mouse injected with a fluorescent bone marker revealed vertebral structural and morphometric data that correlated well with data derived from volumetric X-ray CT images. The results suggested that ADFI is a useful technique for sub-millimeter mapping of the distribution of fluorescent biomarkers in small animals.

7.2 Introduction

⁶ The following chapter has been published in Journal of Biomedical Optics, 15, 016023 (2010), under the co-authorship of M. Belton, B. Kaminska, G. H. Chapman, and J. J. L. Carson.

Fluorescent agents are important tools for mechanistic studies on biomolecular function and disease processes [7-1,7-2]. Confocal and multiphoton microscopies have emerged as powerful methods for imaging of fluorescent agents in tissues up to a few hundred micrometers below the surface of skin [7-3]. Alternative methodologies based on macroscopic epi-illumination imaging have employed sensitive cameras to acquire surface-weighted images of fluorescence from agents up to a few millimeters below the surface of the skin [7-4]. These imaging approaches have been highly successful in furthering our understanding of biological systems, but they have been limited to imaging function and processes near the surface largely on account of the optical scattering properties of tissue. Scatter degrades the spatial resolution as the depth increases. Therefore, there is a need for new methodologies that can overcome the limitations imposed by optical scatter to enable the capture to *in vivo* fluorescence images with larger fields-of-view and precise measures of fluorescent agent distribution at deeper sites within tissues.

7.3 ADFI principle

Here, we describe the use of silicon micro-machined Angular Filter Array (AFA) to reject unwanted scattered photons and pass the image forming photons (in the form of ballistic and quasi-ballistic photons from the source) that have straight or nearly straight trajectories [7-5-7-9]. The angular filter array discriminates non-deviated photons from the much more numerous diffusely scattered photons emitted from a fluorophore embedded at depth within tissue. As shown in Figure 7-1a, the multiply scattered photons emitted from the

fluorophore are less likely to exit from the tissue surface with a trajectory acceptable to the AFA, while those that are not scattered (or weakly scattered) will have a trajectory within the angular acceptance range of the AFA. Consequently, the accepted photons will be detected by the camera whereas the multiply scattered photons will not. The resultant line image formed on the camera represents a projection of the fluorophore distribution within the tissue. The performance of the AFA is not dependent on coherence, or the wavelength of light [7-6]. We tested the performance of angular domain fluorescence imaging (ADFI) to map fluorophores over a large field-of-view with sub-millimeter spatial resolution at tissue depths up to 2 mm.

7.4 ADFI methods

The main component of the AFA was an array of 1.5-cm long micro-tunnels micro-machined on to a silicon substrate as shown in Figure 7-1b. The opening of each micro-tunnel was square in cross-section and had dimensions of $80\ \mu\text{m} \times 80\ \mu\text{m}$ (acceptance angle $\sim 0.42^\circ$). The walls of the AFA were patterned with many small features ($2\ \mu\text{m}$ height with periodicity of $20\ \mu\text{m}$) to suppress internal reflections within each micro-tunnel. A flat silicon wafer was used as the top piece to enclose the micro-tunnels to form the AFA (not shown). The aspect ratio and micro-tunnel size for the square geometry provided optimal image contrast compared to other filter geometries [7-10]. An alternative to the AFA is the lens-pinhole optical setup that provides similar angular filtration to the AFA and can be realized by inserting a pinhole into a Keplerian lens system (Figure 7-1c). However, our previous work has shown that, in comparison to the

pinhole, the AFA has superior spatial resolution [7-7] and is insensitive to the lens aberrations.

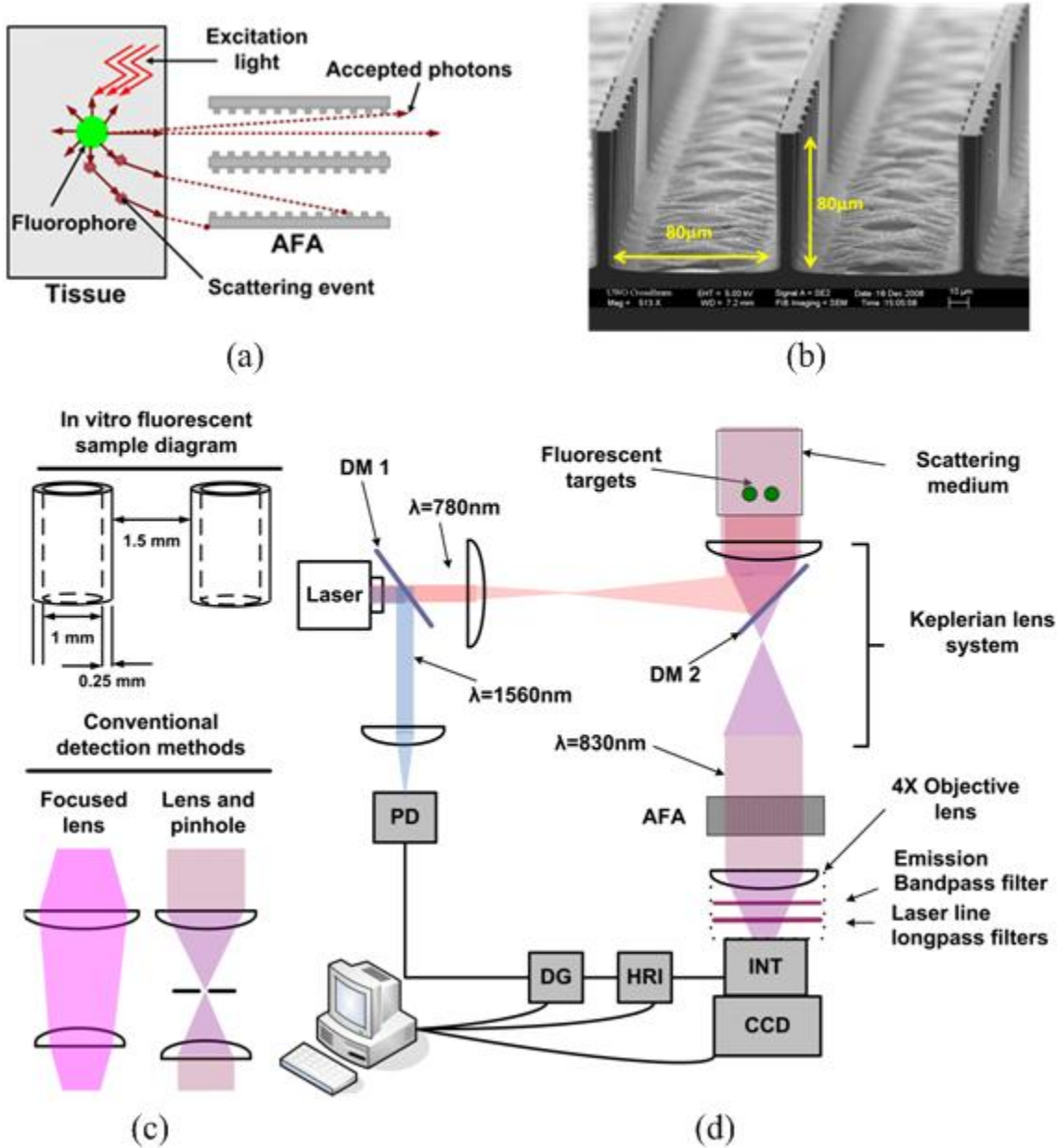


Figure 7-1. Principle and method for Angular domain fluorescent imaging. (a) Angular domain fluorescent imaging principle. (b) Silicon micro-machined angular filter array (bottom piece). (c) Diagram of glass capillary tubes used to contain fluorescent agents during phantom-based experiments (top). Schematic of imaging setups used to compare performance of ADFI system (bottom). (d) Optical imaging setup (Abbreviations: CCD, charge-coupled device; HRI, high rate imager; INT, intensifier; DG, delay generator; DM, dichroic mirror; AFA, angular filter array; and PD, photo diode).

The one dimensional linear array of micro-tunnels necessitated a scanning system for the capture of 2D images. We employed a computer-controlled z-axis stage to incrementally raise the sample between scans. One horizontal line image of the sample was taken through the AFA at each step and a final 2D image was assembled from the stacked line images. Hence, an entire region of the sample could be passed through the field of view of the AFA and imaged. The experimental setup shown in Figure 7-1d was based on the reflection based angular domain imaging configuration. A thin uniform line of light from a pulsed laser source was used to excite the fluorescent target. The AFA accepted the minimally deviated photons while the photons outside the acceptance angle of the AFA were rejected. The addition of time gating to the imaging system created a mode-lock mechanism which minimized the effects of stray light by synchronization of the gate intensified CCD with the incoming laser pulse. Although we used a pulsed illumination setup, the gate width of the camera was wide enough to capture the entire light pulse mimicking a CW laser setup (i.e. early arriving photons were not discriminated). The light intensity on the detection side of the AFA had a sinusoidal pattern due to the periodic pattern of micro-channels and walls between them. To remove the artifact effect of the micro-channel profile on the resultant images (as shown in our previous work [7-5-7-10]), the upper-limit envelope of the sinusoidal pattern was calculated for each AFA line profile to interpolate the maximum light intensity at each micro-channel.

7.5 ADFI results

In order to evaluate the performance of ADFI, the spatial resolution and contrast were quantified and compared with results from two conventional fluorescent imaging configurations: [(i) a focused lens system, and (ii) a Keplerian lens and pinhole system] as shown in Figure 7-1c.

Spatial resolution and contrast were quantified by fluorescent imaging of two glass tubes filled with 3,3-diethylthiatricarbocyanin (DTTC, 20 μM) embedded in a 1% Intralipid™ scattering medium. Figure 7-2a presents representative fluorescent images for the three detection methods at two depths within the scattering medium (i.e. at the surface and 1 mm deep). Figure 7-2b shows the horizontal line intensity profile computed for each image for the 1 mm depth shown in Figure 7-2a. Figure 7-2c presents the spatial resolution analysis based on the measurement of the target diameter at various depths divided by the measured diameter at the surface. The fluorescent target diameter (***Dia.** [depth x]*) was calculated based on twice the distance between the position of the maximum and the location where the intensity was 0.707 of the maximum using the line profiles (e.g. Figure 7-2b). The graph clearly shows the broadening of the fluorescent target as the depth increases, which was improved by implementation of the AFA. The focused lens system had the poorest spatial resolution at every depth tested.

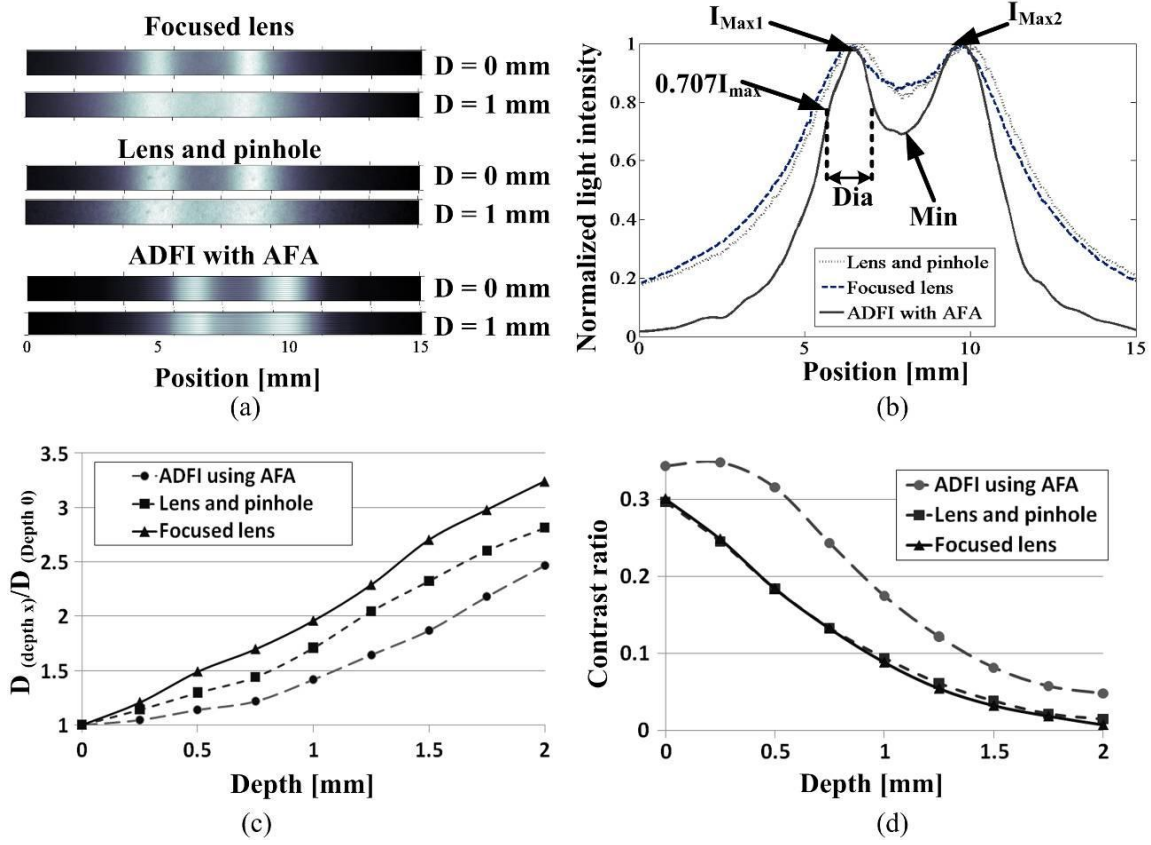


Figure 7-2. Angular domain fluorescent imaging in turbid media. Targets were two glass tubes filled with 20 μ M DTTC diluted in ethanol and placed at various depths ($D \leq 2$ mm) from the detection surface of an optical cuvette (5 cm \times 5 cm \times 2 cm) filled with 1% Intralipid™: (a) image from lens system focused ($f/\# 2$) to the surface of the sample (top), lens and pinhole system (acceptance angle = 1.15°) (middle), and ADFI using AFA (bottom). (b) Line profiles from the images in (a) for $D = 1$ mm. (c) Spatial resolution analysis of the fluorescent targets as a function of depth. (d) Contrast ratio analysis of the fluorescent targets as a function of depth

The lens-pinhole arrangement provided spatial resolution performance intermediate to the AFA and conventional lens-based systems. The image contrast as a function of depth was evaluated using formula:

$$Contrast\ ratio = \frac{Average(I_{max\ 1}, I_{max\ 2}) - I_{min}}{Average(I_{max\ 1}, I_{max\ 2}) + I_{min}} \quad 7-1$$

Where $I_{\max 1}$ and $I_{\max 2}$ represent the maximum light intensity of two fluorescent tubes 1.5 mm far from each other and I_{\min} represents the minimum light intensity between them shown in Figure 7-2b. The contrast ratio was much higher for ADFI than the conventional and lens-pinhole approaches at all target depths tested (Figure 7-2d). Furthermore, the contrast ratio appeared to be relatively invariant up to a depth of 0.5 mm for ADFI, where with the other methods the contrast ratio dropped by nearly 2-fold. These results demonstrated that ADFI had better overall imaging performance when compared to a conventional lens or lens and pinhole arrangement.

In order to demonstrate the capability of the ADFI at small animal imaging, a near infrared optical bone marker (IRDye® 800CW BoneTag) in a hairless mouse was used. This compound combined a fluorescent agent with a calcium-chelator and served as a marker of the mineralization process. For this experiment, we used a SKH1 mouse (6 weeks old) and an intraperitoneal injection of 2 nmol (100 μ l) dye. The mouse was euthanized 48 h later and the spine was imaged. For imaging, the mouse was placed in a 5-cm optical path cuvette in a prone position (i.e. back to the detector). We also obtained volumetric images from the same animal using a clinical X-ray CT scanner (GE) for comparison. As shown in Figure 7-3, vertebrae of the mouse spine were visible by X-ray CT (Figure 7-3a & b), ADFI (Figure 7-3c), and conventional reflection-based fluorescence imaging (Figure 7-3d). The lens based imaging system used the same optical setup (including pulsed laser and gated camera), but without the use of AFA and Keplerian lens system.

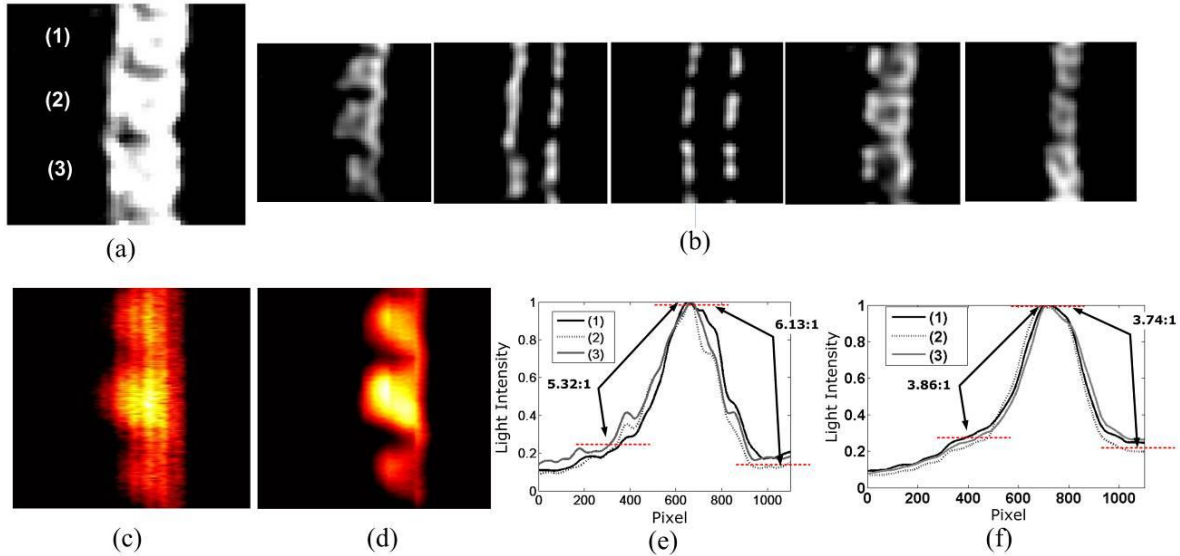


Figure 7-3. Mouse ADFI bone imaging with comparison to X-Ray CT and conventional reflectance-based imaging. (a) Maximum intensity projection of five X-ray CT slices (b) showing three vertebrae of the spine of a hairless mouse. Images in (b) represent 0.625mm thick slices though the animal proceeding from shallowest (left) to deepest (right) in increments of 0.625 mm. (c) Angular domain fluorescent image of three vertebrae of the mouse spine corresponding to (a & b). Camera integration time was 2 s for each line scan. (d) Conventional reflectance-based image of three vertebrae of the mouse spine indicated in (a & b). Each image (a-d) represents a field of view of 1 cm wide by 1 cm high. (e) Fluorescence intensity line profiles corresponding to (c). (f) Fluorescence intensity line profiles corresponding (d).

Analysis of the X-ray projection images of the horizontal diameter of the vertebra numbered 1 to 3 in Figure 7-3a were 2.7 mm, 3.0 mm, and 3.0 mm, respectively. By a similar analysis on the corresponding vertebrae using the ADFI image (Figure 7-3c), we obtained 2.8 mm, 3.2 mm, and 2.5 mm in the same order. Similar measurements performed with conventional lens-based detection were 2.9 mm, 3.2 mm, and 2.1 mm (Figure 7-3d). These measurements showed an error between ADFI and X-ray of less than 17% for the third vertebrae (deepest as shown in Figure 7-3b), while the error between the lens-based measurement and X-ray for the third vertebrae was 30%. The measured light intensity of ADFI was more uniform compared to the surface-

weighted conventional lens-based measurement. For all vertebrae, the background fluorescence intensity (measured 300 pixels to the left and right of the peak intensity) decreased by approximately 5.3 and 6.1 times to the left and right, respectively (shown in Figure 7-3e). Similar measurements performed using the lens-based imaging system without the AFA (Figure 7-3f) resulted in the background fluorescence intensity decreasing by approximately 3.9 and 3.7 times to the left and right, respectively. Therefore, based on the worst case ADFI contrast measurements there was at >30% improvement in contrast compared to corresponding contrast measurements made with the conventional lens-based imaging system.

In addition, ADFI appeared to have better sensitivity to fluorescent emission from deep within the animal compared to conventional lens-based imaging. Although conventional lens-based imaging resulted in more defined spatial boundaries of the fluorescent target, the resultant image was surface-weighted (i.e., fluorescence originating close to the surface appeared brighter compared to deeper emissions). This effect was clearly observed for vertebra 3, which was deeper in tissue when compared to the other two vertebrae (as shown in shallow X-ray images in Figure 7-3b). As expected, vertebra 3 appeared dimmer in the conventional reflection-based image (Figure 7-3d). However, in ADFI scan, the same vertebra was brighter and more representative of the true diameter as measured by X-ray CT imaging (Figure 7-3a).

In summary, phantom and animal model tests demonstrated the usefulness of employing an angular filter array for fluorescent imaging to

enhance the localization of fluorescently-labelled targets. ADFI has several advantages over other fluorescence imaging modalities including a larger field of view, higher image resolution, and better image contrast at tissue depths exceeding 1 mm. This system could be used ultimately for the detection and sizing of tumour-targeted fluorescent agents at tissue depths significantly greater than conventional reflection-based imaging.

7.6 Acknowledgement

This project was funded by grants from the Natural Sciences and Engineering Research Council of Canada (NSERC) to Bozena Kaminska and Dr. Jeffery J.L. Carson. In addition, partial funding was provided by the Translational Breast Cancer Studentship for Fartash Vasefi from the London Regional Cancer Program.

7.7 Reference list

- 7-1. R. Weissleder & V. Ntziachristos, "Shedding light onto live molecular targets," *Nature Medicine* 9, 123 - 128 (2003)
- 7-2. F. R. Wouters, P. J. Verveer, P. I. H. Bastiaens, "Imaging biochemistry inside cells," *Trends Cell Biol.* 11, 203–211 (2001)
- 7-3. E. B. Brown, R. B. Campbell, Y. Tsuzuki, , L. Xu, P. Carmeliet, D. Fukumura, R. K. Jain, "In vivo measurement of gene expression, angiogenesis and physiological function in tumors using multiphoton laser scanning microscopy," *Nat. Med.* 7 , 864–868., (2001)
- 7-4. R. Hoffman, "Green fluorescent protein imaging of tumour growth, metastasis, and angiogenesis in mouse models," *Lancet Oncol.* 3(9):546-56. (2002)
- 7-5. G.H. Chapman, M. Trinh, N. Pfeiffer, G. Chu, and D. Lee, "Angular domain imaging of objects within highly scattering media using silicon micromachined collimating arrays," *IEEE J. Sel. Top. Quantum Electron.* 9, 257, (2003)

- 7-6. F. Vasefi, B. Kaminska, P. K. Y. Chan, and G. H. Chapman, "Multi-spectral angular domain optical imaging in biological tissues using diode laser sources," *Opt. Express* 16, 14456 (2008)
- 7-7. N. Pfeiffer, P. K. Y. Chan, G. H. Chapman, F. Vasefi, and B. Kaminska, "Optical imaging of structures within highly scattering material using a lens and aperture to form a spatiofrequency filter," *Proceedings of SPIE*, 6854, 68541D (2008)
- 7-8. F. Vasefi, B. Kaminska, G. H. Chapman, and J. J. L. Carson, "Image contrast enhancement in angular domain optical imaging of turbid media," *Opt. Express* 16, 21492 (2008)
- 7-9. F. Vasefi, P.K.Y. Chan, B. Kaminska, G. H. Chapman, N. Pfeiffer, "An Optical Imaging Technique Using Deep Illumination in the Angular Domain," *IEEE J. Sel. Top. Quantum Electron*, 13, 1610 (2007)
- 7-10. F. Vasefi, B. S. Hung, B. Kaminska, G.H. Chapman, J. J. L. Carson, "Angular domain optical imaging of turbid media using enhanced micro-tunnel filter arrays", *Proceedings of SPIE* 7369 , 73691N (2009)

8: SUMMARY AND FUTUREWORK

8.1 Overview

The following chapter summarizes the dissertation outcome based on the studies that have been reported in chapters 2 through 7 followed by a perspective and outlook for future development. The summary discussion is subjective rather than chronological. Each topic is discussed based on the referral studies presented in previous chapters followed with a current opinion and the recommended future work. The summary is divided into two categories: 1) technology advancement and 2) application development. The chapter ends with a conclusion section, where the chief outcomes from each of the studies, with the entire project contribution are reviewed and tied back to the objectives and goals which were planned and described in the Introduction.

8.2 Technology advancement

As discussed in Chapter 3 and 4, the detectability of ADI is limited in high scattering medium ($> 6 \times \text{MFP}'$) because at this scattering the number of ballistic/quasi-ballistic photons steadily decreases, while the number of scattered photons remains high. By assuming that the scattered photons will exit the medium with a uniform distribution of angles, there are always a proportion of scattered photons in the acceptance range of angular filter micro-channels. The unwanted accepted scattered light creates a gray background in the image, resulting in poor image contrast (described comprehensively in section 3.4.2). At

the detection limit, informative photons are more quasi-ballistic (dependent on acceptance angle) while the ballistic light sensing will become less than system noise. This makes the AFA's acceptance angle selection difficult. Because by decreasing the acceptance angle of the AFA, we will allow less scattered light to leak through the AFA, however fewer quasi-ballistic photons are permitted to pass through the micro tunnels and reach the detector. On the other hand, increasing the acceptance angle of the AFA may lead to more scattered light, which results in lower image contrast and higher "background scattered noise". In order to improve the clarity of resultant ADI scans at high scattering level, two main tracks has been analyzed: 1) AFA design optimization and 2) image enhancement, which will be described in the following sections successively.

8.2.1 Angular filter array development

A conventional AFA consists of a linear array of semicircular micro-channels which was described in section 1.5. Although using isotropic etchant seems to be convenient, this fabrication process has two major negative aspects. The first issue relates to the poor reproducibility of the wet chemical etching procedure. Agitation of the sample container and time can alter the etch rate of chemical etchant. Therefore, in order to get precise channel aperture size, the sample must be inspected frequently and then again soaked in the etchant solution to etch more because of etch rate inconsistency. The second issue is due to physical geometry of the conventional micro channels. The resultant micro channels are asymmetric in the horizontal versus the vertical direction, because of semi-circular aperture geometry. The same asymmetric geometry happens for

the channel walls (see Figure 1-9). Aside from the fabrication issues, the micro-channel internal walls are extremely reflective especially in shallow incident angles. The unwanted reflection affects the true acceptance angle of angular filters and lets in more unwanted scattered, which leaks through the filter and is sensed by the detector (described in section 4.3.4).

Our solution was to replace the silicon wet etching process with the Deep Reactive Ion Etching (DRIE) process resulting in square-shaped micro channels. The fabrication process is highly reproducible with excellent uniformity throughout the entire area of the 4-inch silicon wafer. The square-shaped micro-channels have symmetric geometry in both horizontal and vertical axes. As a result, AFA's with various aspect ratios can be manufactured precisely as shown in section 4.3.2. AFAs with different aspect ratios were fabricated for experimental performance testing. The experimental analysis described in Chapter 4 was a continuation of previous Monte Carlo analysis presented in [8-1] and analyzed the effect of AFA geometry on ADI performance. The results showed that decreasing aperture size below $40\ \mu\text{m} \times 40\ \mu\text{m}$ can degrade the image contrast and the scanning time. The edge sharpness for L-shape resolution targets with thickness $>100\ \mu\text{m}$ was consistent for the aperture size from $20\ \mu\text{m}$ to $80\ \mu\text{m}$. The results also showed that the longer channels can improve image contrast, in agreement with previous Monte Carlo simulations [8-1].

In order to minimize channel wall reflections, many studies were done in teamwork with Paulman Chan [8-2] including carbon evaporation deposition and

surface roughening via chemical procedure by an NH_4OH -based solution. However, both methods turned out to be somewhat inefficient. The carbon evaporation deposition process was a messy procedure, with high levels of particulates and debris remaining behind [8-2]. This tended to clog the AFA channels. Furthermore, the carbon film did not adhere to the channel surface well, which resulted in carbon film lift off during the cleaning procedure. As an alternative, carbon deposition by sputter coating machine was tested (see Appendix A) and resulted in improved uniformity and adherence of the carbon layer. However, even with carbon coating, the channel walls were fairly reflective for shallow angles of incidence.

The procedure selected initially for roughening the AFA tunnel topology consisted of chemical wet etching using a NH_4OH solution [8-2]. The early results of ADI using roughening of the AFA tunnels considerably attenuated the reflected scattered light within the micro-tunnels [8-3] which seemed to be a better approach compared to carbon deposition since it resulted in fewer occlusion of the tunnels. However, the roughening process still affected the micro channel shape, which led to clogging of some of the channels. Therefore, a cleaner way of surface roughening was highly desirable [8-3].

In order to attenuate the shallow angled reflections, RTAFA was introduced in section 4.3.3 by inserting small periodic ridges into the square shaped micro channel walls to trap the reflected light. The full description of RTAFA fabrication process is described in Appendix A. The reflectivity can be further diminished by carbon deposition of RTAFA device. Our experiment results

showed that 50% image contrast improvement can be achieved by using RTAFAs compared to non-patterned AFAs (see section 4.4.2).

8.2.2 Image enhancement methods

In addition to AFA device developments, image contrast was enhanced by improving other system aspects such as instrumentation and software. The image enhancement techniques can be summarized to three subsections: (1) artefact correction methods, (2) background scattered noise estimation and subtraction, and (3) combinations of ADI with polarization and time gating methods.

8.2.2.1 Artefact correction methods

Due to the physical nature of the AFA, the light intensity profile detected by the camera was not only affected by illumination uniformity, but also it was largely affected by the micro-tunnel aperture and channel wall geometries (see Figure 8-1). The ADI line images have periodic square-like patterns with bright centers surrounded by dark corners. As described in section 5.9.1, in the ADI scans, gaps between the channels resulted in dark vertical bands that were considered an image artifact. The dark bands made image contrast enhancement and edge detection difficult and degraded the horizontal spatial resolution in the resultant ADI images [8-4].

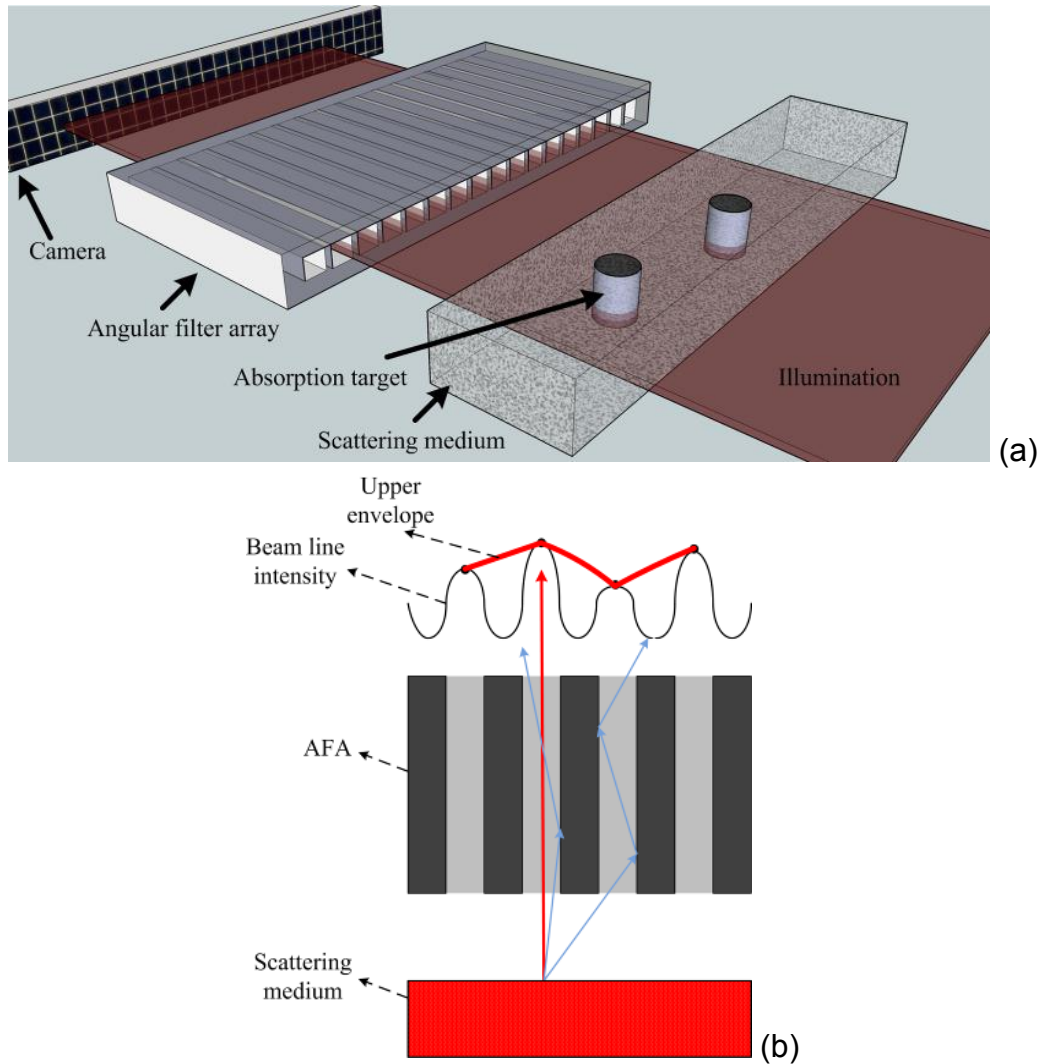


Figure 8-1. (a) Transillumination ADI System Schematic (b) Line profile due to micro – channel array physical geometry.

One potential solution to the artefact problem is to fabricate two-dimensional angular filters with one array of tunnels above the other, but with one array shifted horizontally to eliminate the gaps between the lower arrays of tunnels during imaging. However, this approach depends on the fabrication of an AFA with two levels that are precisely aligned. A simpler solution is to take two scans as shown in section 5.9.1, where one scan is taken normally, and the second scan is collected after shifting the test sample horizontally by half of the

channel spacing. Using both scans to reconstruct a full image without dark vertical gaps between the tunnels, the full-reconstructed image should improve image resolution horizontally. This reconstruction process involved comparing a column of pixels from one image with the corresponding column in the second image, and inserting the brighter of the two columns into the new reconstructed image. The full image is reconstructed for all columns, from left to right, thus forming the new image without vertical bands.

After full image reconstruction, the image result still contains square-shaped areas of illumination surrounded by darker areas. These patterns are frequently repeated both horizontally (channel walls) and vertically (scanning procedure) with a constant period. In order to remove the darkened areas surrounding the areas of illumination, periodic noise removal in the Frequency domain was presented in section 5.9.2. Transferring the image to the Fourier domain, the periodic noise can be removed by a notch filter. The periodic noise removal procedure had a marginal improvement though and needed to be addressed with other DSP procedures. Besides, doubling the scanning time is not an applicable procedure towards improving scanning procedure toward in vivo imaging.

As shown in Figure 8-1(b), the light intensity at the output of the AFA is spatially modulated based on the channel size and spacing as shown in Figure 8-1. The line intensity profile has a sinusoidal pattern with the same periodicity as the channel spacing, where the signal due to the channel opening is represented at the peak of each period. In principle, the peak intensities are

more affected by (quasi-)ballistic photons, while the minimum intensities are more affected by scattered light that leaks through the adjacent micro-channels due to wall reflections as shown in Figure 8-1(b).

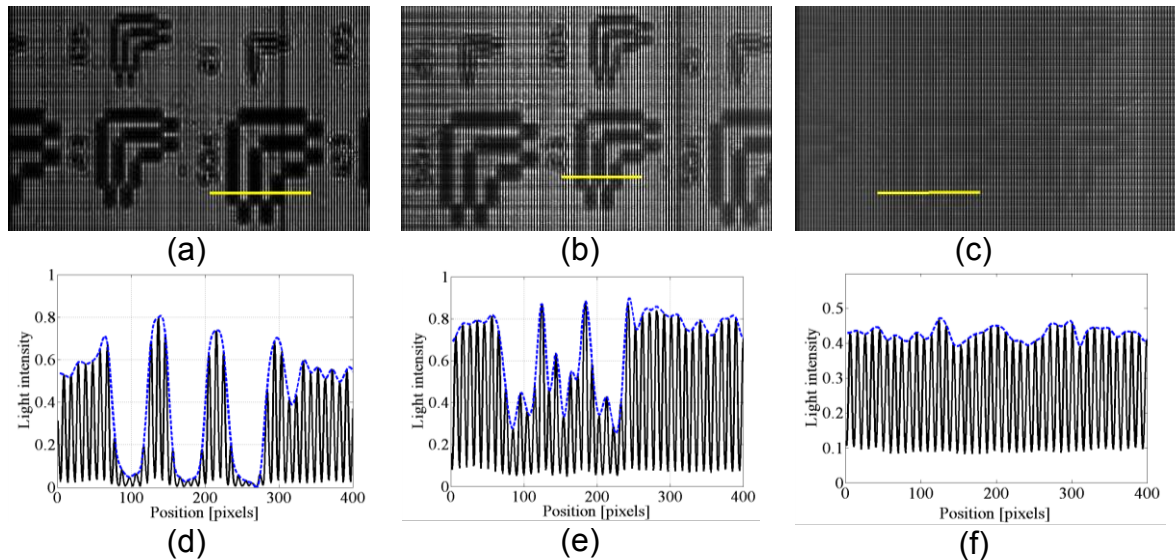


Figure 8-2. ADI scan of sample including resolution target (L-shaped targets with lines and spaces of $\sim 51 \mu\text{m}$, $102 \mu\text{m}$, $153 \mu\text{m}$, and $204 \mu\text{m}$) placed in the middle position of 2 cm thick optical cell filled (a) Water, (b) 0.25% IntralipidTM ($\text{MFP}' = 5$), and (c) 0.3% IntralipidTM ($\text{MFP}' = 6$) using an 808 nm laser diode. The line profile of yellow bar corresponding to images from (a) to (c) is shown in (d) – (f) respectively. The blue curve is the extracted upper envelope for each profile.

Therefore, the upper envelope data from each line profile represented the signal with a greater weighting toward (quasi-)ballistic photons. Locating the upper envelope for each ADI line image was successful at removing the image artefacts. Figure 8-2(a)-(c) display the transillumination ADI scan of L-shape resolution targets in a non-scattering medium, a scattering medium with $5 \times \text{MFP}'$, and a scattering level equivalent to $6 \times \text{MFP}'$, respectively. The corresponding line profiles (indicated in images as yellow bars) are presented in Figure 8-2(d)-(f). The calculated upper envelope of each line is shown in blue overlaid onto each line intensity profile.

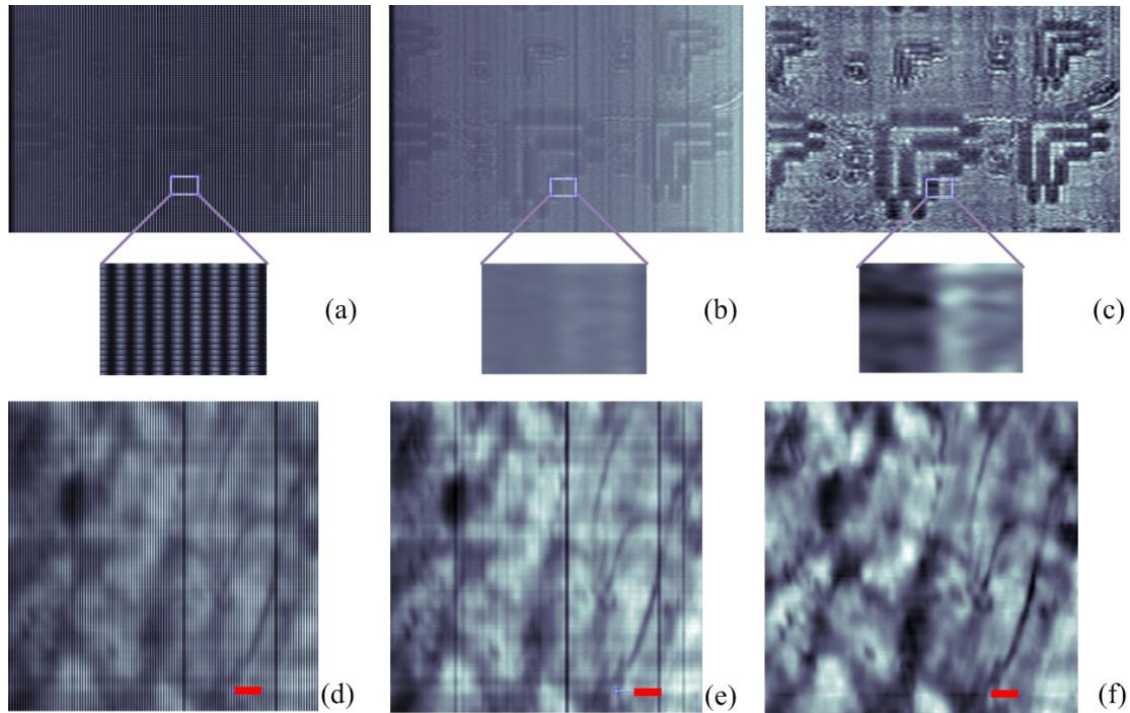


Figure 8-3. Results of ADI Image artifact correction and contrast enhancement for Intralipid™ phantom in scattering level of $6\times$ MFP' (shown in Figure 8-2), (a) original scan, (b) image reformed based on upper envelop extraction, (c) the spatially normalized image. The same process has been implemented for ADI scan of 5 mm chicken breast tissue: (a) original image (b) After envelop extraction (c) after spatial normalization (red bar is 1mm long)

Figure 8-2 clearly shows the effect of scattered light in ADI scans as background noise, which is evident at the minima in the line profiles. At the highest scattering level, the background scattered noise became dominant and the signal was within the range of the noise. Any contrast enhancement algorithm has to be done before correction of artefacts created by the ADI scanning procedure since the dark lines would not be enhanced in the resulted post-processed image. Figure 8-3(a) shows the image of the L-shaped targets corresponding to Figure 8-2(c) enhanced by post processing. After upper envelope calculation, the resultant 2D ADI image can be optionally normalized

both in row and column followed by subtraction of the average intensity to improve the image uniformity

In order to test the efficiency of proposed image processing procedure on a real tissue sample, the same image enhancement procedure was used on an ADI image collected from a 4-mm thick chicken breast sample (Figure 8-3(d)). The chicken breast tissue was sandwiched between two glass slides and placed perpendicular with respect to the collimated line illumination and AFA. In addition to the banding artefacts due to the AFA, patterns in the ADI image corresponded to the heterogeneity of the tissue, and were likely due to the muscle fibre orientation and presence of fatty tissue. However, the image enhancement results provided a substantial reduction in banding artefacts and qualitative improvement in image contrast (Figure 8-3(f)). The full manuscript describing this methodology is under preparation.

Compared to double scanning and periodic noise removal procedure, the envelope detection is faster since it requires one scan and is less computationally intensive. Furthermore, this methodology can also be applied for non-transmission based measurements such as deep illumination ADI, or ADFI arrangements.

8.2.2.2 Background scattered noise estimation and subtraction

As discussed in 3.4.2, in high scattering level, there are always small proportions of scattered photons in the acceptance range of our angular filter, thus creating the gray background in the imaging result. In this thesis, three procedures were attempted to estimate the background scattered noise.

The first background estimation method (described in section 5.9.3) was based on digital image processing algorithm, which was implemented using a morphological opening operation with line-shape element. The line-shape element helped remove the illumination pattern caused by the laser beam profile. However, the background estimated image had poor spatial resolution, namely the estimated background image did not contain pixel-by-pixel correlation with original image, which was suboptimal.

In morphological opening or any other DSP methods, background estimation of each pixel is extracted from a group of adjacent pixels which may lead to false estimation. As a result, estimation of background noise using optical methods without using the neighbouring pixels can be more efficient compared with only DSP. Chapter 3 introduced two separate optical system modifications to pursue the background noise estimation using polarization gating and deviation of collimated illumination. The rationale behind polarization gating was based on the fact that ballistic photons retain their initial polarization when passing through a turbid sample, while scattered photons lose their initial polarization memory. Therefore, the image resultant from cross polarization arrangement would contain merely scattered photons and could lead to reliable background estimates. In the polarization gating approach, the image resultant from the parallel polarization configuration contained both ballistic and scattered photons, while the cross polarization created an image that excluded ballistic photons. However, experiments described in 3.6.3 show that this assumption cannot be employed at a scattering level of more than $4 \times \text{MFP}$. Because at a higher

scattering level, The ADI technique is mainly dependent on quasi-ballistic photons for image formation, which alter their initial polarization after passing through the turbid media.

The third methodology for background noise estimation (described in section 3.5.4) was implemented by taking advantage of angular filtration by the AFA to collect only background scattered light in the image and perform a simple subtraction. By deviating the laser beam, the unscattered photons were directed completely out of AFA's field of view and only scattered photons were detected. Deviation of the laser beam was accomplished with a wedge prism with angular deviation of larger than $2\times - 3\times$ of AFA's acceptance angle. The wedge subtraction method for ADI image contrast enhancement demonstrated to be a successful method that was more effective than the DSP enhancement procedure as well as the polarization method. However, wedge subtraction could only be implemented by double scanning which increased the total scanning time. For future work, using a two level AFA one with set of channels for capturing unscattered photons and another set for capturing only scattered photons might represent a potential solution to decrease the scanning time.

8.2.2.3 Combination of time or polarization gating with ADI

The effects of polarization gating combined with ADI as well as time gating and ADI combination were investigated in chapters 3 and 4 respectively. The results showed only slight improvements in image contrast for the combination of ADI and polarization gating (named PADI), which was likely due to the loss of polarization memory of quasi-ballistic and multiply scattered photons. As shown

in section 4.3.7, Time-resolved ADI (TADI) was implemented with a pulsed laser and ultra fast gated ICCD camera system. The scan results indicated that TADI with 250 ps temporal gate width provided noticeable image contrast improvement compared to ADI alone. Because the leaked scattered photons through the AFA mainly exited the sample later than unscattered photons. However, 250 ps temporal gate is not short enough to reject all late-arriving photons for a 1 cm thick tissue equivalent medium. TADI would be much more effective if the temporal gate width of the fast camera could be decreased down to 30-40 ps, which is not currently available with MCP camera technology, but could be implemented with a streak camera.

8.3 Application development

Besides technological advancements, the thesis encapsulated a wide range of investigation on ADI technology applications. The main goal of application exploration was based on defining ADI technology limitations and advantages in application specific perspective rather than only transillumination based arrangement. The presented systems were implemented to image tissue-mimicking phantoms or real biological tissue samples to characterize more precisely the technological challenges and benefits.

8.3.1 Multispectral/ Hyperspectral imaging

One important benefit of employing AFA technology compared to lens based filters (with common aberrations) is due to their wavelength independent operation making this technology ideal for multispectral/hyperspectral

measurements. Chapter 2 presented a series of ADI measurements in transillumination mode at various wavelengths from an Argon laser (532 nm) to three longer wavelengths (670 nm, 808 nm, and 975 nm) using laser diode sources. Shifting from a green laser to red and near infrared allowed for real biological tissue samples such as chicken breast tissue to be examined. The limitation and possibilities of biological tissue imaging was observed thoroughly. Transmitted photons through turbid samples, which are passed through the AFA were successfully fitted to the Beer-Lambert Law up to a scattering level equivalent to 5 mm of soft tissue. Beer-Lambert law fitting provides the potentials to apply ADI for quantitative estimation of the concentration of specific chromophores such as haemoglobin.

The potential quantitative abilities of hyperspectral ADI is currently under investigation. Hyperspectral imaging constructs a hyper-cube of information enclosing both spectral and spatial data regarding a scene. Classically, the hyperspectral cubes are obtained by capturing many images of the sample under various bandwidth illuminations, or with different band-pass filters inserted before the detector [8-5]. Approaches for getting hyperspectral imaging data include acoustic filters [8-6], liquid crystal filters [8-7] and filter wheels [8-5].

An alternative method of hyperspectral imaging is the “Pushbroom” imaging spectrometer [8-5]. In this methodology, the spectroscopic imager collects a slit image from the object and transform it onto a two-dimensional camera in which the spatial information is displayed in one axis while wavelength information presented along the other axis. Wavelength dispersion can be made

by a prism, reflection, or transmission based grating. The advantages of this method can be expressed as its high spectral resolution which is well suited for scanning samples with unknown or complex spectral features. Because the entire spectrum of the each pixel in the slit is available in real time. In order to get an entire image cube, a scanning procedure has to be implemented by the imaging spectrometer. For example, in high scattering media like biological tissue, the optical absorption/scattering of normal and cancerous tissue have sometimes small variations especially in near infrared range [8-8]. Therefore full spectral analysis becomes inevitable for cell identification based on spectral transmission pattern.

Angular Filter arrays can be combined with a “Pushbroom” imaging spectrometer since the angular filter consists of a linear array which can be inserted between the sample and the spectrometer slit (See Figure 8-4). The filtered photons accepted by the AFA can be sensed by the imaging spectrometer and transformed into a two-dimensional image on the CCD camera.

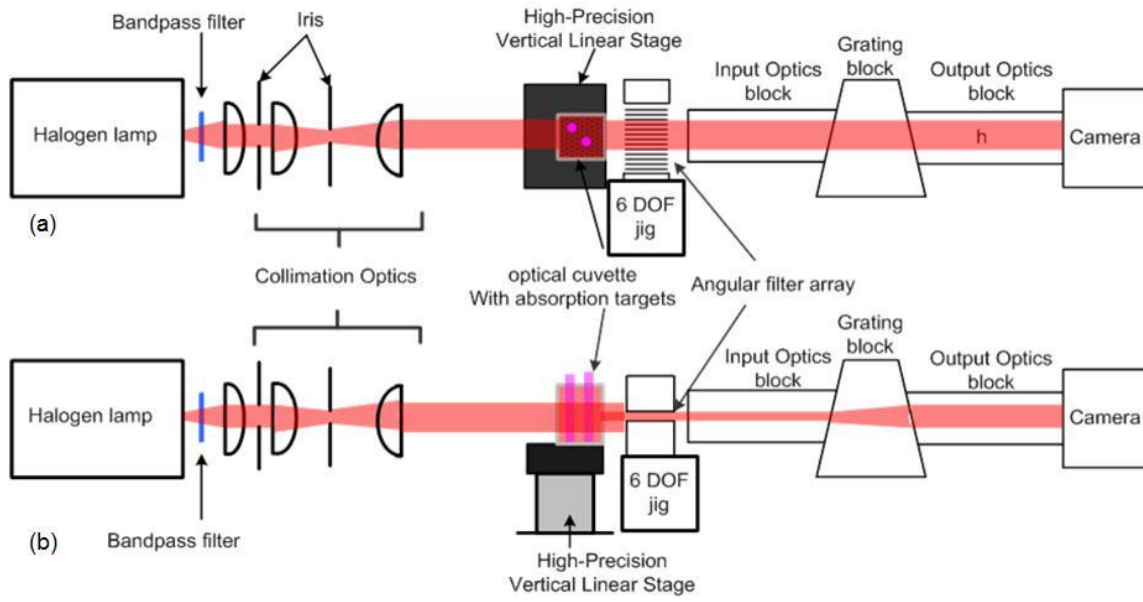


Figure 8-4. Angular domain hyperspectral imaging diagram in transillumination mode: (a) top view, (b) side view.

Figure 8-4 shows an Angular Domain Spectroscopic Imaging (ADSI) system that employs an AFA for angular filtration of the incoming light. The ADSI consists of a broadband non-coherent source (e.g. Halogen lamp), a collimation system, an Angular Filter Array (AFA), and an imaging spectrometer (e.g. P&P Optica Inc., Kitchener, Canada). As shown in Figure 8-4, the free-space collimation system was implemented to trans-illuminate the sample over a wide range of wavelengths in the red/ near infrared region of the spectrum (650 nm - 950 nm). The AFA rejected nearly all scattered light exiting the turbid sample and selected the image forming quasi-ballistic light. The imaging spectrometer decomposed the output of the AFA into hyperspectral images representative of spatial location and wavelength (shown in Figure 8-5). Each pixel at the detector presents 12 μm of spatial space along with 0.6 nm of spectral bandwidth. More details about ADSI system can be found in [8-9].

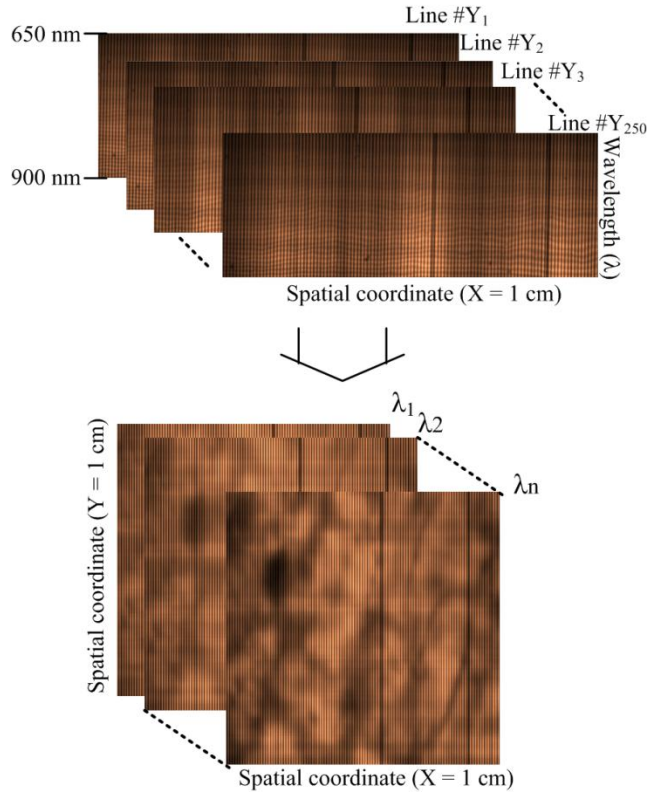


Figure 8-5. Transformation of ADSI images from the CCD camera (top) to multiple 2D images of tissue sample at different wavelengths (5 mm fresh chicken breast tissue)

At each step, the ADSI system collects an angularly filtered line shadowgram from the object with both spatial and wavelength information. The 2D image can be reconstructed by stacking up the different line scans at specific wavelength bands as shown in Figure 8-5.

The ADSI system was tested on a 5mm thick fresh chicken breast tissue sample as shown in Figure 8-6. The scan consisted of a 1 cm × 1 cm field of view of the 5 mm chicken breast internal projection images of breast muscles with fat layers at various depths. In order to get 8 spectral images with 30 nm spectral

differences, every 50 rows of the resultant image in the spectrometer were accumulated ($50 \times 0.6 \text{ nm} = 30 \text{ nm}$).

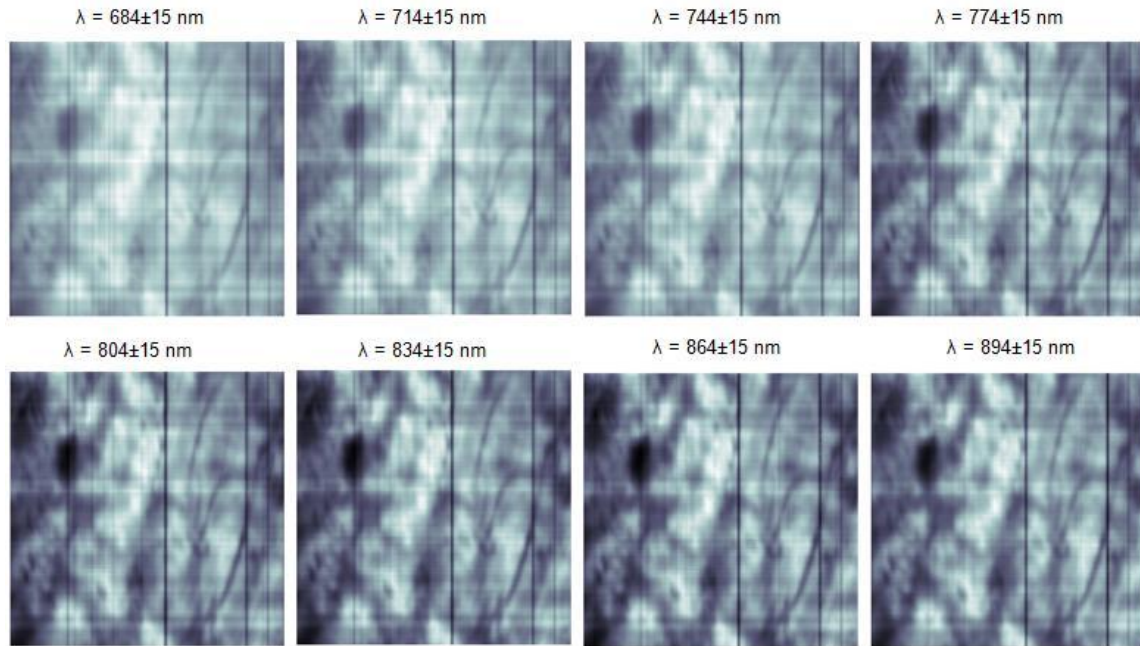


Figure 8-6. Angular domain spectroscopic imaging results of a 5 mm fresh chicken breast tissue sample at 8 wavelength ranges.

The spectral transmission or absorption of each region can also be extracted to identify the existence of tissue types based on spectral signature. Figure 8-7 shows the spectral difference of different regions in 2D map due to differences in tissue type.

More development on a pattern recognition algorithm is required to precisely classify different tissue types based on their spectral transmission characteristics.

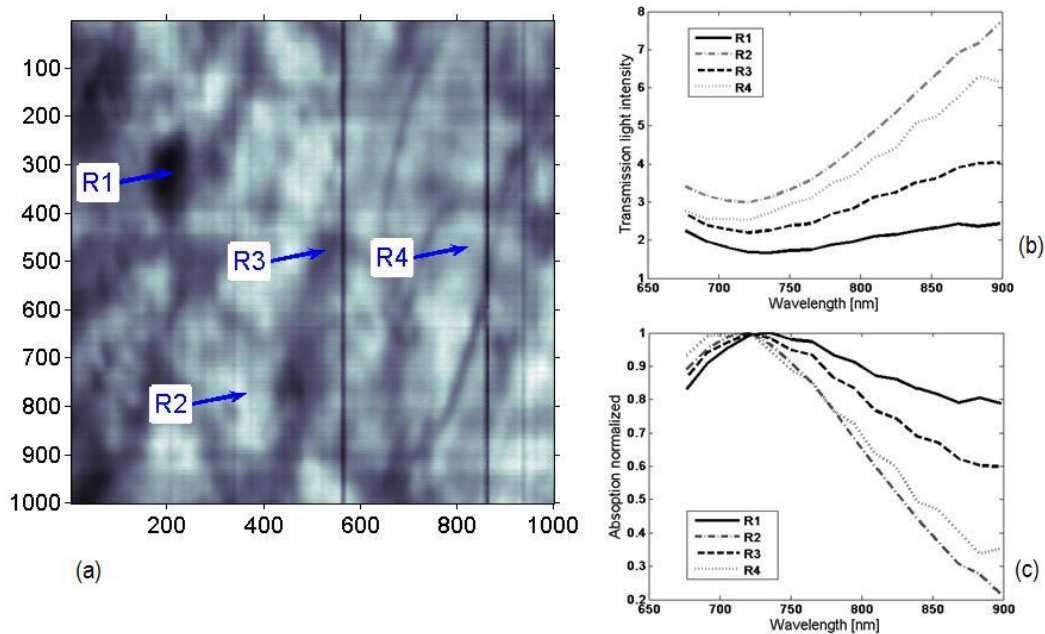


Figure 8-7. Transmission and absorption (normalized) characterization of 5 mm chicken breast tissue at different regions of interest: (a) projection image with regions of interest, (b) transmitted light intensity through sample in selected regions, (c) normalized absorption curve for selected regions of interest

8.3.2 Deep illumination ADI

Initially, the main focus of my ADI research was in transillumination arrangement. However, many optical imaging methods operate in reflection mode due to the light penetration limitations in human body. ADI measurement in reflection mode can lead to a wide range of new applications. Based on this motivation, I have developed (See chapter 5) a new imaging system based on ADI technology named deep illumination ADI to capture photons originating within the scattering medium in a reflection-based configuration. Photons that diffuse deep into the tissue and travel back to the tissue surface can be used as a source of illumination. Using this principle, the diffused photons which have minimal deviation related to the AFA acceptance angle can bear information from

absorptive targets located within the sample. The injected light will tend to propagate isotropically, forming what can be named a “glow ball”. A small acceptance angle angular filter is placed at the medium’s surface and aligned to the detector to record a projected shadowgram of absorptive targets deep inside the sample. A proportion of the emitted light will always fall within the ADI acceptance angle and act as a new source of “ballistic” and “quasi-ballistic” photons that pass from the “glow ball” to the detector. In this configuration, deep illumination ADI can operate with an illumination source located laterally to one side of the sample, or even on the same side of the sample.

Successful imaging of L-shape targets inserted in tissue-mimicking phantoms at different depths (up to 3 mm) was achieved using the deep illumination ADI system with an Argon laser as the illumination source. The similar system was constructed using a near infrared laser diode to detect absorption targets 2.5 mm below the surface of chicken breast tissue for proof of principle validation.

Hyperspectral deep illumination ADI can be implemented (as a future work) with a combination of AFA and spectroscopic imager in order to extract spectral characteristics of subsurface objects beneath the tissue surface.

8.3.3 Angular domain optical projection tomography

ADI with micro-channel arrays was originally developed to construct projection image from internal structures of a turbid medium. The resultant image is a two dimensional shadowgram which does not contain any depth information.

However, imaging through small tissue slabs or small animals (e.g. newborn mice), it is highly desirable to extract the axial position of optical contrast within the whole tissue sample. Chapter 6 extended the two dimensional capture of projection images of conventional ADI to tomographic image reconstruction with adapting ADI with computed tomography techniques. Similar to X-ray CT technology, the depth information (transverse image) was extracted by collecting images at various angles and processing with a filtered back-projection algorithm. As shown in section 6.5, the tomographic system was capable of obtaining transverse images of absorptive targets in a scattering medium with sub-mm resolution. Tomographic ADI had the same penetration limitation as transillumination ADI, which can image through ~ 5 mm biological specimens. The tomography system was also able to collect fluorescent signals in a dark field illumination setup, resulting in a tomographic map of fluorescent targets in a tissue mimicking phantom. Concurrent absorption and fluorescence CT can be implemented by integrating t-ADOPT and f-ADOPT systems.

ADOPT system can be extended to hyperspectral measurement by addition of imaging spectrometer after AFA which can be used for tissue sample hyperspectral analysis on a 4D data set.

8.3.4 Angular domain fluorescence imaging

Photons from fluorescence generation that propagate from deep tissues mostly undergo multiple scattering events and appear to follow a random walk. Thus, remitted fluorescence light declines rapidly with depth of fluorescence generation. By capturing remitted photons using conventional epi-illumination

detection for targets below 1 mm depth in tissue, the resultant images have low spatial resolution (with unwanted broadening), which leads to poor localization of fluorescent markers located deep in tissue. Collimation detection methodology using AFAs can reject some of the scattered photons reemitted from fluorescent dyes and create higher resolution images compared to conventional epi-illumination fluorescence detection.

As described in chapter 7, the angular filter device can differentiate between minimally scattered fluorescent photons from the more plentiful scattered fluorescent photons emitted from fluorophores located in tissue. The scattered photons emitted from fluorophores have less likelihood of exiting the tissue surface with an angular deviation acceptable to the AFA.

Since the performance of the AFA is not dependent on coherence, or the wavelength of light, angular domain fluorescence imaging can be used to map fluorophores over a large field-of-view with sub-millimetre spatial resolution at larger depths into tissue.

Chapter 7 shows how the collimation detection capabilities of an angular filter array (AFA) were exploited for fluorescent imaging in both tissue-mimicking phantoms and murine model. The phantom study showed that ADFI had superior performance by improving both image contrast and resolution compared to conventional methods.

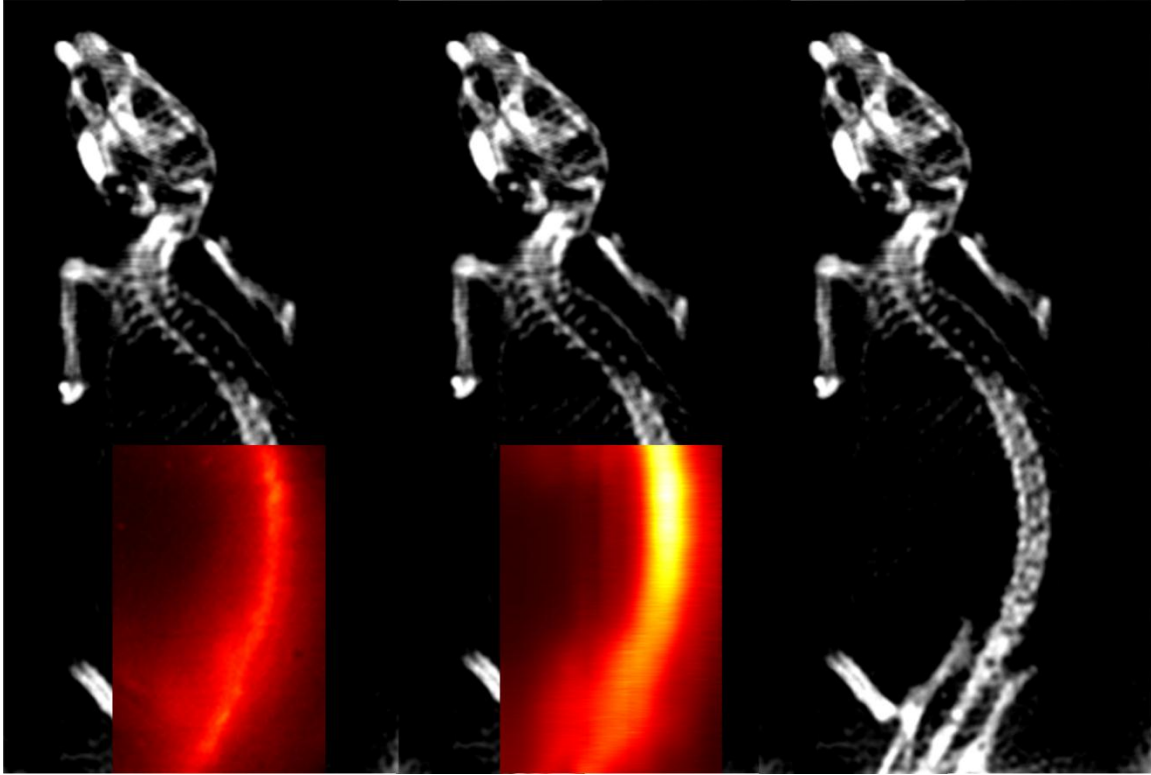


Figure 8-8. Mouse ADFI bone imaging result (middle image) with comparison to X-Ray CT (right) and conventional reflectance-based imaging (left). (The ADFI artefacts are corrected based on the envelop detection method described in section 8.2.2.1)

As shown in Figure 8-8 (described in section 7.5), ADFI was also used to collect images of a hairless mouse injected with a fluorescent bone marker. Structural and morphometric data of vertebrae collected using ADFI in correlation with data derived from volumetric X-ray CT and conventional optical imaging shows that ADFI can provide higher contrast and a less surface-weighted image compared to epi-illumination fluorescence imaging system.

8.3.4.1 Angular domain fluorescence lifetime imaging

The same arrangement for ADFI with addition of time-resolved measurement can be used for detection of a fluorescent dye below the surface of

turbid media with lifetime property extraction. The method exploits the collimation detection capabilities of an angular filter array to form a projection image of a fluorophore embedded within the tissue-mimicking phantom. A femto-second pulsed laser was used to illuminate the tissue and excite the fluorophore within the medium. Fluorescent emission passing through the angular filter array was detected by an ultra fast gate intensified CCD camera. The array accepted photons with trajectories within the acceptance angle of micro-channels and rejected most of the scattered fluorescent light exiting the tissue. Like ADFI, angular-domain fluorescence lifetime imaging (ADFLI) should provide images with greater spatial resolution of imbedded sources compared to conventional techniques. More details about ADFLI system are described in Appendix B.

8.4 Conclusions

This thesis described multiple novel advancing techniques for angular domain optical imaging along with implementation of new applications for the technology. The technological developments presented improved the ADI detectability in higher scattering levels. The advancements are described in three parts: *i)* silicon micro-machined angular filter array design optimization along with fabrication and testing, *ii)* background scattered noise estimation and subtraction using digital image processing techniques as well as optical methods such as polarization gating and detection of sample with deviated illumination by wedge prism, and *iii)* system design and implementation of combination of ADI with polarization gating and time domain imaging systems to evaluate the efficiency of merging different methods on the power of scattered photon rejection.

The most important outcomes from the technology development demonstrate that for AFA optimization square-shaped aperture geometry using DRIE process can lead to cleaner and more consistent devices. Patterning the AFA micro-channel walls followed with carbon deposition by a sputtering system can reduce the reflections incident to channel walls, which lead to less leakage of scattered photons to the detector. Estimation of background scattered noise by deviated illumination was the most effective method for image contrast enhancement when compared to DSP only and cross polarization methods. Finally, the combination of time and angular domain imaging (TADI) can increase the ADI detectability level to higher scattering levels by using a shorter temporal gating width by a fast camera.

Building on previous studies with ADI in a trans-illumination arrangement, it was confirmed that ADI could be employed to capture information-carrying photons from scattered light back-reflected from tissue. This approach will enable applications of ADI for tissue imaging where illumination and detection need to be on same side of the sample. I also developed an ADOPT system, which provided transverse images of internal structures of turbid samples by incorporating ADI with a CT algorithm. I also exploited the collimation detection capabilities of the AFA to localize fluorescent targets embedded at depth within a turbid medium. The fluorescent imaging system using AFA offered higher resolution and contrast compared to a conventional detection system in both in vitro and animal tests. Multispectral and hyperspectral angular domain systems

were introduced and tested with tissue-mimicking phantoms as well as real biological tissues.

8.5 Reference list

- 8-1 N. Pfeiffer, "Imaging of turbid media using trajectory filter methods" Ph.D. thesis, Simon Fraser University, Burnaby, BC, Canada, 2009
- 8-2 P. Chan, "Angular Filters for Angular Domain Imaging Optical Tomography in Highly Scattering Media" M.A.Sc. thesis, Simon Fraser University, Burnaby, BC, Canada, 2008.
- 8-3 Chan, P. K. Y, Vasefi, F., Chapman, G. H., Kaminska, B., and Pfeiffer, N. (2007) Multispectral angular domain optical tomography in scattering media with argon and diode laser sources. Proceedings of SPIE Vol. 6435 (SPIE, Bellingham, WA), 64350M.
- 8-4 Vasefi, F., Chapman, G. H., Chan, P., Kaminska, B., and Pfeiffer, N. (2008) Enhanced angular domain optical imaging by background scattered light subtraction from a deviated laser source. Proceedings of SPIE Vol. 6854 (SPIE, Bellingham, WA), 68541E.
- 8-5 Tuan Vo-Dinh, Ed., "Biomedical Photonics Handbook," Publisher: CRC, (2003)
- 8-6 V. Voloshinov and N. Gupta, "Tunable acousto-optic filters for monitoring of atmospheric ozone," in Instrumentation for Air Pollution and Global Atmospheric Monitoring, J. O. Jensen, ed., Proc. SPIE 4574, p. 162–173 (2002).
- 8-7 C. Mao, and J. Heitschmidt, "Hyperspectral imaging with liquid-crystal tunable filter for biological and agricultural assessment," Proc. SPIE 3543, 172 (1999)
- 8-8 R. L. P. van Veen, H. J. C. M. Sterenborg, A. W. K. S. Marinelli, and M. Menke-Pluymers, "Intraoperatively assessed optical properties of malignant and healthy breast tissue used to determine the optimum wavelength of contrast for optical mammography", J. Biomed. Opt. 9, 1129 (2004)
- 8-9 F. Vasefi, E. Ng, M. Najiminaini, G. Albert, B. Kaminska, G.H. Chapman, J.J.L. Carson, "Angular Domain Spectroscopic Imaging of turbid media using silicon micro-machined micro-channel arrays," Accepted in Imaging, Manipulation, and Analysis of Biomolecules, Cells, and Tissues VIII conference part of SPIE Photonics West 2010.

APPENDICES

Appendix A: Fabrication process of reflection trapped angular filter array

The angular filter array is fabricated using bulk micromachining techniques on a silicon wafer. During my studies, I fabricated several AFA devices at SFU in a Class 100 clean room (School of Engineering Science) all with semi-circular shaped apertures. More recently, I utilized the UWO Nanofabrication laboratory facilities to fabricate AFA devices with square-shaped apertures. The semi-circular micro-channel fabrication details are well described in [A1]-[A3]. The micro-fabrication process for the square-shaped micro channels fabricated at the UWO Nanofabrication laboratory is described below.

Overview of process flow

In this process, a RCA cleaned silicon wafer (figure A.1(a)) was oxidized using a thermal process in a furnace (figure A.1(b)). Then, the photolithography process was started. A thin photoresist layer was spun onto the wafer (figure A.1(c)). A chrome mask having a design pattern that approximately resembled the micro-tunnel wall structures was used. The pattern on photomask was transferred from the chrome mask onto the photoresist layer via an ultraviolet light photolithography process (figure A.1(d)). The photoresist layer was used as a masking layer for underlying oxide etching process. After patterning the oxide layer and stripping the photoresist, the patterned oxide was used as a mask for

the DRIE process (figure A.1(e)). The oxide layer was chemically stripped away after DRIE (figure A.1(f)). A flat top piece from an unpolished silicon wafer was used to cover the etched micro-channels creating wall-pattered square-shaped tunnels.

Photomask design and wafer preparation

The fabrication of the RTAFA started with designing the photomask layout using *MEMS Pro L-Edited software*. The design was sent for fabrication to the University of Alberta NanoFab laboratory [A4]. An RCA cleaning processes was used to clean the surface of silicon substrate from organic and inorganic residues. The RCA cleaning process consisted of dipping the wafers in a mixture of $H_2O:NH_4OH:H_2O_2$, followed by a brief dip in Hydrofluoric Acid (HF), and then immersion in a mixture of $H_2O:HCl:H_2O_2$. Afterward, A clean silicon wafer was oxidized to grow a layer of SiO_2 approximately 0.5 to 0.7 μm thick. The Thermal oxidation was done by Mr. Woods at the SFU clean room.

Photolithography

The photoresist layer was deposited as a masking layer for the oxide layer etching process. Before spinning the photoresist layer on the SiO_2 layer, a primer layer was spun to enhance the adhesion between oxide and photoresist layer. In order to do so, the wafer was transferred into the *HMDS Vapor Prime Oven* for 30 minutes at temperature 150 $^{\circ}C$ [A5]. The wafer then was pre-baked on a hot plate at 80 $^{\circ}C$ for 5 minutes before the positive photoresist was spun.

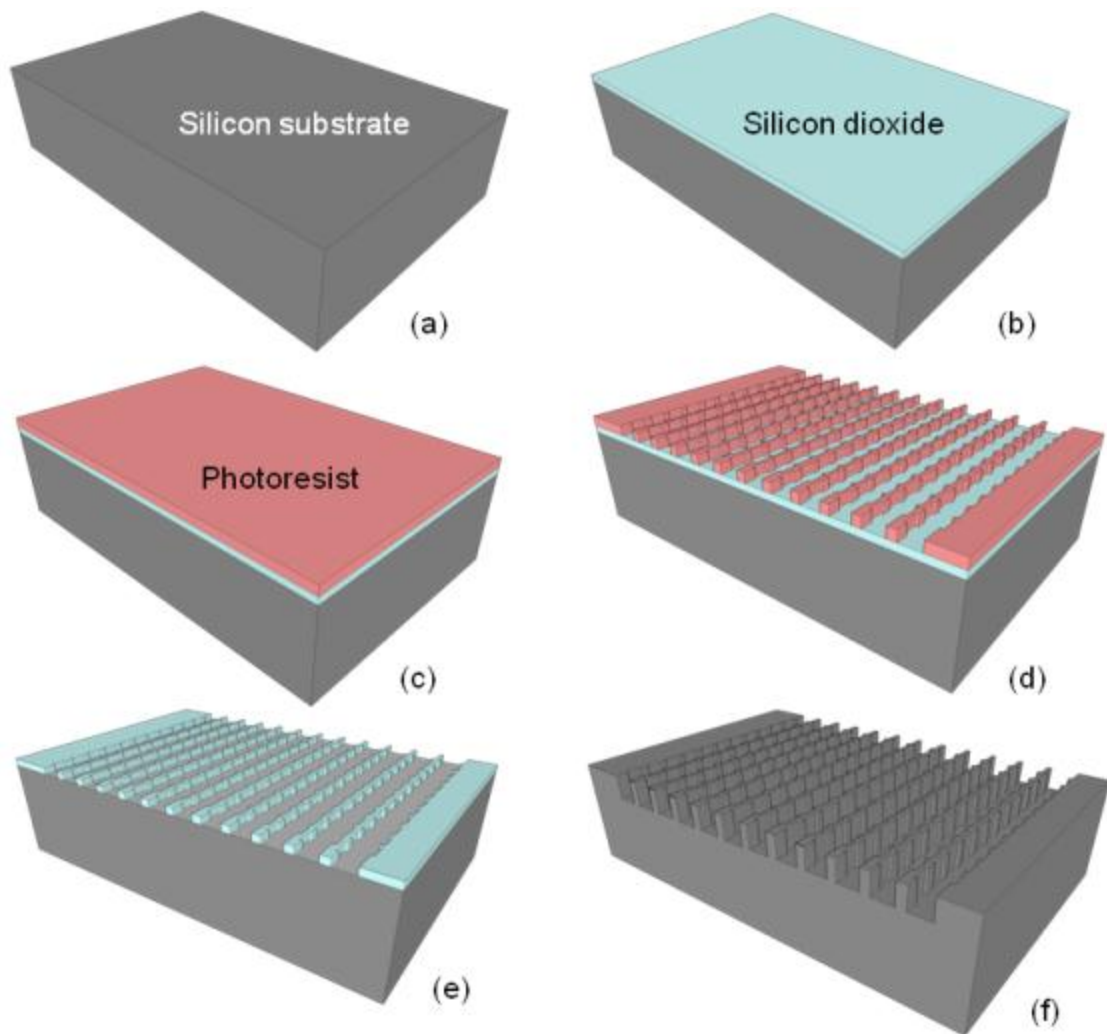


Figure A.1. Illustration of Angular Filter Array micro-fabrication process steps. (a) silicon wafer as a substrate, (b) after oxidization process, (c) photoresist spun before photolithography process, (d) Patterned photoresist layer after photolithography, (e) patterned oxide layer, (f) final silicon etched micro channels.

Shibley S1827 Positive Photoresist was used in this process. The spinning process started with spreading the photoresist at 500 RPM for 5 seconds and then spinning at 3000 RPM for 60 seconds using Solitec 5110

Spinner/Developer system [A5]. The thickness of the photoresist layer was estimated to be approximately 3.25 μm by referring to the data sheet in UWO NanoFab. After soft baking the wafer at 115 $^{\circ}\text{C}$ for 2 minutes, the wafer was processed by photolithography using a *Karl Suss MA6 Mask Aligner* [A5], exposure to UV-light, and the pre-designed positive photomask. The energy used for exposure was 18 mW/cm^2 with 25 seconds exposure time. The areas of photoresist exposed to UV light were removed in a subsequent developing process.

FMTM – 319 Developer was used for developing the photoresist layer. The development time was 2 minutes. After the development, the wafer was soaked in DI-water to stop the photoresist development. The wafer was hard-baked on a hot plate at 115 $^{\circ}\text{C}$ for 10 minutes before the SiO_2 etching process.

Wet Etching SiO_2 process

Buffered HF Improved solution, also called Buffered-Oxide-Etchant (BOE), was used as the etchant for the SiO_2 layer. The BOE is classified as a isotropic etchant. The BOE has a documented etch rate of 0.1 $\mu\text{m}/\text{min}$. In our case, the measured etching rate was around 100 - 110 nm per minute at room temperature. Therefore, the oxide layer was etched away using buffered HF for over 5 minutes with agitation. During the oxide layer etching process, container agitation was continuously applied to increase the uniformity of the etching profile. After etching, *PG-Remover* (80 $^{\circ}\text{C}$) was used to strip off the photoresist layer after the etching process. The wafer was transferred to the *Gasonics Aura*

Plasma Asher machine to further strip off any of the remaining photoresist on the wafers [A5]. A much cleaner wafer surface was observed after this process.

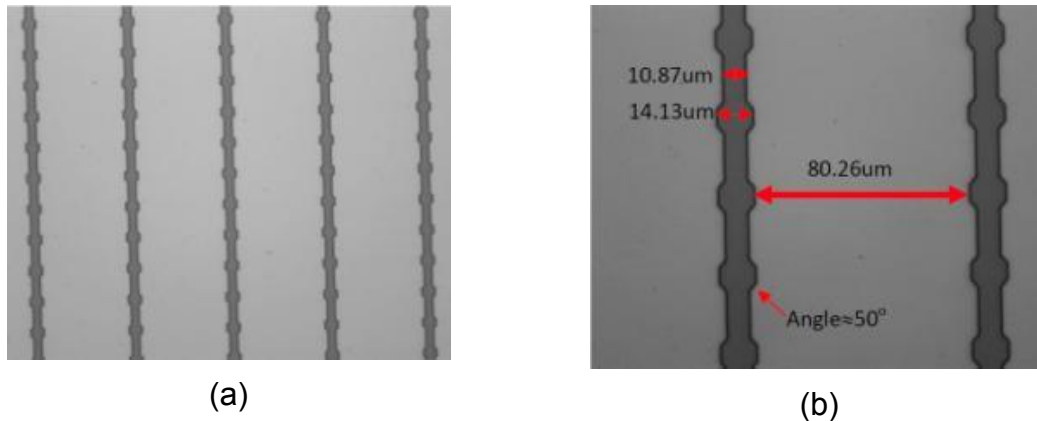


Figure A.2. Microscope top View of 80um RTAFA oxide mask after Wet Etch Process, (a) 20x Magnification, (b) 50x Magnification

Figure A.2 shows the top view of photoresist and oxide layer patterned on top of silicon wafer. The measured width of the inner wall was 10.87 μm , the width of the outer wall was 14.13 μm , and the distance between channel openings, W , was 80.26 μm . The patterned rectangular ridges on the channel wall formed an angle of approximately 50° between the normal direction to the inner wall and the side of the outer wall. This was a result of the isotropic wet etch of the SiO_2 . Compared to the initial design with a 90° pattern obstacle on the wall, this still served the purpose of trapping the reflected light in the channel because any incident light bounces back toward the incident light direction at a 50° angle.

DRIE for silicon substrate

Alcatel 602E Deep Silicon Etch machine was used for the DRIE process. The etching rate was determined by previous measurement on a test wafer (~ 4 μm per minute) with the following setting shown in Table A.1. Therefore, the etching time for 80 μm micro-channel would be approximately 20 minutes.

Table A.1: Setting for DRIE Process in Alcatel 602E DRIE Machine

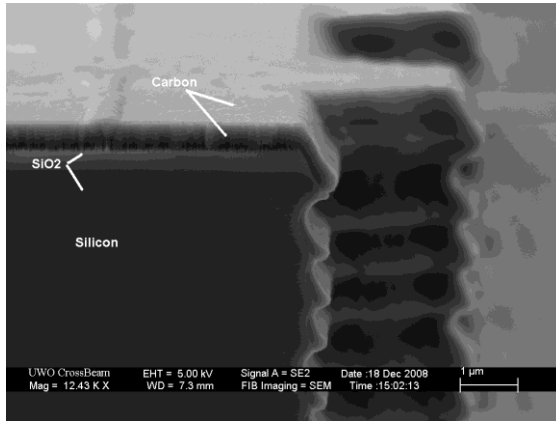
Temperature	20° Celsius
SF ₆	300 sccm (for 7 seconds)
C ₄ F ₈	150 sccm (for 3 seconds)
Pressure	6.6E-2m Bar
Source RF for plasma	1800 Watts
SH RF for substrate	120 Watts

Carbon sputtering (optional)

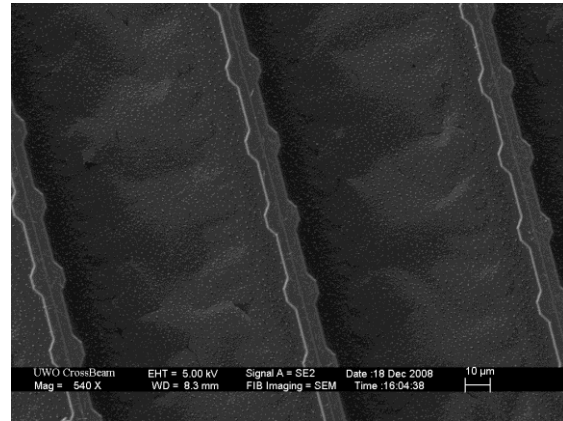
In this particular design, the target thicknesses for carbon coating layer was 200 nm. A sputter system was considered for this process because it provides a clean film of carbon layer with high uniformity and excellent adhesion. The target material for deposition was 99.9999% pure carbon. The coating process was performed with the *Edwards auto 500 Sputter Deposition System* [A5]. The deposition rate for the carbon was characterized previously (4.5 nm per minute) with the setting shown in table A.2. Therefore, the deposition time for 200nm carbon layer is approximately 45 minutes. Figure A.3 shows the SEM picture of a fabricated device.

Table A.2: Setting for Edwards Auto 500 Sputter Deposition System

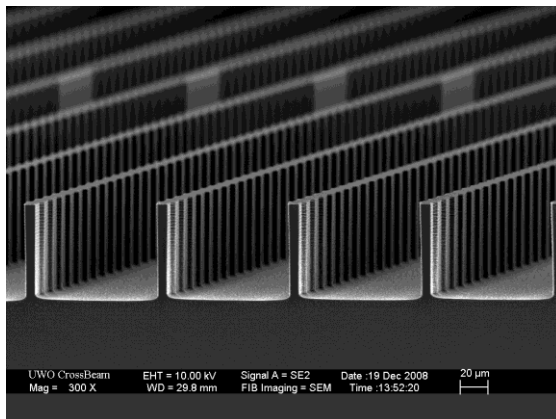
Gas Flow	19.67 sccm
Pressure	6.4 E-3 Torr
Power	500 Watts for W_F and 9 Watts for W_R
Pre-Sputtering Time	5 minutes (for cleaning the Carbon)



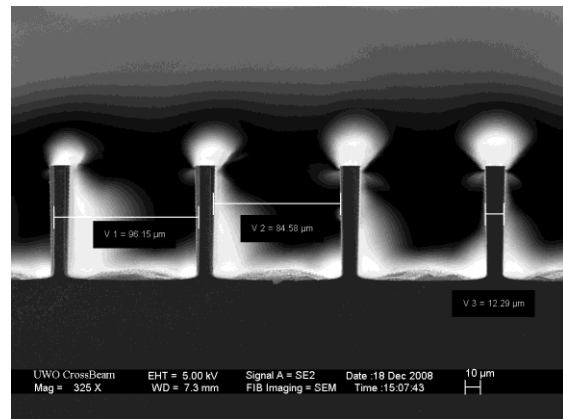
(a)



(b)



(c)



(d)

Figure A.3. SEM pictures of RTAFA: (a) micro channel wall with oxide and carbon layers, (b) Top view of the micro channels, (c) front view of the RTAFA, (d) geometrical measurements of the RTAFA

Dicing the wafer

The resultant wafer contained multiple AFA devices with different array sizes. For instance, as shown in Figure A.4, the silicon wafer contained 2 AFA

devices with 3 cm × 1cm, 2 devices with 3 cm × 1.5 cm, and 2 devices with 3 cm × 2 cm areas. Dicing of the wafer was performed with an automatic *K&S 780 dicing saw* machine [4]. Before dicing the wafers, a photoresist layer (*MicroChem S-1805*) was spun on the wafer to prevent any loose particles from dropping into the channels during the saw cutting process.

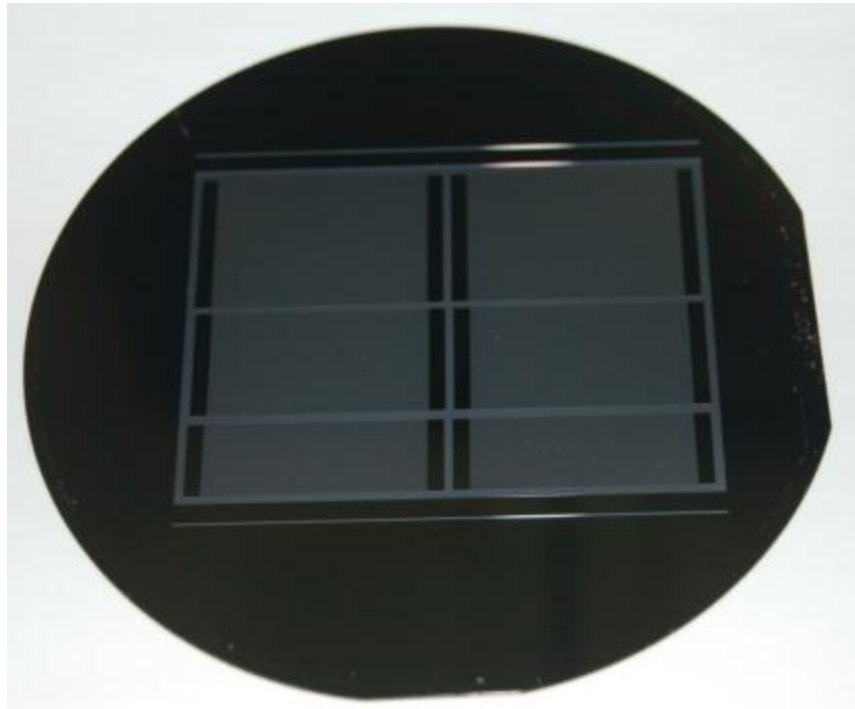


Figure A.4. Picture of silicon wafer with multiple RTAFA devices.

The cutting process started with programming the machine to preconfigured reference level and number of the cycle for the sawing time. After cutting, the wafer pieces were kept under the UV-light exposure for a couple of minutes to reduce the stickiness of the tape. Thereafter, the photoresist was stripped off with the *PG-Remover* solution

References

- A1. M. Tank, "Development of a Silicon Micromachined Collimator Array to Detect Objects within Highly Scattering Mediums," M.A.Sc. thesis, Simon Fraser University, Burnaby, BC, Canada, 2001.
- A2. P. Chan, "Angular Filters for Angular Domain Imaging Optical Tomography in Highly Scattering Media" M.A.Sc. thesis, Simon Fraser University, Burnaby, BC, Canada, 2008.
- A3. P. Chan, "Exploring the Limits of Silicon Micromachined Collimating Array Assisted Optical Tomography" B.A.Sc. thesis, Simon Fraser University, Burnaby, BC, Canada, 2005.
- A4. The University of Alberta Nanofab website:
<http://www.nanofab.ualberta.ca/>
- A5. The University of Western Ontario Nanofab website:
<http://www.uwo.ca/fab/>

Appendix B: Angular domain florescent lifetime imaging in turbid media⁷

Abstract

We describe a novel florescent lifetime imaging methodology applicable to fluorophores embedded in turbid media. The method exploits the collimation detection capabilities of an angular filter device to extract photons emitted by a fluorophore embedded at depth within the medium. A laser source is used to excite the fluorophore within the medium. Photons emitted by the fluorophore that are not scattered to a high degree pass through the angular filter array and are detected by the intensified CCD camera (200 ps minimum gate width). Scattered photons are rejected by the filter and do not pass through to the camera. We fabricated angular filter arrays using silicon bulk micromachining and found that an array of 80 μm square aperture micro-tunnels, 1.5 cm in length accepted photons with trajectories within 0.4° of the axes of the micro-tunnels. The small acceptance angle rejected most of the scattered light exiting the turbid medium.

Introduction

In general, fluorescence measurements are classified into steady-state, frequency-domain, or time-resolved measurements. Steady-state measurements are the most frequently presented due to their simplicity and the use of reasonably priced equipment, while frequency-domain and time-resolved

⁷ The following appendix has been published in Proceedings of SPIE Vol. 7183 (SPIE, Bellingham, WA 2009) , 71830I (2009) under the co-authorship of Eldon Ng, Bozena Kaminska, Glenn H. Chapman, Jeffrey J.L. Carson.

measurements require a more complex light source and detection system. Steady-state measurements are performed through the continuous excitation of a sample, subsequent with recording an excitation or emission spectrum. As a result, they represent an average of the time-resolved measurements. The light intensity of the fluorescence emission, I_F , is proportional to the quantity of the radiation power from the excitation source that is absorbed and the quantum yield for fluorescence. The I_F rises with an increase in quantum efficiency, incident power of the excitation source and concentration of the fluorophore [B1]

In time resolved measurements, the fluorescence emission intensity decay of a sample (fluorescent lifetime), following a short pulse of excitation light, is measured using a temporally fast pulsed laser and fast camera system, typically performed on the nanosecond timescale. The fluorescence lifetime is an intrinsic property of the excited state of the fluorophore. Hence, the fluorescence lifetime is independent of the concentration of the fluorescing species and the incident power of the excitation source [B2]. Therefore, the fluorescence lifetime is independent of the variations in the excitation light source, the optical path, and system optical aberrations. However, the use of fluorescence intensity to quantify samples is severely hampered by effects such as radiation scattering, optical aberrations, inhomogeneous excitation, photon path length, collection efficiency and autofluorescence [B2]. Therefore, fluorescence lifetime measurements can provide a more powerful tool to quantify samples due to inherent insensitivity to instrumental variations, photo-bleaching, and auto-fluorescence.

The lifetime of fluorophores in human tissue can offer extra information such as tissue glucose, oxygenation, and pH [B3] Tissue fluorescence is generally measured at or near the tissue surface [B4] such as is performed with epifluorescence microscopy [B1] and confocal fluorescent microscopy [B5]. Only recently have investigators begun to develop the methods needed to extract the fluorophore lifetime information from deep within heterogeneous turbid media characteristic of tissue [B6]-[B10] Diffuse fluorescence in deep tissues has also been investigated lately as a tool of tumour detection by tracing the center of fluorescing targets [B11]-[B13]. This advancement relies on the fact that the fluorophore will accumulate in tumours more [B14] In this paper, we demonstrate a novel fluorescent lifetime imaging method whereby one can, in principle, simultaneously derive a spatial map of the concentration and lifetime of fluorophore distribution. This new method has relatively large depth of field and allows imaging deep (up to 5 mm) in turbid medium by selecting the fluorescent photons that travel straight from the fluorescent source with small angular deviation. The technique is an extension of Angular Domain Imaging (ADI) technology.

Angular domain imaging principle

The transmission-based ADI method operates by selecting ballistic and quasi-ballistic light closely confined within a small angle of the incoming photon trajectory while filtering out highly scattered light. This follows from the observation that highly scattered light tends to have a nearly uniform angular distribution while image forming non-scattered light is highly directional [B15]-

[B17]. As shown in Figure B.1, the Angular Filter Array (AFA) employs high-aspect ratio micro-tunnels to create extended apertures through which photons can pass. Photon passage is ensured if arrival is within the allowable acceptance angle with respect to the longitudinal axis of each micro-tunnel. Photons that arrive with incident angles beyond the acceptance angle will strike the micro-tunnel sides and be attenuated. The performance of ADI is largely dependent on the design of the array of angular filter micro-tunnels. The AFA must be designed with a high aspect ratio, length (l) over diameter (d), to provide sufficiently strict angular filtering of scattered photons.

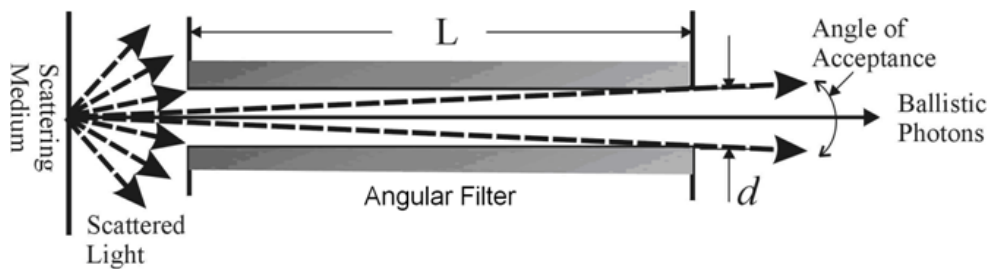


Figure B.1. Angular domain imaging in trans-illumination mode.

The ADI technique works successfully in transmission geometry, where the laser source is aligned to the angular filter to trans-illuminate the turbid medium from front to back. ADI can also be employed using an illumination source on the same side as the angular filter to capture quasi-ballistic photons generated deep within the scattering medium. In the reflective geometry, collimated light is injected into the turbid medium, thus generating a source of illumination from inside the medium and behind the imaging target. This newly formed light source in the scattering medium emits non-scattered and scattered

light relative to the AFA micro-tunnels. When these back reflected photons pass an imaging target, which can be either absorbing or fluorescent material, and reach the AFA, the relative non-scattered photons are accepted through the micro-tunnels and reach the camera, whereas scattered photons are rejected by the filter. Reflection geometry ADI has been investigated previously [B18].

Angular filter array

Recently, we investigated a new design for the angular filter array (see Figure B.2), which consisted of a parallel array of square-shaped micro-tunnels, 80 microns wide and tall along a 1.5 cm long plate to obtain aspect ratios of approximately 188:1. The main part of the AFA is an array of long tunnels etched on to a silicon substrate as shown in Figure B.2 (bottom piece). The walls of the AFA were patterned with many small features to suppress internal reflections within each micro-tunnel. A flat silicon wafer was used as the top piece to enclose the micro-tunnels to form the AFA. The square shape with small spacing had higher performance compared to our previous semi-circular micro-tunnels. Compared to the semi-circular geometry, the square geometry employed smaller spacing between adjacent micro-tunnels and provided a larger cross-sectional area for a given nominal acceptance angle; therefore, it was more efficient at accepting the informative photons exiting the turbid sample. The aspect ratio and micro-tunnel size for the square geometry reported above provided optimal image contrast compared to other filter geometries (data presented in [B19]). Because the micro-tunnels were square in geometry, there existed an angular acceptance angle variation from 0.3° (wall to wall) to 0.42° (corner to corner).

This design was selective enough to collect quasi-ballistic photons that provided at least 200 μm spatial resolution for targets embedded in turbid media.

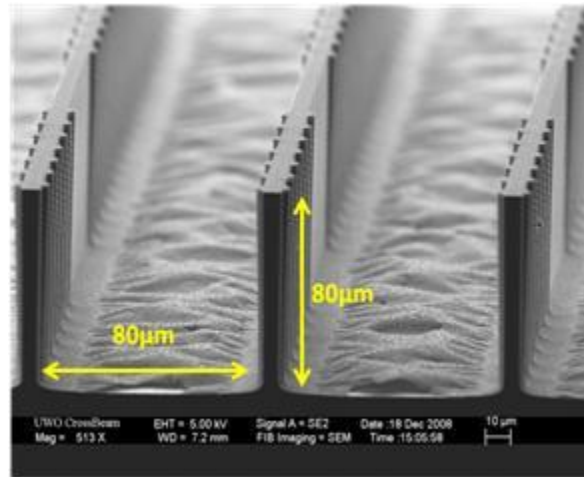


Figure B.2. Silicon micro-machined angular filter array (bottom piece).

The one dimensional linear array of micro-tunnels had a limited field of view as shown in Figure B.3. This led to two limiting issues. First, light from regions of the sample that were not imaged could still scatter, penetrate AFA and reach the sensor. This resulted in a background signal at each pixel location and reduced image contrast. This effect could be suppressed somewhat by reducing the amount of unnecessary illumination of the sample using a collimated line source coincident with the AFA. Second, the limited vertical field of view of the AFA necessitated a scanning system for the capture of 2D images. We employed a computer-controlled z-axis stage to incrementally raise the sample between scans. One horizontal line image of the sample was taken through the AFA at each step and a final 2D image was assembled from the stacked line images.

Hence, an entire region of the sample could be passed through the field of view of the AFA and imaged.

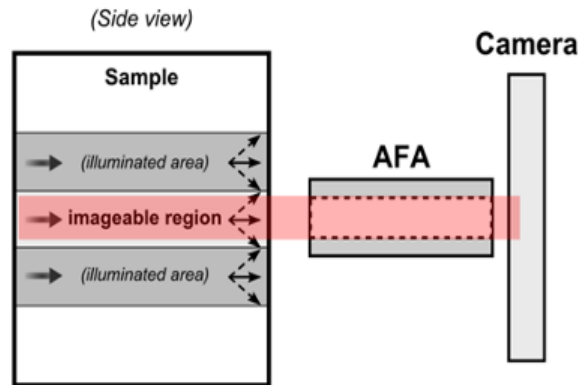


Figure B.3. Illustration of limited field of view for a one dimensional AFA.

Angular domain imaging possesses multiple benefits as an optical imaging method. These include: *i)* wavelength independence, which allows for broadband or multi-spectral light sources; *ii)* non-coherent source compatibility, which implies that ADI can be performed with inexpensive light sources, and *iii)* multimodal capability, that is ADI is useful not only for detection of absorbing targets in a turbid medium, but also for fluorescence targets, which has promise for imaging genetic reporters and molecular contrast agents in biological tissue.

Objective and approach

The objective of this work was to adapt the ADI method to fluorescence lifetime imaging for the purpose of detection and characterization of fluorophores hidden in turbid media. Our approach was to take advantage of the scattered light rejection properties of the AFA in a reflection mode ADI configuration. To do this, we first constructed an imaging system utilizing an AFA and characterized

the image contrast of a fluorescent target in a turbid medium at different scattering levels. Second, we performed temporally-resolved measurements of fluorescent emission from the fluorophore using a fs-pulsed laser, the AFA, and a ultrafast time-gated camera to reveal the fluorescent signal decay due to the fluorescent lifetime property. The imaging system was tested with tissue-like phantoms prepared with Intralipid™ that contained the fluorescent targets.

Experiment setup

Apparatus overview

The experimental setup shown in Figure B.4 was based on the ADI configuration in the reflection mode. In this mode, both the illumination source and the aligned detector system were placed on the same side of the imaged specimen. Light from the pulsed laser source was used to excite the fluorescent target. The AFA accepted the minimally deviated photons due to fluorescence emission that exited the turbid medium and rejected the photons that exited the turbid medium at angular deviations outside the acceptance angle of the AFA. Photons outside the acceptance angle of the AFA were most likely subject to multiple scattering events and were not expected to carry information about the position of the fluorescent target. The addition of time gating to ADI involved the use of a pulsed laser source with a short pulse width and a fast detector, which synchronized with the incoming pulsed laser source.

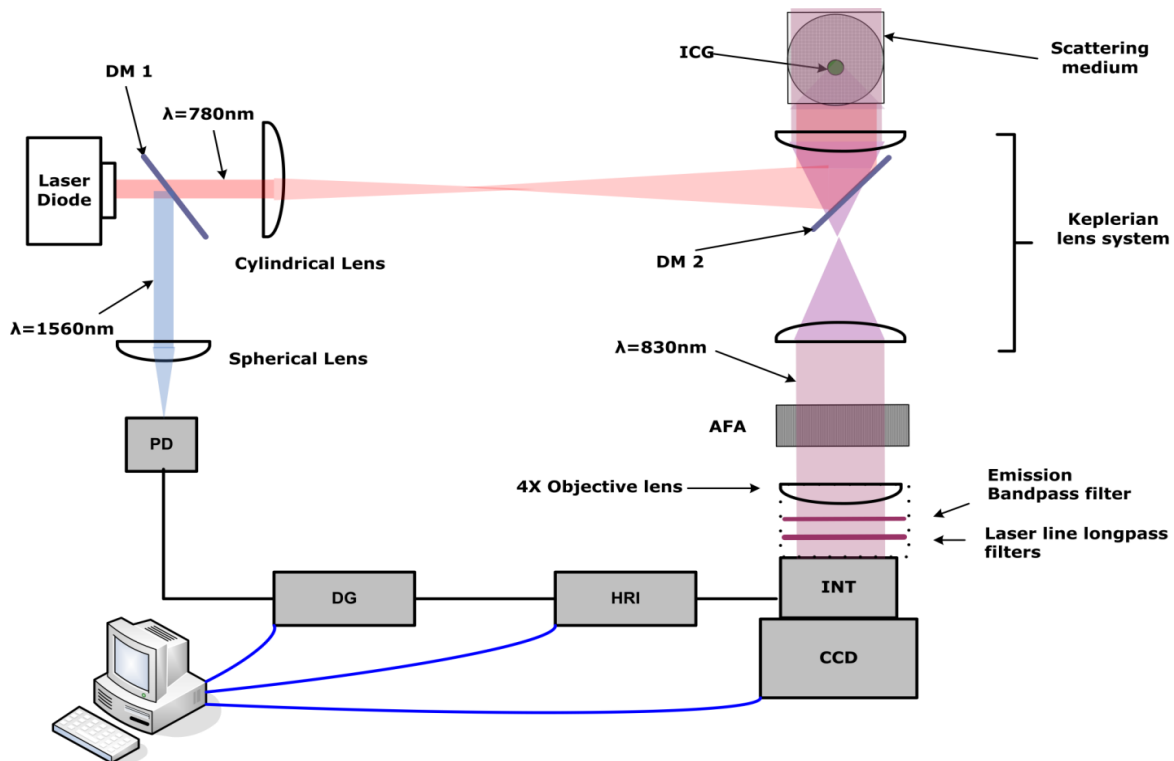


Figure B.4: Optical imaging setup, Abbreviations: CCD, charge-coupled device; HRI, high rate imager; INT, intensifier; DG, delay generator; DM, dichroic mirror; AFA, angular filter array; ICG, indocyanine green; and PD, photo diode. The system was designed to acquire time-resolved measurements of the fluorescent target combined with reflection based angular domain imaging using a silicon micro-machined AFA.

Light source

Illumination for imaging was performed with a fiber-based pulsed laser (Femtolite Ultra CX-20, IMRA America, Inc.), which had a pulse width of 100 fs, a repetition rate of 50 MHz, and an average power of 20 mW. The pulsed laser emitted two wavelengths (780 nm and 1560 nm). The free space beam was 2.4 mm in diameter and collimated. The beam was transformed into a line of light to cover the openings of the AFA. Beam shaping was performed with a cylindrical-spherical lens system to horizontally expand ($\sim 1:5$) and vertically focus the beam at a point 75 mm beyond the spherical lens.

Sample preparation

For all experiments, an aqueous suspension of Intralipid™ was used. Intralipid™ is a phospholipid emulsion used usually as an intravenous nutrient and is a practical phantom medium for light dosimetry studies. Like tissue, Intralipid™ is turbid at visible and near infrared wavelengths. Additionally, Intralipid™ lacks strong absorption bands in the visible and near infrared region of the spectrum [B20]. As a scattering medium, the optical properties of Intralipid™ have been well characterized [B21]. To test the spatial resolution of the system, 1.2 mm diameter clear glass tubes filled with 20 μ M indocyanine green (ICG) diluted with water were used. The ICG samples were prepared on the same day as each experiment since the optical properties of water/ICG solution change over time. ICG was chosen since it is excited at the same wavelength as the pulsed laser source.

Detection stage

During conventional ADI measurements, photons exiting the imaged sample were discriminated via an AFA with a small acceptance angle. The introduction of the AFA into the optical path required that the AFA be aligned precisely at the same height as the light source to enable capture of the in-line fluorescent emission. A Keplerian lens system was placed between the sample and the AFA. The lens system transferred fluorescent emission from the sample to the AFA and permitted a dichroic mirror to be placed into the light path for laser light delivery. The AFA holder was mounted on a six degree-of-freedom jig to facilitate precise alignment of the micro-tunnel array with the light source.

Detection of light that passed through the micro-tunnels was performed with an ultra-fast gated ICCD camera (PicoStar HR, LaVision). The intensifier used a voltage-gated micro-channel plate (MCP) controlled via a high rate imager (HRI, Kentech Instruments, UK) for single-photon detection sensitivity. Gating of the intensifier was achieved by applying a pulsed negative voltage across a photocathode in front of the MCP. The gate width was controlled using an ultra-short pulse generated by the HRI, with nominal gate width settings from 200 to 1000 ps. A voltage across the MCP, adjustable from 260 to 800 V, provided a variable intensifier gain. The output of the intensifier was coupled to a 12-bit CCD camera of 1370 by 1040 pixels. The ICCD worked as a very fast shutter and was synchronized with the laser pulses through a delay unit (Delay Unit, LaVision, Germany). The delay between the laser pulses and gated detection was adjusted with a 5 ps step. After the image intensifier, the CCD camera integrated light over a fixed exposure time below the camera exposure level. With the image intensifier operating in a “comb” mode, a sequence of gated transmissions accumulated on the CCD. The fluorescence emission passing through the scattering medium was temporally resolved by scanning the delay time (T_d) between the source laser pulse and the time-gated detection using image capture and control software (DaVis, LaVision). The system enabled a parallel recording of all the micro-tunnels of the AFA, which were imaged on to the CCD array. To record the temporal point spread function (TPSF) of the detector, the delay was scanned electronically, typically in 15-ps steps. The fluorescent photons were spectrally separated from the incident illumination by a short band-pass interference filter

(FL830-10, Thorlabs, NJ, USA), and 785nm laser line long-pass filter (NT47-508, Edmund Optics Inc., NJ, USA) before reaching the camera. In order to acquire the reference signal for synchronization between the pulsed laser and the fast camera, a dichroic mirror was used to reflect the 1560 nm component emitted by the pulsed laser. The deviated beam was focused on to an InGaAs photodiode (ET-3000, Electro-Optics Technology, Inc.). The photodiode output signal was connected to the sync in port of the delay generator unit (as shown in Figure B.4).

Results and discussions

The goal of the proposed fluorescent imaging system was to be able to image time-resolved fluorescent signals over a large two-dimensional area of the sample with sub-millimeter resolution. Sub-millimeter spatial resolution was possible due to the use of an AFA with sub-millimeter channel openings. The AFA covered a long line-shaped field of view, which permitted two-dimensional images to be captured by scanning the sample with the AFA and stacking the line images into a 2-dimensional image. The ability to perform time-resolved measurements during ADI enabled fluorescence lifetime imaging. In order to test the spatial resolution limitation of the imaging system, the spatial map of the fluorescent targets (two glass tubes filled with 20 μM ICG) in non-scattering media (water) was captured and illustrated in Figure B.5. The fluorescent targets were placed 5 mm deep into a 5 cm optical cuvette filled with water, the glass tubes had 1 mm internal diameter and 1.2 mm outer diameter (see Figure B.5(a)). The two tubes were positioned with a 0.8-mm spacing between them.

The fluorescence emission was captured with the ultra fast-gated ICCD camera with 1000 ps temporal gate width, which captured the first 1000 ps of fluorescence emission due to each laser pulse (i.e. quasiballistic plus scattered photons). Since the AFA had limited vertical field of view, the sample was scanned and line images at each position were stacked to form a two-dimensional image (see Figure B.5(b)). Some degradation of the fluorescent emission was observed and attributed to photo-bleaching. Figure B.5(c) shows the average light intensity of all the scanned rows shown in Figure B.5(b).

The average detected fluorescence emission intensity variation was approximately 2:1 when comparing a region within each ICG-filled glass tube to the mid-point between the two tubes. Image contrast was much higher (10:1) when the region within one ICG-filled tube (i.e. representative of fluorescence emission) was compared to a region 1.5 mm away from the edge of the tube. This demonstrated that even though the fluorescence emission had a uniform angular distribution there were few emitted photons that scattered along a trajectory that was within the acceptance angle of the AFA and captured by the camera. The same scan was performed with two ICG-filled tubes spaced 4-mm apart and placed 5 mm deep into a 5 cm thick optical cuvette as shown in Figure B.6. The image contrast was reduced from (10:1) to (3:1) in this condition.

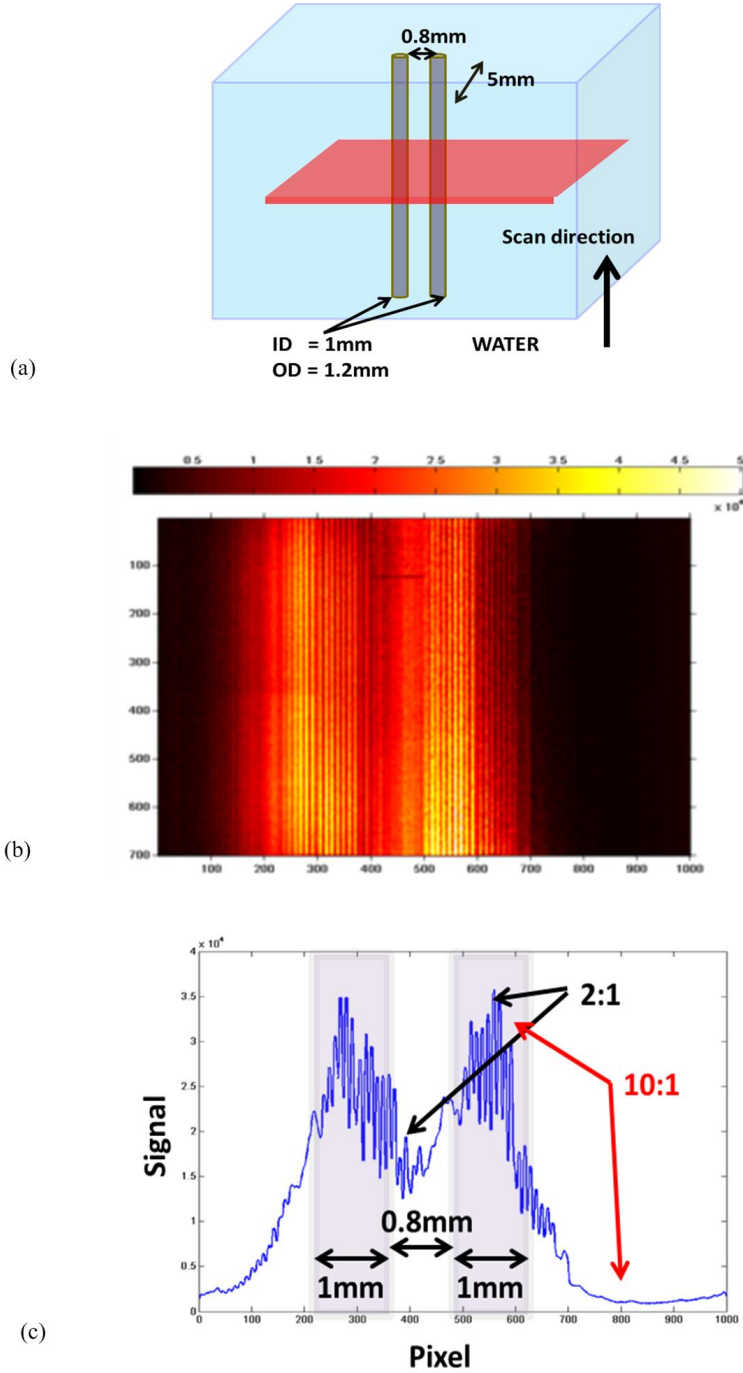


Figure B.5: (a) Angular domain fluorescent imaging sample configuration in non-scattering media. Two glass rods filled with $20 \mu\text{M}$ ICG diluted with water, excited with 780 nm laser in water. (b) Angular domain fluorescence image represented as a two-dimensional scan (total scan area is $7 \text{ mm} \times 10 \text{ mm}$) (c) Average light intensity of the scanned rows of the Figure(a) sample setup.

The image contrast degradation was due to scattered fluorescent light that underwent a random walk in the scattering medium and happened to enter the acceptance angle of the AFA. Photo-bleaching was also apparent in the scan, which degraded the signal intensity over time.

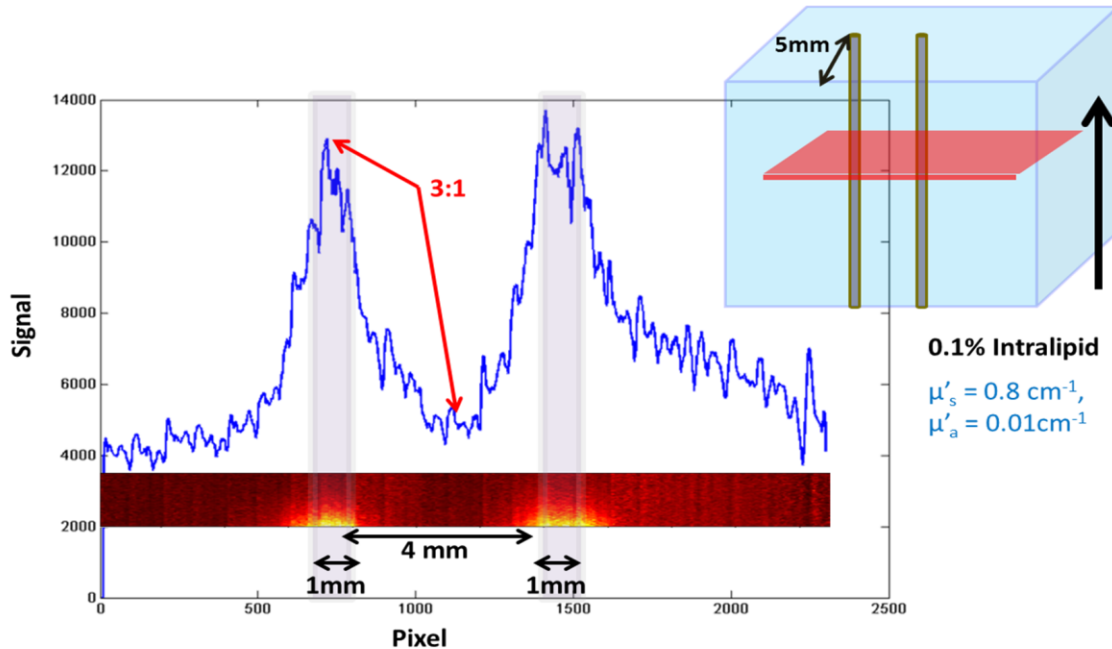


Figure B.6: Angular domain fluorescent imaging in turbid media. Targets were two glass tubes filled with $20 \mu\text{M}$ ICG diluted in water and placed in a 5 cm path length cuvette filled with 0.1% Intralipid (top right). Tubes were located 5 mm from the detection surface. Excitation with laser was at 780 nm (shown as red plane in top right panel). Average emission signal (blue line, left panel) due to ICG-filled tubes is indicated with relative location of ICG-filled tubes shown as shaded areas. The two-dimensional scan is shown below the curve and demonstrated the signal loss due to photo bleaching of ICG as the scan progressed from bottom to top.

Other fluorescent dyes with better immunity to photo-bleaching and higher quantum yield would be more desirable to improve the number of captured fluorescent photons. In these experiments, the integration time for each line of the scan was 160 ms and could be extended to improve the signal to noise in the

images. For example, the integration time could have been extended to up to 2 s with only a 50% increase in acquisition time, since up to 2 seconds was associated with the overhead of the communication between the stage controller and other electronics.

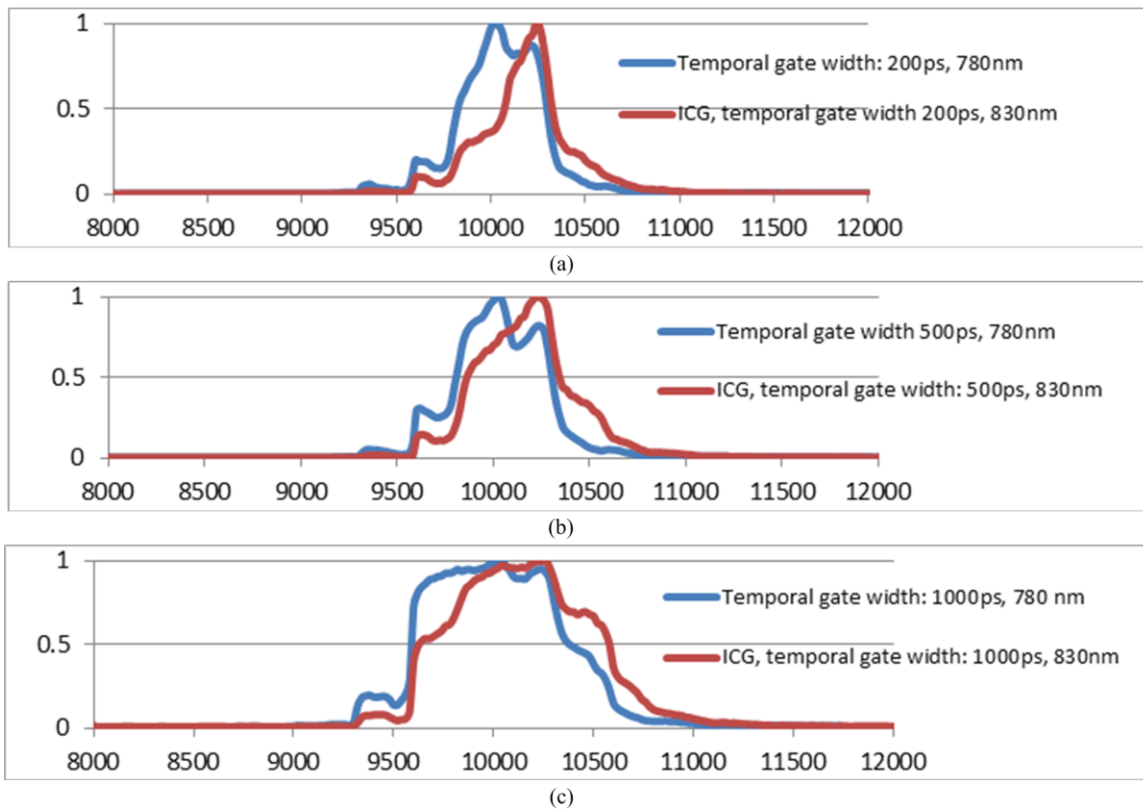


Figure B.7: Temporal scan of ICG fluorescence (normalized) versus the reflected excitation light, which travelled the same optical path. (a) temporal gate width of 200 ps, (b) temporal gate width of 500 ps, and (c) temporal gate width of 1 ns

Multiple temporal scans using different temporal gate widths and shifting on different delay times is shown in Figure B.7. The temporal scan of the fluorescent emission was recorded at the 20 ps step size to obtain the fluorescent lifetime information. Figure B.7 shows excitation light (780 nm) which underwent the same optical path as the fluorescence emission with different

temporal gate widths. The fluorescent emission signal was the convolution of the instrument temporal response and the temporal decay of fluorescent dye (approximately 500 ps for ICG).

The fluorescent temporal response was compared with the instrument temporal response and indicated that a delay was present and likely due to the intrinsic fluorescent lifetime decay. The delay was approximately 250 ps. The delay between fluorescent emission signal and the excitation signal is the result of the convolution of an exponential decay function of fluorescent lifetime with the excitation signal. This lifetime decay function has to be constant by the variation of camera's temporal gate width. The full scan will cover 4000 ps with 200 steps.

Conclusion

This paper presents a fluorescent imaging system based on ADI that can detect fluorescent targets deep (~ 5 mm) within a turbid medium. Fluorescent line targets <1 mm in diameter could be resolved. The informative fluorescent photons that travelled straight trajectories exited the turbid medium with small angular deviation. These minimally deviated photons could be distinguished by inserting an angular filter array with a small acceptance angle into the optical path before the detector. The time-resolved measurements using the pulsed laser, the AFA, and an ultra fast gated ICCD camera demonstrated fluorescence lifetime imaging using the ADI methodology was possible. The temporal scan of the fluorescence emission of ICG was time-shifted relative to the instrument temporal response by at least 250 ps and was consistent with the expected lifetime for ICG (< 0.5 ns).

Acknowledgment

This project was funded by grants from the Natural Sciences and Engineering Research Council of Canada (NSERC) to Bozena Kaminska and Dr. Jeffery J.L. Carson. In addition, partial funding was provided by the Translational Breast Cancer Studentship for Fartash Vasefi from the London Regional Cancer Program.

References

- B1. B. Valeur, "Molecular Fluorescence: Principles and Applications", Wiley-VCH. (2001)
- B2. R.M. Clegg, O. Holub and C. Gohlke, "Fluorescence lifetime-resolved imaging: measuring lifetimes in an image", *Methods Enzymol* 360, 509. (2003)
- B3. S. B. Bambot, J. R. Lakowicz, G. Rao, "Potential applications of lifetime-based, phase-modulation fluorimetry in bioprocess and clinical monitoring", *Trends in Biotechnology*, 13 (3), 106, (1995)
- B4. D. W. Piston, M. S. Kirby, H. Cheng, W. J. Lederer, and W. W. Webb, "Two-photon-excitation fluorescence imaging of three-dimensional calcium-ion activity," *Appl. Opt.* 33, 662-669 (1994)
- B5. Diaspro, "Confocal and Two-Photon Microscopy: Foundations, Applications and Advances", Wiley-VCH. , 576. (2001)
- B6. Eva M. Sevick-Muraca and Christina L. Burch, "Origin of phosphorescence signals reemitted from tissues," *Opt. Lett.* 19, 1928 (1994)
- B7. M. S. Patterson and B. W. Pogue, "Mathematical model for time-resolved and frequency-domain fluorescence spectroscopy in biological tissues," *Appl. Opt.* 33, 1963-1974 (1994)
- B8. J. Tromberg, S. Madsen, C. Chapman, L. O. Svaasand, and R. C. Haskell, "Frequency-domain photon migration in turbid media," in *Advances in Optical Imaging and Photon Migration OSA Proceedings*, 21 , 93, (1994)
- B9. J. Durkin, S. Jaikumar, N. Ramanujam, and R. Richards-Kortum, "Relation between fluorescence spectra of dilute and turbid samples," *Appl. Opt.* 33, 414-423 (1994)
- B10. J. Wu, M. S. Feld, and R. P. Rava, "Analytical model for extracting intrinsic fluorescence in turbid media," *Appl. Opt.* 32, 3585-3595 (1993)

- B11. Knuttel, J. M. Schmitt, R. Barnes, and J. R. Knutson, "Acousto-optic scanning and interfering photon density waves for precise localization of an absorbing (or fluorescent) body in a turbid medium", *Rev. Sci. Instrum.* , 64, 638. (1993)
- B12. M. A. O'Leary, D. A. Boas, B. Chance, and A. G. Yodh, "Reradiation and imaging of diffuse photon density waves using fluorescent inhomogeneities", *J Lumin*, 60, 281. (1994)
- B13. J. Wu, Y. Wang, L. Perelman, I. Itzkan, R. R. Dasari, and M. S. Feld, "Time-resolved multichannel imaging of fluorescent objects embedded in turbid media," *Opt. Lett.* 20, 489-491 (1995)
- B14. X. D. Li, B. Beauvoit, R. White, S. Nioka, B. Chance, and A. G. Yodh, "Tumor localization using fluorescence of indocyanine green (ICG) in rat models," *Proc. SPIE* 2389, 789 (1995)
- B15. G.H. Chapman, M. Trinh, N. Pfeiffer, G. Chu, and D. Lee, "Angular Domain Imaging of Objects Within Highly Scattering Media Using Silicon Micromachined Collimating Arrays", *IEEE J. Sel. Top. Quantum Electron.*, 9, 257, (2003).
- B16. F. Vasefi, B. Kaminska, P. K. Y. Chan, and G. H. Chapman, "Multi-spectral angular domain optical imaging in biological tissues using diode laser sources," *Opt. Express* 16, 14456 (2008)
- B17. F. Vasefi, B. Kaminska, G. H. Chapman, and J. J. L. Carson, "Image contrast enhancement in angular domain optical imaging of turbid media," *Opt. Express* 16, 21492 (2008)
- B18. F. Vasefi, P.K.Y. Chan, B. Kaminska, G. H. Chapman, N. Pfeiffer, "An Optical Imaging Technique Using Deep Illumination in the Angular Domain," *IEEE J. Sel. Top. Quantum Electron*, 13, 1610 (2007).
- B19. F. Vasefi, Benny S. L. Hung, B. Kaminska, G. H. Chapman, and J. J. L. Carson, "Angular domain imaging (ADI) in turbid media using reflection trapped micro-tunnel filter arrays" Submitted to the 2009 European Conference on Biomedical Optics, ECBO09, Munich, Germany (2009)
- B20. S. Jacques, Optical properties of "Intralipid™", an aqueous suspension of lipid droplets, <http://omlc.ogi.edu/spectra/intralipid/index.html> .
- B21. HG van Staveren, CJM Moes, J van Marle, SA Prahl, MJC van Gemert, "Light scattering in Intralipid-10% in the wavelength range of 400-1100 nanometers," *Appl. Opt.*, 30, 4507-4514, (1991).

LIST OF PUBLICATIONS:

ARTICLES IN PEER-REVIEWED JOURNALS:

1. Mohamadreza Najiminaini, Fartash Vasefi, Kenneth M. Tichauer, Ting-Yim Lee, Bozena Kaminska, and Jeffrey J. L. Carson, "Angular domain fluorescence lifetime imaging: a tissue-like phantom study," *Opt. Express* 18 (22), 23247-23257 (2010)
2. Mohamadreza Najiminaini, Fartash Vasefi, Bozena Kaminska, and Jeffrey J. L. Carson, "Experimental and numerical analysis on the optical resonance transmission properties of nano-hole arrays," *Opt. Express* 18 (21), 22255-22270 (2010)
3. F. Vasefi, M. Najiminaini, E. Ng, B. Kaminska, G.H. Chapman, and J.J.L. Carson, "Angular domain trans-illumination imaging optimization with an ultra-fast gated camera," *Journal of Biomedical Optics*, SPIE, Vol. 15, 061710 (2010).
4. E. Ng, F. Vasefi, B. Kaminska, G. H. Chapman, and J. J.L. Carson, "Contrast and resolution analysis of iterative angular domain optical projection tomography," *Opt. Express* 18 (19), 19444-19455 (2010) Also appeared in *Virtual Journal for Biomedical Optics*, OSA, Vol. 5, Iss. 13.
5. F. Vasefi, M. Belton, B. Kaminska, G.H. Chapman, and J.J.L. Carson, "Angular Domain Fluorescence Imaging for Small Animal Research,"

Journal of Biomedical Optics, Vol. 15(01), 15, 016023,
doi:10.1117/1.3281670. (2010) Also appeared in Virtual Journal Biological
Physics Research, APS & AIP, Vol. (19)3, (2010)

6. F. Vasefi, E. Ng, B. Kaminska, G. H. Chapman, K. Jordan, and J.J.L. Carson, "Transmission and fluorescence angular domain optical projection tomography of turbid media," Applied Optics, Vol. 48, 6448-6457, doi:10.1364/AO.48.006448, PMID: 19935964. (2009) (featured as the cover story) Also appeared in Virtual Journal for Biomedical Optics, OSA, Vol. 4 (13) (2009)
7. F. Vasefi, B. Kaminska, G.H. Chapman, and J.J.L. Carson, "Image contrast enhancement in angular domain optical imaging of turbid media," Optics Express, Vol. 16, 21492-21504, doi:10.1364/OE.16.021492, PMID: 19104579 (2008) Also appeared in Virtual Journal for Biomedical Optics, OSA, Vol. 4(2) (2009)
8. F. Vasefi, B. Kaminska, P.K.Y. Chan, and G.H. Chapman, "Multi-spectral angular domain optical imaging in biological tissues using diode laser sources," Opt. Express, Vol. 16, 14456-14468, doi:10.1364/OE.16.014456, PMID: 18794982 (2008). Also appeared in Virtual Journal for Biomedical Optics, OSA, Vol. 3(11) (2008)
9. F. Vasefi, P.K.Y. Chan, B. Kaminska, G.H. Chapman, N. Pfeiffer, "An Optical Imaging Technique Using Deep Illumination in the Angular Domain," IEEE J. Sel. Top. Quantum Electron. 13(6), 1610-1620, doi: 10.1109/JSTQE.2007.910997 (2007).

CONFERENCE PROCEEDINGS:

1. Vasefi, F., Najiminaini, M., Ng, E., Kaminska, B., & Carson, J. J. L., "Angular Domain Spectroscopic Imaging of Turbid Media: Derivative Analysis" Accepted in to SPIE Photonics West conference, Optical Interactions with Tissue and Cells XXII, San Francisco, January 2011.
2. Vasefi, F., Najiminaini, M., Kaminska, B., & Carson, J. J. L., "Experimental analysis of cross-talk effects between a series of nano-hole structures on the same metal film" Accepted in SPIE Photonics West conference, Nanoscale Imaging, Sensing, and Actuation for Biomedical Applications VII, San Francisco, January 2011.
3. Najiminaini, M., Vasefi, F., Kaminska, B., & Carson, J. J. L., "Experimental Analysis of Optical Resonance Transmission Properties of Sub-wavelength Hole Arrays in Optically Thick Metal Films," Accepted in SPIE Photonics West conference, Plasmonics in Biology and Medicine VIII, San Francisco, January 2011.
4. Najiminaini, M., Vasefi, F., Kaminska, B., & Carson, J. J. L., "Effect of Adhesion Layer on Optical Resonance Transmission Properties of Nano-hole Arrays in an Optically Thick Gold Film," Accepted in SPIE Photonics West conference, Plasmonics in Biology and Medicine VIII, San Francisco, January 2011.
5. Ng, E., Vasefi, F., Kaminska, B., & Carson, J. J. L., "Three dimensional angular domain optical projection tomography", Accepted in SPIE Photonics

West conference, Optical Interactions with Tissue and Cells XXII, San Francisco, January 2011.

6. Zhang, Y., Vasefi, F., Ng, E., Chamson-Reig, A., Kaminska, B., & Carson, J.J. L., "Deep Illumination Angular Domain Spectroscopic Imaging (ADSI): a Tissue-Mimicking Phantom Study", Accepted in SPIE Photonics West, Optical Tomography and Spectroscopy of Tissue IX conference, San Francisco, January 2011.
7. Zhang, Y., Vasefi, F., Najiminaini, M., Kaminska, B., & Carson, J.J. L., "Optimization of Radial Angular Filter Arrays for Detecting Angular Light Distributions", Accepted in SPIE Photonics West, Optical Fibers, Sensors, and Devices for Biomedical Diagnostics and Treatment XI conference, San Francisco, January 2011.
8. Vasefi, F., Chamson-Reig, A., Kaminska, B., & Carson, J.J.L., "Hyperspectral optical imaging of tissues using silicon micromachined microchannel arrays," Proceedings of SPIE 7750, 77500G (2010).
9. Najiminaini, M., Vasefi, F., Landrock, C. K., Kaminska, B., & Carson, J. J. L., "Optical Transmission Analysis of Nano-Hole Array as a Function of Incident Light Propagation Angles," in Biomedical Optics, OSA Technical Digest (CD), paper BTuD105 (2010).
10. Tichauer, K. M., Najiminaini, M., Vasefi, F., Lee, T., Kaminska, B., Carson, J. J. L., "Improved Lifetime Analysis Using Angular-Domain Fluorescence

Imaging in a Tissue-Like Phantom," in Biomedical Optics, OSA Technical Digest (CD), paper BTuD75, (2010).

11. Vasefi, F., Akhbardeh, A., Najiminaini, M., Kaminska, B., Chapman, G. H., & Carson, J. J. L., "Correction of Artifacts in Angular Domain Imaging," in Biomedical Optics, OSA Technical Digest (CD), paper BSuD36 (2010).
12. Vasefi, F., Ng, E., Najiminaini, M., Albert, G., Kaminska, B., Chapman, G. H., & Carson, J. J. L., "Angular domain spectroscopic imaging of turbid media using silicon micromachined microchannel arrays," Proceedings of SPIE, 7568, 75681K (2010).
13. Vasefi, F., Ng, E., Najiminaini, M., Kaminska, B., Chapman, G.H., Zeng, H., & Carson, J.J.L., "Angle-resolved diffused scattered light spectroscopy using radial angular filter arrays," Proc. SPIE, 7562, 756209 (2010)
14. Ng, E., Vasefi, F., Kaminska, B., Chapman, G. H., & Carson, J. J. L., "Contrast and resolution analysis of angular domain imaging for iterative optical projection tomography reconstruction," Proceedings of SPIE, 7557, 755714 (2010)
15. Najiminaini, M., Vasefi, F., Landrock, C. K., Kaminska, B., & Carson, J. J. L., "Experimental and numerical analysis of extraordinary optical transmission through nano-hole arrays in a thick metal film," Proceedings of SPIE, 7577, 75770Z (2010)

16. Vasefi, F., Hung, B. S. L., Kaminska, B., Chapman, G. H., & Carson, J. J. L., "Angular domain optical imaging of turbid media using enhanced micro-tunnel filter arrays," Proceedings of SPIE Vol. 7369, 73691N (2009).
17. Najiminaini, M., Vasefi, F., Kaminska, B., Chapman, G.H., & Carson, J.J.L., "Macroscopic fluorescent lifetime imaging in turbid media using angular filter arrays," The 31st Annual International Conference of IEEE EMBS, Pages: 5364-5368, (2009).
18. Vasefi, F., Kaminska, B., Chapman, G. H., & Carson, J. J. L., "Angular distribution of quasi-ballistic light measured through turbid media using angular domain optical imaging," Proceedings of SPIE, 7175, 717509 (2009).
19. Vasefi, F., Kaminska, B., Jordan, K., Chapman, G. H., Carson, J. J. L., "Angular domain optical projection tomography in turbid media," Proceedings of SPIE, 7174, 71740D (2009)
20. Vasefi, F., Ng, E., Kaminska, B., Chapman, G. H., & Carson, J. J. L., "Effect of time gating and polarization discrimination of propagating light in turbid media during angular domain imaging (ADI)," Proceedings of SPIE, 7182, 718217 (2009).
21. Vasefi, F., Ng, E., Kaminska, B., Chapman, G. H., & Carson, J. J. L., "Angular domain fluorescent lifetime imaging in turbid media," Proceedings of SPIE Vol. 7183, 71830I (2009)

22. Ng, E., Vasefi, F., Kaminska, B., Chapman, G. H., & Carson, J. J. L.,
"Image contrast enhancement during time-angular domain imaging through
turbid media by estimation of background scattered light," Proceedings of
SPIE, 7182, 71821C (2009)
23. Tsui, P. B. L., Chapman, G. H., Cheng, R. L. K., Pfeiffer, N., Vasefi, F., &
Kaminska, B., "Spatiofrequency filter in turbid medium enhanced by
background scattered light subtraction from a deviated laser source,"
Proceedings of SPIE, 7175, 71750A (2009)
24. Vasefi, F., Kaminska, B., & Chapman, G.H., "Domain Optical Imaging Using
a Micromachined Tunnel Array and a Keplerian Lens System," The 30th
Annual International Conference of IEEE EMBS, Pages: 3730-3734, (2008)
25. Vasefi, F., Chapman, G. H., Chan, P., Kaminska, B., & Pfeiffer, N.,
"Enhanced angular domain optical imaging by background scattered light
subtraction from a deviated laser source," Proceedings of SPIE, 6854,
68541E, (2008)
26. Pfeiffer, N., Chan, P., Chapman, G. H., Vasefi, F., & Kaminska, B., "Optical
imaging of structures within highly scattering material using a lens and
aperture to form a spatiofrequency filter," Proceedings of SPIE, 6854,
68541D, (2008)
27. Chan, P. K. Y, Vasefi, F., Chapman, G. H., Kaminska, B., & Pfeiffer, N.,
"Multispectral angular domain optical tomography in scattering media with

- argon and diode laser sources,” Proceedings of SPIE, 6435, 64350M, (2007)
28. Vasefi, F., Chan, P.K.Y., Kaminska, B., and Chapman, G.H., “Subsurface Bioimaging Using Angular Domain Optical Backscattering Illumination”, The 28th Annual International Conference of IEEE EMBS Proceedings, 1932-1936, (2006)
 29. Vasefi, F., Chan, P.K.Y., Kaminska, B., and Chapman, G. H., “Deep Illumination Angular Domain Imaging of Objects within Highly Scattering Media with Enhanced Image Processing,” Proceedings of SPIE, 6380, 63800Q, (2006).
 30. Chapman, G. H., Rao, J., Liu, T., Chan. P.K.Y., Vasefi, F., Kaminska, B. and Pfeiffer, N., “Enhanced angular domain image in turbid medium using Gaussian line illumination,” Proceedings of SPIE, 6084, 60841D (2006).
 31. Vasefi, F., Kaminska, B., Chapman, G.H., and Chan., P.K.Y., “Angular Domain Imaging for Tissue Mapping,” IEEE Bio Micro and Nanosystems Conference, BMN '06 , 39-45, (2006)
 32. Vasefi, F., & Abid, Z.E., “Design of Silicon Devices for Pass-Transistor-Logic Circuits,” Proceedings of 2005 International Semiconductor Device Research Symposium (ISDRS), WP7-09-06, 396 – 397, (2005)
 33. Vasefi, F., & Abid, Z.E., “Low power n-bit Adders and Multiplier using the lowest-number-of-Transistor 1-bit Adders,” The 18th Canadian Conference

on Electrical and computer Engineering, CCECE Proceeding. 1731 – 1734, (2005).

34. Vasefi, F., & Abid, Z.E., “10-Transistor 1-bit Adders for n-bit Parallel Adders,” The 16th International Conference on Microelectronics, ICM 2004 Proceedings, 174 – 177, (2004).